DOCTORAL THESIS

Gamma-Ray Spectroscopy of Neutron-Deficient Nuclides ^{129}Nd, ^{131}Pm and ^{132}Pm

Author:
Conor Sullivan

Supervisors:
Dr. Eddie Paul
Prof. David Joss

Thesis submitted in accordance with the requirements of the University of Liverpool for the degree of Doctor in Philosophy by

Conor Michael Sullivan

April 21, 2023

Declaration of Authorship

I, Conor Sullivan, declare that this thesis titled, "Gamma-Ray Spectroscopy of Neutron-Deficient Nuclides ^{129}Nd, ^{131}Pm and ^{132}Pm" and the work presented in it are my own. I confirm that:

- This work was done wholly or mainly while in candidature for a research degree at this University.
- Where any part of this thesis has previously been submitted for a degree or any other qualification at this University or any other institution, this has been clearly stated.
- Where I have consulted the published work of others, this is always clearly attributed.
- Where I have quoted from the work of others, the source is always given. With the exception of such quotations, this thesis is entirely my own work.

Signed:

Date:

UNIVERSITY OF LIVERPOOL

Abstract

Department of Physics

Doctor of Philosophy

Gamma-Ray Spectroscopy of Neutron-Deficient Nuclides ^{129}Nd, ^{131}Pm and ^{132}Pm

by Conor Sullivan

The newly commissioned MARA recoil separator has been coupled with the efficient high-purity germanium (HPGe) JUROGAM γ-ray spectrometer and a suite of focal-plane detector systems to facilitate detailed studies of in-beam and isomeric delayed radiation emitted by various types of nuclides. Excited quantum states were populated in the highly neutron-deficient nuclides ^{129}Nd, ^{131}Pm and ^{132}Pm utilising the fusion-evaporation reaction $^{58}\text{Ni} +^{78}\text{Kr} \longrightarrow^{136} \text{Gd}^*$.

In the study of ^{129}Nd, three new isomeric states were observed at excitation energies of 1893, 2109 and 2284 keV, respectively. The state at 2284 keV was measured to have a half-life of 679 ± 60 ns. Excited states existing above this level were measured using the JUROGAM spectrometer and characterised within the framework of the cranked shell model.

The study of ^{131}Pm focused on detailed in-beam γ-ray measurements, resulting in extensions to the yrast band at high and low spin. To accommodate the lowest spin states, reinterpretation of the band in terms of its deformation aligned nature resulted in reassignment of the yrast band to Nilsson orbital [532]$5/2^-$. The lowest spin state of $5/2^-$ is then proposed to be the ground state, in agreement with theoretical studies.

Finally, band extensions at high and low spin were made in the study of doubly-odd ^{132}Pm. Two low-spin isomeric states were measured, with half-lives of 187 ± 4 ns and 19.9 ± 0.5 μs. γ radiation observed to depopulate these states is proposed to feed the ground state of the this nucleus, allowing unambiguous assignment of absolute excitation energies for two of the four observed bands.

Author Contribution

The wonder is, not that the field of stars is so vast, but that man has measured it. - Anatole France, The Garden of Epicurus (1894)

Acknowledgements

Realistically, no amount of words can express the heartfelt gratitude and insurmountable debt I owe to the incredible human beings who have carried (and at times, dragged) me to this point, the completion of a PhD. I never intended this page to be longer than just that, but writing this section made me realise just how many people to whom I owe everything I am.

My first thanks go to my supervisor, Dr Eddie Paul. A man who is warm, modest and a genius, I couldn't have completed this work without you. A tesseract (hypercube) could not contain the knowledge accumulated by you over your stellar career, spanning nearly four decades. In aiding me with my work, you have been indispensable. Conversations with you consistently leave me humbled, and I can only hope that the work I have produced here can live up to the mighty standards you have set.

Equal gratitude is due to my other supervisor, Professor David Joss. Dave, without you I would have had no project to complete, after my search for ultra high-spin states in ^{161}Lu proved ill fated. Your endless patience for my tedious questions and lengthy emails was and is always appreciated. Your approachable nature and ability to answer the vaguest question with a comprehensive hour long mini-lecture course earned my admiration and the admiration of all those lucky enough to be your student. You also gave me the opportunity to travel to Jyväskylä. Not only did I gain invaluable experimental knowledge there, but I made friends and memories from once-in-a-lifetime experiences that I will carry with me forever. Proving to be an excellent travelling companion, your mutual enjoyment of an airport Burger King is gratefully acknowledged by both myself and the School Finance Team who are always keen to keep costs down!

Thanks must go to Professor Robert Page, whose considerable time and effort spent helping with my analysis have undoubtedly shaped this thesis and my learning experience into better versions of themselves. Robert, I know I

always joked that our meetings would leave me with more questions than answers, but I sincerely appreciated your input at all times. Science and scientific collaborations are more powerful thanks to those who can think outside of the box and you are one of the best at it.

When it came to some of my most esoteric questions, Professor Rodi Herzberg's encyclopedic knowledge was barely scratched. Figure 3.10 in Chapter 3 — my personal favourite figure in this thesis — is dedicated to you.

No thesis is complete without data, and no data would have been recorded if not for the stellar team at the accelerator laboratory in the University of Jyväskylä. Professors Juha Uusitalo and Paul Greenlees, Doctors Jan Saren and Panu Rahkila, and many others too innumerable to list, thank you.

Special thanks to Professor Mark Riley at Florida State University for allowing me access to his unpublished data on the nucleus ^{135}Pm. Your generosity allowed my systematic comparison of odd-Z even-N promethium isotopes to be wholly more substantial.

To my girlfriend Yuliana: throughout my work you have elevated and encouraged me with steadfast persistence. Your optimism and kindness were indispensable and at times you cared more about my work than your own. Whenever my own confidence waned (which was often), sharing your own experience in completing a PhD allowed me to find my footing again. Your humble demeanour and caring nature are always tempered by precision, collectedness and skill. A true professional, I hope one day to be even half the researcher that you are. Thank you.

Some of the things I felt the loss of during lockdown were the energy, creativity and collaboration stimulated by informal, daily, in-person interactions with my fellow post-graduate colleagues. Particular recognition goes to Andy Briscoe, Josh Hilton, Lorna Waring and Holly Tann - you guys are the best.

Despite my age advancing linearly with time, the same can not be said for my maturity. Though I am a saner person as an adult, I recognise that I was

not the easiest child to interact with. Miss Casey — who was my high school science teacher — sparked my interest in physics. Really, you started this journey for me and I hope that, whatever you're doing now, you're satisfied in the knowledge you helped shape countless young people's lives and careers for the better. Mrs Garner and Mrs Watterson were the poor souls tasked with taking my physics and maths learning to advanced level. Mrs Garner, you made physics exciting, giving me the chance to progress and believing in me despite my subpar AS-level result. That you also loved Noel Gallagher was an added bonus! Mrs Watterson your one-to-one support, frank and unadulterated conversations on what I could achieve — if I set my mind to it — and unparalleled maths teaching cement you as one of my all time favourite teachers. To both of you, I still hold vivid memories of your classes, and the lessons I learned there — concerning all of physics, mathematics and life — I will never forget.

Thank you to the STFC for funding my research and lifestyle throughout my time in Liverpool. To paraphrase a Japanese proverb: "physics and funding are like the two wheels of a cart".

I've spoken much about my struggle to get to this point, and as with all journeys it is often the last stretch that is the most arduous - particularly when the last stretch is under the conditions of a pandemic. I seriously doubt that I could have made it through the last two years if not for the calming influence of my closest friends Paul, Steve, LT, Callum and Charlotte. Paul, you've been my friend since we were 4. You've been there since day one and it's my sincere hope that our friendship lasts for all time. Steve and LT, our friendship was cemented during the legendary reign of Steve Jobs and The Apples, and you've both proven to embody some of the best characteristics friends can have: good humour and loyalty, but most importantly providing that service of honest and introspective critique that only true friends can level with you. Callum and Charlotte, you're two of my newest friends, but that says

nothing to diminish our bond. Charlotte, you were my student at one point. From struggling to put together a MATLAB script to becoming a fully qualified teacher and passing the seed to the next generation, I'm so proud of you and of our friendship. Callum, there are few people who have ever been able to connect with me on such a visceral and emotional level. From the first instance we simply understood each other. You've both been there for me during some of the darkest times in my life, and I'll never forget that.

Finally to my Mum and Dad, without whose predisposition toward patience, problem solving and intelligence, I would never have reached this point. You guys pushed and prodded me every step of the way and look at me now. Thank you.

Contents

Declaration of Authorship **iii**

Abstract **v**

Author Contribution **vii**

Acknowledgements **ix**

1 Introduction **1**

1.1 Why Study Nuclear Structure? 1

1.2 Experiment JM06 5

2 Theoretical Overview of Nuclear Models **9**

2.1 Historical Nuclear Structure 9

2.2 The Shell Model Of The Nucleus 10

2.2.1 Harmonic Oscillator Potential 11

2.2.2 Spin-Orbit Correction 14

2.2.3 Woods-Saxon Potential 16

2.3 The Deformed Shell Model Of The Nucleus 17

2.3.1 Anisotropic Harmonic Oscillator Potential 19

2.3.2 Nilsson Potential 22

2.4 Nuclear Rotation - Non-Collective Excitation and Collective Rotation 26

2.4.1 Single Particle Excitation 27

2.4.2 Collective Excitation 28

$K = 0$ Rotational Bands 28
$K \neq 0$ Rotational Bands 29
2.4.3 Pairing / Coriolis Antipairing 30
2.5 Quasiparticles 32
2.6 Cranked Shell Model 33
2.7 Nuclear Isomers 35
2.7.1 K-Isomer 35
2.7.2 Yrast/Spin Trap Isomer 38
2.7.3 Fission Isomer 38
2.8 Measurable Quantities 39
2.8.1 Rotational Frequency 39
2.8.2 Moments of Inertia 40
2.8.3 Experimental Alignment 41
2.8.4 Experimental Routhian 41
2.9 B(M1)/B(E2) Ratios 42

3 Experimental Theory, Setup & Methods **43**
3.1 Gamma Emission in Nuclei 43
3.2 Gamma-Ray Spectroscopy 48
3.2.1 Interaction of Gamma Rays with Matter 48
3.2.2 Fusion-Evaporation Reactions 48
3.2.3 Limitations of Conventional Gamma-Ray Spectroscopy . 51
3.3 Recoil-Decay Tagging (RDT) 52
3.4 Total Data Readout (TDR) & GRAIN 54
3.5 JYFL-ACCLAB Experimental Setup 56
3.5.1 K130 Cyclotron 56
3.5.2 The JUROGAM3 Spectrometer 57
3.5.3 Mass selection using MARA 67
m/q Selection Using MARA 67

Selection Using Mass Slits 69
3.5.4 Multi-Wire Proportional Counter (MWPC) 69
3.5.5 Double-Sided Strip Detector (DSSD) 71
3.5.6 Focal Plane Germanium Detectors 73
3.6 JUROGAM3 and Focal Plane Germanium Calibration 73
3.7 Doppler Correction 77
3.8 RADWARE 79

4 High-Spin Isomers in $^{129}_{60}$Nd 81
4.1 Previous work 82
4.2 Experimental Details 83
4.3 Results 84
4.3.1 Isomer-delayed γ-ray coincidences 84
4.3.2 Prompt γ-ray coincidences 94
4.3.3 Half-life Measurements 97
4.4 Theoretical Comparison and Discussion 100
4.4.1 Other isomeric states 109
4.4.2 B(M1)/B(E2) Ratios 111

5 Signature-partner and extensions to the yrast band in $^{131}_{61}$Pm 113
5.1 Previous work 113
5.2 Experimental Procedure 114
5.3 Results 115
5.3.1 Prompt γ-ray coincidences 115
5.3.2 Extending Below the $11/2^-$ Level 123
5.4 Systematic comparison with other odd-Z even-N Pr, La, Pm and Cs isotopes in the region 133
5.5 Structure, Alignments and Experimental Routhians 141
5.6 Other Considered Level Schemes 147

6 Detailed Gamma-Ray Spectroscopy of $^{132}_{61}$Pm 153

6.1 Literature Review 154

6.2 γ-ray spectroscopy 157

6.2.1 Prompt γ-ray coincidences 157

Band 1 157

Band 2 159

Bands 3 and 4 163

6.2.2 Delayed γ rays 168

6.3 Half-life measurements 183

6.4 Discussion 186

6.4.1 B(M1)/B(E2) Ratios 196

7 Conclusion 199

7.1 ^{129}Nd 199

7.2 ^{131}Pm 200

7.3 ^{132}Pm 201

7.4 Limitations of the JM06 Experiment and Future Improvements . 203

A Relativistic Doppler Correction 207

B Phase 1 Gain Matching 209

List of Figures

1.1 Predicted relative production cross-sections as a function of beam energy for a selection of nuclides given a ^{78}Kr beam on a target of ^{58}Ni. Production cross-sections are produced by Monte-Carlo simulation using the software PACE4 [11, 12]. 6

1.2 Predicted relative production cross-section for a subsection of the chart of the nuclides, produced by Monte-Carlo simulation using the software PACE4. Larger coloured squares indicate a larger relative yield. Calculation results are displayed for both high beam energy (390 MeV, top panel) and low beam energy (364 MeV, bottom panel). 7

1.3 A subsection of the (Segre) chart of the nuclides focusing on the mass region studied in this thesis. The compound nucleus ^{136}Gd is coloured dark grey. Nuclides discussed in this thesis are coloured dark-green and nuclides observed in the data but not discussed in detail here are coloured light-green. 8

2.1 Energy eigenvalues for the first five N states of the harmonic oscillator potential. Energy states are labelled by the oscillator quantum number N (equal to the number of nodes in the waveform), and their principal and angular momentum quantum number components, (nl). l is labelled using the spectroscopic notation. 12

2.2 Quantum harmonic oscillator potential eigenstates with l^2 and $\vec{l}\cdot\vec{s}$ corrections. Final energy states are labelled nl_j, where n is the principal quantum number, l is the angular momentum quantum number, and $j = l \pm \frac{1}{2}$ is the total angular momentum quantum number. 15

2.3 Comparison of different nuclear potential wells as a function of the radial distance from the center of the nucleus, r. The full nuclear radius is labelled R. Parameters used in the model include $V_0 = 50$ MeV, $a = 1.5$ fm and $R = 15$ fm. 16

2.4 The Lund Convention for specification of triaxial deformation along three principal axes. Lines along the deformed nucleus represent nucleon orbital paths, with their individual angular momenta aligned in the plane perpendicular to this orbital. Figure courtesy of Ref [19]. 19

2.5 Nuclear energy eigenstates for the anisotropic harmonic oscillator potential as a function of nuclear deformation, ϵ. We have, $\omega_0 = \frac{1}{3}(2\omega_\perp + \omega_z)$, $N = n_\perp + n_z$, degeneracy $d = 2(n_\perp + 1)$ where the factor 2 is for each nucleon spin $s = \pm\frac{1}{2}$ and the orbital degeneracy is illustrated by false splitting of the lines. The labels on the x-axis indicate minimum to maximum axis ratios corresponding to axially oblate, spherical, and axially prolate superdeformed and hyperdeformed shapes. Equations used to produce figure adapted from [20]. 21

2.6 Projections of the spin quantum numbers (s, l, j) labelled with the asymptotic quantum numbers Σ, Λ and Ω. 23

2.7 Nilsson diagram for protons calculated using an anisotropic Woods-Saxon potential. Full shell closures at zero deformation are indicated, along with the spherical shell numbers l_j. 24

2.8 Nilsson diagram for neutrons calculated using an anisotropic Woods-Saxon potential. Full shell closures at zero deformation are indicated, along with the spherical shell numbers l_j. 25

2.9 Depiction of a deformed and rotating nucleus with two valence particles. The projection of the total single-particle contribution to the nuclear spin, $J = j_1 + j_2 \rightarrow \Omega = \Omega_1 + \Omega_2$ is detailed. The projection of the total nuclear spin, $I = J + R \rightarrow K$ is also indicated, where R is the contribution arising from the collective motion of the nuclear core. 26

2.10 Static moment of inertia as a function of the square of angular frequency for the two rotational ground state bands in ^{162}Hf (crosses) and ^{164}Hf (dots). The phenomenon known as backbending is exhibited here in spectacular fashion, with ^{162}Hf showing two backbends, corresponding to the alignment of pairs of $i_{13/2}$ neutrons and $h_{11/2}$ protons, respectively [22]. 31

2.11 Panel a): quasiparticle Routhians for protons with $Z = 61$. Panel b): quasiparticle Routhians for neutrons with $N = 71$. Both diagrams calculated using parameters $\beta_2 = 0.35, \beta_4 = 0.0, \gamma = 0.0$. (π, α): solid = (+,+1/2), dotted = (+,–1/2), dot–dash=(–,+1/2), dashed=(–,–1/2). 34

2.12 Left: Four unpaired nucleons contribute a large amount of angular momentum to the total nuclear angular momentum, I. The projections of each of these contributions along the z (symmetry) axis make for a large K. Right: the same nucleus but with small single-particle contribution making for a small K; all unpaired nucleons are aligning with the rotational axis and make a limited contribution to the total angular momentum. 36

2.13 Partial level scheme for the nucleus ^{178}Hf. Here, the ground-state band and two connected isomeric bands are displayed. The nature of the isomerism for both bands is due to the requirement of a large change in K for decay to occur. 37

2.14 Hypothetical first and second (superdeformed) potential energy minima for a heavy and highly deformed nucleus. 39

3.1 Weisskopf half-life estimates as a function of transition energy, for multipolarities M1-5 and E1-5, assuming a mass-130 nucleus. 47

3.2 Schematic diagram of a fusion-evaporation reaction depicting the impact parameter, b. 49

3.3 Schematic diagram indicating two hypothetical decay paths from the moment of fusion to the ground state of the recoil. 50

3.4 Schematic diagram of a typical recoil-decay experimental setup where the recoiling nucleus is travelling from left to right [41]. Here, $t = 0$ is when the recoil implants into the DSSD. γ emission at the target position is then in the past relative to the implantation event. 52

3.5 Schematic diagram representing the timeline of an excited nucleus as it travels throughout the detector equipment. 55

3.6 Overview schematic diagram of the K130 Cyclotron and its components [44]. 56

3.7 Schematic rendering of the JUROGAM3 highly-purified germanium (HPGe) array. The various detector rings are marked and coloured for ease of identification. The ion beam delivered by the K130 cyclotron moves from right to left as indicated by the arrow. [45] 57

3.8 Measured efficiency as a function of energy for the entire JUROGAM3 array at the beginning of the JM06 run. Fit given by Equation 3.14 with fit parameters for the whole array: A: 122.56, B: -215.07, C: 85.26, D: -12.49, E: 0.64; the Clovers only: A: 1389.97, B: -1039.59, C: -285.41, D: -34.04, E: 1.51; and the Phase 1 detectors only: A: -207.72, B: 100.21, C: -15.56, D: 0.76, E: 0.01. 59

3.9 Main figure: Rendering of the relative positions of the 24 composite Clover detectors. The detectors are arranged in two rings, mounted at $\theta = 75.5^\circ$ and 104.5° respectively, with respect to the beam axis. A γ ray (black arrow) is incident on one of the detectors. Angles θ and ϕ represent the polar and azimuthal angles between the γ ray and the beam. Inset: example of the preferential direction a γ ray will Compton scatter depending on the orientation of its electric field vector, $\vec{E}$, relative to the reaction plane. 60

3.10 Top: Projections of the Compton scattering cross-section (all axes in barns) for linearly polarised γ rays (Equation 3.17) for all angles of ϵ and ζ with E_γ, $E_{\gamma'} = 0.5$, 0.27 MeV. Bottom: The same as above, but with the scattering angle, ϵ, fixed at 90°. 63

3.11 Measured linear polarisations and DCO ratios for transitions in ^{117}I measured using the EUROGAM-II spectrometer. Data from [49], figure adapted from [19]. 65

3.12 Experimentally observed scatters throughout the JM06 experimental run for the yrast band in ^{132}Pm. Overlaid on this spectrum is the theoretical curve for incoherent (Compton) scattering events, obtained from the calculations in Ref [12]. 65

3.13 3-dimensional rendering of the experimental setup including the MARA recoil separator. The beam direction is from right to left with the static target installed at the center of the JUROGAM array. Figure adapted from Ref [50]. 67

3.14 Ion trajectories inside MARA from above (top figure) and the side (bottom figure) with a straightened beam axis. Adapted from Ref [51]. 69

3.15 Measured centroid position for each DSSD-Y strip after gain matching is applied. Green lines indicate "true" energy of the alpha source. 72

3.16 Measured centroid position (channel) for each Clover crystal after gain matching, overlaid on the "true" energy for each major photopeak in the ^{152}Eu^{133}Ba spectrum. Missing points for crystals 9, 41, 43, 92 are because these detectors were not counting during the experimental run. 74

3.17 Measured centroid position (channel) for each Phase 1 detector after gain matching, overlaid on the "true" energy for each major photopeak in the ^{152}Eu^{133}Ba spectrum. 75

3.18 Measured centroid position (channel) for each focal plane Clover crystal after gain matching, overlaid on the "true" energy for each major photopeak in the ^{152}Eu^{133}Ba spectrum. Calibration data was taken from the end of the experimental run as described in the text. 76

3.19 Doppler shift of an in-beam photopeak from the JM06 dataset. . 77

3.20 Measured (Doppler shifted) centroid position for an in-beam peak as a function of θ for the JUROGAM setup in the JM06 experiment. χ^2/ndf: 0.13. 78

3.21 Graphical representation of 1D, 2D and 3D γ coincidence matrices. Each "dimension" is E_γ, with the number of counts projected along the extra axis. 3D representation adapted from [19]. 80

3.22 Number of events as a function of the γ-ray multiplicity for all events in correlation with a valid recoil for the entire JM06 run. Inset: same plot with linear scale. 80

4.1 Partial energy-level scheme for ^{129}Nd comprising the four previously known one-quasineutron bands as published by Zeidan, *et al* [58]. Band numbering scheme is the same in this thesis as it is in the reference. 82

4.2 Panel (a): all γ rays detected at the MARA focal plane following implantation of a valid recoil. Panel (b): all γ rays detected at the MARA focal plane following implantation of a valid mass 129 or mass 133 recoil. Panel (c): all γ rays detected at the MARA focal plane following implantation of a valid mass 129 or mass 133 recoil and in coincidence (< 1 μs) with an 847 keV γ ray. Dominating this spectrum are γ rays depopulating levels beneath the $17/2^+$ level in band 3. The peaks visible at 36 and 42 keV respectively correspond to the K_α and K_β internal-conversion x-rays for neodymium. 85

4.3 γ rays observed in prompt coincidence with both 146 **and** 178 keV, using the JUROGAM spectrometer. Transitions belonging to band 3 of ^{129}Nd are observed, but notably not the 847 keV and 69 keV transitions, which are isomer delayed and only observed at the focal plane. 86

4.4 Focal-plane γ rays associated with mass 129 and mass 133 recoils and measured in delayed coincidence with any two γ rays seen at JUROGAM from a list composed of the γ rays built atop the isomeric state, listed in Table 4.1. Known transitions belonging to bands in ^{129}Nd are observed, along with new transitions feeding these states (highlighted in bold). The colour scheme helps identify which γ ray belongs to which band, and follows the same scheme as in Table 4.1 and Figure 4.10 (Pink = Band 1, Blue = Band 2, Purple = Band 3). 87

4.5 γ-ray spectra extracted from a "delayed", focal-plane doubles (γ^2) matrix with a coincidence window of 1μs. Panel a): focal-plane transitions in coincidence with 130 **or** 162 keV, associated with band 1. γ rays associated with band 1 are visible, alongside evidence for new transitions with energies 175, 391, 566, 847, 1050, 1139 and 1182 keV. Panel b): transitions in coincidence with 146 **or** 178 keV, associated with band 3. γ rays associated with band 3 are visible, alongside evidence for new transitions with energies 69, 536 and 847 keV. Panel c): transitions in coincidence with 439 keV, associated with band 2. γ rays associated with band 2 are visible, alongside evidence for a new transition with energy 795 keV. 88

4.6 Partial level scheme for ^{129}Nd composed from the delayed γ^2 analysis displayed in Figure 4.5. The newly observed isomeric states are labelled levels A, B and C, and are connected to the existing level scheme by the γ rays displayed in Figures 4.4 and 4.5. 90

4.7 γ-ray spectra extracted from a "delayed" doubles (γ^2) matrix with a coincidence window of 1μs. Panel a): transitions associated with the 1182 keV transition. Evidence is seen here for a transition of energy 216 keV, linking levels B and C in the partial level scheme of Figure 4.6. Panel b): transitions associated with the 1139 keV transition. Here, only the 175 keV transition is visible and not the 216 keV transition, supporting the partial level scheme displayed in Figure 4.6. 91

4.8 γ-ray spectra extracted from a "delayed" doubles (γ^2) matrix with a coincidence window of 1μs. All four spectra display transitions belonging to the low-spin states of band 3. Panel a): γ rays in coincidence with 673 keV. Panel b): γ rays in coincidence with 739 keV. Panel c): γ rays in coincidence with 955 keV. Panel d): γ rays in coincidence with 1009 keV. 93

4.9 γ rays observed at the target position by JUROGAM in delayed coincidence with the 146, 178, 239, 392, 453, 551 **or** 847 keV transitions detected at the focal plane. The correlation time for recoil-isomer decay correlations was limited to 1μs. 94

4.10 The final (partial) level scheme for ^{129}Nd. Here, band 5, the bandheads of bands 6 and 7, and all of the γ rays depopulating them are original work. Bands 1, 2 and 3 are constructed using data obtained from the study performed by Zeidan, *et al.* The levels associated with the bandheads of bands 6 and 7 have no definite spin/parity assignments, but their excitation energies are fixed. So too are the excitation energies of all levels presented in this scheme, with the proposed ground state being the $7/2^-$ level of band 1. For easier viewing, the γ rays depopulating band 5 are colour coded to the band that they decay into. The proposed configuration for band 5 is discussed and substantiated in the following section. 96

4.11 Time difference between the implantation of a recoil into the DSSD and the detection of an 847 keV γ ray at the focal plane. The fit is a single-term exponential with a single-term polynomial background. Fit parameters $A : 895 \pm 69, B : -0.015 \pm 0.001, C : 0.0009 \pm 0.0030, D : 74 \pm 23$. 97

4.12 Measured timing difference between two focal-plane γ-rays. The shift of the peak centroid is representative of the mean lifetime of the level(s) fed and depopulated by the respective transition, as per Equations 4.1 and 4.2. 99

4.13 **Top**: Nilsson diagram for protons centered around the 60 proton shell gap at high deformation. Black circles are proposed configurations for the protons when this nucleus is in the isomeric state at 2283 keV. At the ground-state, both protons are proposed to inhabit the [404]$9/2^+$ state. **Bottom**: Nilsson diagram for neutrons centered around the 70 neutron shell gap at high deformation. The black circle is the proposed level inhabited by the odd neutron when this nucleus is in the isomeric state at 2283 keV. Grey circles represent states with bands known to be built on the odd neutron occupying these states. 101

4.14 Experimental single-particle alignment diagrams for the four known bands in ^{129}Nd (data from [58]) and the new $21/2^+$ isomeric band (band 5). Band numbering is the same as in Ref [58] for simple comparison. 102

4.15 Cranked Shell Model quasiparticle Routhians (Panel π): protons, (Panel ν): neutrons. Both figures generated using a universal, triaxial Woods-Saxon potential with parameters β_2= 0.305, β_4 = 0.006, γ= -1.9°. Parameters used are the same as in Ref [58] to ensure consistency with their results. Labels referring to Nilsson levels — displayed in Table 4.2 — are only valid at zero spin (i.e $0\hbar\omega$) since rotation causes states to become a mixture of different wavefunctions. (π, α) : solid = (+,+1/2), dotted = (+,–1/2), dot–dash = (–,+1/2), dashed = (–,–1/2). 103

4.16 Partial level scheme for ^{135}Nd with the bands labelled by their associated quasiparticles. In The Nilsson levels associated with these quasiparticles are detailed in a tabulated format, alongside a plot of total calculated routhian for each quasiparticle configuration as a function of the triaxiality parameter, γ. The labeling convention has been adapted to match that used in this thesis. Reproduced from [61] with permission. 107

4.17 Ground-state bands and sidebands associated with the EA (for even-even nuclides) or EAe/f (for odd-even nuclides) quasiparticle configurations for various neodymium isotopes. 108

4.18 Experimentally determined B(M1)/B(E2) ratios for the rotational band built atop the isomeric $21/2^{+}$ state. 112

5.1 Sum of doubles gates on triples data using a gate list comprised of the previously known transitions in the yrast band of ^{131}Pm. The yrast rotational cascade is visible, alongside a host of new low-energy transitions. 67 keV is a doublet (66 and 68 keV). . . 117

5.2 Top: γ rays observed in coincidence with 205 and 407 keV. Here, the presence of the 67 keV intraband γ ray is clearly displayed along with a myriad of other γ rays belonging to ^{131}Pm. Bottom: An attempt to gate directly on 67 keV only results in evidence of the 97 keV and 407 keV peaks. This is due to the low level of counting statistics associated with the 67 keV γ ray. 119

5.3 MWPC-x coordinate against γ-ray energy for all recoils associated with γ rays observed in the decay of ^{131}Pm. MWPC coordinate ranges corresponding to different masses are highlighted. 121

5.4 Panel a): γ rays in coincidence with 97 and 273 keV. Immediately the signature partner can be noticed as a series of peaks running alongside the known yrast peaks. Panel b): measured photopeak centroids for the ≈407 keV peak belonging to each band. The solid line and left-hand y-axis details the peak belonging to the yrast band. The dotted line and right-hand y-axis details the peak belonging to the signature partner. The statistical uncertainty on the yrast/signature partner photopeak centroid is 0.05 and 0.02 keV, respectively. χ^2/NDF for each fit is 8.3 and 2.4. Panel c): sum of doubles gates, with list "A" comprising the lowest five E2 transitions in the yrast band (including 97 keV) and list "B" comprising the lowest five E2 members of the signature partner. Intraband M1s observed here are highlighted in bold text. Panel d): γ rays in coincidence with 97 and 406 keV, highlighting the 205 keV M1 transition between the $13/2^- \rightarrow 11/2^-$ states. Panel e): γ rays in coincidence with 273 and 530 keV, highlighting the 338 keV M1 transition between the $17/2^- \rightarrow 15/2^-$ states. Panel f): γ rays in coincidence with 408 and 637 keV, highlighting the 460 keV M1 transition between the $21/2^- \rightarrow 19/2^-$ states. Panel g): Sum of doubles gates across all transitions in the signature partner band. In panels a), c) and g) 67 keV and 407 keV are doublets as described in the text body. 122

5.5 Panel a): γ rays in coincidence with the 97 keV and 273 keV transitions. Here and in panel b), the 67 keV and 407 keV γ rays are doublets as described in the text. Panel b): γ rays in coincidence with the 147 keV and 273 keV transitions. Panel c): Double-γ gate on triples data on the 163 keV and 273 keV transitions. Contaminant decays not from ^{131}Pm are marked in italic. Here, the 408 keV γ ray is visible without the contamination of the 406 keV γ ray, since the gating transitions of 163 keV and 273 keV cascade in parallel to the 406 keV γ ray. 124
5.6 Panel a): Numerical fit to the 67 keV peak, gated by 147 **and** 273 keV as displayed in Figure 5.5, middle panel. Fit model is a single-term Gaussian overlaid on linear background. Number of counts under the peak is equal to 56 $\pm$ 10 after background subtraction. χ^2/NDF = 8.6. Panel b): Numerical fit to the 67 keV peak, gated by 97 **and** 273 keV as displayed in Figure 5.5, top panel. Number of counts under the peak is equal to 110 $\pm$ 13 after background subtraction. χ^2/NDF = 10.2. 125
5.7 Panel a): γ rays in coincidence with the 66 keV and 273 keV transitions. Here, the 408 keV γ ray is visible without the contamination of the 406 keV γ ray, since the gating transitions of 66 keV and 273 keV cascade in parallel to the 406 keV γ ray, even considering contamination from 68 and 271 keV. Panel b): Double-γ sum of gates on triples data between 66 keV and a list comprising transitions (205, 273, 408, 539, 650). The purpose for this is to highlight the 147 keV from among background, providing evidence that 66 keV is in coincidence with both 97 and 147 keV. The peak at 407 keV is a doublet, as described in the text. Panel c): Gaussian fit with linear background to the 147 keV peak displayed in panel b). Integrated peak area: 432 $\pm$ 238. 125

5.8 Panel a): γ rays coincident with 66 keV **and** 97 keV. Evidence for both signatures of the rotational band are observed, providing evidence for the coincidence between 97 keV and 66 keV. Panel b): No γ rays of any statistical significance are observed in coincidence with 77 keV **and** 97 keV. If a transition with energy 77 keV truly belongs to ^{131}Pm, it must be a transition to a level outside of the observed rotational band. 127

5.9 Panel a): γ rays in coincidence with both 147 keV **and** 271 keV. 407 keV is a doublet as described in the text. Panel b): γ rays in coincidence with both 271 keV **and** 406 keV. Panel c): γ rays in coincidence with both 406 keV **and** 530 keV. In all panels, transitions labelled in italic are contaminants belonging to ^{131}Nd. . . 130

5.10 Energy level scheme for ^{131}Pm produced via analysis of double and triple γ ray coincidence matrices. γ rays highlighted in red are new and unobserved before this work. Arrow widths are proportional to the γ ray intensity, with most transitions measured relative to the 97 keV yield. Intensities for transitions not in coincidence with 97 keV have been approximated based on relative peak intensities. Transitions in brackets are tentative and are discussed in more detail in the text body. 132

5.11 Systematic comparison of the relative energy spacing between the $h_{11/2}$ level and the positive parity structure it decays into for various odd-Z even-N nuclides in this mass region. ^{131}Pm level assuming ground state is $5/2^-$ level. 135

5.12 **Top row**: Relative excitation energy of the $11/2^-$ state for various odd-Z, even-N nuclides plotted as a function of their nuclear mass number, A (left panel), and theoretical ground-state quadrupole deformation, β_2 (right panel). **Middle row**: Isomeric half-life of the $h_{11/2}$ level plotted as a function of mass number, A (left panel), and β_2 (right panel). **Bottom row**: Excitation energy of the $9/2^+$ level for various odd-Z, even-N nuclides plotted as a function of mass number, A (left panel), and β_2 (right panel). 136

5.13 Theoretical ground-state deformations for various nuclides in the mass-130 region. The ground-state deformations were obtained from Moller, *et al*: Nuclear ground-state masses and deformations [85]. 138

5.14 Nilsson diagram for protons (top) and (neutrons) for prolate deformation only. The deformed shell gap at 60 protons is labelled, along with a vertical line representative of the predicted deformation of ^{131}Pm. The proposed orbital occupied by the odd proton is highlighted with a black dot. 141

5.15 All figures: solid circles represent the yrast band and crosses represent its signature partner. Harris parameters used in production of this figure, $\mathcal{J}_1 = 29.9\,\hbar^2/\mathrm{MeV}$ and $\mathcal{J}_1 = 15.8\,\hbar^4/\mathrm{MeV}^3$. Panel a): experimental single particle alignment. Panel b): experimental dynamic moment of inertia. Panel c): experimental routhian. 144

5.16 Cranked Shell Model quasiparticle Routhians (top: protons, bottom: neutrons), generated using a universal, triaxial Woods-Saxon potential. Labels corresponding to Nilsson levels are only valid at zero spin (i.e 0 $\hbar\omega$) since rotation causes states to become a mixture of different wavefunctions. β_2= 0.320, β_4 = 0.0, γ= 0.0°. (π, α) : solid = (+,+1/2), dotted = (+,–1/2), dot–dash = (–,+1/2), dashed = (–,–1/2). 145

5.17 Three level schemes considered as alternative explanations for the low spin structure of ^{131}Pm. 148

6.1 ^{132}Pm Band 1. Panel a): sum of doubles gates on triples data using a gate list comprised of all E2 transitions between even-spin levels in band 1. Panel b): sum of doubles gates on all E2 transitions between odd-spin levels in band 1. 158

6.2 ^{132}Pm Band 2. Sum of doubles gates on all γ rays assigned as belonging to band 2 and above $I^{\pi} = 5^{-}$, as displayed in Figure 6.15. 159

6.3 Panel a): γ rays in coincidence with 73 keV **and** 73 keV. The lowest four M1 transitions of band 2 are visible, providing evidence for the existence of two 73 keV transitions at the base of band 2. Panel b): γ rays in coincidence with 73 keV **and** 107 keV. A peak at 73 keV is visible along with various known members of band 2. 160

6.4 γ rays observed at JUROGAM in coincidence with both 142 keV **and** 180 keV. A small peak at 180 keV is visible, along with various other members of band 2. **Inset:** numerical fit to the 180 keV peak of a single term Gaussian superimposed on a linear background. The background subtracted number of counts under the curve is 305 ± 34. χ^2/NDF: 8.4. 162

6.5 ^{132}Pm Band 3. Panel a): sum of doubles gates on all γ rays in the preferred signature (lowest energy) cascade (204, 292, 385, 482, 581, 680, 774, 866, 951, 1028 keV). Panel b): sum of doubles gates on all γ rays in the non-preferred signature (higher energy) cascade (239, 320, 410, 516, 625, 731, 829, 917, 1025 keV). 164

6.6 ^{132}Pm Band 4. Panel a): sum of doubles gates on all γ rays in the preferred signature (lowest energy) cascade (181, 264, 352, 449, 540, 625, 706, 789, 870, 941, 1029, 1113 keV). Panel b): sum of doubles gates on all γ rays in the non-preferred signature (higher energy) cascade (218, 314, 414, 507, 590 674, 758, 854, 928 keV). Transitions marked with a * are contaminants from a nucleus other than ^{131}Pm. 165

6.7 MWPC-x coordinates associated with recoils selected by correlation with prompt γ rays observed in each band of ^{132}Pm. Black vertical lines indicate MWPC-x coordinate ranges associated with mass 128/132 recoils. 166

6.8 MWPC-x coordinate against γ-ray energy for all recoils associated with γ rays observed in the decay of bands 1 and 2 in ^{132}Pm. MWPC coordinate ranges corresponding to different masses are highlighted. 167

6.9 2-dimensional histogram of focal-plane γ-ray energy against the time difference between recoil implantation and the subsequent γ decay. 169

6.10 Focal-plane γ singles observed by tagging on a combination of any two coincident prompt γ rays observed by JUROGAM, from a gate list composed of γ rays belonging to the band labelled on the figure panel. 171

6.11 Focal-plane γ singles observed by tagging on a combination of any three coincident prompt γ rays observed by JUROGAM, from a gate list composed of γ rays belonging to the band labelled on the figure panel. 172

6.12 Panel b): Projection of the focal plane $\gamma\gamma$-coincidence matrix. γ rays incremented into this matrix are measured in correlation with any recoil implantation into the DSSD. The γ rays themselves must be measured within a coincidence window of 100 ns of each other. The green and red bars represent a gate and background gate on 73 keV and 63 keV, respectively. Panel a): Results of the gating procedure displayed in the bottom panel. Here a striking peak at 73 keV is visible, offering evidence of two 73 keV γ rays seen in cascade at the focal plane. 175

6.13 Panel b) Projection of the focal plane $\gamma\gamma$-coincidence matrix produced by gating in sort on 73 keV (effective γ^3 coincidence). The green and red bars represent a gate and background gate on 73 keV and 78 keV, respectively. Panel a) Results of the gating procedure displayed in the bottom panel. Some counts are visible at 73 keV, but are not statistically significant. 176

6.14 Delayed coincidence between 43 keV and 73 keV in a (1μs coincidence window) focal-plane $\gamma\gamma$ matrix. The 199 keV transition seen in this coincidence matrix is associated with the (8+) isomeric state in ^{128}Pr. 177

6.15 ^{132}Pm energy level scheme. Ordering of γ rays has been determined using double and triple γ coincidence analysis as detailed in the text. Structural configuration assignments are discussed in Section 6.4. Levels and γ rays highlighted in red are new to this work. 182

6.16 Timing difference between the implantation of a mass-132 recoil into the DSSD and a subsequent 73 keV γ-decay out of the isomeric state at the base of band 1. The fit is a single-term exponential, with a straight-line background. $A : 209 \pm 92, B : -0.053 \pm 0.001, C : 0.012 \pm 0.003, D : -0.1 \pm 1.7$ 184

6.17 Panel a): 43 and 73 keV transitions associated with two isomeric states in ^{132}Pm measured for three 400 tick wide intervals after recoil implantation. Panel b): Photopeak area for the 43 keV transition as a function of time following recoil implantation. Numerical fit is modelled by a straight line, fit parameters: $m : -(3.48 \pm 0.09) \times 10^{-4}, c : 8.34 \pm 0.03, \chi^2/NDF : 0.78$ 185

6.18 Nilsson diagram calculated using a Woods-Saxon potential for protons (**top**) and neutrons (**bottom**) focused on Z = 60 and N = 70, respectively. A vertical line is rendered at $\beta_2 = 0.34$, representative of the predicted deformation of this nucleus. Grey dots represent the proposed orbitals occupied by the nucleons in the ground state. Black dots represent the proposed orbitals occupied in isomeric states. 187

6.19 Experimental single-particle alignment, dynamic moment of inertia and experimental routhian for bands 1 and 2 in ^{132}Pm. Harris parameters used in production of this figure: $\mathcal{J}_0 = 29.9\,\hbar^2/\text{MeV}$ and $\mathcal{J}_1 = 15.8\,\hbar^4/\text{MeV}^3$. 188

6.20 Experimental single-particle alignment, dynamic moment of inertia and experimental routhian for bands 3 and 4 in ^{132}Pm. Harris parameters used in production of this figure: $\mathcal{J}_0 = 29.9\,\hbar^2/\text{MeV}$ and $\mathcal{J}_1 = 15.8\,\hbar^4/\text{MeV}^3$ 189

6.21 Cranked Shell Model quasiparticle Routhians (Panel π: protons, Panel ν: neutrons), generated using a universal, triaxial Woods-Saxon potential. Labels corresponding to Nilsson levels are only valid at zero spin (i.e $0\hbar\omega$) since rotation causes states to become a mixture of different wavefunctions. β_2= 0.340, β_4 = 0.0, γ = 0.0°. (π, α) : solid = (+,+1/2), dotted = (+,–1/2), dot–dash = (–,+1/2), dashed = (–,–1/2) 191

6.22 Experimental B(M1)/B(E2) ratios determined for each of the four rotational bands in ^{132}Pm. 196

7.1 Top panel: focal-plane γ rays associated with beta-delayed protons with an energy range of 1.5 - 7.0 MeV. Bottom panel: prompt radiation seen in delayed correlation with the 159 and 324 keV focal-plane γ rays. 205

7.2 Proposed partial level scheme for transitions obtained via recoil-decay correlation with the beta-delayed proton decay of ^{131}Sm. The observed transitions are proposed to be part of a very signature split band based on the [411]1/2$^+$ orbital; comparison is made with the band built on this orbital in isotone neighbour ^{129}Nd. 206

B.1 Measured channel centroid for each phase 1 detector, for each of major the peaks in the ^{152}Eu^{133}Ba spectrum, against the "true" energy of each of these peaks. Coefficients obtained from the second-order polynomial fitting were used for gain matching of these detectors throughout the analysis of this data. 211

List of Tables

3.1 Comparison of the estimated transition rates for electric (E) and magnetic (M) radiation for various multipole orders, as per the Weisskopf single-particle estimates. 46

4.1 Top table: List of γ rays built atop the new high-spin isomer (band 5/level A) in ^{129}Nd and their measured properties. Bottom table: List of γ rays depopulating bands 5, 6 and 7. Quantities in brackets denote uncertainty in the last quoted significant digit. Assigned (λL) values in brackets are tentative. 95

4.2 Quasiparticle labelling scheme for ^{129}Nd along with their assigned Nilsson configuration at zero rotational frequency. 104

5.1 List of γ-rays and their measured properties for ^{131}Pm. Quantities in brackets denote uncertainty in the last quoted significant digit. Assigned (λL) values in brackets are tentative. 131

5.2 Systematic comparison of the relative energy (R.E) level of the $h_{11/2}$ level with respect to the positive parity structure it decays into. 133

5.3 Predicted properties for nuclei without experimental measurements for these quantities. Predictions are based on the above systematical comparisons and relationships observed there. . . 140

5.4 Quasiparticle labelling scheme for ^{131}Pm along with their assigned Nilsson configuration at zero rotational frequency. 146

6.1 Compilation of the band configurations, bandhead excitation energies (where known), proton-neutron coupling mode, isomerism and other notes for various odd-odd nuclides in this mass region. Where multiple spins have been listed for K, this has resulted from coupling the spins parallel or antiparallel, with each possibility allowed in the context of the level scheme and selection rules. 156
6.2 Weisskopf single-particle estimates of transition rate for 146 and 180 keV γ rays. 162
6.3 List of γ rays and their measured properties for ^{132}Pm. Quantities in brackets denote uncertainty in the last quoted significant digit. Assigned (λL) values in brackets are tentative. 179
6.4 Quasiparticle labelling scheme for ^{132}Pm along with their assigned Nilsson configuration at zero rotational frequency. 190
6.5 Weisskopf single-particle estimates of transition rate for 43 and 73 keV. Owing to the low energy of these transitions, the estimates have been adjusted to account for their internal conversion coefficients which can be significant within this energy regime. 194

B.1 Phase 1 gain-matching coefficients used in the JM06 run. Parameter D is reserved for a cubic polynomial but this is not used here as a quadratic polynomial was deemed sufficient. The detector number corresponds phase 1 detector numbers as they are used in the tdrnames.txt configuration file. 210

Chapter 1

Introduction

1.1 Why Study Nuclear Structure?

Nuclear matter makes up 99.9% of all baryonic matter in the Universe. Confined to a portion of space on the order of femtometers ((10^{-15}m)), the nucleus gifts nuclear spectroscopists with a minuscule laboratory through which we can observe the complex interactions of nuclear matter at this scale. The simple idea that these protons and neutrons — collectively, nucleons — are indeed confined leads to some startling implications. If a nucleon is bound to a region of space of $\Delta x \sim 1$ fm, then, according to the Heisenberg uncertainty principle,

$$\Delta x \Delta p \geq \frac{\hbar}{2}, \tag{1.1}$$

the particle has an uncertainty in its momentum of at least 98 MeV/c. In the case of a single proton, the resultant (relativistic) velocity is 3.3×10^7 m/s or 10% of the speed of light! It is obvious then, that the forces exhibited on nucleons within the nucleus must be vast. We have the aptly named strong nuclear force, but the nucleus also exhibits simultaneously the effects of the weak nuclear force and the electromagnetic force — the only known system of any order of magnitude to do so.

The weak nuclear force is, by comparison, somewhat harder to visualise than the electromagnetic or strong forces. The weak force is so named because it operates over a distance much less than that of a femtometer [1, 2], with an interaction strength of around 100,000 times less than the electromagnetic force [2]. The process of β decay, which manifests itself through the weak interaction, influences our Universe in systems of every order of magnitude. The weak interaction plays a role in the production of large nuclei via nuclear fusion [3], a fact to which stars owe their existence. At the other end of the scale, the weak interaction mediates the decay of an isolated neutron, which decays into a proton [4, 5] — the most stable form of matter we know of.

The many-body nature of the nucleus is what makes it fascinating, but also complicated to describe mathematically. Even assuming that the nucleon-nucleon interaction is a simple two-body process, the number of interaction terms would still be proportional to $N!$ — a light nucleus such as ^{12}C would have more than 479 million interaction terms. Alas, the nucleon-nucleon interaction presents complexities that make exact computation of even a small number of nuclear interactions a challenge:

- the force is repulsive at very short distances ($< \sim$0.5 fm), attractive at short ($\sim$1 fm) distances, and feebly attractive at larger distances ($>\sim$3 fm).
- the force is dependent on the intrinsic spins of the nucleons: anti-parallel spin nucleons experience a "pairing" effect, attracting them together.
- some evidence [6, 7, 8] suggests that nucleons interact by three-body interactions, as well as two-body. That is to say, the relationship between the position of nucleons 2 and 3 affect the force on nucleon 1, *in addition to* the individual positions of nucleons 2 and 3.

Instead of trying directly solve the many-body problem of the nucleus, the study of nuclear structure involves development of semi-empirical models that describe the behaviour of the nucleus using approximations. Some of these models are discussed in more detail in Chapter 2.

To answer the initial question: "why study nuclear structure?", we must pose yet more questions.

How do nuclear forces result in the observed structure of nuclei? Vast leaps of progress answering this question were made in the latter half of the 20th century. A successful description of nuclear states in terms of the shell model was developed, replicating observed enhancement of stability at certain "magic" numbers of nucleons representing closed quantum shells. However, extending this model to exotic and deformed nuclei provides evidence that these magic numbers are not absolute. Nuclei far from stability can feature some very unusual properties. A striking example is the neutron halo seen in ^{11}Li; the radius of the halo is equal to the radius of the heavy nucleus ^{208}Pb [9].

What is the role of radioactive processes in producing the Universe's visible matter? It is well known that elements up to bismuth are readily produced in actively burning stars through the steady accumulation of neutrons: the s-process. Radioactive nuclei heavier than bismuth are accounted for by the fast neutron-capture process, or r-process. Early models were unable to make themselves consistent with the observed abundances of solar r-process nuclei, though they adequately described the relative production yields in terms of the time distribution of the process. In 2017, evidence was observed for the first time of a binary neutron-star merger [10], providing strong evidence for the major contribution of neutron-star mergers to the observed galactic r-process element abundances.

How can we utilise this knowledge to improve our quality of life? From metastability in medical tracers to the accelerator technology that produces them, the contribution of nuclear structure discoveries to humanity are numerous. One of civilisation's pressing issues is the increasingly burdened energy supply underpinning our industrialised way of life. For over 60 years nuclear fission reactors have provided a reliable and carbon-free contribution to our electric power grids. However, this was not without shortfall, with long-lived radioactive waste, lack of adequate decommissioning and disposal procedures, and well publicised meltdown incidents such as those seen at Chernobyl and Fukushima precluding a full-scale adoption of fission power. That said, our best hope for a sustainable and clean energy source may lie with nuclear fusion based reactors.

As questions are answered the rate at which new ones appear remains consistent. It is clear that the study of nuclear structure is as relevant to the layman as much as it is of fundamental importance to physics. The documentation of nuclear properties and identification of systematic trends such as those presented in this thesis contribute toward the final realisation of a complete nuclear description.

1.2 Experiment JM06

In April 2019, an experiment took place at the JYFL Accelerator Laboratory in Jyväskylä, Finland. The experimental objective was to combine the techniques of recoil-decay tagging and γ-ray spectroscopy to elucidate the first known excited states in the highly-deformed proton emitting nucleus ^{131}Eu.

Across two weeks of beam time, a plethora of nuclei were produced and studied - three of which make up the data chapters in this thesis. Figures 1.1 and 1.2 detail the results of calculations made by the software PACE4 [11, 12], which uses Monte-Carlo methods to simulate production cross-sections in a fusion-evaporation experiment, given a particular beam, beam energy and target. This experiment was performed with a ^{78}Kr beam on a target of ^{58}Ni. Though the predicted absolute cross-section values are known to not always correspond to the experimental values, the relative values are useful to predict which nuclides are expected to dominate the spectroscopic data. Figure 1.3 displays nuclides that were observed (light-green) and studied (dark-green) in the analysis of this experiment. Identifying nuclides largely involved observation of the prompt γ-radiation emitted by them immediately following their production. The JUROGAM3 spectrometer was used to this end. Composed of twenty four "clover" style detectors, and fifteen tapered phase-1 detectors, the spectrometer delivers an absolute efficiency of 13% at 200 keV. The experimental setup boasted the newly commissioned MARA recoil separator. Recoiling nuclei are implanted into a double-sided silicon strip detector (DSSD), which is equipped with its own high-purity germanium detectors for measurement of delayed γ radiation at the focal plane. Altogether, the formidable suite of equipment provides an excellent environment for studying all manner of radioactive decay. In this thesis, γ decay is the main focus, with three nuclei providing a detailed insight into how dynamic the decay of an excited nucleus can be.

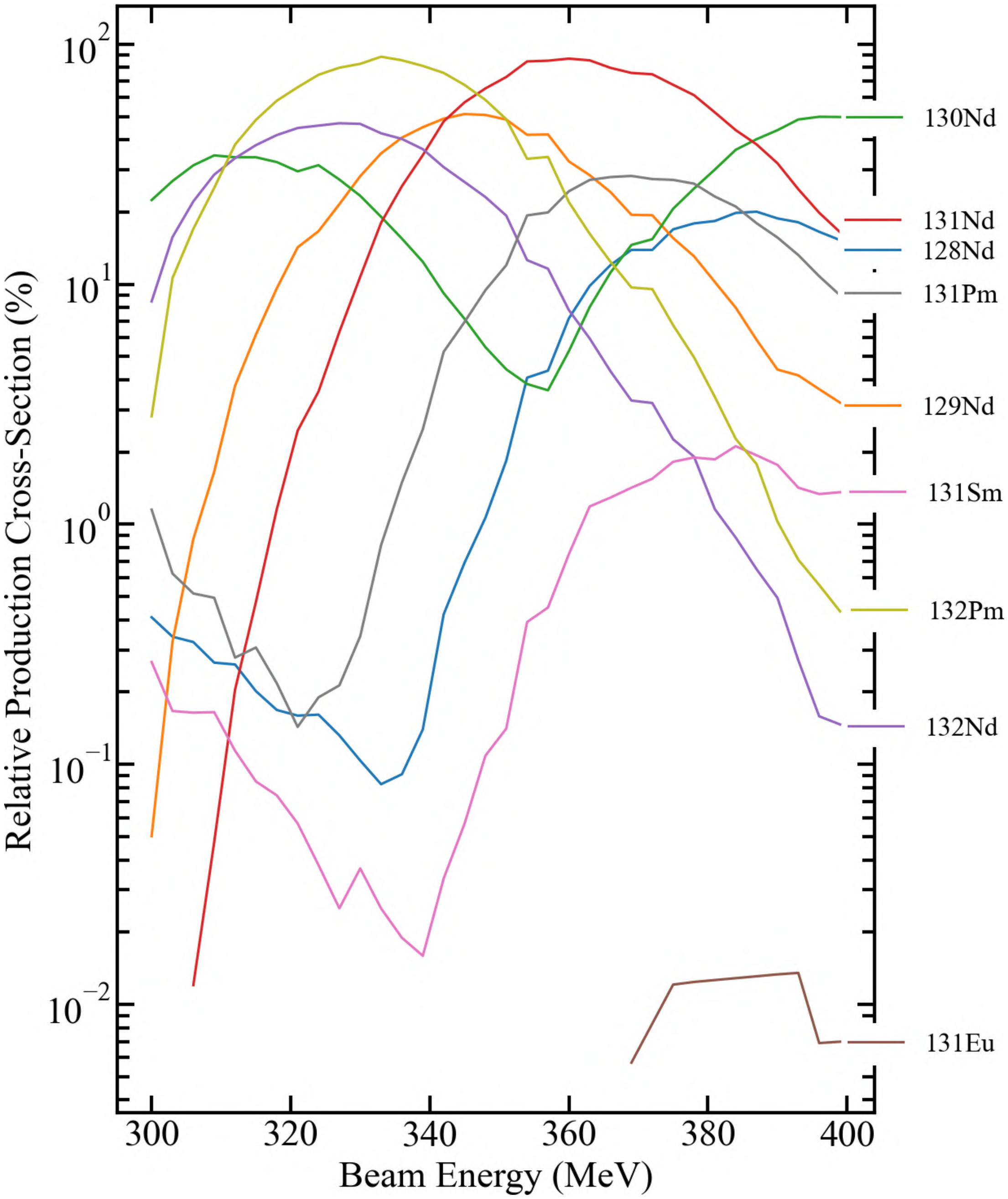

FIGURE 1.1: Predicted relative production cross-sections as a function of beam energy for a selection of nuclides given a ^{78}Kr beam on a target of ^{58}Ni. Production cross-sections are produced by Monte-Carlo simulation using the software PACE4 [11, 12].

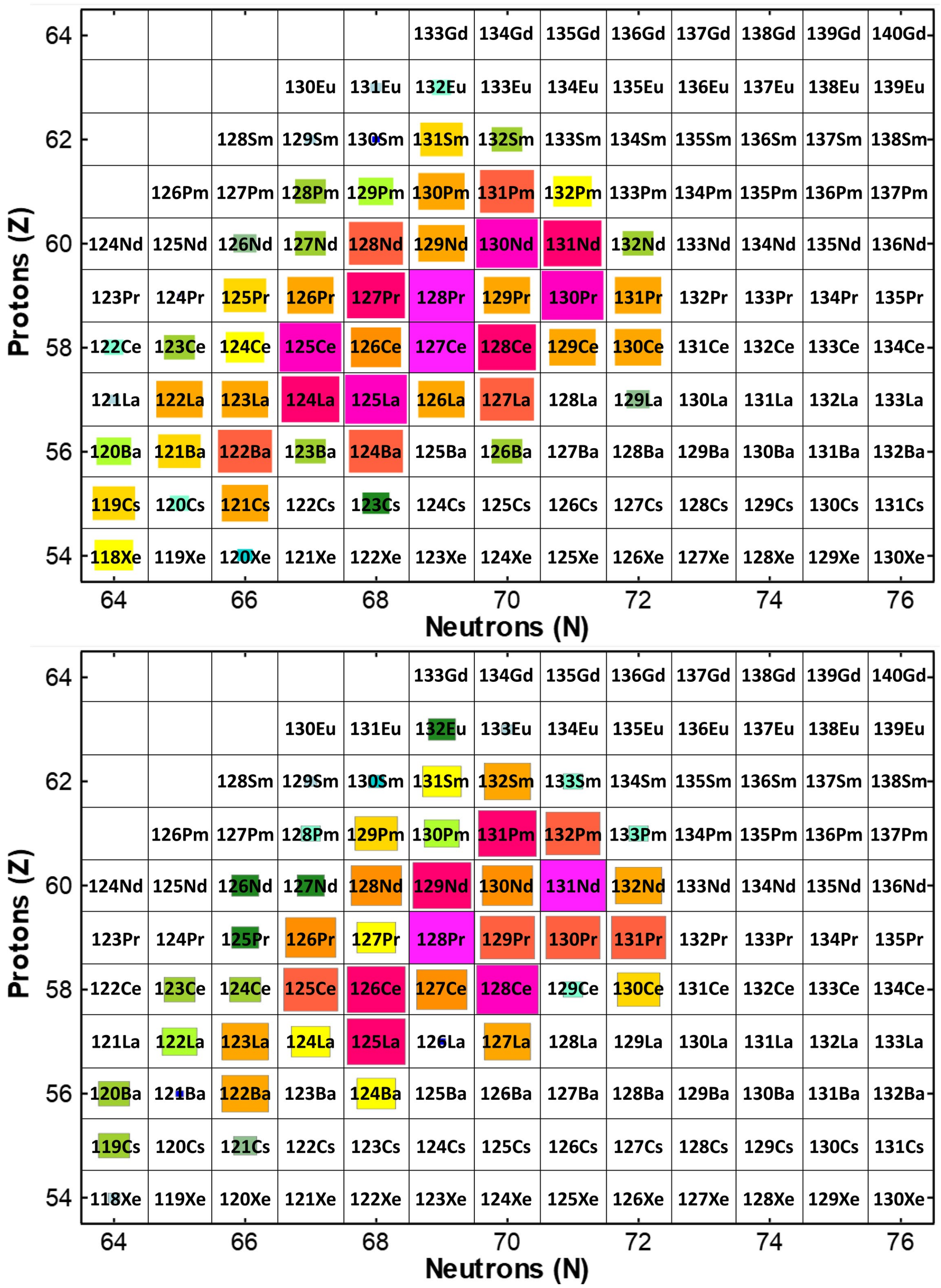

64						133Gd	134Gd	135Gd	136Gd	137Gd	138Gd	139Gd	140Gd
				130Eu	131Eu	132Eu	133Eu	134Eu	135Eu	136Eu	137Eu	138Eu	139Eu
62			128Sm	129Sm	130Sm	131Sm	132Sm	133Sm	134Sm	135Sm	136Sm	137Sm	138Sm
		126Pm	127Pm	128Pm	129Pm	130Pm	131Pm	132Pm	133Pm	134Pm	135Pm	136Pm	137Pm
60	124Nd	125Nd	126Nd	127Nd	128Nd	129Nd	130Nd	131Nd	132Nd	133Nd	134Nd	135Nd	136Nd
	123Pr	124Pr	125Pr	126Pr	127Pr	128Pr	129Pr	130Pr	131Pr	132Pr	133Pr	134Pr	135Pr
58	122Ce	123Ce	124Ce	125Ce	126Ce	127Ce	128Ce	129Ce	130Ce	131Ce	132Ce	133Ce	134Ce
	121La	122La	123La	124La	125La	126La	127La	128La	129La	130La	131La	132La	133La
56	120Ba	121Ba	122Ba	123Ba	124Ba	125Ba	126Ba	127Ba	128Ba	129Ba	130Ba	131Ba	132Ba
	119Cs	120Cs	121Cs	122Cs	123Cs	124Cs	125Cs	126Cs	127Cs	128Cs	129Cs	130Cs	131Cs
54	118Xe	119Xe	120Xe	121Xe	122Xe	123Xe	124Xe	125Xe	126Xe	127Xe	128Xe	129Xe	130Xe
	64		66		68		70		72		74		76

64						133Gd	134Gd	135Gd	136Gd	137Gd	138Gd	139Gd	140Gd
				130Eu	131Eu	132Eu	133Eu	134Eu	135Eu	136Eu	137Eu	138Eu	139Eu
62			128Sm	129Sm	130Sm	131Sm	132Sm	133Sm	134Sm	135Sm	136Sm	137Sm	138Sm
		126Pm	127Pm	128Pm	129Pm	130Pm	131Pm	132Pm	133Pm	134Pm	135Pm	136Pm	137Pm
60	124Nd	125Nd	126Nd	127Nd	128Nd	129Nd	130Nd	131Nd	132Nd	133Nd	134Nd	135Nd	136Nd
	123Pr	124Pr	125Pr	126Pr	127Pr	128Pr	129Pr	130Pr	131Pr	132Pr	133Pr	134Pr	135Pr
58	122Ce	123Ce	124Ce	125Ce	126Ce	127Ce	128Ce	129Ce	130Ce	131Ce	132Ce	133Ce	134Ce
	121La	122La	123La	124La	125La	126La	127La	128La	129La	130La	131La	132La	133La
56	120Ba	121Ba	122Ba	123Ba	124Ba	125Ba	126Ba	127Ba	128Ba	129Ba	130Ba	131Ba	132Ba
	119Cs	120Cs	121Cs	122Cs	123Cs	124Cs	125Cs	126Cs	127Cs	128Cs	129Cs	130Cs	131Cs
54	118Xe	119Xe	120Xe	121Xe	122Xe	123Xe	124Xe	125Xe	126Xe	127Xe	128Xe	129Xe	130Xe
	64		66		68		70		72		74		76

FIGURE 1.2: Predicted relative production cross-section for a subsection of the chart of the nuclides, produced by Monte-Carlo simulation using the software PACE4. Larger coloured squares indicate a larger relative yield. Calculation results are displayed for both high beam energy (390 MeV, top panel) and low beam energy (364 MeV, bottom panel).

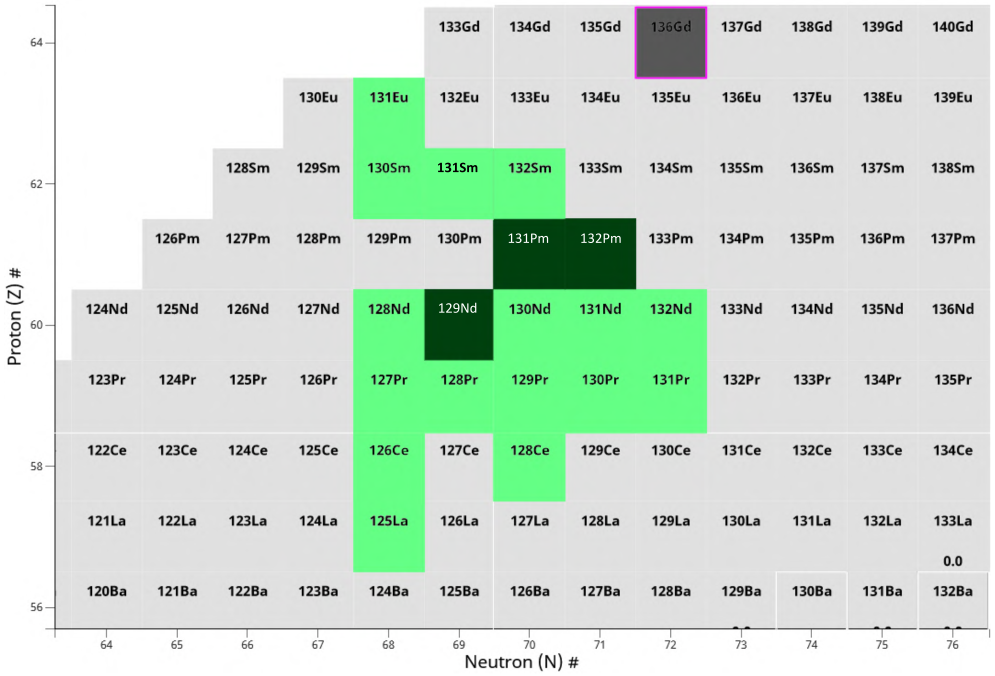

FIGURE 1.3: A subsection of the (Segre) chart of the nuclides focusing on the mass region studied in this thesis. The compound nucleus ^{136}Gd is coloured dark grey. Nuclides discussed in this thesis are coloured dark-green and nuclides observed in the data but not discussed in detail here are coloured light-green.

The mass-130 region of the Segre chart is ripe with exotic nuclei exhibiting all manner of interesting behaviour. First and perhaps most obviously is the close proximity to which the nuclides are to the proton dripline. These nuclei are extremely neutron deficient, resulting in exotic decay modes and relatively short half-lives. Secondly, this region of the chart is situated in the middle of the full shell closure for both protons and neutrons — we expect to see nuclei with high deformation here. As will be described in detail in Chapter 2, highly deformed nuclei are stabilised by the formation of new shell gaps. Measurements of absolute excitation energies can provide valuable constraints to the theoretical models used to describe them. Finally, nucleons occupying excited states in this mass region often have their angular momenta projected along the axis of deformation in such a way that their decay to lesser excited states is hindered, resulting in unusually large (isomeric) half-lives for these states.

Chapter 2

Theoretical Overview of Nuclear Models

2.1 Historical Nuclear Structure

In the early 20^{th} century, the liquid-drop model became one of the first successful in describing the nuclear mass in terms of its constituent nucleons [13]. Here, the nucleus is thought of as an incompressible melee of protons and neutrons held together by the strong nuclear force. The model is described mathematically by the Bethe–Weizsäcker formula [14]. The liquid-drop model is remarkably successful in describing the overall trend of binding energy per nucleon. It is not as accurate for the lightest nuclei, where the image of a liquid-drop isn't well adapted. Inability to account for the experimental observation of higher binding energies at certain numbers of protons and neutrons is another failing of the liquid-drop model. These so-called "magic numbers" are one of the primary pieces of evidence pointing to the shell model of the atomic nucleus.

2.2 The Shell Model Of The Nucleus

As well as the experimentally measured deviation from the liquid-drop model discussed previously, there are other pieces of evidence that clearly point toward nuclei exhibiting shell structure behaviour. One such example of this is the disappearance of the nuclear electric quadrupole moment at numbers close to closed shells. The quadrupole moment arises out of distributed charge in a deformed (non-spherical) nucleus. With filled closed shells, it is expected that the nucleus would reattain spherical shape, and the electric quadrupole moment would fall to zero, which is observed experimentally [15]. Further evidence arises from the relative natural abundance of nuclei at closed shell numbers compared to other nuclei [16]. The observed shell numbers

$$2, 8, 20, 28, 50, 82, 126 \tag{2.1}$$

represent the total number of nucleons needed to fill each successive shell. A nuclear shell model is a single-particle model. Individual nucleons can be thought of as moving in an average field which is built up with contributions from all the other nucleons. This reduces the complexity of the nuclear many-body problem substantially with the nuclear Hamiltonian able to be written as

$$H' = \sum_i [T_i + V_i(r_i)] + \lambda \left[\sum_{i,j} v(r_{i,j}) - \sum_i V_i(r_i) \right] . \tag{2.2}$$

The first term represents the summation of all the individual particle kinetic energy contributions, T_i, moving in a mean-field potential, V. The second term is the "perturbation term", containing the sum of the short-range residual interactions, $v(r_{i,j})$, between the nucleons. A presumption made by the shell model is that the first term is far greater than the residual interactions, so $\lambda \to 0$. The time-independent Schrödinger equation is then

$$\frac{-\hbar^2}{2m}\frac{\partial^2}{\partial r^2}\Psi(r) + V(r)\Psi(r) = E\Psi(r). \tag{2.3}$$

Naturally, it follows that selection of a potential, $V(r)$, descriptive of the nuclear potential is required such that Equation 2.3 yields correct energy eigenvalues, some of which are discussed in the following sections.

2.2.1 Harmonic Oscillator Potential

One of the simplest potentials in terms of its functional form and ease of analytical analysis is the simple harmonic oscillator. This treats particles as though they are a mass suspended on a spring, with the spring representing the potential they move in. The classic harmonic oscillator potential can be obtained from Hooke's law

$$V(r) = \frac{1}{2}Kr^2 = \frac{1}{2}m\omega^2 r^2, \tag{2.4}$$

where K is a constant representing the elasticity of the oscillator, r is the radial distance of an oscillation, ω is the angular frequency of oscillation and m is the particle mass. Setting the depth of the potential well as V, the time-independent Schrödinger equation is then

$$\frac{-\hbar^2}{2m}\frac{\partial^2}{\partial r^2}\Psi(r) + \left[\frac{1}{2}m\omega^2 r^2 - V\right]\Psi(r) = E\Psi(r). \tag{2.5}$$

The equation can be solved and eigenstates extracted using power series methods. The general form for the wavefunction and the system's eigenstates are

$$\Psi(r) = \left(\frac{\alpha}{\pi}\right)^{\frac{1}{4}} \frac{1}{\sqrt{2^N N!}} H_N(\zeta) e^{-\frac{\zeta^2}{2}}, \tag{2.6}$$

$$E_N = \left(2n + l + \frac{1}{2}\right)\hbar\omega = \left(N + \frac{3}{2}\right)\hbar\omega, \tag{2.7}$$

where $\alpha = m\omega/\hbar$, $\zeta = \sqrt{\alpha}r$ and the $H_N(\zeta)$ are the physicist's Hermite polynomials, necessary to orthogonalise the energy eigenvalues.

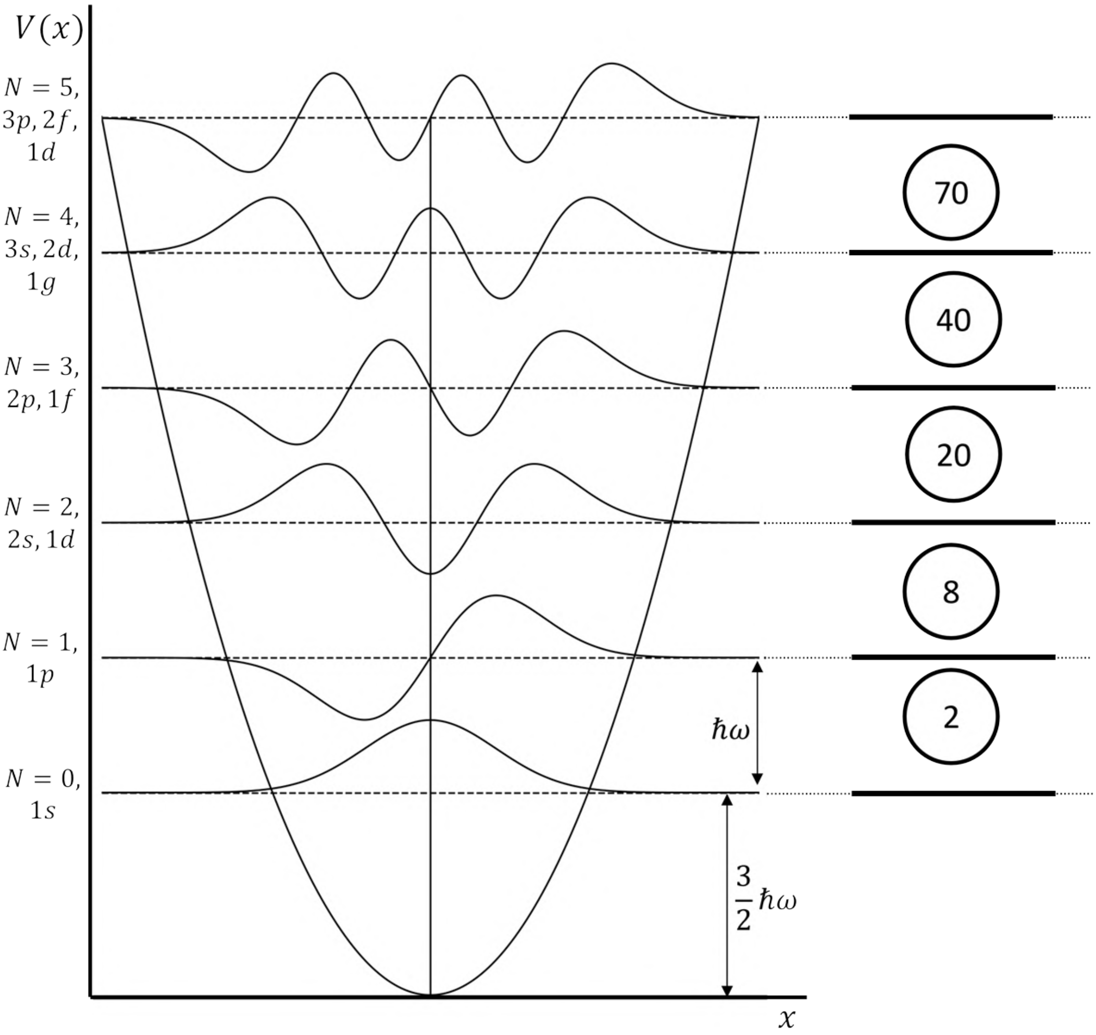
$V(x)$
$N=5$, $3p, 2f$, $1d$
$N=4$, $3s, 2d$, $1g$
$N=3$, $2p, 1f$
$N=2$, $2s, 1d$
$N=1$, $1p$
$N=0$, $1s$
70
40
20
8
2
$\hbar\omega$
$\frac{3}{2}\hbar\omega$
x

FIGURE 2.1: Energy eigenvalues for the first five N states of the harmonic oscillator potential. Energy states are labelled by the oscillator quantum number N (equal to the number of nodes in the waveform), and their principal and angular momentum quantum number components, (nl). l is labelled using the spectroscopic notation.

The energy eigenvalues themselves are provided by Equation 2.7 where n is the principal quantum number, l is the orbital angular-momentum quantum number and $N = 2(n-1) + l$ is the oscillator quantum number. Figure 2.1 displays the energy levels and the wavefunctions superimposed over their respective energy level. It can be seen that the solutions yield a set of discrete energy levels for each shell, with the lowest shell having a non-zero energy of $(3/2)\hbar\omega$. States are degenerate in energy with their components labelled by the principal quantum number, n, and the angular momentum quantum number, l. The selection rule for the angular momentum states is $0 \leq l \leq N$; states are further restricted by the parity selection rule as discussed below. The number of degenerate energy levels for each shell is

$$d_N = (N+1)(N+2), \tag{2.8}$$

arising from two allowed spin states, and multiple allowed angular momentum states. Despite its simplicity, the harmonic oscillator model introduces the concept of parity: the invariance of a wavefunction when reflected around its axis of origin. A wavefunction that is symmetric on reflection has positive parity — the opposite is true for asymmetric wavefunctions. The parity of each state is then

$$\pi = (-1)^N = (-1)^l. \tag{2.9}$$

Parity selection rules dictate that the allowed angular momentum states for a given level are limited to odd/even states for odd/even parity. The "magic number" is then the total of all particles taken to fill the nucleus up to this shell closure. We can see from Figure 2.1 that only the first three magic numbers are reproduced and further improvements are needed to accurately reproduce the experimentally observed shell states.

2.2.2 Spin-Orbit Correction

Analogous to the spin-orbit interaction in atomic physics is the spin-orbit interaction of the nucleus. Here, the interaction between a nucleon's total angular momentum, $j = l \pm \frac{1}{2}$, and the strong nuclear force to which the nucleon is subjected, leads to splitting in the nuclear energy levels. Describing the nuclear potential as a harmonic oscillator leads to energy eigenstates degenerate in energy, with multiple allowed values of j, as per Figure 2.1. However, this degeneracy is lifted with introduction of a spin-orbit term to the potential [17],

$$V(r) \rightarrow V(r) - \alpha \vec{l} \cdot \vec{s}. \tag{2.10}$$

In addition to the spin-orbit term, it is necessary to add the term $-\beta l^2$. This has the effect of "flattening" the bottom of the harmonic potential and making the potential steeper around the Fermi level; without it, high-l orbitals have a higher energy than they should. The effect on the energy eigenstates is displayed in Figure 2.2. It can be seen that each harmonic oscillator level has split into l sublevels, and the l^2 perturbation has pushed high-j levels down in energy, as expected. It is also worth noting that, contrary to the atomic picture, states with *higher* j are *lower* in energy, owing to the nuclear spin-orbit interaction being an attractive force.

The modified harmonic oscillator with spin-orbit correction can successfully reproduce the experimentally observed magic numbers corresponding to stable, closed nuclear shells. It would seem then, that a complete microscopic description of a spherical nucleus is at hand. However, the harmonic oscillator potential has the nonphysical property of tending toward infinity as the nuclear radius increases. Furthermore, evidence of deformed nuclei invalidates the spherical prerequisite of the spherical shell model.

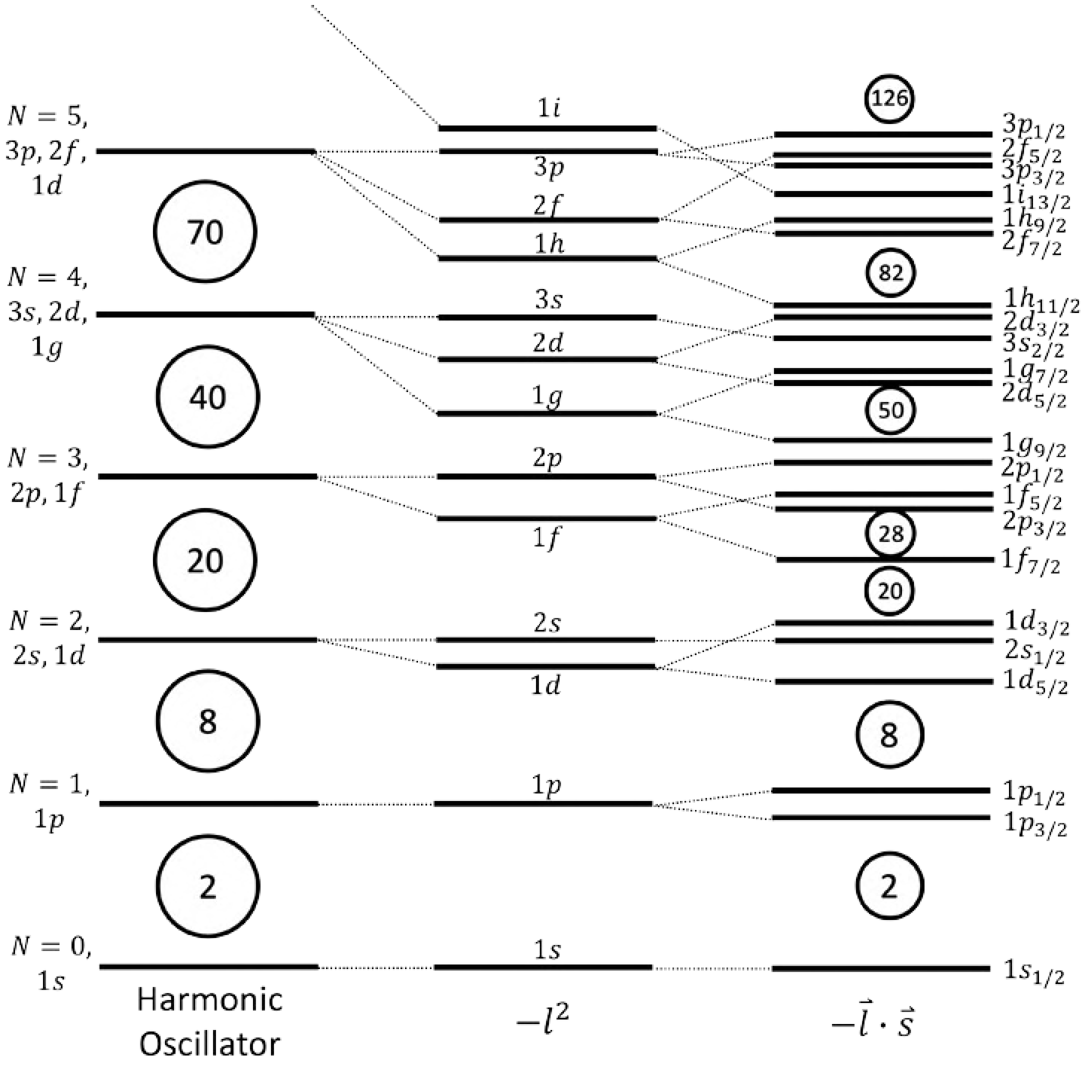
N = 5, 3p, 2f, 1d
N = 4, 3s, 2d, 1g
N = 3, 2p, 1f
N = 2, 2s, 1d
N = 1, 1p
N = 0, 1s
70
40
20
8
2
Harmonic Oscillator
1i
3p
2f
1h
3s
2d
1g
2p
1f
2s
1d
1p
1s
−l²
126
82
50
28
20
8
2
3p1/2
2f5/2
3p3/2
1i13/2
1h9/2
2f7/2
1h11/2
2d3/2
3s1/2
1g7/2
2d5/2
1g9/2
2p1/2
1f5/2
2p3/2
1f7/2
1d3/2
2s1/2
1d5/2
1p1/2
1p3/2
1s1/2
−l · s

FIGURE 2.2: Quantum harmonic oscillator potential eigenstates with l^2 and $\vec{l}\cdot\vec{s}$ corrections. Final energy states are labelled nl_j, where n is the principal quantum number, l is the angular momentum quantum number, and $j = l \pm \frac{1}{2}$ is the total angular momentum quantum number.

2.2.3 Woods-Saxon Potential

Considered to be a more realistic nuclear potential, the Woods-Saxon potential has the same radial dependence as the nuclear matter distribution and does not require infinite separation energies between nucleons.

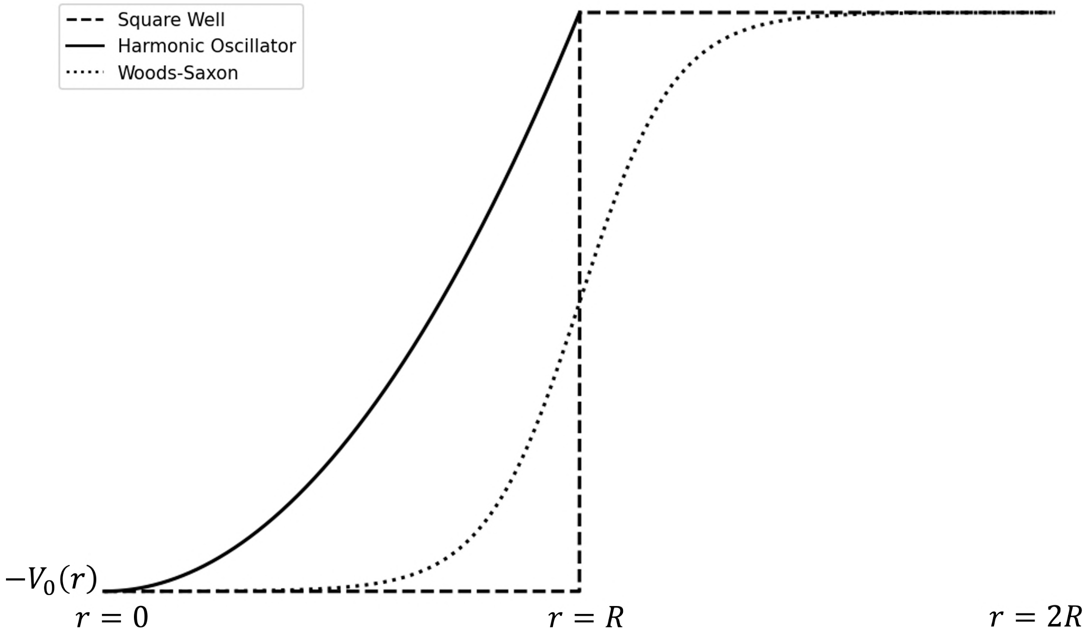

FIGURE 2.3: Comparison of different nuclear potential wells as a function of the radial distance from the center of the nucleus, r. The full nuclear radius is labelled R. Parameters used in the model include $V_0 = 50$ MeV, $a = 1.5$ fm and $R = 15$ fm.

The Woods-Saxon distribution falls off steeply toward zero as the radius approaches the Fermi surface, R. It does not tend to infinity as does the harmonic oscillator and it avoids the sharp discontinuity at R present in the square well. Mathematically, the Woods-Saxon potential [18] is given by

$$V(r) = -\frac{V_0}{1 + e^{\frac{r-R}{a}}}, \tag{2.11}$$

where a is the diffuseness parameter, describing how steep the "drop off" in potential is. Typical values for this are $0.5 - 1.5$ fm [15]. The Woods-Saxon potential with spin-orbit correction yields the correct magic numbers, but also presents further benefits compared to the harmonic oscillator:

- for large numbers of nucleons, the decrease in potential is very sharp at the boundary $r \approx R$, since the diffuseness parameter is small in comparison to the nuclear radius, and
- the potential rapidly goes to zero as $r \approx R$ reflecting the short-range nature of the strong nuclear force.

The Woods-Saxon potential cannot be solved analytically and must be attacked using numerical methods.

2.3 The Deformed Shell Model Of The Nucleus

All the models discussed until this point have assumed a static nucleus which is close to sphericity. Introducing deformation to the picture somewhat complicates things. There are several pieces of evidence pointing towards nuclear deformation:

- the existence of quantum rotational bands obeying the relationship $E \propto I(I+1)$,
- large electric quadrupole moments due to a non-spherical distribution of charge,
- the 2^{+} state having low energy correlates with high nuclear moments of inertia, indicative of deformation,
- enhanced B(E2) decay rates.

These pieces of evidence — particularly existence of rotational and vibrational modes — are important because they paint a picture of *collective* and *coherent* motion, rendering the single-particle nature of the spherical shell model invalid. The deformed nuclear shape can be described mathematically in terms of its equipotential surface,

$$R(\theta,\phi) = CR_0 \left[1 + \sum_{\lambda=0}^{\infty} \sum_{\mu=-\lambda}^{\lambda} \alpha_{\lambda\mu} Y_{\lambda}^{\mu}(\theta,\phi)\right], \tag{2.12}$$

where R_0 is the radius of the spherical nucleus, $Y_{\lambda}^{\mu}(\theta,\phi)$ are spherical harmonics, and $\alpha_{\lambda\mu}$ are coefficients moderating the strength of the $(\lambda\mu)^{th}$ distortion from sphericity. The parameter λ represents the mode of deformation. In general, most nuclei can be described by quadrupole ($\lambda = 2$) deformations with a small hexadecapole ($\lambda = 4$) correction. Taking the axis of our coordinate system to be equal to the axes of nuclear deformation, Equation 2.12 reduces to

$$R(\theta,\phi) = CR_0 \left[1 + \alpha_{2,0} Y_{2,0} + \alpha_{2,2}(Y_{2,2} + Y_{2,-2})\right]. \tag{2.13}$$

This in turn allows a useful parameterisation of the α in terms of the total deformation, β_2, and the lengths along the principal axes, γ.

$$\alpha_{2,0} = \beta_2 \cos\gamma, \qquad \alpha_{2,2} = \frac{\beta_2}{\sqrt{2}} \sin\gamma \tag{2.14}$$

The effect of the parameter γ is depicted pictorially in Figure 2.4. Here we can see the difference between collective and non-collective modes of deformation. Briefly, non-collective deformations occur when the angular momenta of the nucleons are aligned with the axis of deformation and the opposite is true for collective excitations. This is discussed in more detail in Section 2.4.

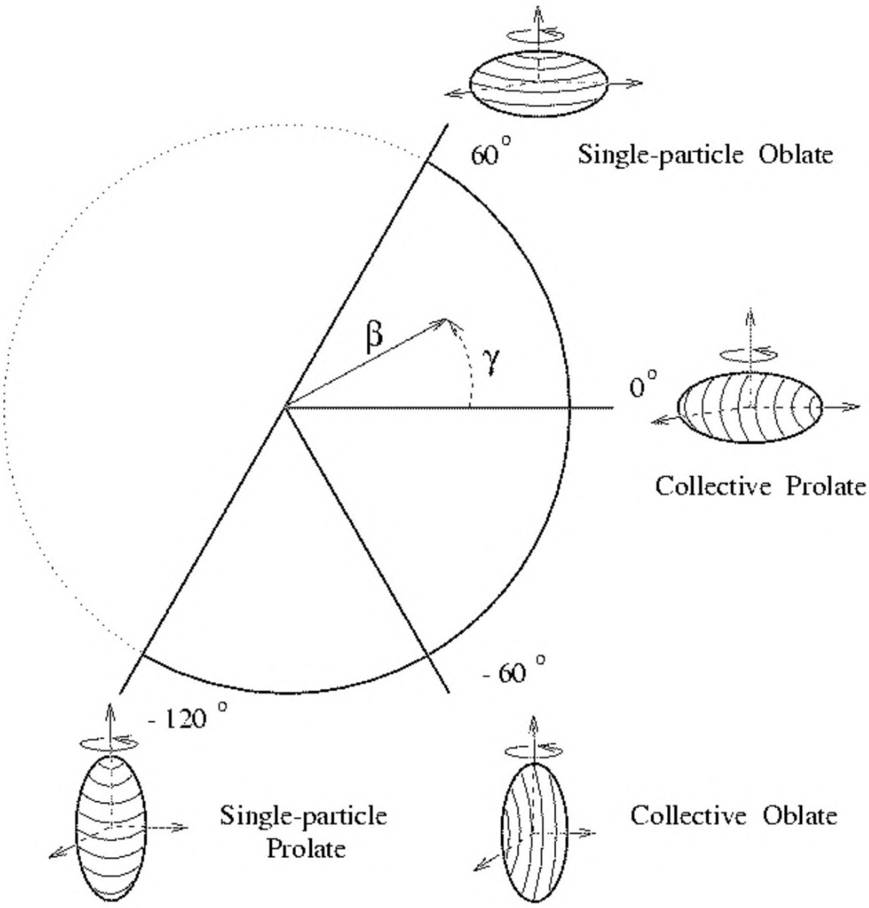
60°
Single-particle Oblate
β
γ
0°
Collective Prolate
- 60°
- 120°
Single-particle Prolate
Collective Oblate

FIGURE 2.4: The Lund Convention for specification of triaxial deformation along three principal axes. Lines along the deformed nucleus represent nucleon orbital paths, with their individual angular momenta aligned in the plane perpendicular to this orbital. Figure courtesy of Ref [19].

2.3.1 Anisotropic Harmonic Oscillator Potential

As was the case for the spherical shell model, one of the simplest potentials to describe a deformed nucleus's eigenstates is the harmonic oscillator potential. This time, however, the form of the potential is modified to reflect the anisotropy of the principal nuclear axes,

$$V(x,y,z) = \frac{1}{2}m(\omega_x^2 x^2 + \omega_y^2 y^2 + \omega_z^2 z^2). \tag{2.15}$$

The three ω parameters can be written in terms of the polar coordinates $\beta(\approx \epsilon_2)$ and γ as detailed in Figure 2.4 and Equations 2.14,

$$\begin{aligned}
\omega_x &= \omega_0(\beta,\gamma)\left[1-\frac{2}{3}\beta\cos(\gamma+\frac{2\pi}{3})\right],\\
\omega_y &= \omega_0(\beta,\gamma)\left[1-\frac{2}{3}\beta\cos(\gamma-\frac{2\pi}{3})\right],\\
\omega_z &= \omega_0(\beta,\gamma)\left[1-\frac{2}{3}\beta\cos(\gamma)\right].
\end{aligned} \tag{2.16}$$

If we make the assumption that the nucleus is only deformed along one axis (conventionally z), then we have axial symmetry. Thus, $\gamma = 0$ and $\omega_x = \omega_y$. Equation 2.15 can then be written

$$V(x = y = \perp, z) = \frac{1}{2}m(\omega_\perp^2 \perp^2 + \omega_z^2 z^2). \tag{2.17}$$

The eigenstates are given by

$$\begin{aligned}
E(n_\perp, n_z) &= \left(n_z + \frac{1}{2}\right)\hbar\omega_z + (n_\perp + 1)\hbar\omega_\perp,\\
&= \left(N + \frac{3}{2}\hbar\omega_0 - \frac{\epsilon}{3}\left[3n_z - N\right]\right),
\end{aligned} \tag{2.18}$$

where $N = n_\perp + n_z$ and $\epsilon = (\omega_\perp - \omega_z)/\omega_0$ is the eccentricity of the nuclear shape. Neglecting the spin-orbit and potential flattening terms, the energy eigenstates are visualised in Figure 2.5. A striking feature of this plot is the emergence of new shell gaps at particular axis ratios, the so-called "deformed magic numbers". Though Figure 2.5 is instructive in displaying how stable deformed nuclear shapes can arise, a more realistic representation of the nuclear eigenstates come from inclusion of the spin-orbit and flattening terms as represented in a *Nilsson diagram*, detailed in the following section.

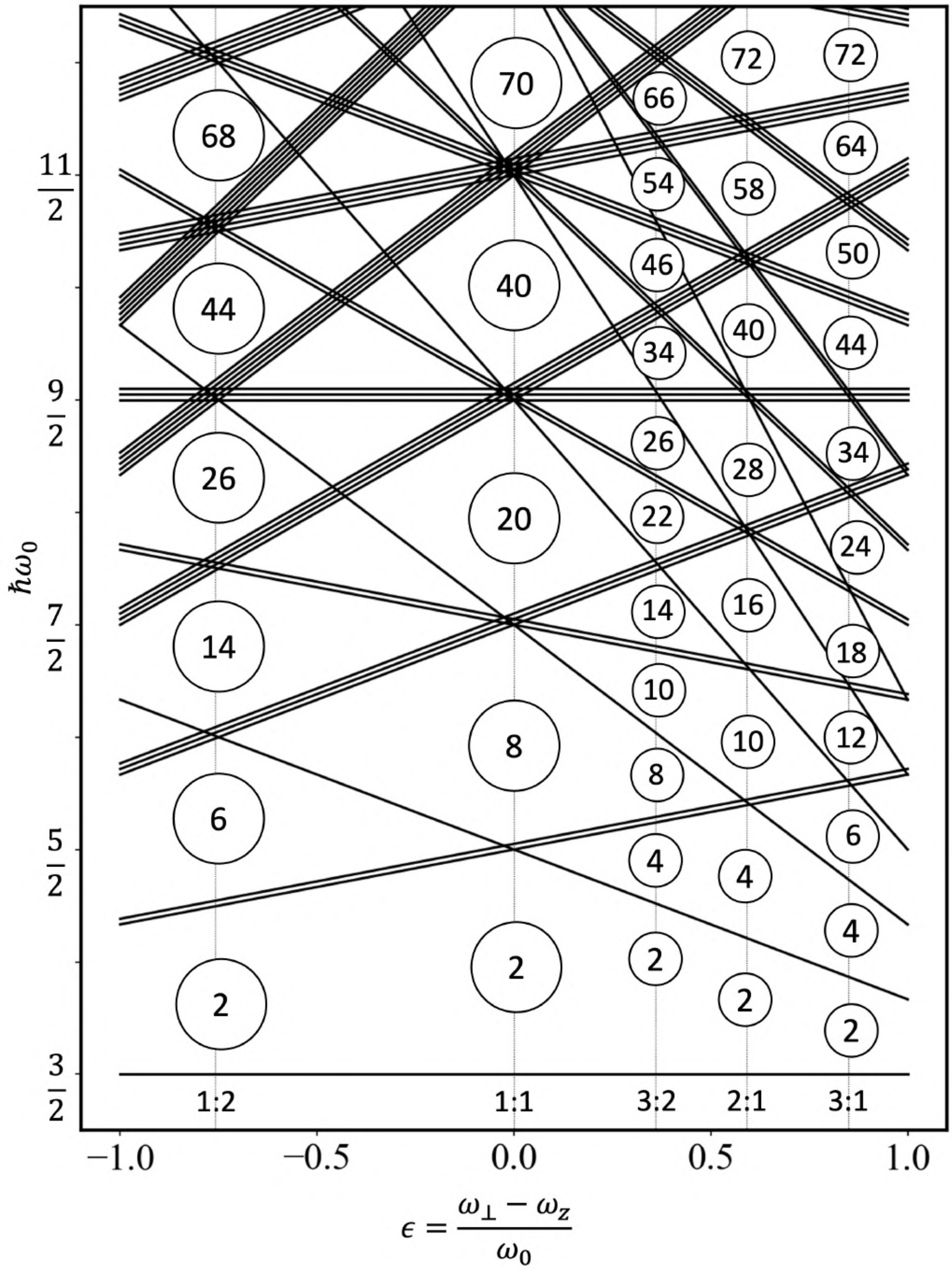

FIGURE 2.5: Nuclear energy eigenstates for the anisotropic harmonic oscillator potential as a function of nuclear deformation, ϵ. We have, $\omega_0 = \frac{1}{3}(2\omega_\perp + \omega_z)$, $N = n_\perp + n_z$, degeneracy $d = 2(n_\perp + 1)$ where the factor 2 is for each nucleon spin $s = \pm\frac{1}{2}$ and the orbital degeneracy is illustrated by false splitting of the lines. The labels on the x-axis indicate minimum to maximum axis ratios corresponding to axially oblate, spherical, and axially prolate superdeformed and hyperdeformed shapes. Equations used to produce figure adapted from [20].

2.3.2 Nilsson Potential

Nilsson diagrams based on a universal triaxial Woods-Saxon potential are modelled in this work using the codes of [21]. The codes can model single particle energies as a function of the deformation parameter, β. The result of these calculations are detailed in Figures 2.7 and 2.8. Energy levels in the Nilsson scheme are represented by the quantum numbers,

$$[N\, n_z\, \Lambda]\Omega^{\pi}, \tag{2.19}$$

where Ω is the projection of the single-particle total angular momentum, j, onto the axis of deformation; π is the parity of the state; $N = n_x + n_y + n_z$ is the oscillator quantum number which, in turn, is the sum of the principal quantum number for each axis; Λ is the projection of the single particle angular momentum, l, onto the axis of deformation. The quantities are depicted pictographically in Figure 2.6.

The Nilsson diagram can look overwhelming at first, but interpreting it is straightforward. Each line on the diagram is doubly degenerate, so two nucleons can lie at that energy state. For a nucleus of known deformation, β, and known proton/neutron number, one can find the energy state of the last nucleon by counting up the Nilsson diagram in multiples of two until you reach the desired proton/neutron number. It can be observed that levels with the same Ω^{π} numbers repel each other due to the Pauli exclusion principle forbidding spacial overlap of two identical fermions. At these crossings, levels exchange character (quantum numbers) with each other. Other rules to be aware of include:

- Solid lines indicate positive parity waveform and dashed lines indicate negative parity.
- As β becomes negative, high values of Ω are brought down in energy and low values are raised in energy. The opposite case applies for positive

values of β.

- Subtle differences between proton and neutron diagrams can be observed, accounting for Coulomb repulsion between protons (i.e, ordering of the $h_{11/2}$, $s_{1/2}$ and $d_{3/2}$ levels).

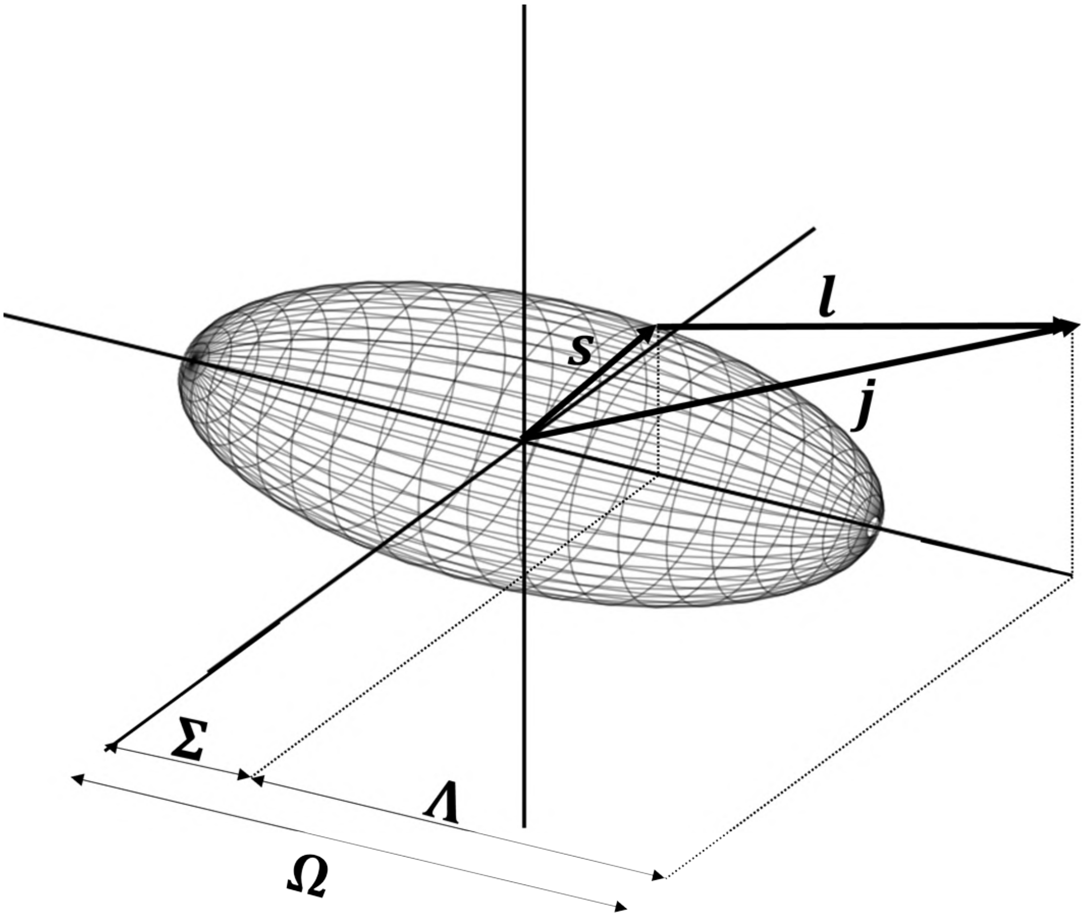

FIGURE 2.6: Projections of the spin quantum numbers (s, l, j) labelled with the asymptotic quantum numbers Σ, Λ and Ω.

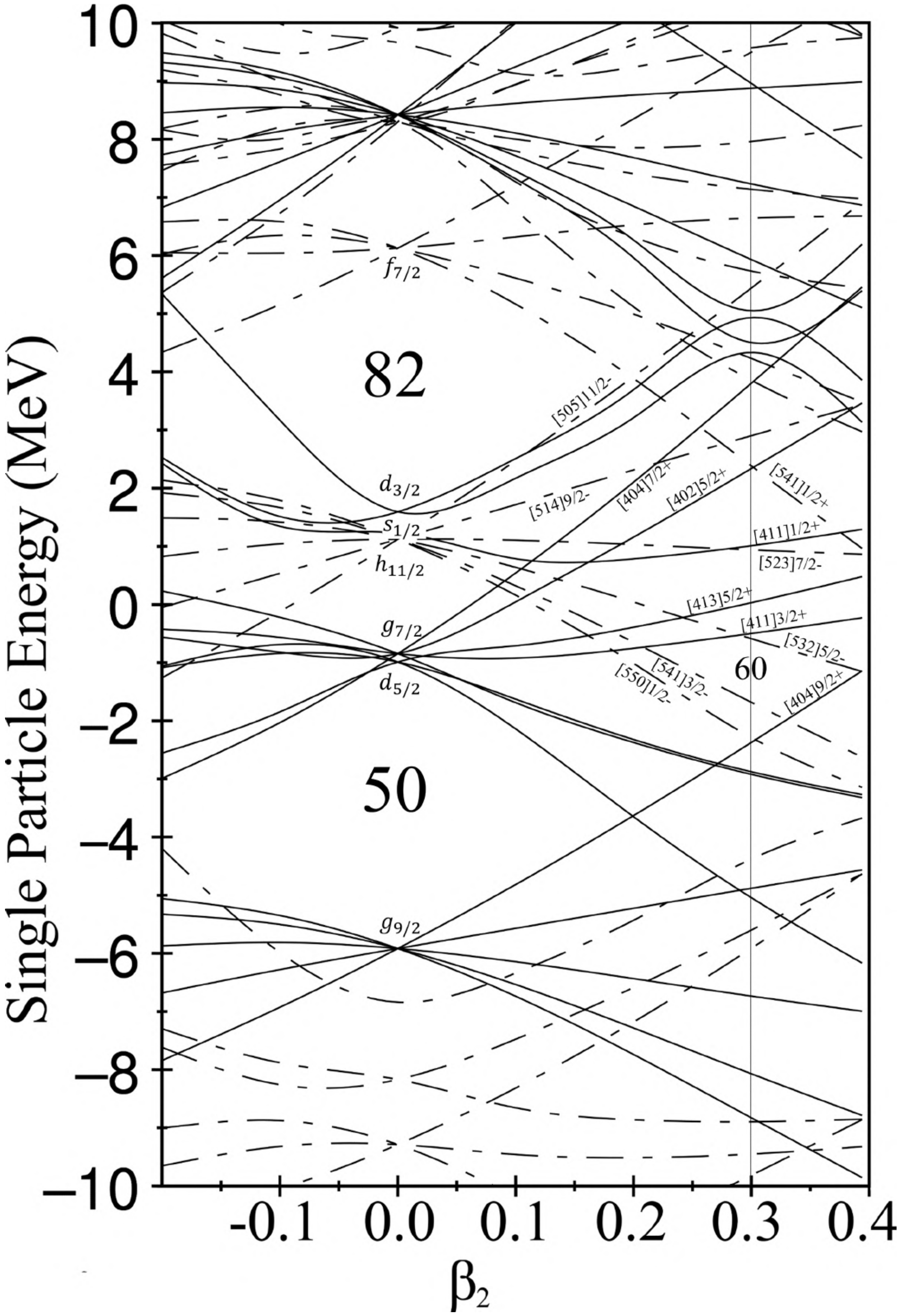

FIGURE 2.7: Nilsson diagram for protons calculated using an anisotropic Woods-Saxon potential. Full shell closures at zero deformation are indicated, along with the spherical shell numbers l_j.

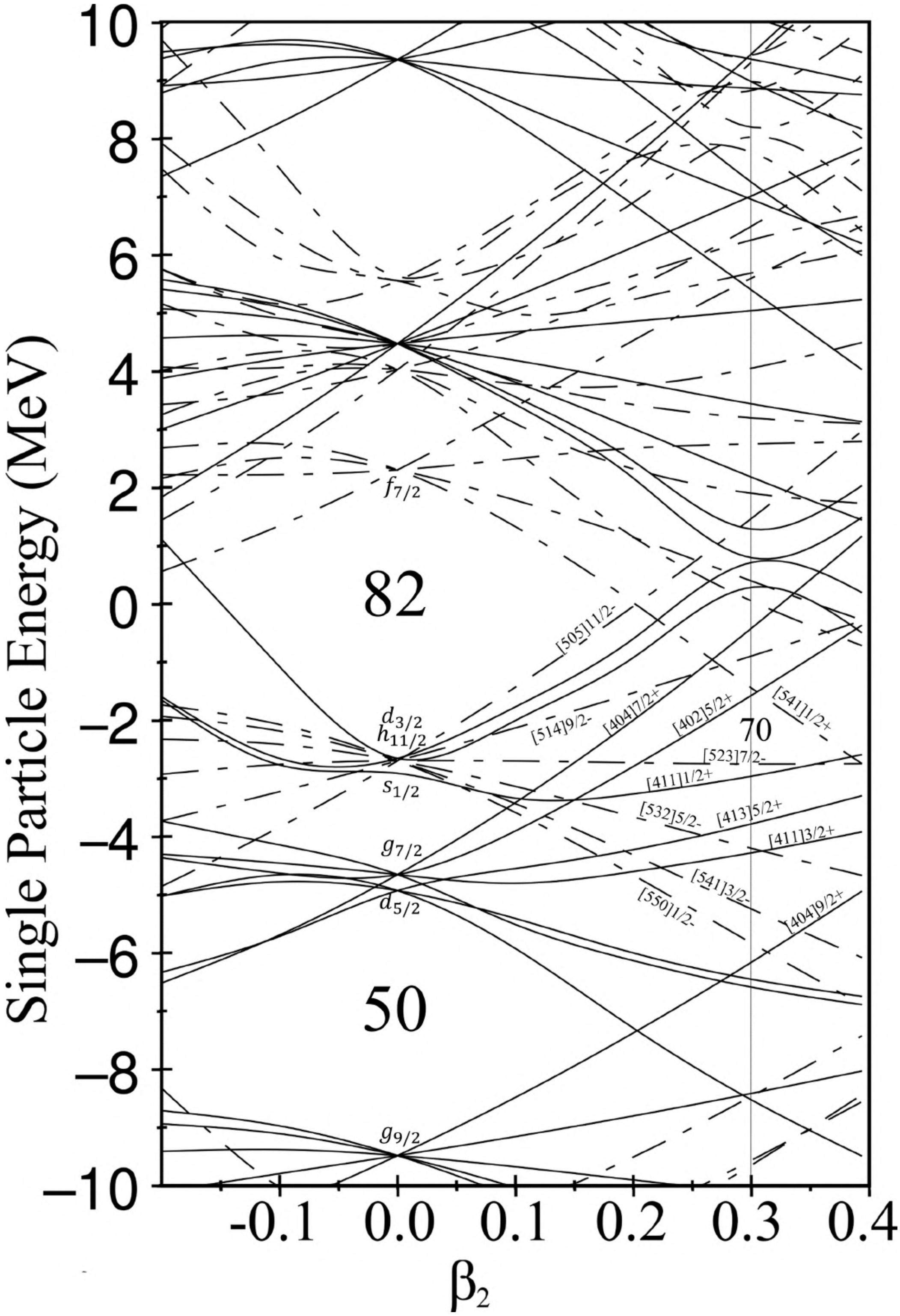

FIGURE 2.8: Nilsson diagram for neutrons calculated using an anisotropic Woods-Saxon potential. Full shell closures at zero deformation are indicated, along with the spherical shell numbers l_j.

2.4 Nuclear Rotation - Non-Collective Excitation and Collective Rotation

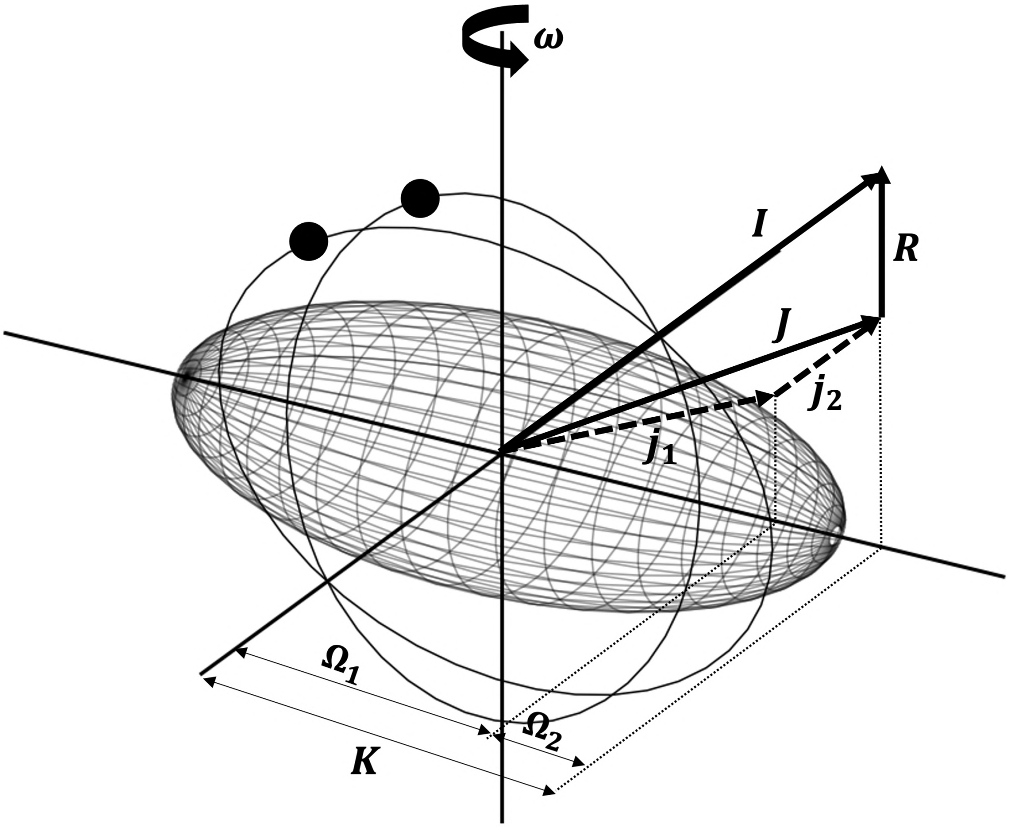

FIGURE 2.9: Depiction of a deformed and rotating nucleus with two valence particles. The projection of the total single-particle contribution to the nuclear spin, $J = j_1 + j_2 \rightarrow \Omega = \Omega_1 + \Omega_2$ is detailed. The projection of the total nuclear spin, $I = J + R \rightarrow K$ is also indicated, where R is the contribution arising from the collective motion of the nuclear core.

The nuclear models discussed to this point have described the nucleus consisting of single nucleons moving in a mean-field potential composed by the residual strong nuclear force of all the other nucleons. The models have been corrected and perturbed to account for deformation, but still describe a static nucleus. Here we introduce rotation to the nuclear frame. Rotation has the effect of varying some of the nuclear parameters as a function of the nucleus's rotational frequency, ω. Consequently, some of the numbers used to label energy states in a non-rotating nucleus are no longer good or even applicable, so we introduce new ones as depicted in Figure 2.9.

A key difference between the rotating nucleus and the static picture is that the total nuclear spin, I, has contributions from both the single particle (J) and collective (R) regimes. Here, the nucleus is axially symmetric with the collective rotational angular momentum, R, aligned with the rotational axis and so $I_z = J_z = K$. I and J can interact and couple with each other in different ways — this is discussed in more detail in Section 2.4.2. There are two simple categories for generating excitations in a nucleus: *collective* and *single particle* excitations.

2.4.1 Single Particle Excitation

Perhaps the most simple mode of excitation to imagine, nuclear single particle excitation is similar to the atomic picture; a nucleon is promoted to a higher energy orbital, leaving a hole state within the orbital it previously occupied. The summation of the collective single particle angular momenta can be expressed as the vector J as depicted in Figure 2.9. Quantum mechanics forbids rotation of a perfectly spherical object, since it is not possible to define a unique frame of reference for this object. Consequently single-particle excitations manifest themselves as a complicated set of energy levels, lacking the regular features and patterns characteristic of a collective, rotational spectrum. As the nucleus moves away from sphericity and is allowed to rotate, single-particle angular momentum can and does make a contribution to the total rotational energy; this is discussed in more detail in Section 2.4.2.

2.4.2 Collective Excitation

Nucleons can couple together to produce collective, *in-phase*, excitations such as rotational and vibrational modes. From the classical expression for rotational energy, an equation describing excited rotational states as a function of spin can be derived:

$$E(I) = \frac{\hbar^2}{2\mathcal{J}}\mathbf{I}^2 = \frac{\hbar^2}{2\mathcal{J}}I(I+1). \tag{2.20}$$

The simple proportionality with $I(I+1)$ gives rise to rotational bands that vary smoothly with increasing spin. Straightaway, we can derive simple, measurable relationships which are ubiquitous with rotational bands:

$$\frac{E(4+)}{E(2+)} = 3.33, \frac{E(6+)}{E(2+)} = 7. \tag{2.21}$$

At $I = 0$, each Nilsson orbital is doubly degenerate. Paired nucleons in each orbital occupy time-reversed orbits, making for maximum spacial overlap. When the nucleus is rotated, time reversal symmetry is broken and orbitals are split into two rotational bands with opposite signature. Signature $(r = e^{-i\pi\alpha})$ is a quantum number related to the invariance of a waveform undergoing a transformation around the rotational axis by π^c,

$$R_x(\pi)\Psi_\alpha = e^{-i\pi J_x}\Psi_\alpha = e^{-i\pi\alpha}\Psi_\alpha. \tag{2.22}$$

With the introduction of signature, rotational bands can then be split into categories.

$K = 0$ **Rotational Bands**

When $K = 0$, $r = (-1)^I$, and so for integer spin I, we have the following selection rules:

$$\begin{aligned} I &= 0,2,4... \text{ for } K = 0 \text{ and } r = 1 \\ I &= 1,3,5... \text{ for } K = 0 \text{ and } r = -1. \end{aligned} \tag{2.23}$$

Here, the only contribution to the total angular momentum I, comes from the collective rotation of the nuclear core. Each sequence of excited states is then described by Equation 2.20.

$K \neq 0$ Rotational Bands

When $K \neq 0$, the signature quantum number is $r = (-1)^{I+K}$ and the resultant energy levels alternate in parity for successive spin values. We have contributions to the total nuclear spin arising from both single particle and collective regimes. The collective action of the core and single particle contributions couple together in two different modes: *deformation aligned* and *rotation aligned*.

In the *deformation aligned* case, particle-rotor coupling is strong and K is a good quantum number. There is only a small amount of signature splitting, with the band's spin states defined in terms of K:

$$I = K, K+1, K+2, ... \tag{2.24}$$

and energy states

$$E_{DAL} = \frac{\hbar}{2\mathcal{J}_0}[I(I+1) - K^2]. \tag{2.25}$$

The situation is the opposite way around for the *rotation aligned* case. Here, deformation is small and/or the particle rotation is very fast. The particle-rotor coupling is weak and K is no longer a good quantum number. Successive spin states are described in terms of the single particle angular momentum, J:

$$I = J, J+2, J+4, ... \tag{2.26}$$

and energy states:

$$E_{RAL} = \frac{\hbar}{2\mathcal{J}_0}(I - J_x)(I - J_x + 1) \tag{2.27}$$

2.4.3 Pairing / Coriolis Antipairing

The Pauli exclusion principle forbids two fermions with identical quantum numbers from occupying the same spacial coordinates. Paired nucleons differ in the orientation of their intrinsic angular momentum (spin up and spin down), so maximally two may occupy the same j orbital. This maximal spacial overlap makes for a higher binding energy - a phenomenon observable in a plot of binding energy per nucleon and one not explained by the liquid-drop model.

Two paired nucleons occupy *time-reversed* orbitals — they travel with velocities of opposite sign. When rotation is introduced, it serves to act on the time reversed pairs in a way that breaks them apart. This is analogous to the classical Coriolis effect, which is described mathematically by Equation 2.28,

$$\vec{F_C} = -2m(\vec{\omega} \times \vec{V}). \tag{2.28}$$

It is easy to see that the force acts in opposite directions for each partner in the pair. At high enough rotational frequencies, the force physically breaks the pair and pushes their individual angular momenta to align with the collective rotational axis. This phenomenon is known as *backbending*, so named for the characteristic "s-shaped" curve in a plot of moment of inertia as a function of rotational frequency. Figure 2.10 displays an example of backbending in ^{162}Hf. Here, alignment of pairs of $i_{13/2}$ neutrons and $h_{11/2}$ protons drives sudden and dramatic increases in moment of inertia at rotational frequencies of 0.06 $(\hbar\omega)^2$ and 0.18 $(\hbar\omega)^2$.

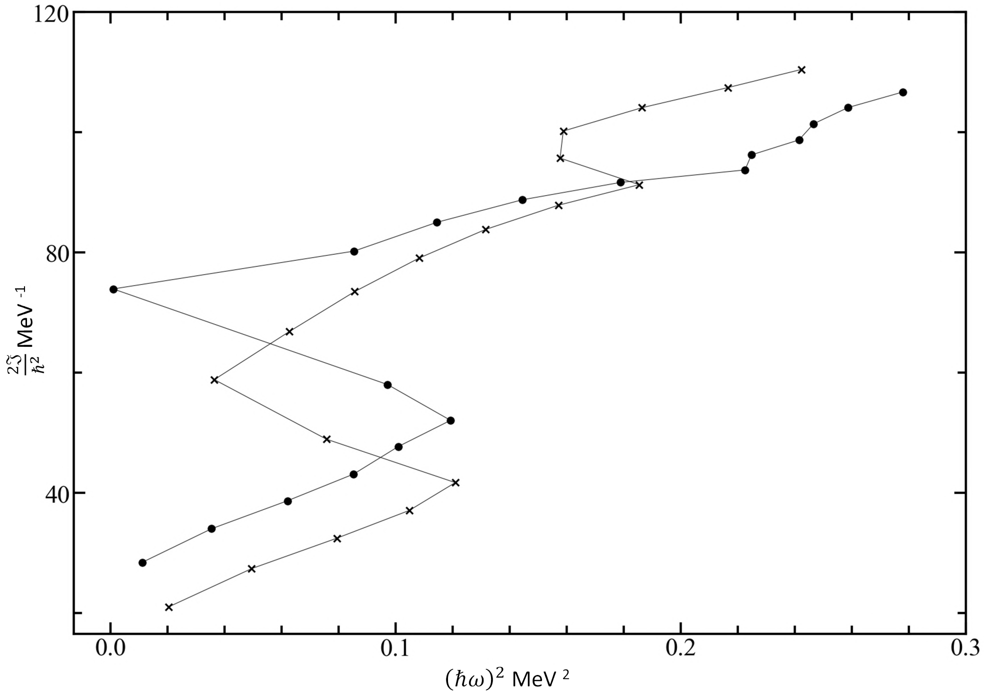

FIGURE 2.10: Static moment of inertia as a function of the square of angular frequency for the two rotational ground state bands in ^{162}Hf (crosses) and ^{164}Hf (dots). The phenomenon known as backbending is exhibited here in spectacular fashion, with ^{162}Hf showing two backbends, corresponding to the alignment of pairs of $i_{13/2}$ neutrons and $h_{11/2}$ protons, respectively [22].

A useful analogy for this is to think of the nucleus as "changing gear", as in a manual transmission car. To maximise angular momentum gain, it is easier for the nucleus to break pairs and align their angular-momentum vectors (J) with the collective rotation of the nucleus (R), than to keep spinning the few unpaired nucleons it has ever faster. The nucleus eventually reaches an upper limit to excitations via this mode, reaching a state known as *band termination*. This exhibits itself in the energy level scheme as a breakdown in regular behaviour at high spin, since all available valence pairs have broken and aligned with the rotational axis [23].

2.5 Quasiparticles

Static models of the nucleus talk about nuclear excitation in terms of the *single-particle* energy. This is adequate when describing excitations of broken nucleon pairs or unpaired, odd nuclei, but becomes problematic when rotation is introduced. Rotation affects single particles and particle pairs alike. Single-particle models cannot, by definition, account for the pairing interaction between two nucleons or the higher-order interactions between nucleon pairs that can be observed experimentally. At the Fermi surface, paired particles in time reversed orbitals can scatter from each other, moving from one orbital to the next. This process cannot happen in the deep nucleus where all energy levels are occupied, and is a process mediated by the pairing interaction. The particles change orbitals in pairs; this is the origin of the "smeared" nature of the Fermi surface. Since particle pairs jump between energy states, it becomes convenient to talk about the *probability* that a particle is occupying a particular energy level. The excited state is then occupied by a particle, and the lesser excited state is occupied by a *hole*. A quasiparticle is then a linear combination of particle-hole occupation probabilities.

$$E_{qp}^2 = (E_{sp} - \lambda)^2 + \Delta^2 \tag{2.29}$$

As can be seen in Figure 2.11, the rotating nucleus behaves as though the orbitals of both particles and holes interact. Analogous to the Nilsson diagram, particle and hole levels of the same parity (π) and signature exponent quantum number (α) repel each other.

2.6 Cranked Shell Model

Just as the spherical shell model can be modified for deformation, it can be modified to account for rotation. The Cranked Shell Model is so-named because it describes the collective rotation of the nuclear field around an external axis located perpendicular to the symmetry axis [24]. Then, the cranking Hamiltonian or *Routhian* is the Hamiltonian in the rotating reference frame. It is given by

$$H_\omega = H_0 - \omega I_x = \sum h_\omega, \tag{2.30}$$

where H_0 is the sum of all the single-particle Hamiltonians, and $h_\omega = h_0 - i_x$ shows that the Routhian can equivalently be constructed as a linear combination of the rotation perturbed Hamiltonians. The correction factor, $-\omega I_x$, is proportional to the projection of the total nuclear angular momentum on the rotational axis and has the effect of making the nucleus less bound for faster rotation and for higher alignment of the angular momentum with the rotational axis.

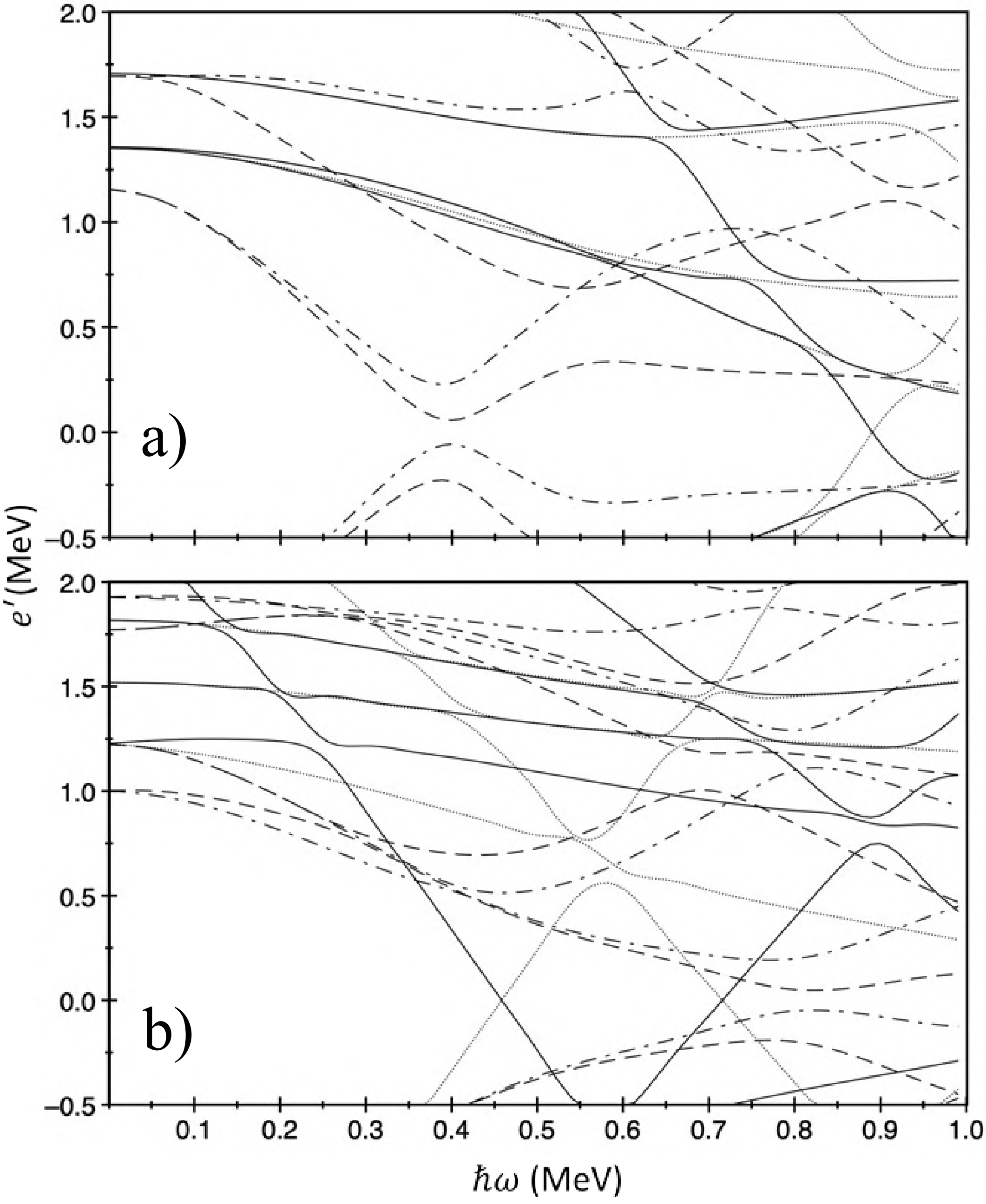

FIGURE 2.11: Panel a): quasiparticle Routhians for protons with $Z = 61$. Panel b): quasiparticle Routhians for neutrons with $N = 71$. Both diagrams calculated using parameters $\beta_2 = 0.35, \beta_4 = 0.0, \gamma = 0.0$. (π, α): solid = (+,+1/2), dotted = (+,–1/2), dot–dash=(–,+1/2), dashed=(–,–1/2).

2.7 Nuclear Isomers

The transition rate for a γ transition between two energy states is dependent on the multipolarity of the emitted radiation. This is covered in more detail in Chapter 3, but for M1/E2 transitions, the emission time is smaller than a nanosecond. This transition rate is far quicker than the 100 MHz timing precision the data acquisition system, or even the response rate of the detector systems. As a result, cascades of transitions through excited bands are usually seen in *prompt-coincidence*; as far as the equipment is concerned, these γ rays were emitted simultaneously. Occasionally a situation will arise where a nucleus decays into a metastable excited state where it is "stuck". The half-life of the subsequent decay from this level is very long in comparison to an ordinary decay — anywhere from tens of nanoseconds to hundreds of years [25]. This metastable state is labelled *isomeric*. Multiple mechanisms can cause isomerism in the atomic nucleus, some of which are discussed below.

2.7.1 K-Isomer

In Section 2.4, we saw how the single-particle angular momenta can sum together and couple with the collective angular momentum to produce a vector representing the total nuclear angular momentum, I. Here, the axially symmetric nature of the nucleus allows us to write for the projection of these quantities on the z (symmetry) axis

$$I_z = J_z = \sum j_{i,z} = \sum \Omega_i = K. \tag{2.31}$$

The vector K represents the summation of the projection of the nucleus's total angular momentum. In the deformation aligned case, there is a large contribution to the total angular momentum from the individual single particle states and K is large. The situation is the opposite way around for the rotationally aligned case.

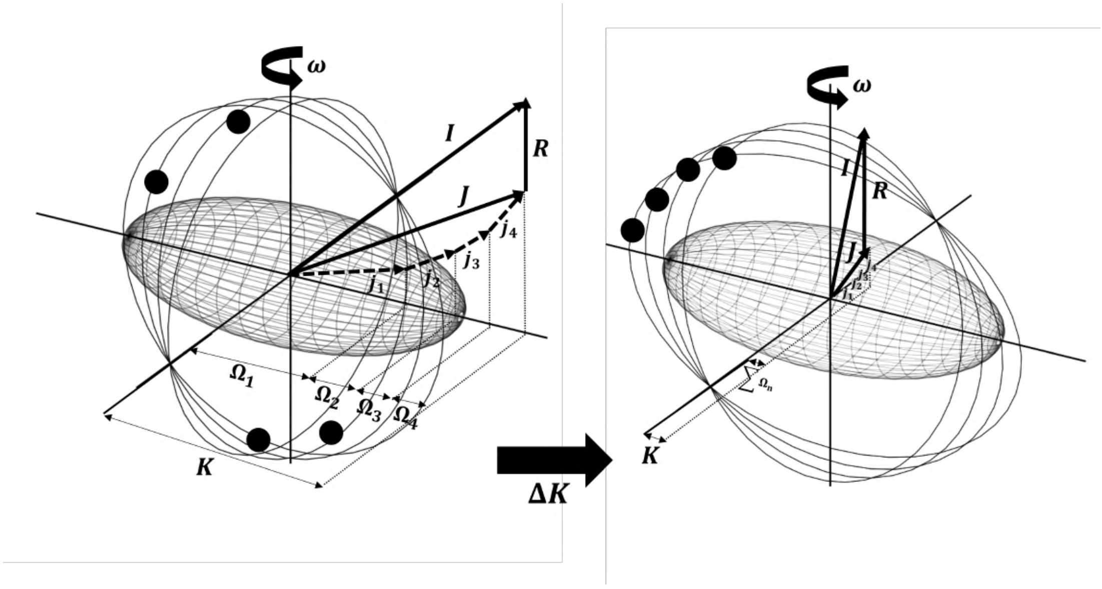

FIGURE 2.12: Left: Four unpaired nucleons contribute a large amount of angular momentum to the total nuclear angular momentum, I. The projections of each of these contributions along the z (symmetry) axis make for a large K. Right: the same nucleus but with small single-particle contribution making for a small K; all unpaired nucleons are aligning with the rotational axis and make a limited contribution to the total angular momentum.

K-isomers occur when a quantum state underneath the isomeric bandhead has a much smaller K value than the isomer. As displayed in Figure 2.12, the nucleus must reorient its entire angular momentum, I, to account for the large change in K. The delayed transition can then be understood as arising from the requirement for the nucleus to drastically rearrange its structure so that the single particle angular momentum vectors align with the rotation and not the deformation.

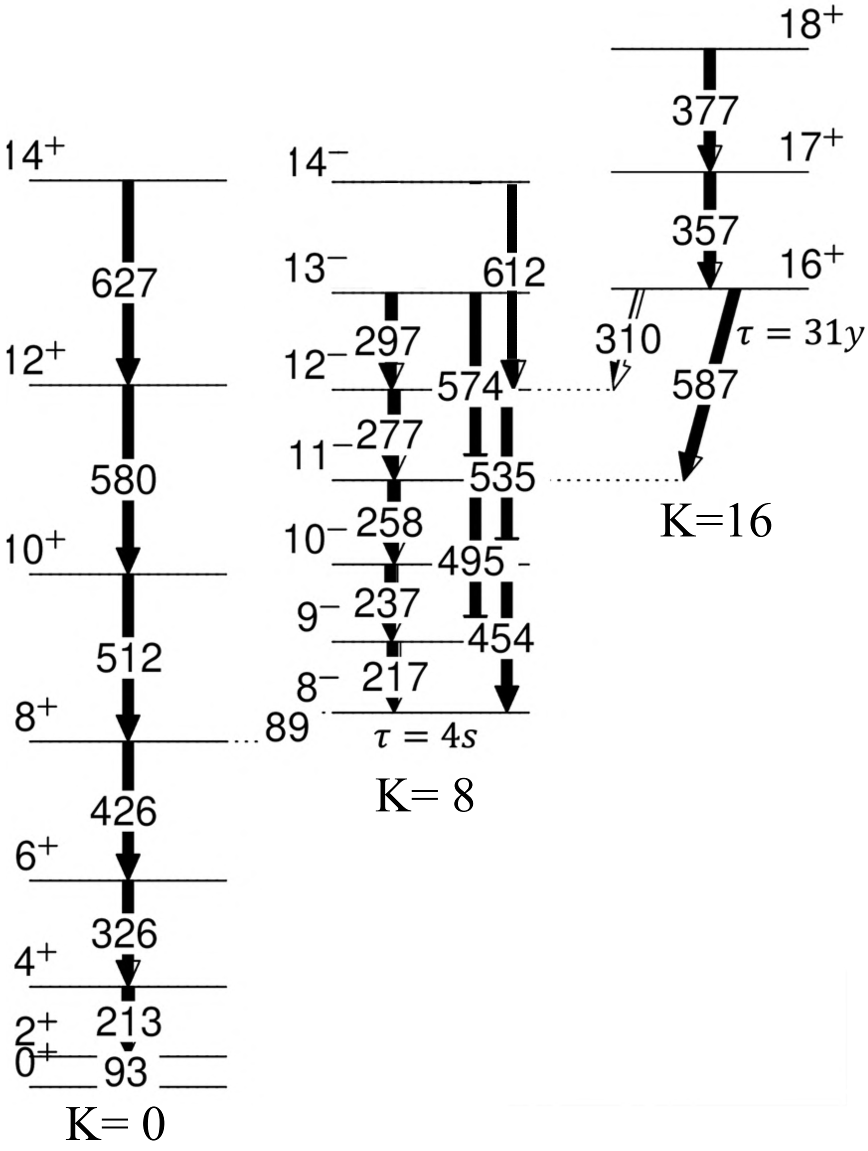
18+
377
17+
357
16+
τ = 31y
310
587
K=16
14+
627
12+
580
10+
512
8+
426
6+
326
4+
213
2+
0+
93
K= 0
14−
612
13−
297
12−
574
277
11−
535
258
10−
495
237
9−
454
217
8−
89
τ = 4s
K= 8

FIGURE 2.13: Partial level scheme for the nucleus ^{178}Hf. Here, the ground-state band and two connected isomeric bands are displayed. The nature of the isomerism for both bands is due to the requirement of a large change in K for decay to occur.

A classic example is the $K^{\pi} = I^{\pi} = 16^{+}$ isomer in ^{178}Hf [26], displayed in Figure 2.13. Here, the isomerism arises not only from the large $\Delta K = 8$, but also because the energy level for the excited 16^{+} state is lower in energy than the 14^{-} state in the neighbouring band. The latter condition is known as spin-trap isomerism and is discussed in the next section. The combination of the two hindrances results in an isomeric half-life of 31 years. A less impressive example of k-isomerism is the $K^{\pi} = I^{\pi} = 8^{-}$ isomer in the second band of the same nucleus. The half life for this state is (only) 4 seconds; here, spin-trapping inhibiting the decay is not present, so the delay is less immense.

2.7.2 Yrast/Spin Trap Isomer

Simply, a spin trap isomer occurs when the isomeric bandhead is lower in energy than the nearest energy level of the same spin or lower that it would otherwise have decayed into. This is illustrated in Figure 2.13, where the $K^{\pi} = I^{\pi} = 16^{+}$ isomer is lower in energy than the neighbouring 14^{-} state. As a result, it must decay into the next nearest energy states. Here, ^{178}Hf decays into the $(13, 12, 11)^{-}$ states requiring a γ ray of a high multipolarity (E3, M4, E5 are seen here) to be emitted in order to account for this large angular momentum change. As detailed in Chapter 3, an increase in one multipole order L results in a reduction of emission probability by a factor of 10^{5}.

2.7.3 Fission Isomer

The preserve of the heaviest nuclei, fission isomers are not observed in this work but shall be briefly discussed here for completeness. Fission isomerism is best illustrated in Figure 2.14. As a heavy nucleus becomes very deformed, it forms up a physical shape like a peanut. This superdeformed state is stablised by a secondary "local" minimum of potential energy. However, the very same "mountains" of potential that stabilise the shape also cause the state to be isomeric. It can be seen that quantum tunnelling can occur either side of the secondary minimum. Tunneling through toward the side of lower deformation offers a decay path through to the primary minimum and further decays to the ground state. All other tunneling paths result in fission.

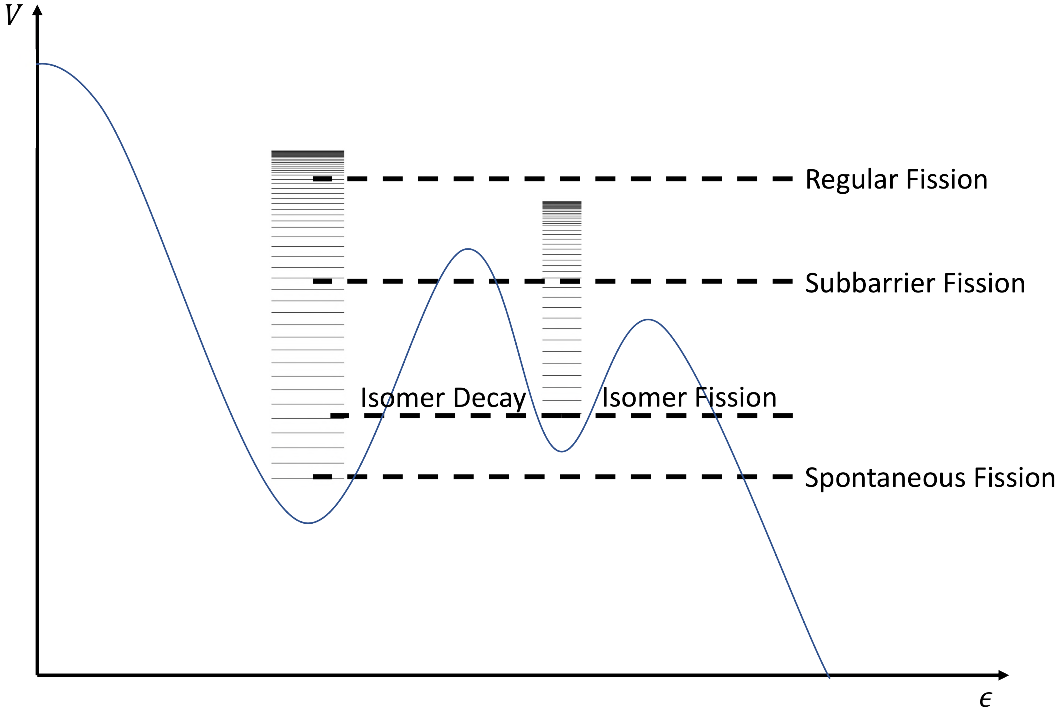
V
Regular Fission
Subbarrier Fission
Isomer Decay
Isomer Fission
Spontaneous Fission
ϵ

FIGURE 2.14: Hypothetical first and second (superdeformed) potential energy minima for a heavy and highly deformed nucleus.

2.8 Measurable Quantities

Quantities that are both relevant and comparable to nuclear theory and readily extractable from the data are summarised in this section [24, 27].

2.8.1 Rotational Frequency

The rotational frequency of a nucleus is given by the simple relation

$$\hbar\omega = \frac{dE}{dI} = \frac{\Delta E}{\Delta I} \approx \frac{E_\gamma}{2}. \tag{2.32}$$

The right hand side assumes finite differences — which is valid since there are no continuous energy states between discrete levels within the nucleus. The relation $\hbar\omega = \frac{E_\gamma}{2}$ is valid for a cascade of E2 gammas and is useful since it makes it so we do not need to know the spin of the level of interest to calculate the rotational frequency.

2.8.2 Moments of Inertia

The rigid body value for the nuclear moment of inertia is given by

$$\mathcal{J}^{rig} = \frac{2}{5} m_n A^{5/3} r_0^2 [1 + 0.3\beta], \tag{2.33}$$

where m_n is the mass of a nucleon, A is the number of nucleons, $r_0 (= 1.2 \text{ fm})$ is the radius of a single nucleon, and β is the quadrupole deformation parameter. It is observed experimentally that the nuclear moment of inertia varies as a function of spin, and usually differs from the rigid body value. Experimentally, we define the kinematic and dynamic moments of inertia:

$$\mathcal{J}^{(1)} = I \left[\frac{dE}{dI} \right]^{-1} = \frac{I}{\omega}, \tag{2.34}$$

$$\mathcal{J}^{(2)} = I \left[\frac{d^2E}{dI^2} \right]^{-1} = \frac{4}{\Delta E_\gamma}, \tag{2.35}$$

respectively. The definition of the dynamic moment of inertia, $\mathcal{J}^{(2)}$, again uses finite differences to simplify its definition and absolute spins of the levels in question do not need to be known for its calculation. The quantity ΔE_γ is simply the difference in energy between two successive transitions in a rotantional cascade. $\mathcal{J}^{(2)}$ is very sensitive to single-particle alignments; generally a high $\mathcal{J}^{(2)}$ means a high deformation.

2.8.3 Experimental Alignment

The single-particle alignment to the rotational axis (x-axis) is given by

$$i_x(\omega) = I_x(\omega) - I_{\text{ref}}(\omega). \tag{2.36}$$

where $I_{\text{ref}}(\omega)$ is the contribution to the total angular momentum from the collective rotation of the nucleus. This reference angular momentum can be taken by fitting to a reference band, usually taken from a neighbouring even-even nucleus

$$I_{ref}(\omega) = \omega\left[\mathcal{J}_0 + \mathcal{J}_1\omega^2\right] + i_x, \tag{2.37}$$

where $\mathcal{J}^{(0,1)}$ are the Harris parameters which are obtained numerically from the fitting algorithm and i_x is the single-particle contribution ($i_x = 0$ for the ground state rotational band of an even-even nucleus).

2.8.4 Experimental Routhian

The experimental Routhian can be expressed as

$$E(I) = \frac{1}{2}\left[E(I+1) - E(I-1)\right] - \omega(I)I_x(\omega). \tag{2.38}$$

This equation is inclusive of both collective and single (quasi) particle effects, and can be corrected by subtracting the collective excitation energy:

$$e'(I) = E(I) - E_{\text{ref}}(I), \tag{2.39}$$

and the collective rotational contribution to the total angular momentum as defined in Equation 2.36 and 2.37. The energy correction E_{ref} is expressed in terms of the Harris parameters

$$\begin{aligned} E_{\mathrm{ref}} &= -\hbar \int I_{\mathrm{ref}}\, d\omega, \\ &= -\frac{1}{2}\omega^2 \mathcal{J}_0 - \frac{1}{4}\omega^4 \mathcal{J}_1 + \frac{1}{8}\frac{\hbar^2}{\mathcal{J}_0}. \end{aligned} \tag{2.40}$$

2.9 B(M1)/B(E2) Ratios

Where both $\Delta I = 1, 2$ transitions are allowed in the decay out of an excited nuclear state, measurement of the reduced B(M1)/B(E2) transition probability ratios can be made. Contrary to the process of measuring singular reduced transition probabilities, the process of extracting the ratio is simple, depending only on the (efficiency corrected) photopeak intensities and energies. The experimental ratios are given by

$$\frac{B(M1; I \rightarrow I-1)}{B(E2; I \rightarrow I-2)} = 0.697 \frac{E_\gamma(E2)^5}{E_\gamma(M1)^3} \frac{I_\gamma(M1)}{I_\gamma(E2)} \frac{1}{1+\delta^2_{E2/M1}} \tag{2.41}$$

where E_γ, I_γ are the γ ray energies and intensities and $\delta_{E2/M1}$ is the multipole mixing ratio, which is generally not larger than 5%. Measurement of the B(M1)/B(E2) ratios can give insight into its underlying structure. The geometric model of Donau and Frauendorf [28] details the proportionality of the ratio to intrinsic nuclear properties,

$$\frac{B(M1; I \rightarrow I-1)}{B(E2; I \rightarrow I-2)} \propto \frac{K^2(g_k - g_r)^2}{Q_0^2}, \tag{2.42}$$

where K is the projection of the nuclear spin along the axis of deformation, Q_0 is the intrinsic quadrupole moment, and g_r and g_k are the gyromagnetic ratios of the rotating nuclear core and single particle, respectively. We can see that a large ratio is influenced by a high K value and/or large gyromagnetic ratios, yielding very intense magnetic dipole transitions. A small ratio is associated with a large quadrupole moment, and therefore a large quadrupole deformation and greater intensity for the electric quadrupoles.

Chapter 3

Experimental Theory, Setup & Methods

3.1 Gamma Emission in Nuclei

The electromagnetic force behaves in a fairly straightforward manner within the nucleus. The Coulomb repulsion between protons gives rise to the well known asymmetry in the chart of the nuclides [5]. The electromagnetic force also mediates the decay of excited nuclei from high energy states. Almost all nuclear reactions leave the nucleus in an excited state [29], where the nucleons occupy discrete energy levels which are higher than some unoccupied levels below them. To maximise binding energy, the nucleons want to move to these lower energy, more tightly bound states. To conserve energy when a nuclear transition is made, a γ ray is produced, which has an energy equal to (save for a small recoil correction) the difference in energy between the nuclear states [30]. The field of γ-ray spectroscopy is based entirely on this phenomenon, and has allowed us to probe the inner machinations of the nucleus with an unprecedented level of detail.

That γ emission is so important to this field means the mechanism by which the radiation is produced should get a more thorough treatment within this text. The following section is drawn together from the texts [31, 32], as well as the original work by Blatt and Weisskopf [33]. Radiation can be generated either by an oscillating charge, which causes an oscillation in the external electric field, or by a varying current or magnetic moment, which sets up a varying magnetic field. Radiation emitted by the former mechanism is called electric (E) radiation and the latter is said to give rise to magnetic (M) radiation. Classically, the power emitted by a multipole radiator is given by

$$P(\sigma L) = \frac{2(L+1)c}{\epsilon_0 L[(2L+1)!!]^2} \left(\frac{\omega}{c}\right)^{2L+2} [m(\sigma L)]^2, \tag{3.1}$$

where σ denotes the type of radiation (E or M), L is the multipole order ($L = 1$ for dipole, 2 for quadrupole, etc), and $m(\sigma L)$ is the amplitude of the electric or magnetic multipole moment. To quantise Equation 3.1, one must quantise the classical multipole moments which serve as the source of the radiation. This is done by changing the multipole moment to the multipole moment operator, $m_{\mathrm{fi}}(\sigma L)$. We can say Equation 3.1 is the energy radiated per unit time in the form of photons — each of which has energy $\hbar\omega$. The decay constant (probability for photon emission) is then given by

$$\begin{aligned} \lambda(\sigma L) &= \frac{P(\sigma L)}{\hbar\omega} \\ &= \frac{2(L+1)}{\epsilon_0 \hbar L[(2L+1)!!]^2} \left(\frac{\omega}{c}\right)^{2L+1} [m_{\mathrm{fi}}(\sigma L)]^2. \end{aligned} \tag{3.2}$$

To take this calculation further, we have to evaluate the matrix element $m_{\mathrm{fi}}(\sigma L)$. The multipole moment operator for electric radiation is given by the following approximate (valid for long wavelengths) expression:

$$m_{\mathrm{fi}}(EL) = \sum_{k=1}^{Z} \int r_k^L \, Y^*_{\mathrm{LM}}(\theta_k, \phi_k) \, \rho(\mathbf{r}) \, dV, \tag{3.3}$$

where the discrete summation is over all the contributions for each proton in the nucleus, the integral is over the nuclear volume, and the quantum mechanical analogue for the charge density is given by

$$\rho(\mathbf{r}) = e\,\Psi_f^*(\mathbf{r})\,\Psi_i(\mathbf{r}). \tag{3.4}$$

To simplify this process, we consider that a transition causing an emission is purely due to the motion of a single proton moving from one shell-model state to another. We call this the single-particle estimate. We also take the spin of the proton to be L in its initial state, and 0 in the final state. The two wave functions describing the final (Ψ_f) and initial (Ψ_i) states then have the form

$$\Psi_i = u_i(r)\,Y_{\mathrm{LM}}(\theta,\phi)\,\alpha, \tag{3.5}$$

$$\Psi_f = \frac{1}{\sqrt{4\pi}}u_f(r)\,\alpha, \tag{3.6}$$

where α is the spin function for a particle with spin up, and Ψ_i, Ψ_f are functions of the radial component, $\mathbf{r} = |r|$, only. Substituting these wave functions into Equation 3.3, and accounting for the single particle estimate (only the first contribution for the discrete summation over the protons is needed), we get:

$$m_{\mathrm{fi}}(EL) = \frac{e}{\sqrt{4\pi}} \int_0^\infty r^L\,u_i(r)\,u_f(r)\,r^2 dr, \tag{3.7}$$

where the factor of r^2 comes from the radial part of the volume integral. Proceeding to evaluate the radial integral, we set both $u_i(r), u_f(r)$ to the same constant for values of r less than the nuclear radius, R, and 0 for values beyond R. The constant is found by the normalisation of the wave functions:

$$\frac{\int_0^R r^2 r^L\,dr}{\int_0^R r^2\,dr} = \frac{3}{L+3}R^L. \tag{3.8}$$

The estimate used for the form of $u_i(r), u_f(r)$ is a very rough one; the radial wave functions are not constant within the nucleus and oscillate somewhat as they reach the nuclear surface, and drop gradually to zero beyond the surface. Because of this it is expected that the actual value of Equation 3.8 is somewhat smaller. Pressing ahead with our estimate, we substitute Equation 3.8 into our equation for the multipole moment operator (Equation 3.7), which results in

$$[m_{\text{fi}}(EL)]^2 \approx \frac{e^2}{4\pi}\left(\frac{3}{L+3}\right)^2 R^{2L}. \tag{3.9}$$

Finally, we substitute this into the equation for the decay constant (Equation 3.2) which gives an estimate for the transition rate

$$\lambda(EL) = \frac{8\pi(L+1)}{L[(2L+1)!!]^2}\left(\frac{\omega}{c}\right)^{2L+1}\frac{e^2}{4\pi\epsilon_0\hbar}\left(\frac{3}{L+3}\right)^2 R^{2L}. \tag{3.10}$$

A similar analysis can be performed for the magnetic radiation. The transition rate for magnetic radiation is estimated by

$$\begin{aligned} m_{\text{fi}}(ML) =& \frac{8\pi(L+1)}{L[(2L+1)!!]^2}\left(\mu_p - \frac{1}{L+1}\right)^2\left(\frac{\hbar}{m_p c}\right)^2 \ldots \\ & \ldots\left(\frac{e^2}{4\pi\epsilon_0\hbar}\right)\times\left(\frac{\omega}{c}\right)^{2L+1}\left(\frac{3}{L+2}\right)^2 R^{2L-2}. \end{aligned} \tag{3.11}$$

Taking $R = R_0 A^{1/3}$, we can make the following estimates for some of the lower multipole orders — displayed in Table 3.1.

TABLE 3.1: Comparison of the estimated transition rates for electric (E) and magnetic (M) radiation for various multipole orders, as per the Weisskopf single-particle estimates.

	(E) s^{-1}	(M) s^{-1}
1 (Dipole)	$1.0 \times 10^{14} A^{2/3} E^3$	$5.6 \times 10^{13} E^3$
2 (Quadrupole)	$7.3 \times 10^{7} A^{4/3} E^5$	$3.5 \times 10^{7} A^{2/3} E^5$
3 (Octupole)	$34 A^2 E^7$	$16 A^{4/3} E^7$
4 (Hexadecapole)	$1.1 \times 10^{-5} A^{2/3} E^3$	$4.5 \times 10^{-6} A^2 E^9$

The Weisskopf estimates are designed to give an indication of transition rates of a particular radiation type relative to the other types. Because of the coarse nature of the approximations that were used in their derivation, they are not expected to be comparable to experimental results. That said, some interesting conclusions can be drawn from them. Firstly, it can be seen that magnetic radiation is around an order of magnitude less likely to occur than electric radiation for the same multipole order. Secondly, lower multipole order radiation dominates. Increasing the multipole order by one unit results in a reduction in emission probability by a factor of 10^5 each time.

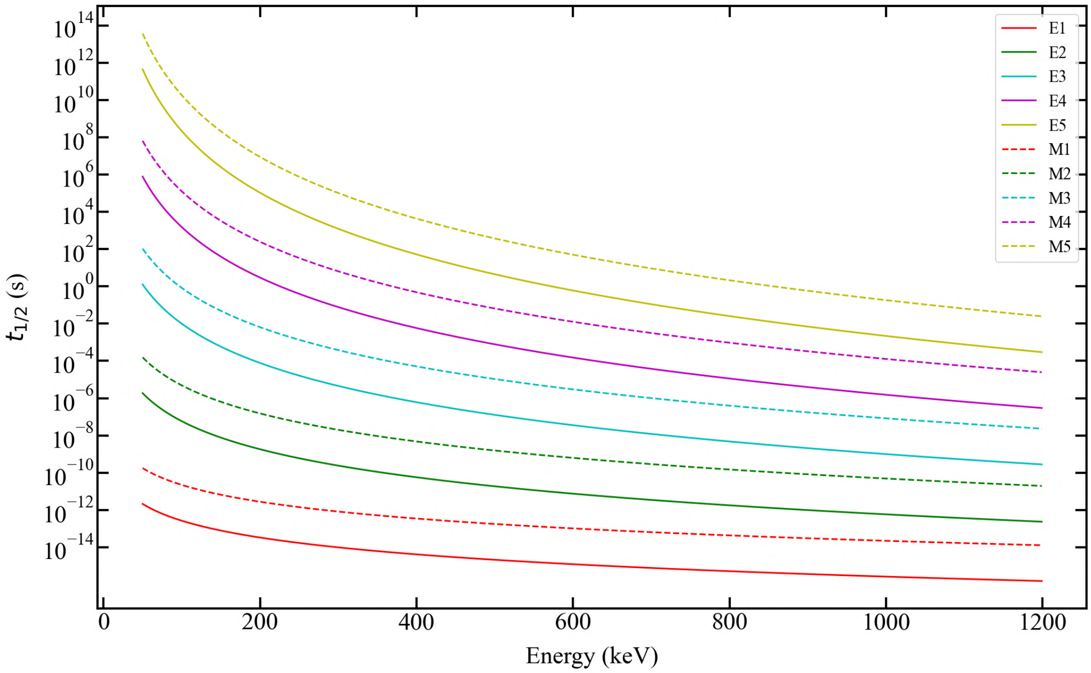

FIGURE 3.1: Weisskopf half-life estimates as a function of transition energy, for multipolarities M1-5 and E1-5, assuming a mass-130 nucleus.

3.2 Gamma-Ray Spectroscopy

3.2.1 Interaction of Gamma Rays with Matter

Three primary interaction mechanisms allow γ rays to deposit their energy into particulate matter. These mechanisms — the photoelectric effect, pair production and Compton scattering — all manifest themselves in the detector by transfer of energy from the interacting γ ray to atomic electrons within the detector material. These "free" electrons are collected via application of an external (reversed) electric bias. The magnitude of collected charge — the so-called pulse — is proportional to the energy of the absorbed γ ray. Detector characteristics should be optimised with a particular application in mind. For instance, if we are interested in accurate energy measurements, it is desirable to use a detector with a large volume of semi-conducting material that produces an output pulse proportional to the deposited energy. Highly-purified germanium detectors are commonly used for this purpose. Other applications include high-precision timing (lanthanum bromide), or maximum detector efficiency with disregard to energy resolution (bismuth germanate, used here as Compton suppressors).

3.2.2 Fusion-Evaporation Reactions

Production of the energetic nuclides studied in this work is via the mechanism of heavy-ion fusion-evaporation reactions. Put simply, the energetic beam delivered by the K130 cyclotron is directed into a static, thin-foil target. When the beam is on target, the kinetic energy of the projectile is enough to overcome the Coulomb barrier at the target and a *compound nucleus* is formed. The kinetic energy required to overcome this *interaction barrier* can be calculated using the Bass model [34], given by

$$\begin{aligned} B_{int} &= \frac{Z_p Z_t e^2}{4\pi\epsilon_0 R_{12}} \left[\frac{R_{12}}{R_{12} + d_{int}} - \frac{1}{x}\frac{d}{R_{12}} e^{\frac{-d_{int}}{d}} \right], \\ x &= \frac{e^2}{a_s R_{12}} \frac{Z_p Z_t}{A_p^{1/3} A_t^{1/3}}. \end{aligned} \tag{3.12}$$

Here, R_{12} is the sum of the nuclear radii, a_s is the surface term from the nuclear drop model (17.23 MeV) and d, d_{int} are empirical parameters representative of the nuclear force's range and the interaction distance, respectively. Bass gives these parameters as $d = 1.35$ fm and $d_{int} = 2d = 2.70$ fm with $r_0 = 1.07$ fm being valid for a wide range of projectile and target masses.

A further consideration to make is the transfer of angular momentum from the beam to the target,

$$\vec{p} = m\vec{v}, \vec{L} = \vec{b} \times \vec{p}. \tag{3.13}$$

Figure 3.2 displays a schematic beam impact onto a target nucleus.

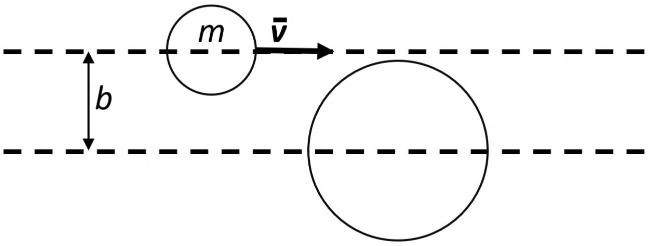

FIGURE 3.2: Schematic diagram of a fusion-evaporation reaction depicting the impact parameter, b.

It is desirable that the angular momentum transfer is sufficient that the nuclei produced have high enough spin to be of interest, but not so much that the nucleus fissions under centrifugal repulsion. From Equation 3.13 it can be seen that angular momentum transfer can be increased by either increasing the beam energy or by increasing the impact parameter. However, if the impact parameter is too large fusion will not occur, becoming dominated by rival interaction processes such as inelastic scattering and Coulomb excitation.

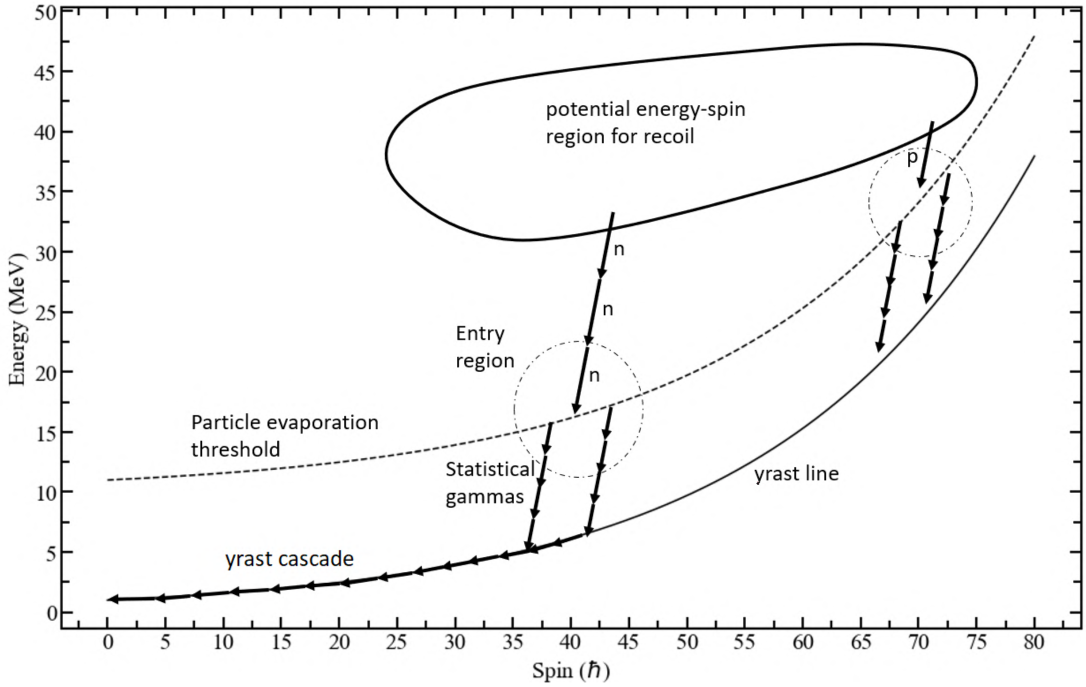
Energy (MeV)
0
5
10
15
20
25
30
35
40
45
50
Spin (ħ)
0
5
10
15
20
25
30
35
40
45
50
55
60
65
70
75
80
potential energy-spin
region for recoil
n
n
n
p
Entry
region
Particle evaporation
threshold
Statistical
gammas
yrast line
yrast cascade

FIGURE 3.3: Schematic diagram indicating two hypothetical decay paths from the moment of fusion to the ground state of the recoil.

Figure 3.3 displays the hypothetical decay of a compound nucleus. In order to lose energy as quickly as possible, it undergoes "boiling off" of protons, neutrons and α-particles. These particles carry away a large amount of energy and a small amount of angular momentum.

Eventually, the excitation energy falls below the threshold for particle evaporation (approximately 8 MeV above the yrast line). To continue losing energy, the nucleus de-excites by emitting statistical γ rays. These are generally high-energy dipoles, again removing a large amount of energy and a small amount of angular momentum [35].

When the nucleus has shed sufficient energy, it reaches states near the yrast line. Yrast, translated literally as "dizziest", is the lowest-energy state for a given spin. Such as it is, the nucleus will decay by transition through an orderly cascade of near-yrast γ rays. This is advantageous to us as spectroscopists; since every non-yrast transition must eventually feed the yrast cascade, these transitions are very intense relative to the radioactive background.

3.2.3 Limitations of Conventional Gamma-Ray Spectroscopy

Modern γ-ray spectroscopy emerged with the development of larger arrays of escape-suppressed high-purity germanium (HPGe) detectors. One of the first such arrays, TESSA (The Escape Suppressed Spectrometer Array), was assembled in 1980 and consisted of 5 HPGe detectors surrounded by NaI scintillator escape suppressors. TESSA heralded the start of the "golden age" of nuclear structure, pushing the boundaries of high-spin nuclear spectroscopy and eventually making possible the groundbreaking discovery of superdeformation in ^{152}Dy [36]. Larger arrays were eventually constructed, with detectors such as GAMMASPHERE consisting of $\approx$ 100 HPGe detectors, and the EUROBALL detector consisting of a myriad of detectors [37]. The two large detector arrays continued the successful period of discovery overseen by their precursors [38, 39, 40]. Augmenting these detectors with recoil separators, recoil-implantation detectors and focal-plane γ spectrometers, we can expand the range of decay types and lifetimes an experiment is sensitive toward. Compared to an isolated γ spectrometer:

- Correlation between isomeric decays and the prompt states built upon them is possible.
- High probability of recoil fission at the target position makes for a large γ ray background. Increased selectivity from recoil-decay tagging/recoil gating methods allows suppression of this background.
- Exotic nuclei are often produced with a low cross-section on the order of nanobarns. Furthermore, particular decay paths compete with other decay paths for the same nucleus as a result of the distribution of spin-energy states the compound nucleus begins with. Again, selective tagging techniques help alleviate this problem by suppressing unwanted decay signals.

3.3 Recoil-Decay Tagging (RDT)

Key to understanding how to effectively analyse data is to understand the experimental setup and the "timeline" of a typical excited nucleus. When analysing data from a recoil-decay experiment, we look for some unique identifier of a particular nucleus, for example a characteristic γ ray, or alpha particle.

After fusion, the resultant compound nucleus is dislodged from the static target due to the kinetic energy of the impinging beam and approximately follows the original trajectory of the beam. Beyond this point, the compound nucleus can be referred to as the "recoil" because of how it recoils from the beam/target collision. This recoil will now de-excite through a variety of mechanisms, each of which occur over very different time scales, requiring a suite of detector systems placed along the beamline as depicted in Figure 3.4.

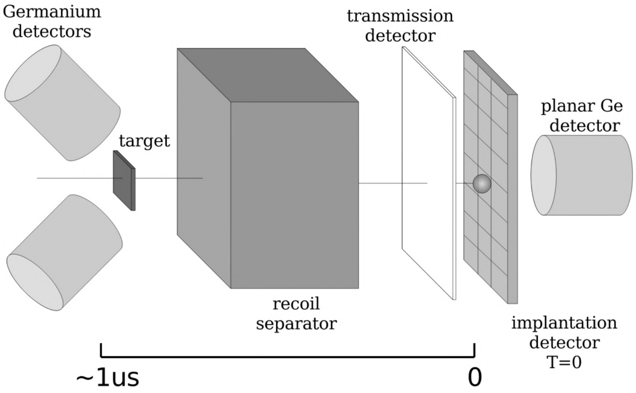

FIGURE 3.4: Schematic diagram of a typical recoil-decay experimental setup where the recoiling nucleus is travelling from left to right [41]. Here, $t = 0$ is when the recoil implants into the DSSD. γ emission at the target position is then in the past relative to the implantation event.

The first mechanism is that of "boiling off" protons, neutrons and α particles. This can be thought of as the recoil shedding nucleons that the strong nuclear force cannot capture due to their highly energetic nature. As nuclear spectroscopists, this presents us with a useful opportunity to identify the recoil based on how many protons and neutrons are boiled off. JYFL-ACCLAB uses a collective of CsI crystals — known as UoYTube — to detect evaporated protons and alpha particles, though this was not installed for the JM06 experiment. Evaporation of nucleons occurs incredibly quickly; the recoil will still be well within the vicinity of the target position at this point even though it is travelling at a significant fraction of the speed of light.

Eventually the recoil settles into a bound — but still highly excited — state. Now the nucleus will seek to lose energy via γ decay. The recoil can still be thought of as being within the vicinity of the target position when this happens. Because of this, it makes sense to include a γ spectrometer near to the target position; the JUROGAM spectrometer serves this purpose for the JYFL-ACCLAB experimental setup.

The recoil has shed the vast majority of its angular momentum and energy at this point. As it travels onward beyond the target position, it may have even reached its ground state. It is possible however, that the recoil is in a semi-stable excited state known as an isomeric state — these are discussed in greater detail in Section 2.7. As of 2019, the JUROGAM spectrometer is mounted on rails, meaning it can be easily transported between two recoil separators utilised at JYFL-ACCLAB: MARA (Mass Analysing Recoil Apparatus) and RITU (Recoil Ion Transport Unit). Specific differences between the two recoil separators are covered in Section 3.5.3. The purpose of a recoil separator is, as the name suggests, to separate recoil products out from the unreacted beam. This serves two main purposes: firstly we want to study the recoils and not the beam, so it makes sense to separate them out; the second is to prevent the highly energetic and intense beam from reaching the delicate detector equipment situated beyond the separator.

Separated recoils end their journey with an implantation into a Dual-Sided-Silicon-Detector (DSSD, indicated as implantation detector in Figure 3.4). The

DSSD is arranged as a series of horizontal strips over a series of vertical strips. This grid arrangement makes it such that a recoil interacting with both layers of strips can be spatially located to within a single "pixel" on the DSSD. There are numerous methods of decay that can occur at this point: common decay modes such as alpha, beta and gamma, but also more exotic kinds of decay such as direct proton decay. As well as being able to measure the energy of the implanted recoil, the DSSD can measure the energy of any subsequent decay particles. This is useful to us as spectroscopists seeking to identify this unique segment of a recoil's timeline.

3.4 Total Data Readout (TDR) & GRAIN

A conventional nuclear physics experiment will define a nuclear timeline — technically referred to as an event — using a hardware or software based "trigger". The whole event comprises measurements registered as occurring a set period of time before and after the trigger. An example of a hardware based trigger can be seen at GAMMASPHERE where you might require a minimum of 3 temporally coincident γ rays at the γ spectrometer to register an event. This makes sense, since it is unlikely background radiation would give rise to such a large amount of coincident gammas within several nanoseconds. A big disadvantage of a hardware trigger is that any time-gating denoting coincidence is fixed at the start of the experiment. It is not possible to retroactively look at the data with a different definition of what constitutes an event and what does not. The Total Data Readout system provides a solution to this. Here, every single (uncorrelated) measurement is labelled with a precise 10 ns (100 MHz) time stamp, packaged into a single sequential data steam and saved to disk: the Total Data Readout. A full event is displayed pictographically in Figure 3.5.

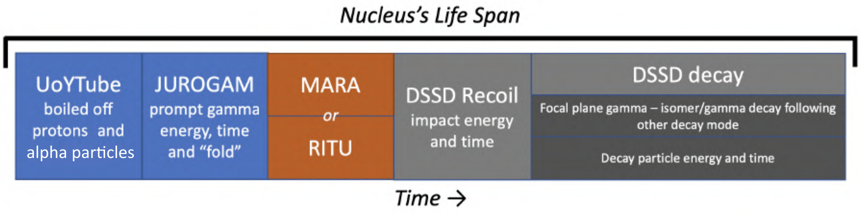
Nucleus's Life Span
UoYTube
boiled off protons and alpha particles
JUROGAM
prompt gamma energy, time and "fold"
MARA
or
RITU
DSSD Recoil
impact energy and time
DSSD decay
Focal plane gamma – isomer/gamma decay following other decay mode
Decay particle energy and time
Time →

FIGURE 3.5: Schematic diagram representing the timeline of an excited nucleus as it travels throughout the detector equipment.

Selecting an event that corresponds uniquely to a nucleus requires choice of a unique, characteristic, measurable property of that nucleus. We can then in principle look either backwards or forwards at the rest of the event and extract all of the information about this nucleus.

The primary online and offline sorting code is processed using the Grain software package [41]. Sortcodes are written in the Java programming language and render the filtered results as histograms (1D and 2D), n-tuples (a table-like list of correlated variables) and/or save the sorted data to disk for further processing. Secondary processing was performed using custom python scripting, and software package RADWARE [42]. Peak fitting was performed using custom Python scripting, or, where peak integration was required, the software HDTV [43].

3.5 JYFL-ACCLAB Experimental Setup

3.5.1 K130 Cyclotron

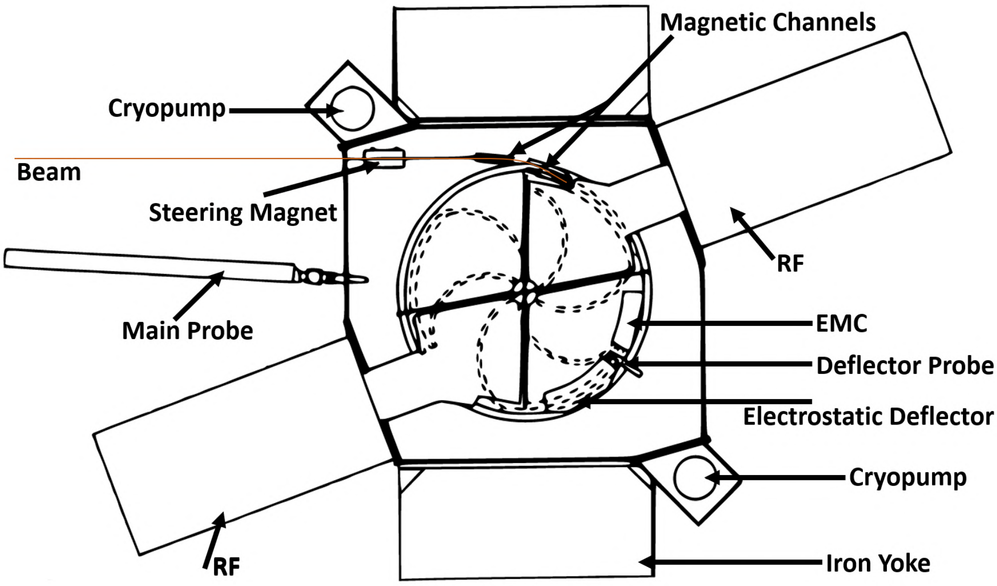
Magnetic Channels
Cryopump
Beam
Steering Magnet
Main Probe
RF
EMC
Deflector Probe
Electrostatic Deflector
Cryopump
RF
Iron Yoke

FIGURE 3.6: Overview schematic diagram of the K130 Cyclotron and its components [44].

The K130 Cyclotron (Figure 3.6) was commissioned in the late 80′s as a replacement for the department′s ageing MC-20 cyclotron. Primary design considerations were influenced by cost and manpower needs, so the accelerator was ordered from commercial manufacturer Scanditronix AB. To produce the highly-charged ions required for the primary beam, an ECR-ion source is used. ECR (Electron Cyclotron Resonance) involves the collision of electrons — which are excited using microwaves — and an electrically neutral gas confined in a magnetic field. Electrons in a static magnetic field will move in a circle due to the Lorentz force. The frequency of this motion is determined by the magnitude of the field. If, simultaneously, an electric field (provided by the microwave) is incident at the same (resonant) frequency of this motion, then the electrons will undergo cyclonic motion. The energetic electrons subsequently collide with the uncharged gas, ionising it. The ions are transported to the main cyclotron and are accelerated to a beam energy of several hundred keV, forming the primary beam for the experiment.

3.5.2 The JUROGAM3 Spectrometer

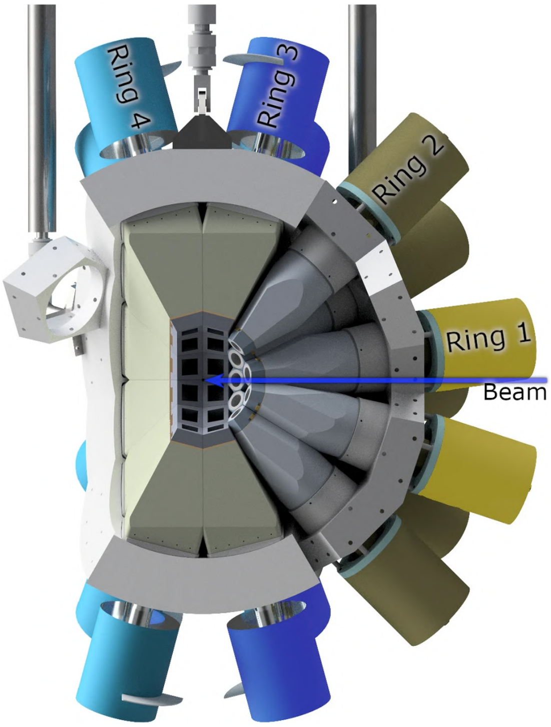

FIGURE 3.7: Schematic rendering of the JUROGAM3 highly-purified germanium (HPGe) array. The various detector rings are marked and coloured for ease of identification. The ion beam delivered by the K130 cyclotron moves from right to left as indicated by the arrow. [45]

The main γ ray spectrometer used throughout this experiment was JUROGAM3. The JUROGAM3 spectrometer comprises 39 highly-purified, liquid nitrogen cooled germanium detectors. Each of these detectors are surrounded by bismuth germanate (BGO) Compton suppression shields for efficient escape suppression, and are further supplemented by heavy-metal collimators in front of each shield to prevent false event veto from γ rays directly incident on the BGO shield.

JUROGAM3 is comprised of two detector types. The first is a conventional, single-crystal, tapered Phase 1 type detector. 15 of these detectors are arranged in a configuration that has 5 detectors at 157.6° and 10 detectors at 133.6°, relative to the beam axis. The second detector type is the more complicated composite "Clover" style detector. As the name suggests, this detector type consists of 4 separate HPGe crystals. These detectors are arranged in 2 rings of 12 detectors at angles 104.5° and 75.5° relative to the beam axis, as detailed in Figure 3.9.

Figure 3.8 details the measured efficiency of JUROGAM3 at the beginning of the JM06 data run. It can be seen that the array is at its most efficient at $\sim$ 200 keV. Absolute efficiency measurements were made with a ^{152}Eu^{133}Ba source with an initial activity (certified on 1st April 2003) of 4.01 kBq for the europium and 4.24 kBq for the barium.

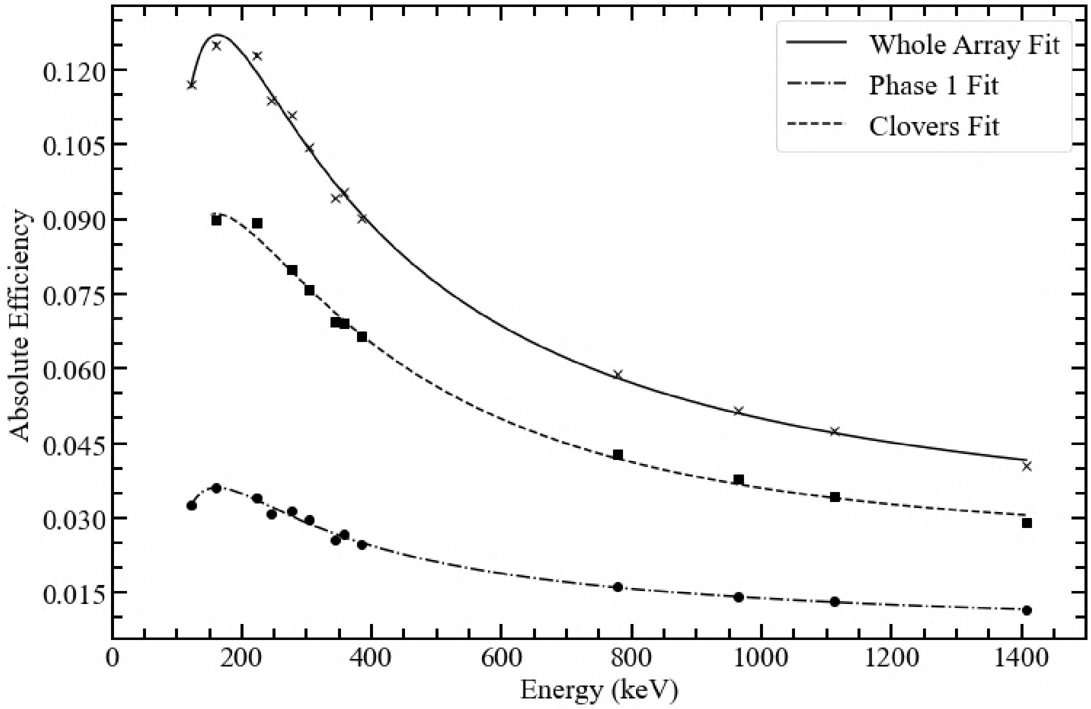

FIGURE 3.8: Measured efficiency as a function of energy for the entire JUROGAM3 array at the beginning of the JM06 run. Fit given by Equation 3.14 with fit parameters for the whole array: A: 122.56, B: -215.07, C: 85.26, D: -12.49, E: 0.64; the Clovers only: A: 1389.97, B: -1039.59, C: -285.41, D: -34.04, E: 1.51; and the Phase 1 detectors only: A: -207.72, B: 100.21, C: -15.56, D: 0.76, E: 0.01.

The equation used to model the efficiency curve as a function of γ-ray energy is adapted from [46],

$$\epsilon(E) = \frac{1}{E}\left[A + B\ln(E) + \mathrm{C}\ln(E)^2 + D\ln(E)^3 + E\ln(E)^4\right]. \tag{3.14}$$

It should be noted that where efficiency corrections have been made in this work, they have only been made within the energy bounds of this fit. No extrapolation has been made beyond the minimum/maximum bounds of 121.8 / 1408.0 keV.

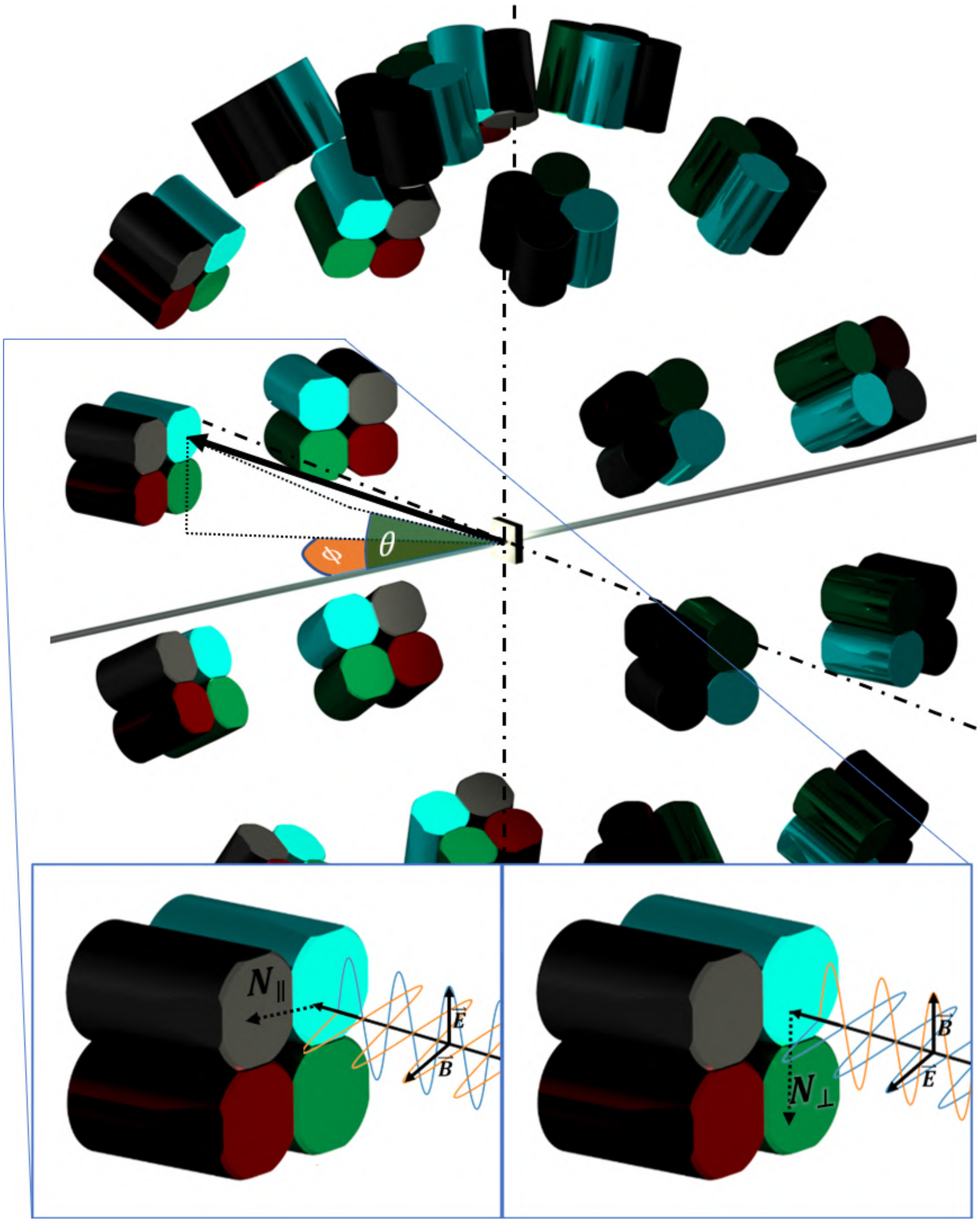

FIGURE 3.9: Main figure: Rendering of the relative positions of the 24 composite Clover detectors. The detectors are arranged in two rings, mounted at $\theta = 75.5°$ and 104.5° respectively, with respect to the beam axis. A γ ray (black arrow) is incident on one of the detectors. Angles θ and ϕ represent the polar and azimuthal angles between the γ ray and the beam. Inset: example of the preferential direction a γ ray will Compton scatter depending on the orientation of its electric field vector, $\vec{E}$, relative to the reaction plane.

In addition to the obvious benefit of gathering more statistics, having a large array of detectors arranged geometrically around the target is advantageous for spectroscopy since we can use the array to directly measure γ-ray multipolarities. Following a fusion-evaporation reaction, the nuclear spin is generally aligned in a plane perpendicular to the beam direction ($\vec{L} = \vec{r} \times \vec{p}$). This provides an axis against which experimentally measured angular distributions of γ rays can be compared. The measured distribution, $W(\theta)$, is given by Equation 3.15,

$$W(\theta) = A_0 + Q_2 A_2 P_2(\cos\theta) + Q_4 A_4 P_4(\cos\theta), \tag{3.15}$$

where Q_k are attenuation coefficients accounting for the finite size and opening angle of the detectors and $P_k(\cos\theta)$ are Legendre polynomials. θ is the angle between the γ ray incident on the detector and the beam, and is detailed diagrammatically in Figure 3.9. The measured coefficients, A_k, are compared to their theoretical counterparts for different $\sigma\lambda$ radiation.

Since there are only 4 possible values of θ with JUROGAM3 (6 if you divide the Clovers into 2 separate rings), it is not practical to measure the full angular distribution of transitions given lack of measurements at extreme angles. Instead, we may utilise the method of directional correlation of oriented states (DCO) [47]. Envisioning two γ rays in cascade, γ_2 and γ_1 which are emitted at two separate angles relative to the beam direction, we see that if we gate on γ_2 at θ_2, we will see the intensity of γ_1 at θ_1. Similarly, we can gate γ_2 at θ_1 and measure γ_1 at θ_2. The DCO ratio is then given by Equation 3.16,

$$R_{DCO} = \frac{W_{\gamma_1}(\theta_1)}{W_{\gamma_1}(\theta_2)} = \frac{I_{\gamma_1}(\theta_1)}{I_{\gamma_1}(\theta_2)}, \tag{3.16}$$

where W is the angular distribution function and I is the intensity of the gamma measured at that particular angle. Relative differences in detector efficiency are automatically accounted for since either a 2D (or 3D) histogram of E_γ vs

E_γ (vs E_γ) is produced, explicitly requiring coincidence between the two detector types. This process is described in greater detail in Chapter 4.

Clover detectors have the additional benefit of being sensitive to the linear polarisation of the γ radiation. Compton scattering of the γ ray in the HPGe crystal is dependent on the orientation of the electric field vector, $\vec{E}$, relative to the reaction plane. The Compton scattering cross-section for a linearly polarised γ ray is given by the Klein-Nishina formula,

$$\left(\frac{d\sigma}{d\Omega}\right)_\zeta = \frac{r_e^2}{2}\frac{E_{\gamma'}^2}{E_\gamma^2}\left[\frac{E_\gamma}{E_{\gamma'}} + \frac{E_{\gamma'}}{E_\gamma} - 2\sin^2\epsilon\cos^2\zeta\right], \tag{3.17}$$

where r_e is the classical electron radius and E_γ, $E_{\gamma'}$ are the energies of the unscattered and scattered γ rays, respectively. Angles ϵ and ζ are shown diagramatically in the inset of Figure 3.9. ϵ is the angle between the reaction plane (defined by the direction of the beam crossed with the direction of the unscattered γ ray) and the electric-field vector, $\vec{E}$, of the unscattered γ ray. ζ is the angle of the scattered γ ray relative to the initial direction of the unscattered γ ray. Equation 3.17 is detailed as a polar diagram in Figure 3.10. The bottom half of Figure 3.10 is pertinent since it shows that if a γ ray scatters at 90° inside the HPGe crystal, the electric field vector for the initial, unscattered γ ray is most likely to be oriented at 0° or 180° relative to the reaction plane, i.e: parallel to it. This is detailed in the inset of Figure 3.9 where this preferential scattering direction is shown for two γ rays with their $\vec{E}$ vector oriented parallel and perpendicular to the reaction plane.

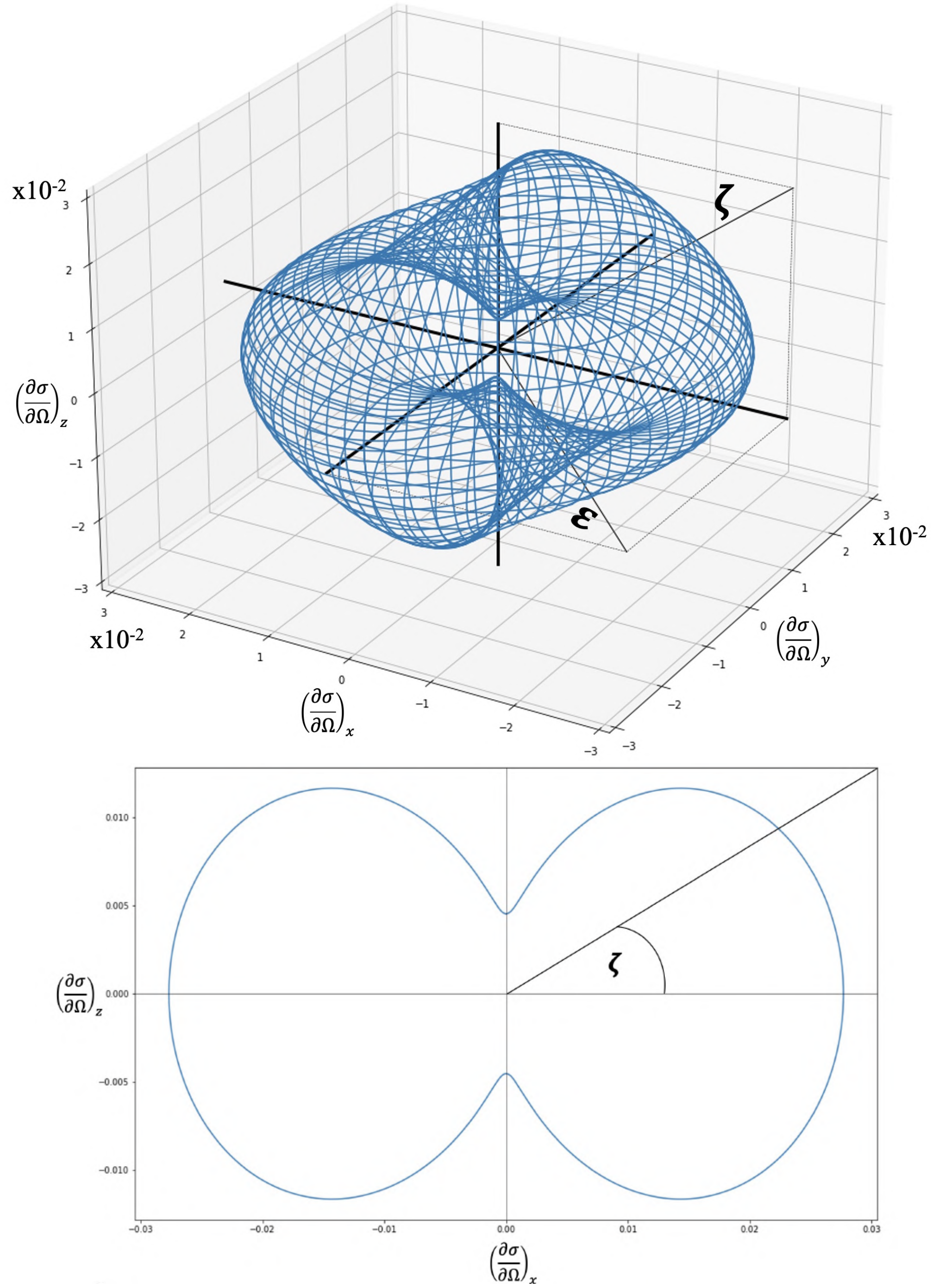

FIGURE 3.10: Top: Projections of the Compton scattering cross-section (all axes in barns) for linearly polarised γ rays (Equation 3.17) for all angles of ϵ and ζ with E_γ, $E_{\gamma'} = 0.5, 0.27$ MeV. Bottom: The same as above, but with the scattering angle, ϵ, fixed at 90°.

As γ spectroscopists, this information is useful to us since measurement of the angular distribution of a transition can only inform us as to the multipole order (the amount of angular momentum, ΔI) carried by the γ ray. Knowledge of the orientation of the electric field vector of a γ ray allows distinction between electric and magnetic character for transitions of the same multipole order, as well as whether the transition is stretched or not. The degree of linear polarisation of the detected γ ray is given by Equation 3.18,

$$P(\epsilon) = \frac{J(\epsilon, \zeta = 0^\circ) - J(\epsilon, \zeta = 90^\circ)}{J(\epsilon, \zeta = 0^\circ) + J(\epsilon, \zeta = 90^\circ)} \tag{3.18}$$

where J is the intensity of the scattered γ ray with an electric field vector parallel to $(\zeta = 0^\circ)$ or perpendicular to $(\zeta = 90^\circ)$ the reaction plane. Experimentally, this can be measured by the number of counts in a photopeak representing a scattered γ ray, as per Equation 3.19,

$$A = \frac{a(E_\gamma)N_\perp - N_\parallel}{a(E_\gamma)N_\perp + N_\parallel}, \tag{3.19}$$

where $N_\perp$, $N_\parallel$ are the number of measured counts in vertical and horizontal scattered crystals, respectively. $a(E_\gamma)$ is a correction factor based on the ratio of the horizontal versus vertical coincidence count rates measured without polarisation at $\epsilon = 0^\circ$. Equations 3.18 and 3.19 are related trivially by Equation 3.20,

$$P = \frac{A}{Q}, \tag{3.20}$$

where Q is the *polarisation sensitivity* of the detector. Q is dependent on both the incident γ ray energy and the geometry of the detector setup. The polarisation sensitivity for JUROGAM was measured and detailed thoroughly in reference [48]. As displayed in Figure 3.11, DCO measurements conflate unstretched dipoles with stretched quadrupoles and stretched dipoles are not distinguishable between their electric and magnetic counterparts. The sensitivity of the linear polarisation to the parity changing nature of the γ ray allows us to alleviate the DCO ambiguity for different multipolarities.

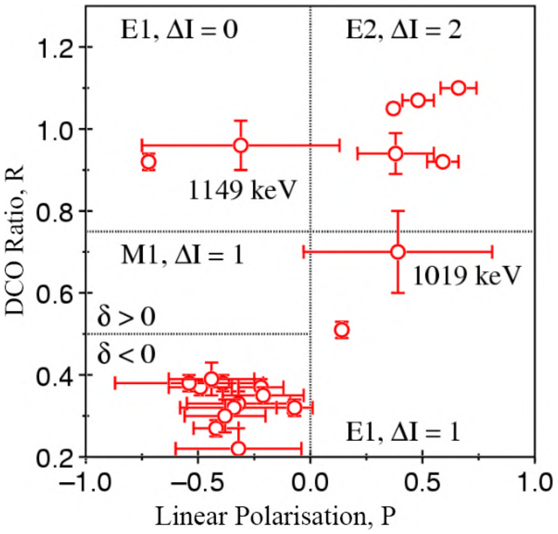

FIGURE 3.11: Measured linear polarisations and DCO ratios for transitions in ^{117}I measured using the EUROGAM-II spectrometer. Data from [49], figure adapted from [19].

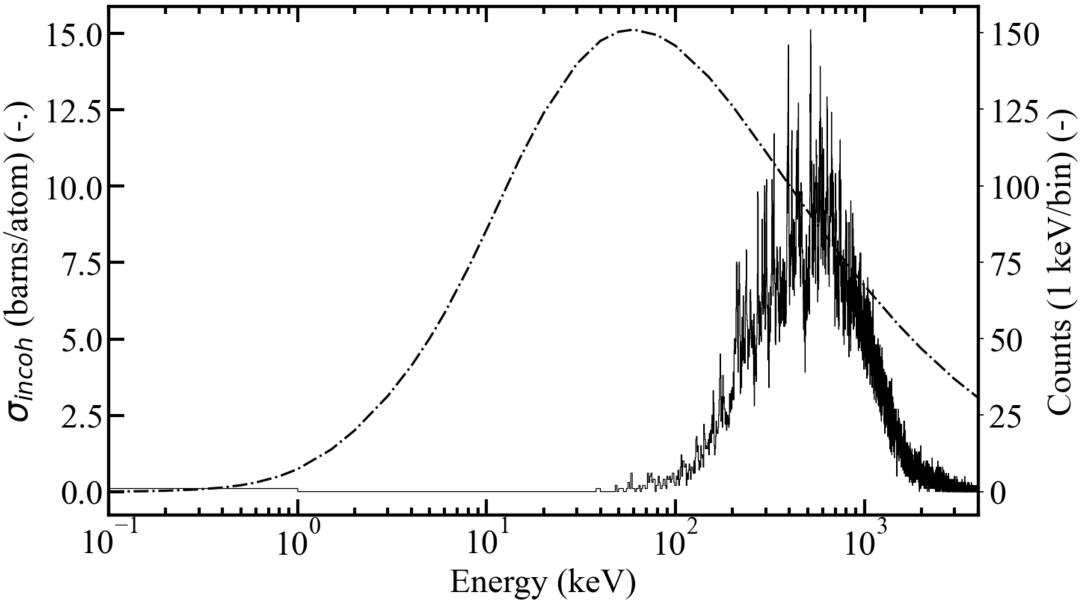

FIGURE 3.12: Experimentally observed scatters throughout the JM06 experimental run for the yrast band in ^{132}Pm. Overlaid on this spectrum is the theoretical curve for incoherent (Compton) scattering events, obtained from the calculations in Ref [12].

Combining linear polarisation measurements with DCO analysis is a powerful spectroscopic tool, but it is not without limitations. The technique's biggest flaw is its working principle: relying on Compton scattered events. By imposing this event selection criteria we immediately lose counts since Compton scattered events represent a fraction of the total. Furthermore, the Compton scattering cross-section is highly dependent on γ ray energy. This relationship can be observed in γ-ray spectra restricted to display scattered events only; the level of counts drops off heavily below 200 keV. Figure 3.12 displays experimentally observed scatters throughout the JM06 experimental run for the yrast band in ^{132}Pm. Overlaid on this spectrum is the theoretical curve for incoherent (Compton) scattering events, obtained from the calculations in Ref [12]. It is interesting to note the similarity between the shape of the theoretical cross-section curve and the detector efficiency curve displayed in Figure 3.8, illustrative of the basis of the detector's operating mechanism on Compton scattering.

3.5.3 Mass selection using MARA

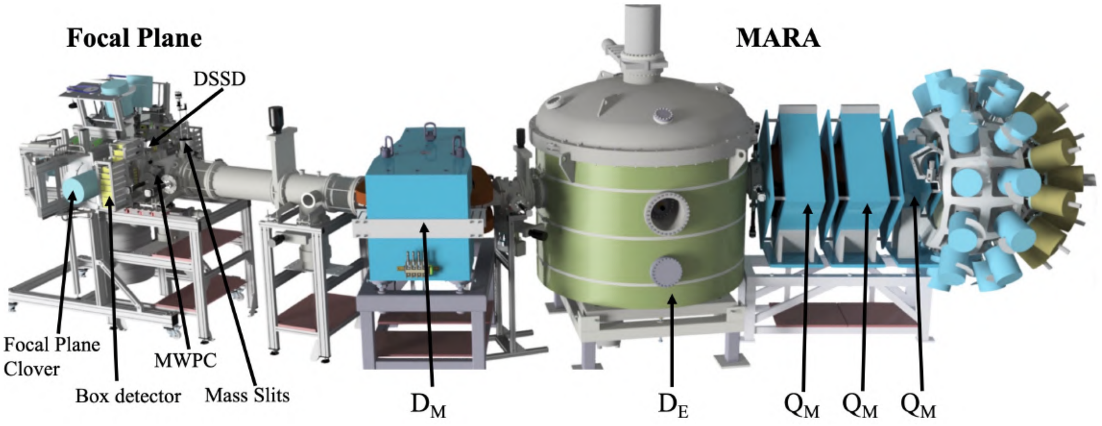

FIGURE 3.13: 3-dimensional rendering of the experimental setup including the MARA recoil separator. The beam direction is from right to left with the static target installed at the center of the JUROGAM array. Figure adapted from Ref [50].

m/q Selection Using MARA

MARA (Mass Analysing Recoil Apparatus, Figure 3.13) is a vacuum mode recoil separator installed at JYFL, complementary to the long running RITU (Recoil Ion Transport Unit) separator. MARA was born out of a desire to study exotic nuclei that exist close to the $N = Z$ line. Compared to RITU, MARA has the following characteristics:

- Increased mass resolution in exchange for decreased transmission efficiency. Since MARA is not gas filled, unlike RITU mass separation information is not lost to collisions inside the detector. Reaction products can be separated by their m/q ratio.
- Inverse kinematic and symmetric reactions are transmittable by MARA.
- Medium-light nuclei can be transmitted since they are not lost to the gas.

MARA is composed of five major ion-optical components in the configuration $Q_M Q_M Q_M D_E D_M$, where Q/D is a quadrupole or dipole and E/M represent the electric or magnetic nature of the component. The primary objective of the initial magnetic quadruple triplet is focusing the beam. Fusion evaporation recoils are naturally projected in a wide cone following fusion; MARA accounts for this with angular acceptance of 45 mrad in the horizontal direction and 55 mrad in the vertical direction. The path of a charged particle in a uniform electric and/or magnetic field is dictated according to the Lorentz equation,

$$\vec{F} = q\left(\vec{E} + \vec{v} \times \vec{B}\right), \tag{3.21}$$

which can be further broken down into individual electric and magnetic components,

$$\vec{F_E} = q\vec{E}, \;\; \vec{F_B} = q\vec{v} \times \vec{B}. \tag{3.22}$$

Separating the electric and magnetic components allows definition of electric and magnetic rigidity: the resistance of the particle beam to being changed in direction by the applied electric or magnetic field.

$$\chi_E = \frac{pv}{q} = \frac{2E_k}{q}, \;\; \chi_B = \frac{p}{q} = \frac{\sqrt{2E_k m}}{q}. \tag{3.23}$$

The motion of a charged particle traversing the electric and magnetic dipoles can be described by equating the relevant component of the Lorentz formula to the centripetal force, and rearranging for the radius, r,

$$r_B = \frac{m}{q}\frac{v}{B} = \frac{\sqrt{2E_k m}}{qB}, \;\; r_E = \frac{mv^2}{qE} = \frac{2E_k}{qE}. \tag{3.24}$$

Equation 3.24 details where MARA's ability to resolve ions by their m/q ratio arises. The energy dispersion, E_k, is present in the formulae for both rigidities and can be negated by setting the electric and magnetic fields such that the E_k component in each is equal and opposite. Figure 3.14 displays the path of recoils through MARA until the moment they converge at the focal plane.

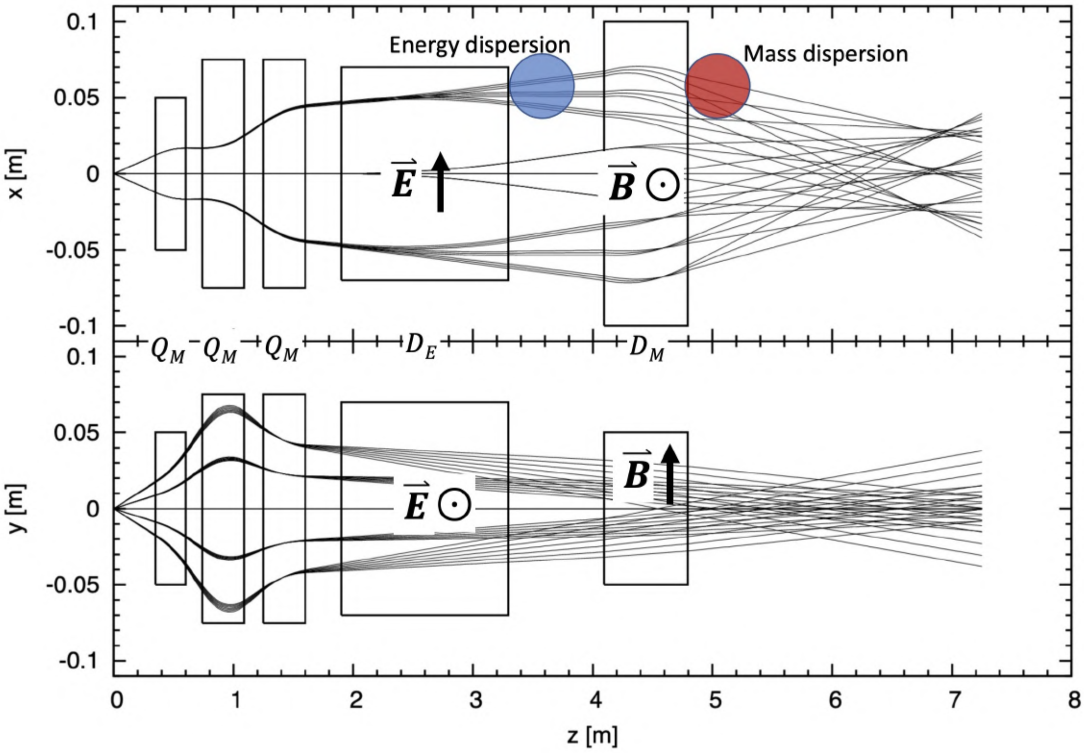

FIGURE 3.14: Ion trajectories inside MARA from above (top figure) and the side (bottom figure) with a straightened beam axis. Adapted from Ref [51].

Selection Using Mass Slits

The beam line at MARA is equipped with several sets of mass slits which have the capability to block the beam at both its energy (between the electrostatic dipole and magnetic dipole) and mass dispersion (before and after the focal plane) regions.

3.5.4 Multi-Wire Proportional Counter (MWPC)

At the MARA optical focal-plane lies a gas-filled Multi-Wire Proportional Counter (MWPC). The MWPC provides the ability to measure the spatial position of a recoil traversing it, as well as suppressing any unwanted beam components that have made it this far. The MWPC is a thin chamber comprising two layers of thin, electrically biased tungsten wires oriented 90° to each other, and filled with isobutane gas. The gas has a low ionisation energy such that a charged recoil passing through it creates a localised ion-cloud. The ion-cloud is then drawn toward the wires, and the proportional response is used to correlate the spacial coordinates of the moving recoil. This is an essential piece of information since the spacial coordinate informs us as to the m/q ratio of the recoil. As detailed in Figure 3.14, mass dispersion occurs along the x-axis only. Such as it is, the measured m/q ratio is dependent only on the MWPC-X coordinate of the recoil

$$\frac{m}{q} = \frac{m_{ref}}{q_{ref}} \left(1 + \left[\frac{x_{mm}^{ref} - (Gx_{mwpc})}{D} \frac{1}{100} \right] \right), \tag{3.25}$$

where m, q, x_{ref} refers to a reference particle of known mass and charge state, $G = 0.0102$ is a ratio used to convert MWPC-X coordinates into millimeters and D is the width of a strip in millimeters.

An essential functionality enabled by the MWPC is the ability to differentiate between recoil and decay particle implantations into the DSSD. The differentiation between the two event types is performed in software with a simple *if()..* statement to check if an event has positive counts at the MWPC associated with it. If yes, the event is a recoil, since a decay does not traverse the MWPC. For mass gating, a two dimensional matrix of MWPC-x coordinate against recoil Δx is produced. The quantity Δx is the difference between MWPC-x coordinate and the DSSD-x coordinate for the implanted recoil. The difference arises from the particle drift between the "optical" focal plane and the physical location of the DSSD. Since the DSSD is placed at a slant to the beam, recoil drift (Δx) is larger for recoils further away from the beam centre. When measuring the mass of an unidentified recoil, it is sufficient to compare the one-dimensional MWPC-x coordinates to those of a known mass - if the two overlap, they have the same m/q ratio.

3.5.5 Double-Sided Strip Detector (DSSD)

Beyond the MWPC is the **D**ouble-**S**ided **S**ilicon **D**etector. Integral to the recoil-decay tagging process, the DSSD is a hugely capable piece of equipment, providing timestamps for recoil and decay implantations and measurements of deposited energy for all deposited particles. The DSSD used in the JM06 run was a 300 μm thick BB20 detector produced by Micron Semiconductor Ltd. Simply, a DSSD is a wafer of silicon with sensitive strips photoetched onto each side of the wafer. The strips are oriented at 90° to each other to provide pixelated spatial correlation in a manner similar to the MWPC wire strips. The BB20 has 192 x-strips and 72 y-strips etched over an active area of (128.61×48.21) mm allowing for spacial correlation as precise as 0.47 mm^2. The p-n junction is established by deposition of boron ions into the sensitive region of the junction strips. The wafer's back side is coated with phosphorous which acts as an n-type donor. Segmenting the DSSD into pixels this way allows for an effective increase in the amount of recoil-decay correlations that can be made simultaneously. For example, one would not correlate a recoil that is implanted into a particular pixel to a decay that happens in a different pixel. This allows the experiment to run with a higher beam intensity, yielding higher counting statistics.

The DSSD acts as a trigger around which an event can be formed; all events built up in software require an associated recoil or decay implantation. This allows clean, recoil-tagged, prompt γ-spectra as well as removing background due to Coulomb excitation and other external contaminants. As with all detectors, the proportional charge response of the detector to the kinetic energy of the absorbed particle requires calibration. The calibration for the JM06 run was performed using a "3-line alpha" source; ^{241}Am ^{244}Cm ^{239}Pu are combined to create a source that emits alpha particles primarily of energies 5.486, 5.798 and 5.150 MeV, respectively [52, 53, 54]. Analysis of the measured channel centroid for each DSSD y-strip, for each peak was performed using an automated fitting process in the software MATLAB. Fitted curves were checked manually for their accuracy, and the measured centroid positions were plotted against the expected energies as detailed in Figure 3.15.

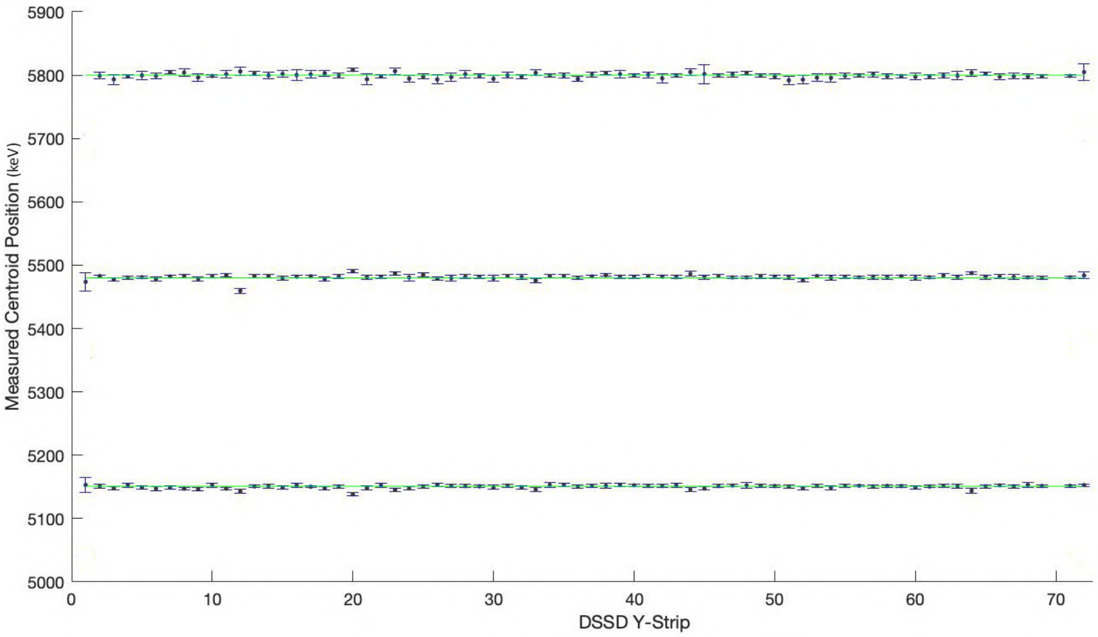

FIGURE 3.15: Measured centroid position for each DSSD-Y strip after gain matching is applied. Green lines indicate "true" energy of the alpha source.

It can be seen that the overwhelming majority of strips are consistent with the accepted energy of the three alpha sources within the uncertainty bound by the resolution of the detector. Low energy calibration has not been performed in this work. In principle, the linearity of the detector response to deposited energy should render this unproblematic. Logistically there is no problem since no particulate decay spectroscopy was performed in this analysis.

The DSSD at MARA can be equipped with a suite of tertiary detector systems designed to supplement its own measurement capabilities. In this experiment, a pair of silicon "punchthrough" detectors were placed directly behind the DSSD. As the name suggests, these detectors are used to veto events where an energetic decay particle has escaped the DSSD volume. ’Box’ detectors with similar functionality can be installed in front of the DSSD.

3.5.6 Focal Plane Germanium Detectors

Detection of delayed γ-radiation emitted by isomeric nuclei implanted at the focal plane is enabled by a suite of Clover detectors installed around the silicon; up to six detectors can be installed simultaneously and varying quantities of these detectors were active throughout the JM06 experiment. The experiment started with three and eventually two more were added for a total of five detectors active during the latter half of the experiment.

3.6 JUROGAM3 and Focal Plane Germanium Calibration

When a charged particle or γ ray is incident on a semiconductor-based detector such as the germanium detectors used here, electrons from the atomic valence band are ionised and flow freely across the bulk of the detector. The magnitude of electron-hole pairs produced is proportional to the energy of the absorbed γ-ray. The ultimate resolution of the detector is determined by the number of electron-hole pairs that can be produced, thus a high-resolution detector material ideally has a low ionisation energy ($\approx$ 3 eV in highly-pure germanium [55]). This charge is then collected and converted into an amplified electrical pulse, the height of which is proportional to the energy of the γ ray. The pulse is then digitised using an analogue-to-digital converter (ADC). Functionally this can be thought of as a series of bins that collect charge, and when one bin fills up, the charge overflows into the next bin. This process continues until the charge is fully collected. Instead of bins, we use the term "channel". For the germanium detectors used here, the channel number is related to the γ-ray energy by a simple second-order polynomial,

$$E = Ax^2 + Bx + C. \tag{3.26}$$

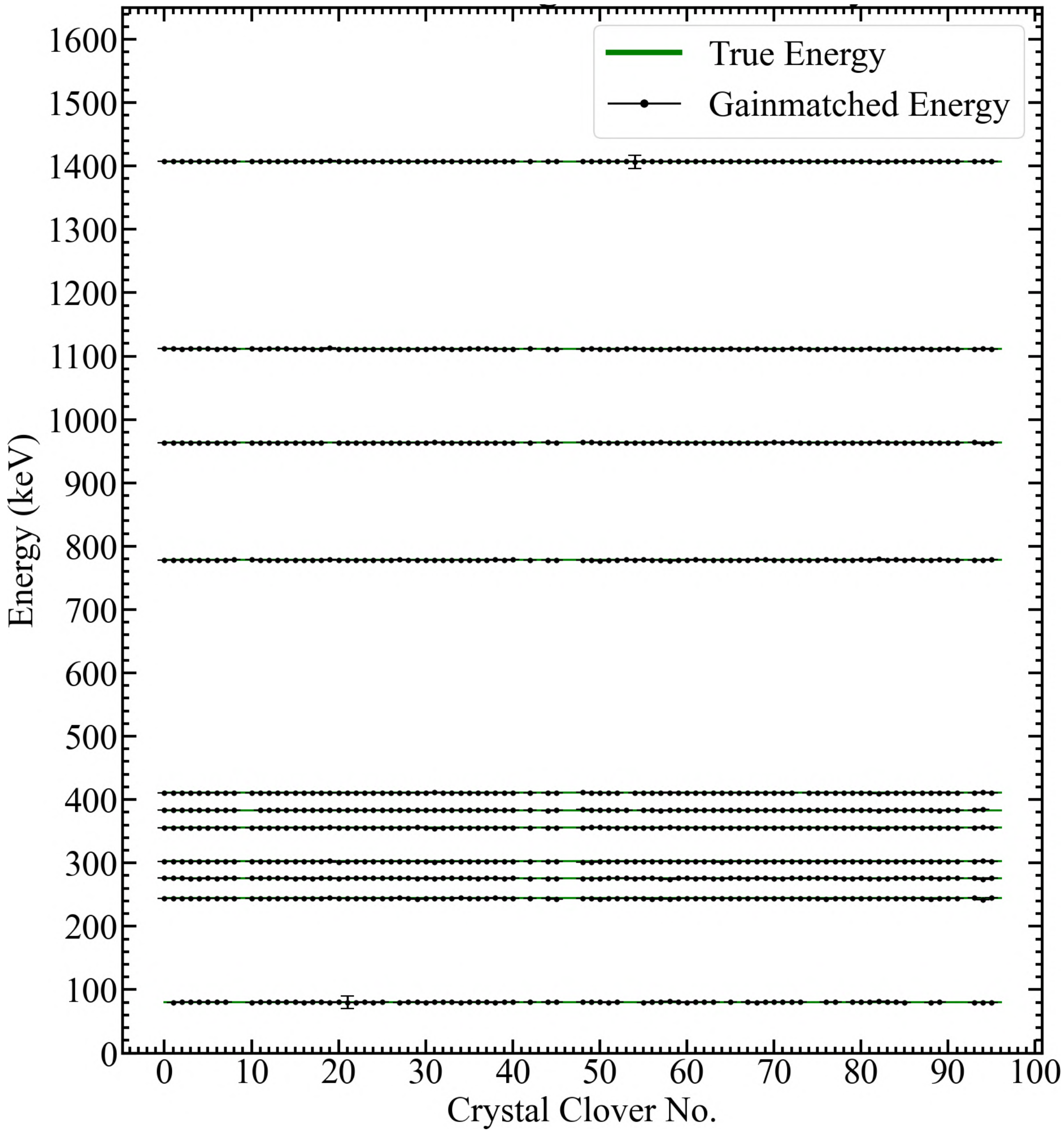

FIGURE 3.16: Measured centroid position (channel) for each Clover crystal after gain matching, overlaid on the "true" energy for each major photopeak in the ^{152}Eu^{133}Ba spectrum. Missing points for crystals 9, 41, 43, 92 are because these detectors were not counting during the experimental run.

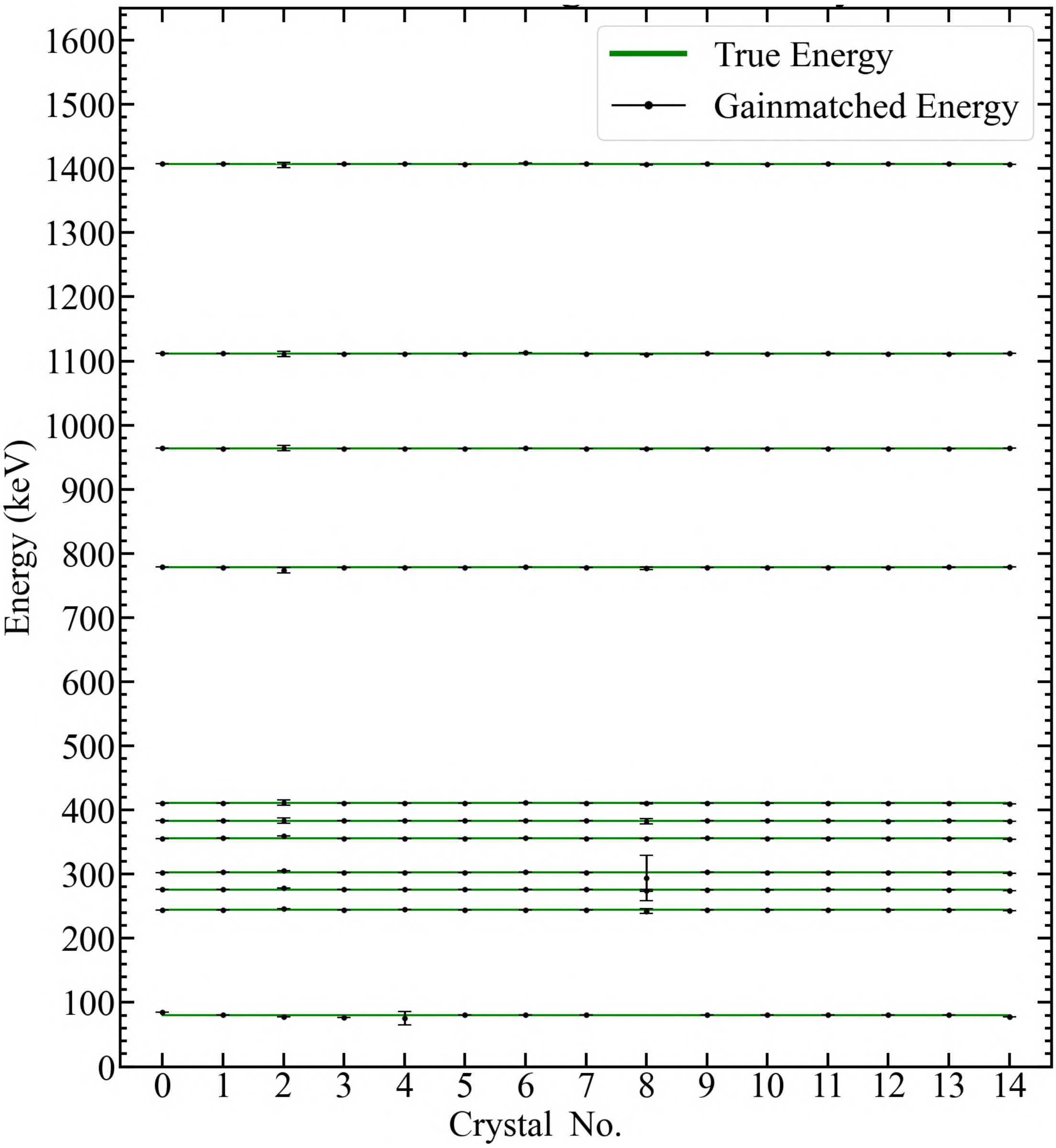

FIGURE 3.17: Measured centroid position (channel) for each Phase 1 detector after gain matching, overlaid on the "true" energy for each major photopeak in the ^{152}Eu^{133}Ba spectrum.

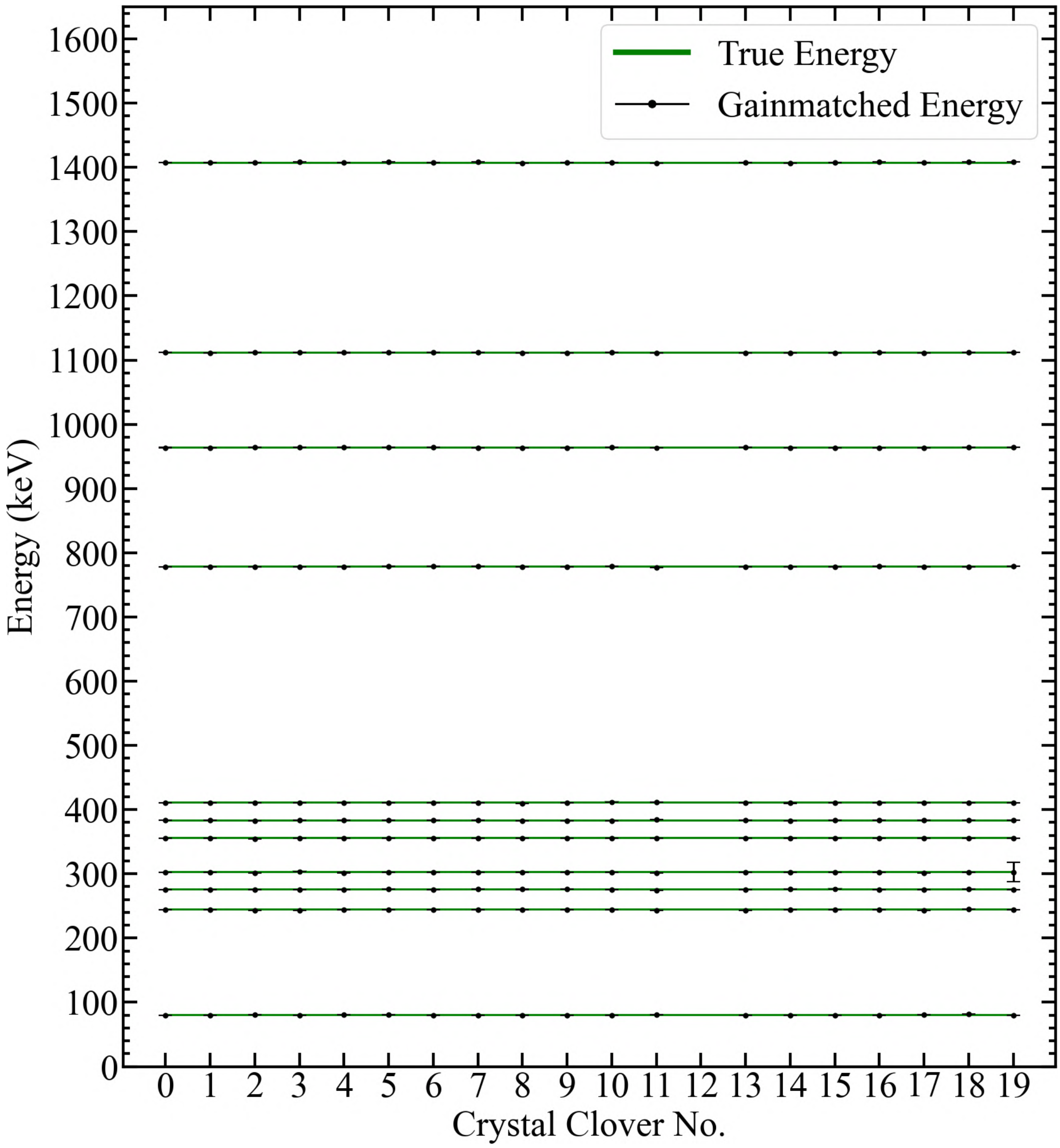

FIGURE 3.18: Measured centroid position (channel) for each focal plane Clover crystal after gain matching, overlaid on the "true" energy for each major photopeak in the ^{152}Eu^{133}Ba spectrum. Calibration data was taken from the end of the experimental run as described in the text.

3.7 Doppler Correction

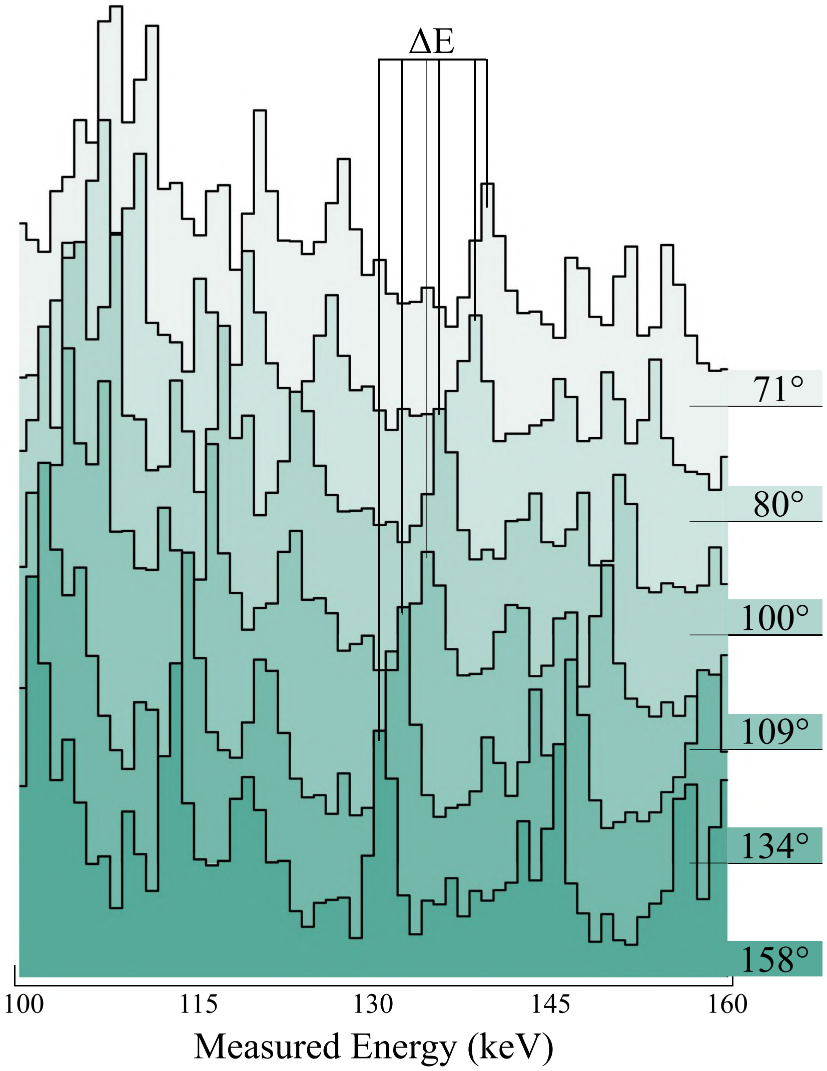

FIGURE 3.19: Doppler shift of an in-beam photopeak from the JM06 dataset.

The Doppler shift for a γ ray emitted by a particle moving with velocity v is

$$E'_\gamma = E_\gamma \left(1 + \frac{v}{c}\cos\theta\right), \tag{3.27}$$

where E'_γ, E_γ are the shifted and unshifted energies, respectively; c is the speed of light, and θ is the polar angle between beam and detector as used in Figure 3.7. The fractional velocity v/c is commonly given as a correction factor β; it is this correction factor that is measured and applied in this analysis. Measurement of the centroid of an in-beam photopeak (Figure 3.19) for each angle of θ was made using a python script. The centroid position (keV) is then plotted against $\cos(\theta)$. The gradient of this graph is equal to $E_{\gamma}\beta$ and the intercept is E_{γ}, so the Doppler correction factor, β, is simply the division of the gradient by the intercept.

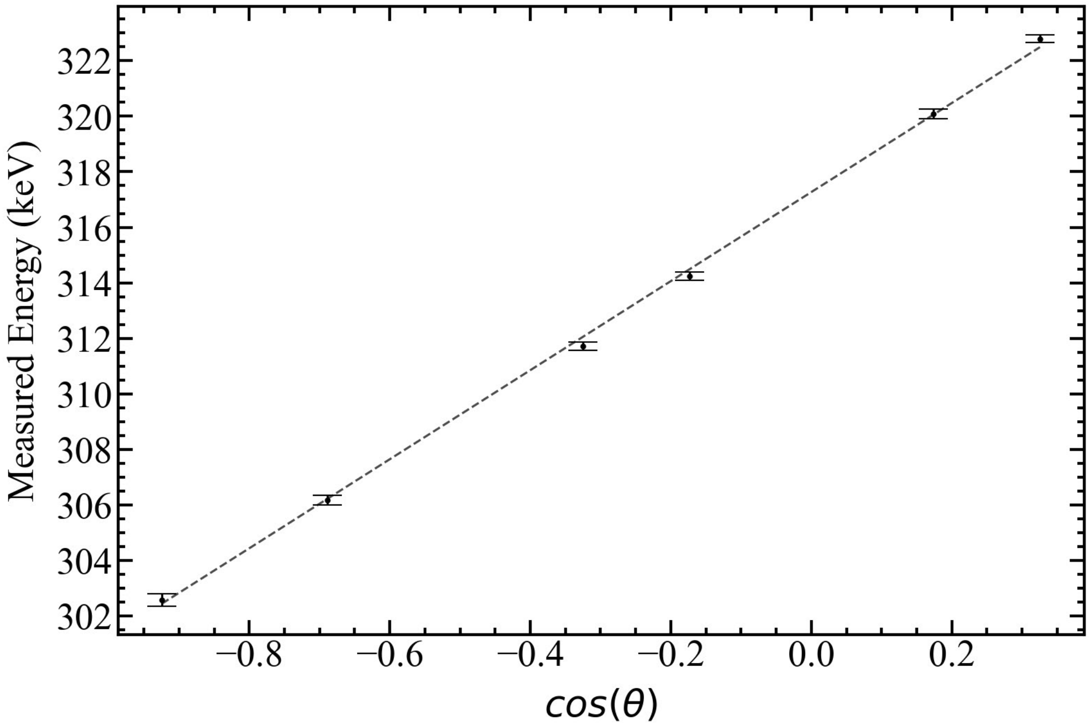

FIGURE 3.20: Measured (Doppler shifted) centroid position for an in-beam peak as a function of θ for the JUROGAM setup in the JM06 experiment. χ^2/ndf: 0.13.

Figure 3.20 summarises these measurements. The measured value of β is 0.055 ± 0.001. This indicates a flight time from the target position to the MARA focal plane of (415 ± 8) ns given an optical axis length of 6.85 m. This value is in good agreement with the value derived from relativistic kinematics, $\beta = 0.0541$, detailed in Appendix A.

3.8 RADWARE

A sizeable portion of the analysis of prompt γ ray coincidence data was performed using the RADWARE [42] suite of programs, chiefly Levit8r. Levit8r makes use of a file format known as a cube, which is effectively a 3D histogram filled with coincident gamma counts. The data must be presorted into this format. Any events with a collective of at least three coincident gammas, and in coincidence with a valid recoil implantation are included. Events with greater than three counts are unfolded into sets of three as per the "spikeless" sorting process described in [56]. Events with fewer than three coincident gammas are discarded. The cube is compressed, fitted for background subtraction and efficiency corrected (as per Figure 3.8). Practically, two transitions of interest are selected (referred to colloquially as gating) and the projection of the third axis of the cube (i.e, all γ rays in coincidence with the two that were selected) is printed to the screen — see Figure 3.21 for a graphical representation of this. The resultant spectra are very clean, since the high-fold multiplicity requirement does away with a large portion of background. Large arrays such as JUROGAM lend themselves nicely to this kind of analysis due to the large amount of counting statistics they can produce. Indeed, Figure 3.22 shows that throughout the JM06 run there were 2.42×10^9 three fold or greater events. Since all recoils are included, the resultant spectra are produced by a broad variety of nuclides. Furthermore, the cube is dominated by the strongest reaction channels. This makes searching for bands belonging to more exotic reaction channels problematic, since they are usually "drowned out" by the signal from strong channels. In addition, though gating on two transitions provides greater selectivity, there is no guarantee that the transitions observed in coincidence with the two gates belong to a particular band; two gammas in coincidence $\gamma_1 = E_1$, $\gamma_2 = E_2$ may belong to multiple bands.

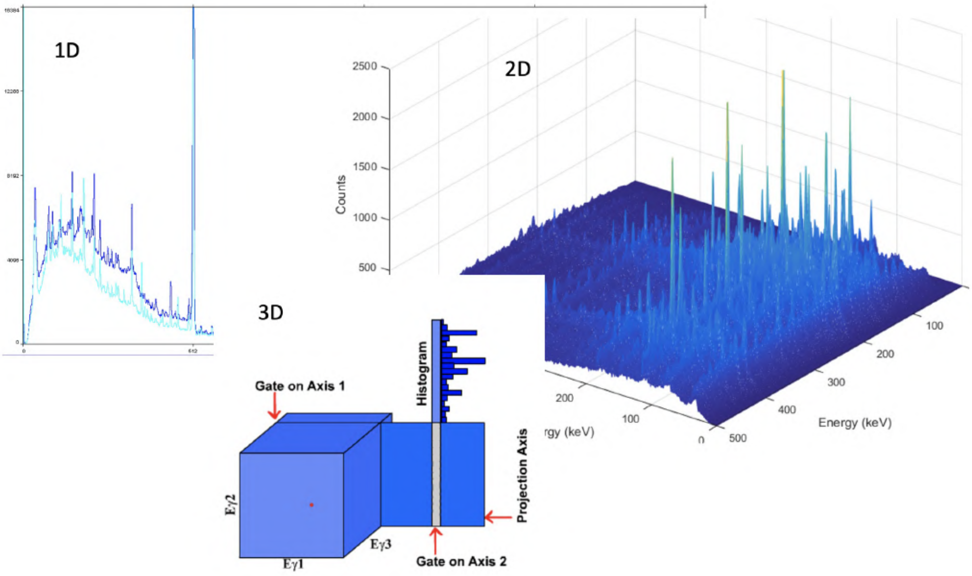
1D
2D
2500
2000
1500
1000
500
Counts
100
200
300
400
500
Energy (keV)
200
100
rgy (keV)
3D
Gate on Axis 1
Histogram
Projection Axis
Gate on Axis 2
Eγ1
Eγ2
Eγ3

FIGURE 3.21: Graphical representation of 1D, 2D and 3D γ coincidence matrices. Each "dimension" is E_γ, with the number of counts projected along the extra axis. 3D representation adapted from [19].

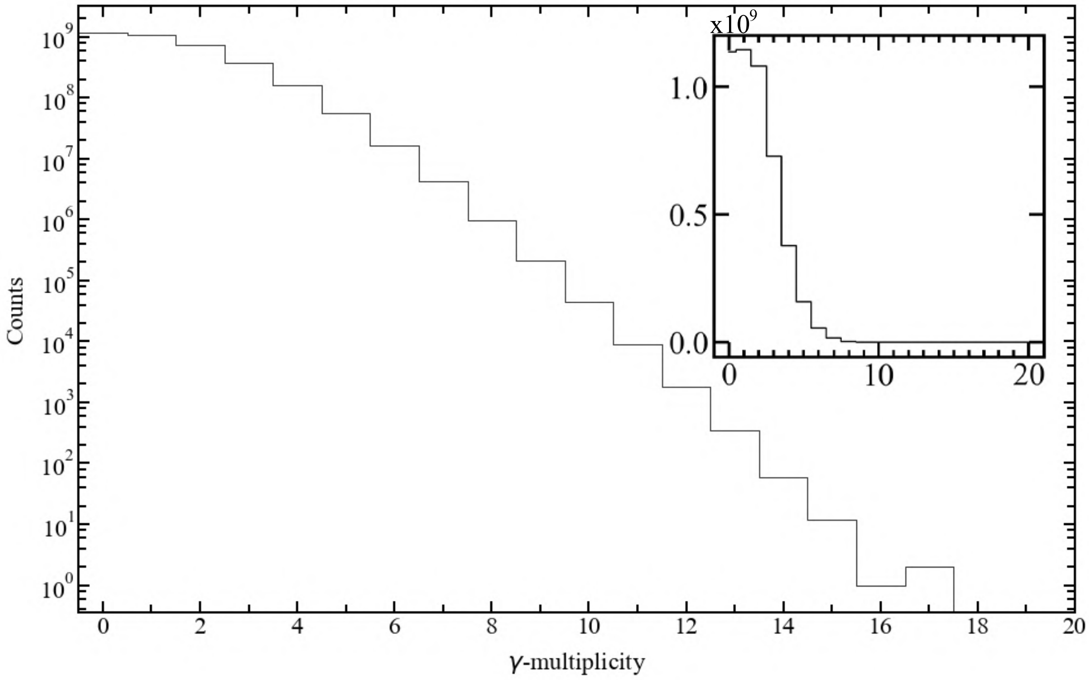

FIGURE 3.22: Number of events as a function of the γ-ray multiplicity for all events in correlation with a valid recoil for the entire JM06 run. Inset: same plot with linear scale.

Chapter 4

High-Spin Isomers in ${}^{129}_{60}$Nd

This chapter presents the discovery of three high-spin isomers, and a strongly coupled band built upon one of these isomers in the deformed, neutron-deficient nucleus ^{129}Nd. The large predicted deformation for this nucleus ($\beta_2 = 0.32$) [57] places the Fermi surface for both protons and neutrons near high-Ω orbitals originating from the $g_{7/2}$, $f_{7/2}$ and $h_{11/2}$ states, providing suitable conditions for the formation of $K-$ isomers. It is argued in this chapter that the strongly coupled band is based on a three-quasiparticle isomer with spin/parity $21/2^+$. Both prompt and isomer-delayed γ radiation is measured in association with this isomer, which decays with a half-life of (679 ± 60) ns, with the isomer-delayed radiation observed to decay into three of four one-quasineutron bands identified in previous studies. The $21/2^+$ isomer decays to the low-spin yrast structures directly and through two further excited states. The observation of delayed γ-radiation in association with these two levels leads to their assignment as isomeric states also. In this work, the MARA recoil separator and its associated focal-plane detector system provide a comprehensive suite of tools for measuring isomeric properties. For the $21/2^+$ isomer, the half-life, decay scheme, gamma rays cascading above the isomer, tentative spin/parity assignments and isomeric configuration have been deduced. The likely configurations of the isomeric states in the decay path of the $21/2^+$ isomer are discussed.

4.1 Previous work

The most recent study of the nucleus ^{129}Nd was performed in 2002 by Zeidan, *et al.* [58], where a comprehensive γ-ray spectroscopy study was undertaken, resulting in the vast majority of extant information known about the excited states identified in ^{129}Nd. In that work, excited states in ^{129}Nd were populated across two experiments using the reaction ^{92}Mo(^{40}Ca, 2pn). The first experiment was performed at Oak Ridge National Laboratory, supported by the CLARION Ge detector array and the HyBall CsI charged-particle detector array. The second experiment was performed at Argonne National Laboratory supported by the Gammasphere and Microball arrays. Four rotational structures were observed and assigned bandhead configurations based on comparisons of their experimental B(M1)/B(E2) ratios and single-particle alignments with theory and systematics. Lack of experimental sensitivity to isomerism prevented observation of transitions connecting these bands, resulting in the bands "floating" with respect to each other as displayed in Figure 4.1.

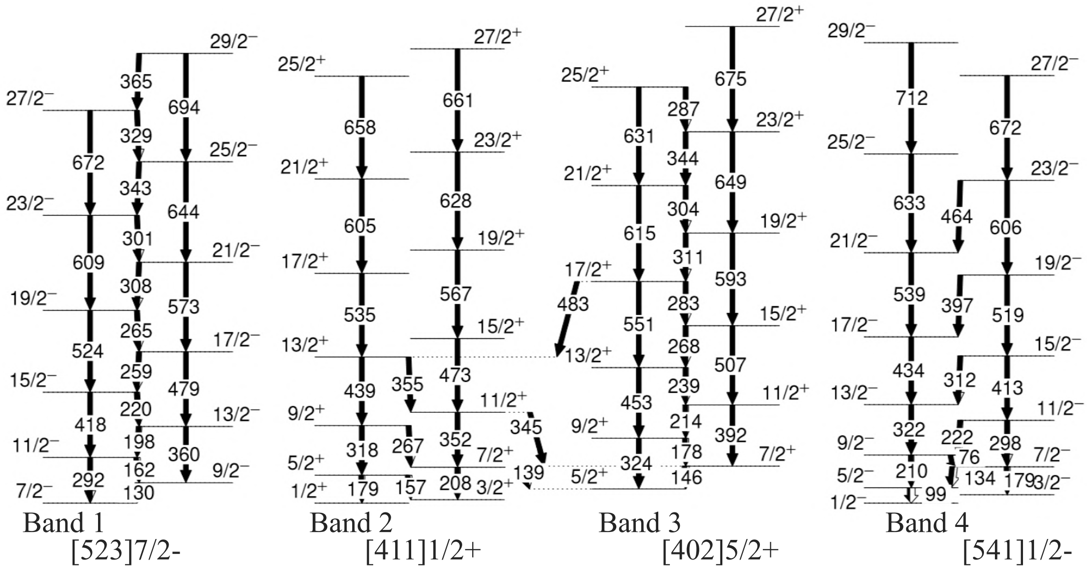
29/2−
27/2−
365
694
329
25/2−
672
343
23/2−
644
301
21/2−
609
308
19/2−
573
265
17/2−
524
259
15/2−
479
220
13/2−
418
198
11/2−
360
162
9/2−
7/2−
292
130
Band 1
[523]7/2-
27/2+
25/2+
661
658
23/2+
21/2+
628
605
19/2+
17/2+
567
535
15/2+
13/2+
473
439
355
11/2+
9/2+
345
318
267
352
7/2+
5/2+
139
1/2+
179
157
208
3/2+
Band 2
[411]1/2+
27/2+
675
25/2+
287
23/2+
631
344
21/2+
649
304
19/2+
615
311
593
17/2+
283
483
551
15/2+
268
13/2+
507
239
453
11/2+
214
9/2+
392
178
7/2+
324
5/2+
146
Band 3
[402]5/2+
29/2−
27/2−
712
672
25/2−
23/2−
633
464
606
21/2−
19/2−
539
397
519
17/2−
15/2−
434
312
413
13/2−
11/2−
322
222
298
9/2−
76
7/2−
5/2−
210
134
179
3/2−
1/2−
99
Band 4
[541]1/2-

FIGURE 4.1: Partial energy-level scheme for ^{129}Nd comprising the four previously known one-quasineutron bands as published by Zeidan, *et al* [58]. Band numbering scheme is the same in this thesis as it is in the reference.

4.2 Experimental Details

In the present work, excited states in ^{129}Nd were populated across two experiments at the University of Jyväskylä Accelerator Laboratory utilising the reaction ^{58}Ni(^{78}Kr, $\alpha 2pn$). The first experiment (M09) benefited from the installation of the UoYTube charged-particle detector at the target position for efficient discrimination of neutron-only decay channels. The JUROGAM spectrometer was not installed throughout the M09 run, so measurements of prompt γ radiation were not performed. The beam energy varied between 340-374 MeV throughout the M09 experimental run.

The second experiment (JM06) featured the full JUROGAM array, comprising fifteen Phase 1 detectors and twenty-four Clover detectors, but did not include the UoYTube charged-particle detector system. For the first 12 days of the JM06 run the beam energy was $K = 390$ MeV, optimised for maximal production of ^{131}Eu. For the remnant of the JM06 run the beam energy was lowered to $K = 364$ MeV, optimising production of ^{129}Nd. Both experiments were coupled with the MARA recoil separator which channelled excited recoiling nuclei from the target position to the MARA focal plane, consisting of a pixelated dual-sided silicon strip detector surrounded by up to 6 HPGe γ detectors. The m/q spacial separation of recoils is measured by a multiwire, gas-filled avalanche counter (MWPC) before implantation into the DSSD.

4.3 Results

4.3.1 Isomer-delayed γ-ray coincidences

The high-spin isomers in ^{129}Nd were identified by measurement of isomer-delayed recoil-γ coincidences at the focal-plane of the MARA recoil separator. Figure 4.2, panel (a), displays all of the γ radiation detected at the focal-plane within 1 μs of a valid recoil implantation throughout the JM06 experimental run. γ rays associated with mass-129 nuclei were discriminated from the other data by application of a software veto condition allowing only mass-129 (and mass-133) recoils (Figure 4.2b).

Utilising the constituent crystals of the focal-plane Clover germanium detectors, it is possible to perform a γ-ray coincidence analysis. A γ^2-coincidence matrix was produced utilising the mass selection methods utilised in Figure 4.2, panel (b). Only decays measured within 1 μs of implantation were incremented into the matrix. Background subtraction of γ rays associated with long-lived recoil implantations were removed by selecting all decays measured up to 1 μs *before* recoil implantation.

Figure 4.2, panel (c), displays transitions in coincidence with an 847 keV γ ray, measured at the focal plane after recoil implantation. This 847 keV γ ray is the strongest transition out of an isomeric state in ^{129}Nd. It is observed that the 847 keV transition depopulates directly into the $17/2^+$ state in band 3 of ^{129}Nd, evidenced by the observation of all of the γ rays beneath this state. Two peaks of energy 36 and 42 keV are present, corresponding to the K_α and K_β internal conversion energies for neodymium, respectively. A further transition of energy 69 keV is observed, assigned as depopulating the $5/2^+$ bandhead of band 3 into the $3/2^+$ state of band 2.

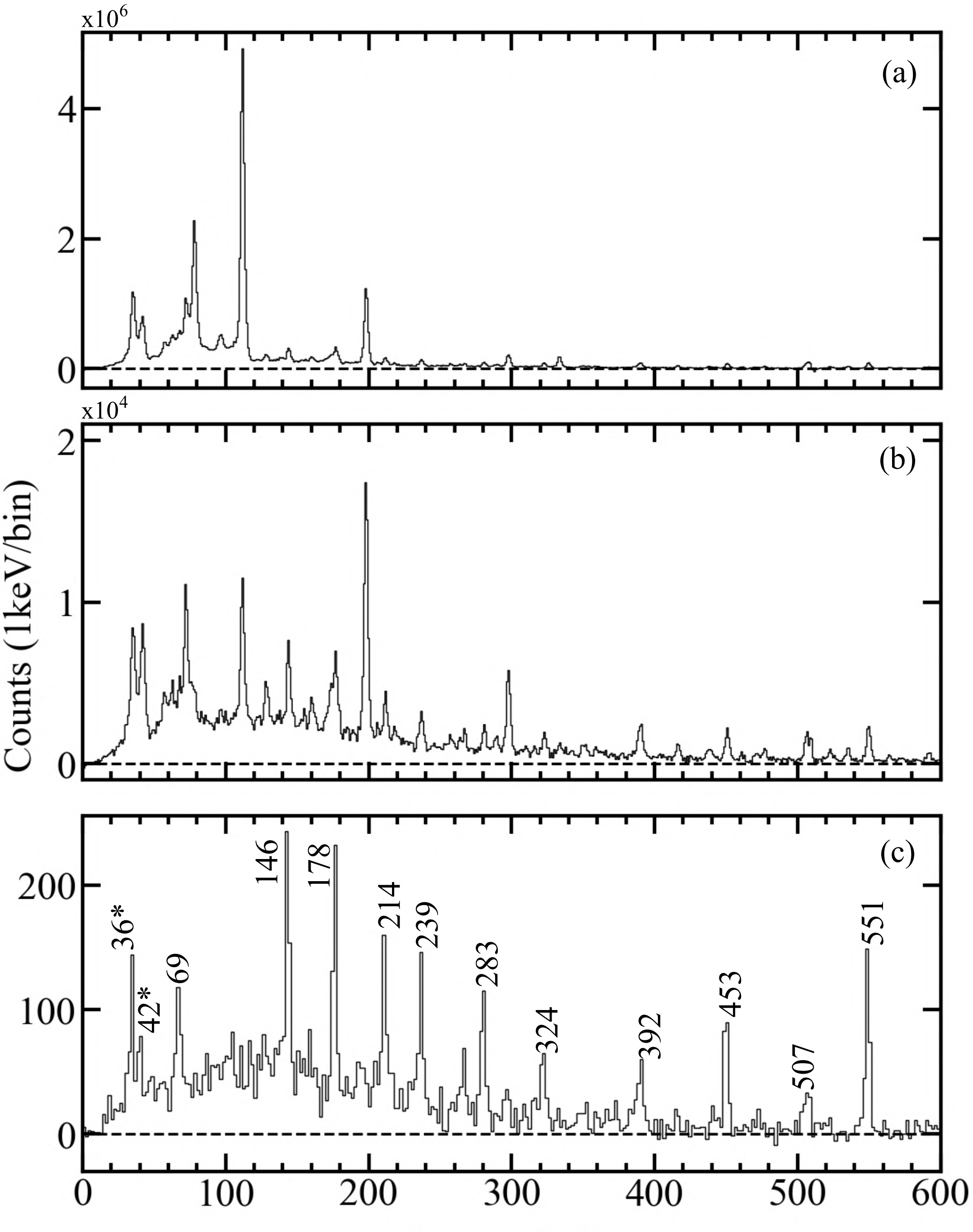

FIGURE 4.2: Panel (a): all γ rays detected at the MARA focal plane following implantation of a valid recoil. Panel (b): all γ rays detected at the MARA focal plane following implantation of a valid mass 129 or mass 133 recoil. Panel (c): all γ rays detected at the MARA focal plane following implantation of a valid mass 129 or mass 133 recoil and in coincidence (< 1 μs) with an 847 keV γ ray. Dominating this spectrum are γ rays depopulating levels beneath the $17/2^+$ level in band 3. The peaks visible at 36 and 42 keV respectively correspond to the K_α and K_β internal-conversion x-rays for neodymium.

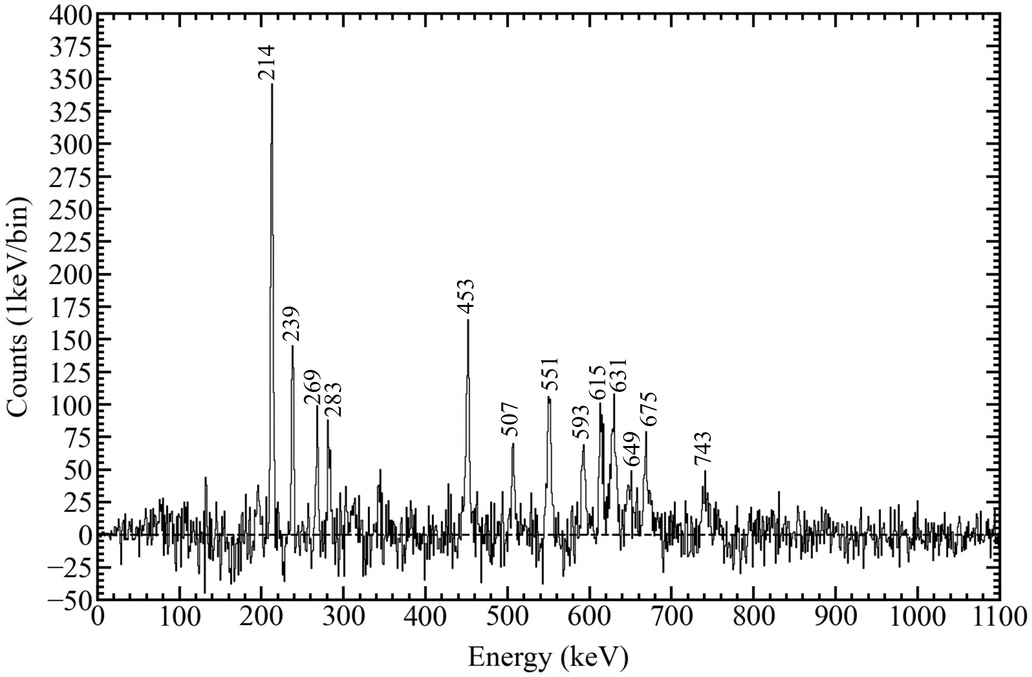

FIGURE 4.3: γ rays observed in prompt coincidence with both 146 **and** 178 keV, using the JUROGAM spectrometer. Transitions belonging to band 3 of ^{129}Nd are observed, but notably not the 847 keV and 69 keV transitions, which are isomer delayed and only observed at the focal plane.

Further evidence for the delayed nature of the new transitions observed in Figure 4.2 is displayed in Figure 4.3, which displays all γ rays observed at JUROGAM in prompt coincidence with 146 and 178 keV. Transitions are observed to spin $31/2\hbar$, but there is no sign of the strong 847 keV γ ray. Non-observation of the 69 keV transition is also pertinent, indicative of the isomeric nature of band 3 at low spin.

We have seen that the decay of this isomer is associated with a γ ray of energy 847 keV, but this is not the only transition depopulating this state. The 847 keV transition fixes the bandhead excitation energy of the high-spin isomer relative to bands 2 and 3. The difference between the energy level of the isomer bandhead and the $19/2^+$, $17/2^+$ levels in band 3, and $17/2^+$ in band 2 implies the existence of competitive transitions with energies 536, 645 and 795 keV. To obtain a preliminary idea of the delayed radiation associated with this isomer, events were selected utilising a gate list comprised of the prompt radiation built on top of the isomeric bandhead. The γ rays used are detailed in Table 4.1. For an event to be considered valid, at least two γ rays from the list must have been observed in prompt coincidence with each other at JUROGAM. Further event veto is enabled by restricting allowed recoils to masses 129 and 133. The results of this search are detailed in Figure 4.4. Several transitions associated with low-spin states in multiple bands belonging to ^{129}Nd are observed. Evidence is seen for new transitions 536, 645, and 847 keV. There are no statistically significant counts at 795 keV. In addition, transitions belonging to band 1 are observed (highlighted pink); we shall see shortly that these levels are fed by a 1050 keV γ ray, which was also statistically insignificant in the JM06 data.

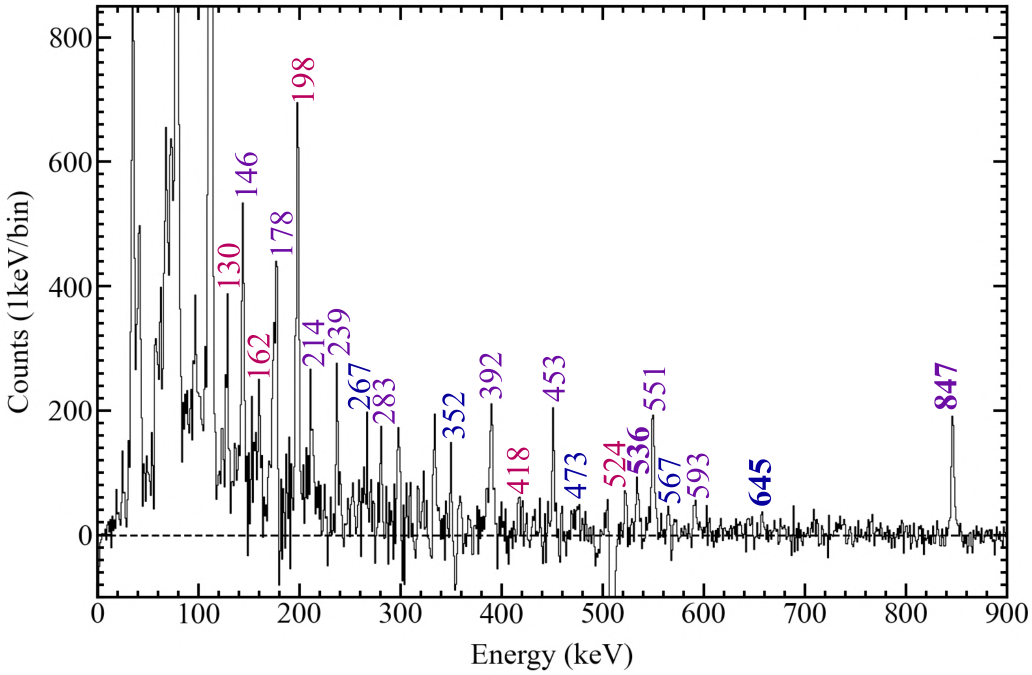

FIGURE 4.4: Focal-plane γ rays associated with mass 129 and mass 133 recoils and measured in delayed coincidence with any two γ rays seen at JUROGAM from a list composed of the γ rays built atop the isomeric state, listed in Table 4.1. Known transitions belonging to bands in ^{129}Nd are observed, along with new transitions feeding these states (highlighted in bold). The colour scheme helps identify which γ ray belongs to which band, and follows the same scheme as in Table 4.1 and Figure 4.10 (Pink = Band 1, Blue = Band 2, Purple = Band 3).

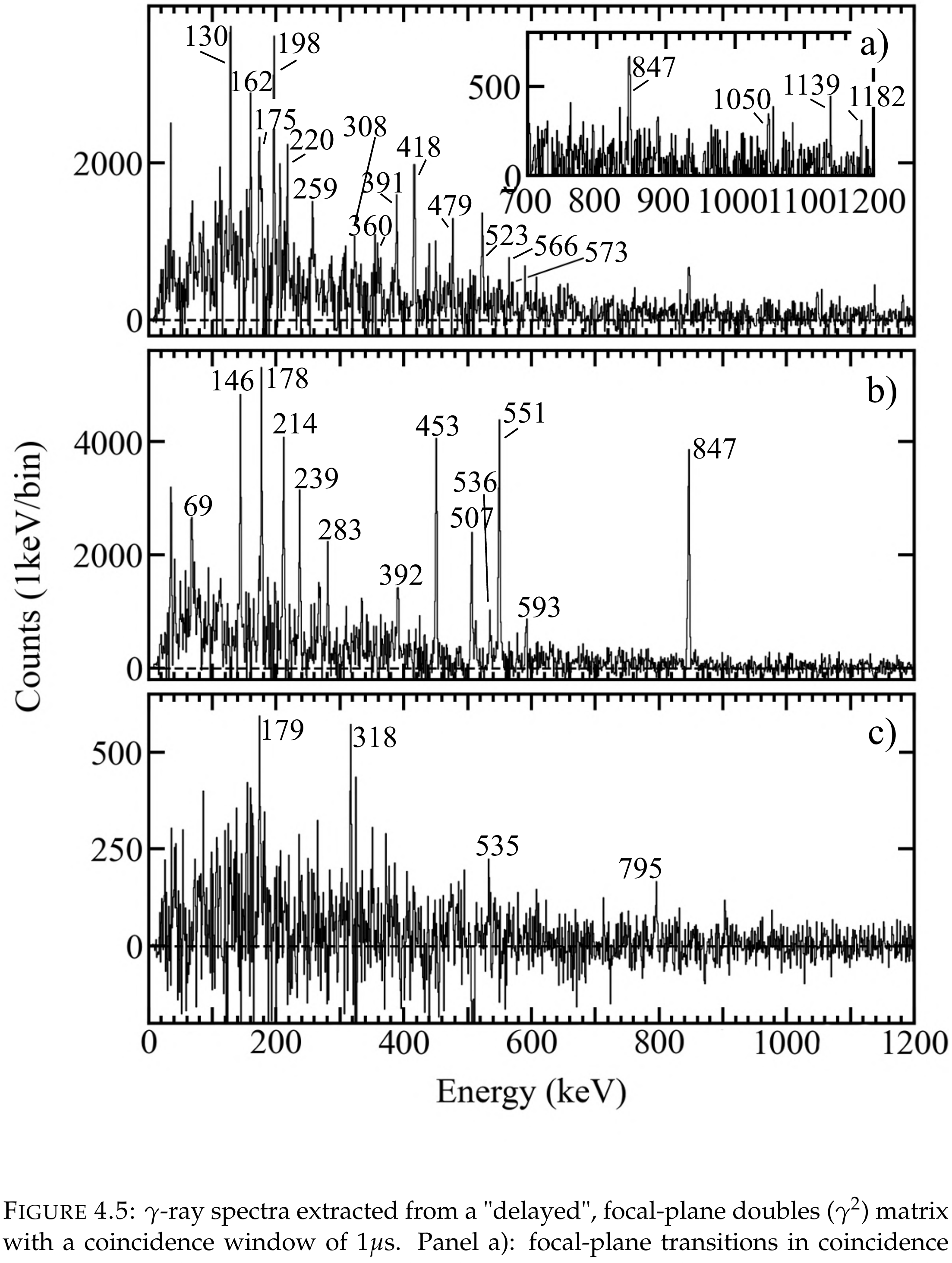

FIGURE 4.5: γ-ray spectra extracted from a "delayed", focal-plane doubles (γ^2) matrix with a coincidence window of 1μs. Panel a): focal-plane transitions in coincidence with 130 **or** 162 keV, associated with band 1. γ rays associated with band 1 are visible, alongside evidence for new transitions with energies 175, 391, 566, 847, 1050, 1139 and 1182 keV. Panel b): transitions in coincidence with 146 **or** 178 keV, associated with band 3. γ rays associated with band 3 are visible, alongside evidence for new transitions with energies 69, 536 and 847 keV. Panel c): transitions in coincidence with 439 keV, associated with band 2. γ rays associated with band 2 are visible, alongside evidence for a new transition with energy 795 keV.

The tenuous evidence for the 795 and 1050 keV transitions prompted a further search for these transitions in the M09 dataset, which benefited from a greater amount of counting statistics compared to JM06. Selecting events using JUROGAM was not possible here, so instead a thorough γ^2 analysis of the delayed transitions observed at the focal plane was performed, finding evidence for the existence of these transitions and a host of other new radiation depopulating the high-spin isomer.

Figure 4.5, panel (a), displays γ rays measured at the focal plane in coincidence with 130 or 162 keV — associated with band 1. We can see that excited states up to the $21/2^-$ level of this band are populated. A plethora of transitions not previously associated with this band are also seen: 175, 391, 566, 847, 1050, 1139 and 1182 keV. The 847 keV transition seen here is likely either because of unaccounted for background effects (the 847 keV line is very strong), or bands 2 and 3 decay into band 1 by some unseen transition. The 1050 keV transition is seen to decay into the $19/2^-$ level of band 1. Assuming this transition directly links the $19/2^-$ level with the isomeric bandhead, we can fix the excitation energy of band 1 relative to bands 2 and 3 for the first time. The $7/2^-$ level of band 3 is then proposed to be the ground state of this nucleus, with the high-spin isomer's bandhead 2284 keV above this state. Transitions 566 and 1139 keV are observed to depopulate the same level as each other, which is not the same level as the high-spin isomer bandhead. To differentiate between the two levels we label the high-spin isomer level A, and the new level, level B. 1182 keV is not seen to depopulate either of these levels, and so is assigned as a further new level, labelled level C. The energy difference between levels A, B and C implies the potential existence of transitions of energies 175, 216 and 391 keV which connect the three levels. Evidence for the 175 and 391 keV transitions is seen in Figure 4.5, panel a). No evidence for the 216 keV transition is found here.

Panel (b) of Figure 4.5 displays γ rays in coincidence with 146 **or** 178 keV —

associated with band 3. The 847 keV transition is very strong here, as expected, and is seen to decay into the $17/2^+$ state of band 3. We confirm the existence of a 536 keV transition linking the high-spin isomer bandhead (level A) and the $19/2^+$ level in band 3. Additionally, we reaffirm the 69 keV transition decaying out of band 3's bandhead into the $3/2^+$ level in band 2.

Panel (c) of Figure 4.5 displays γ rays in coincidence with 439 keV — associated with band 2. Among the transitions below the $17/2^+$ level in this band, we can also confirm the 795 keV transition, depopulating level A into the $17/2^+$ level. The 645 keV transition between the isomer bandhead and the $19/2^+$ level of this band is not seen here since the spectrum was gated by the 439 keV transition and there are no known linking M1 transitions between the $13/2^+$ state and the $19/2^+$ state or its intermediaries.

Analysis of the γ^2 coincidence data allows measurement of the highest level each of these new transitions are associated with. Assuming that the transitions decay directly into these levels, a partial level scheme can be produced (Figure 4.6).

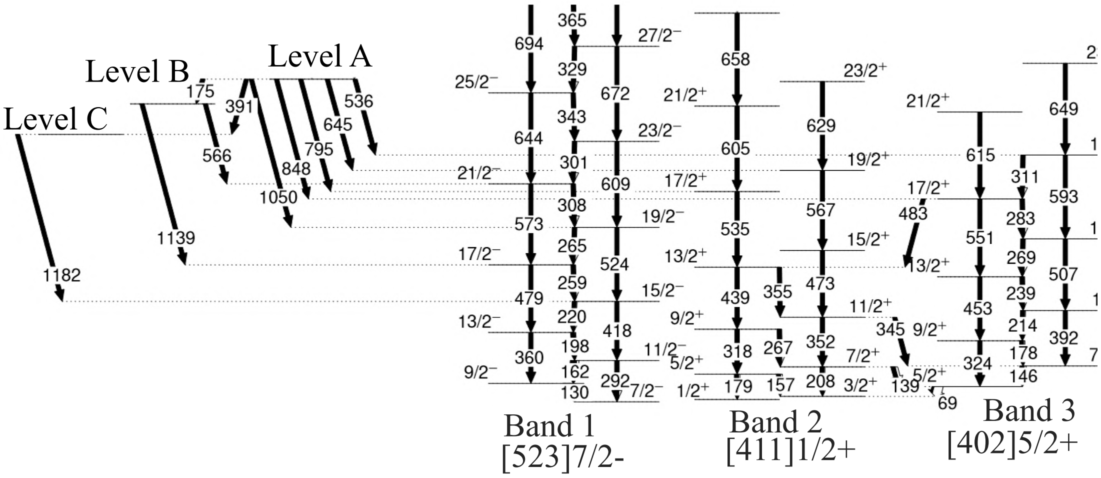
Level A
Level B
Level C
175
391
536
645
795
848
566
1050
1139
1182
694
365
27/2−
329
25/2−
672
343
644
23/2−
301
21/2−
609
308
19/2−
573
265
17/2−
524
259
15/2−
479
220
13/2−
418
198
11/2−
360
162
9/2−
130
292
7/2−
Band 1
[523]7/2-
658
21/2+
605
17/2+
535
13/2+
439
355
9/2+
318
267
5/2+
1/2+
179
157
23/2+
629
19/2+
567
15/2+
473
11/2+
352
7/2+
208
3/2+
Band 2
[411]1/2+
21/2+
615
17/2+
483
13/2+
551
345
9/2+
453
324
139
5/2+
69
311
283
269
239
214
178
146
649
593
507
392
2
1
1
1
7
Band 3
[402]5/2+

FIGURE 4.6: Partial level scheme for ^{129}Nd composed from the delayed γ^2 analysis displayed in Figure 4.5. The newly observed isomeric states are labelled levels A, B and C, and are connected to the existing level scheme by the γ rays displayed in Figures 4.4 and 4.5.

Figure 4.7a, displays γ rays in coincidence with the 1182 keV transition. Further evidence for the 175 and 391 keV transitions is seen here, as well as evidence for a 216 keV transition connecting levels B and C. The 1182 keV transition sees all three γ rays whereas the 1139 keV transition (Figure 4.7b) only sees the 175 keV transition, which is in agreement with the proposed partial level scheme in Figure 4.6.

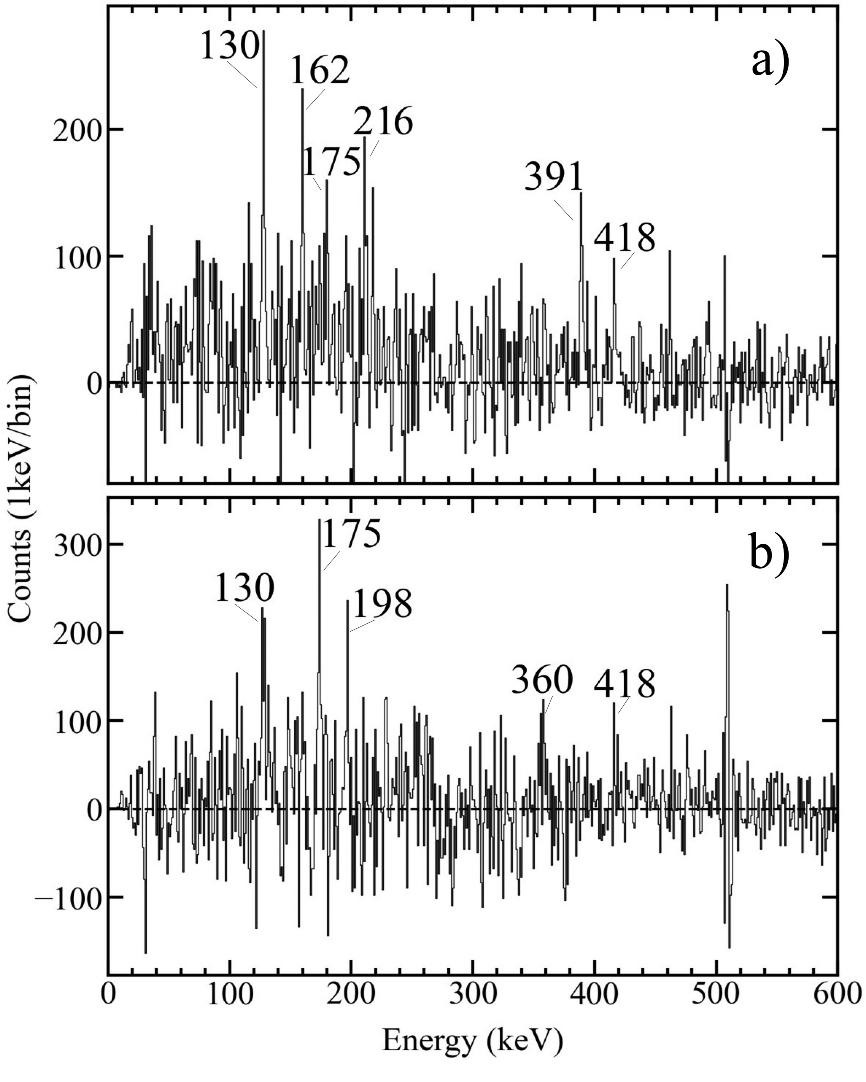

FIGURE 4.7: γ-ray spectra extracted from a "delayed" doubles (γ^2) matrix with a coincidence window of 1μs. Panel a): transitions associated with the 1182 keV transition. Evidence is seen here for a transition of energy 216 keV, linking levels B and C in the partial level scheme of Figure 4.6. Panel b): transitions associated with the 1139 keV transition. Here, only the 175 keV transition is visible and not the 216 keV transition, supporting the partial level scheme displayed in Figure 4.6.

In comparing the energy levels of levels A, B and C, and the energy levels within band 3, there are implied transition energies that were not observed in the coincidence analysis detailed in Figures 4.5 and 4.7. However, by gating on these transition energies directly, we can see evidence that they decay to band 3. Figure 4.8 displays the results of this. From the top panel to the bottom, γ-ray energies of 673, 739, 955 and 1008 are gated. Each spectrum displays clear evidence of transitions belonging to band 3 (69, 146, 178, 214, 239, 392, 507 keV).

Transitions of energies 923 keV and 658 keV were also gated based on their implied existence from energy level differences. The resulting spectra displayed some evidence of decays to band 1, but were not significantly above background level, so these transitions have been designated tentative. In all four figures a transition at approximately 392 keV is seen. The signal here arises from both the 392 keV E2 transitioning between $11/2^+$ and $7/2^+$ in band 3, and, for the case of 739 keV and 1008 keV, the 391 keV transition depopulating the high-spin isomer (level A).

All of these new transitions are tabulated in Table 4.1, and are displayed in the final level scheme depicted in Figure 4.10.

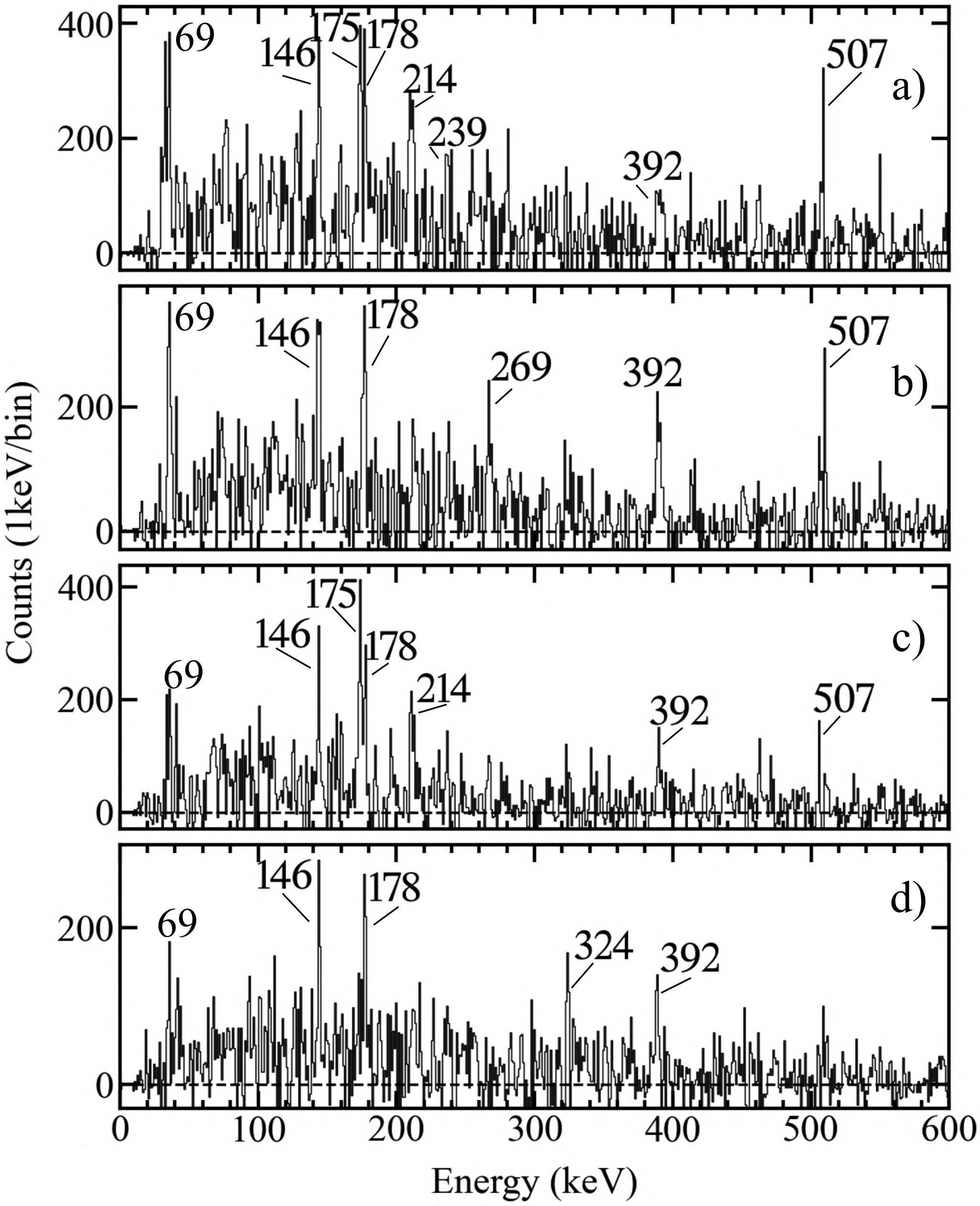

FIGURE 4.8: γ-ray spectra extracted from a "delayed" doubles (γ^2) matrix with a coincidence window of 1μs. All four spectra display transitions belonging to the low-spin states of band 3. Panel a): γ rays in coincidence with 673 keV. Panel b): γ rays in coincidence with 739 keV. Panel c): γ rays in coincidence with 955 keV. Panel d): γ rays in coincidence with 1009 keV.

4.3.2 Prompt γ-ray coincidences

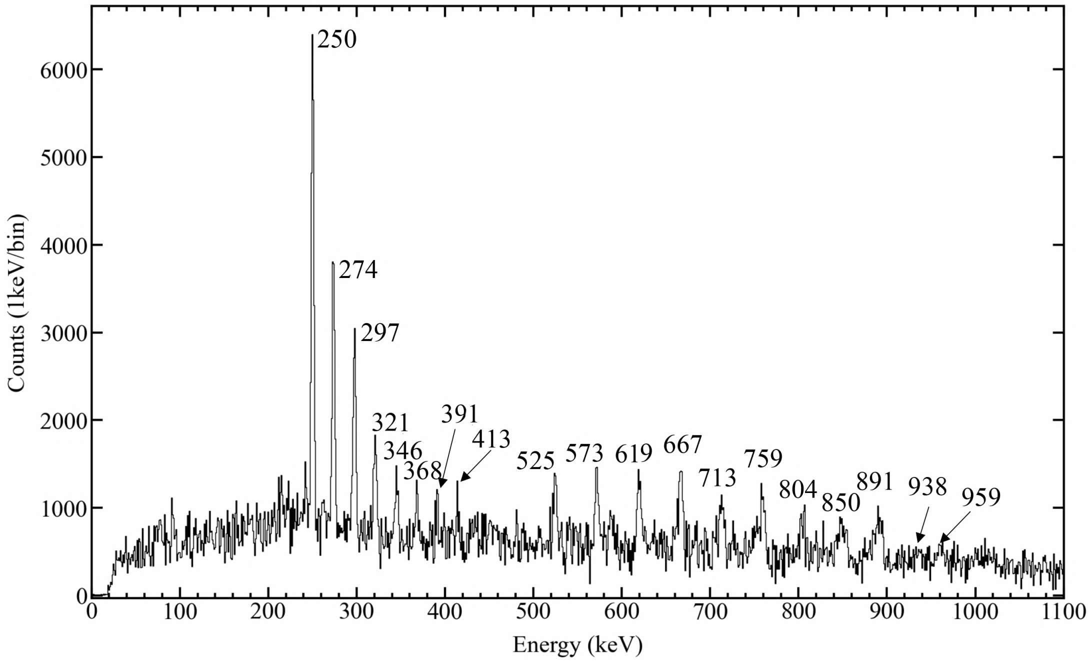

FIGURE 4.9: γ rays observed at the target position by JUROGAM in delayed coincidence with the 146, 178, 239, 392, 453, 551 **or** 847 keV transitions detected at the focal plane. The correlation time for recoil-isomer decay correlations was limited to 1μs.

Utilising the 146, 178, 239, 392, 453, 551 **or** 847 keV focal-plane transitions as event selectors we can isolate the prompt radiation corresponding to the decay of rotational states built atop the high-spin isomer, level A. The results of this selection are displayed in Figure 4.9. The recoil-decay correlation time was limited to 1μs, a time selected to maximise radiation correlated with the decay of ^{129}Nd, but minimising the introduction of background.

Using similar event selection methods, an attempt was made to measure prompt radiation representing the decay of bands built atop levels B and C but was not possible due to low statistics. Further characterisation of these states is discussed in Section 4.4.1, at the end of this chapter. All of the new transitions measured in this work are displayed in a tabulated format in Table 4.1 and in a level scheme in Figure 4.10.

TABLE 4.1: Top table: List of γ rays built atop the new high-spin isomer (band 5/level A) in ^{129}Nd and their measured properties. Bottom table: List of γ rays depopulating bands 5, 6 and 7. Quantities in brackets denote uncertainty in the last quoted significant digit. Assigned (λL) values in brackets are tentative.

E_γ, keV [a]	I_γ [b]	$\bar{r}_{DCO}$	P	σL
250.20(5)	100	0.7(1)	-0.6(5)	M1
273.8(1)	63	0.6(1)	-0.1(6)	M1
297.4(1)	44	0.6(1)	-0.1(6)	M1
320.7(2)	34	0.5(4)	—	Dipole (M1)
345.6(2)	19	—	—	(M1)
368.1(3)	17	—	—	(M1)
391.0(3)	15	—	—	(M1)
413.1(4)	16	—	—	(M1)
525.0(8)	13	—	—	(E2)
573.1(9)	17	1.2(5)	—	Quadrupole (E2)
619.0(4)	45	1.2(2)	—	Quadrupole (E2)
667.4(5)	46	1.1(3)	—	Quadrupole (E2)
713.3(5)	29	1.3(3)	—	Quadrupole (E2)
759.2(3)	34	1.2(1)	—	Quadrupole (E2)
804.3(4)	27	1.1(10)	—	Quadrupole (E2)
849.5(8)	49	—	—	(E2)
890.7(5)	43	—	—	(E2)
938(1)	13	—	—	(E2)
959(1)	9	—	—	(E2)

E_γ (keV)	(σL)	Band
175.1(5)	-	5→6 ⬛
216.2(7)	-	6→7 ⬛
391(1)	-	5→7 ⬛
536(1)	(M1)	5→3 🟪
566(1)	-	6→1 🟥
645(2)	(M1)	5→2 🟦
658(2)	-	7→1 🟥
673(1)	-	6→3 🟪
739(1)	-	7→3 🟪
795.4(5)	(E2)	5→2 🟦
847.21(5)	(E2)	5→3 🟪
923(2)	-	7→1 🟥
955(1)	-	6→3 🟪
1009(1)	-	7→3 🟪
1050(1)	(E1)	5→1 🟥
1139(1)	-	6→1 🟥
1182(1)	-	7→1 🟥

[a] Energy measurement precision quoted representative of the statistical uncertainty in the centroid of a single-term Gaussian fit.

[b] Intensities measured from a spectrum gated by (delayed) 847 keV. Intensities efficiency corrected as per Figure 3.8. Intensities have not been corrected to account for internal conversion.

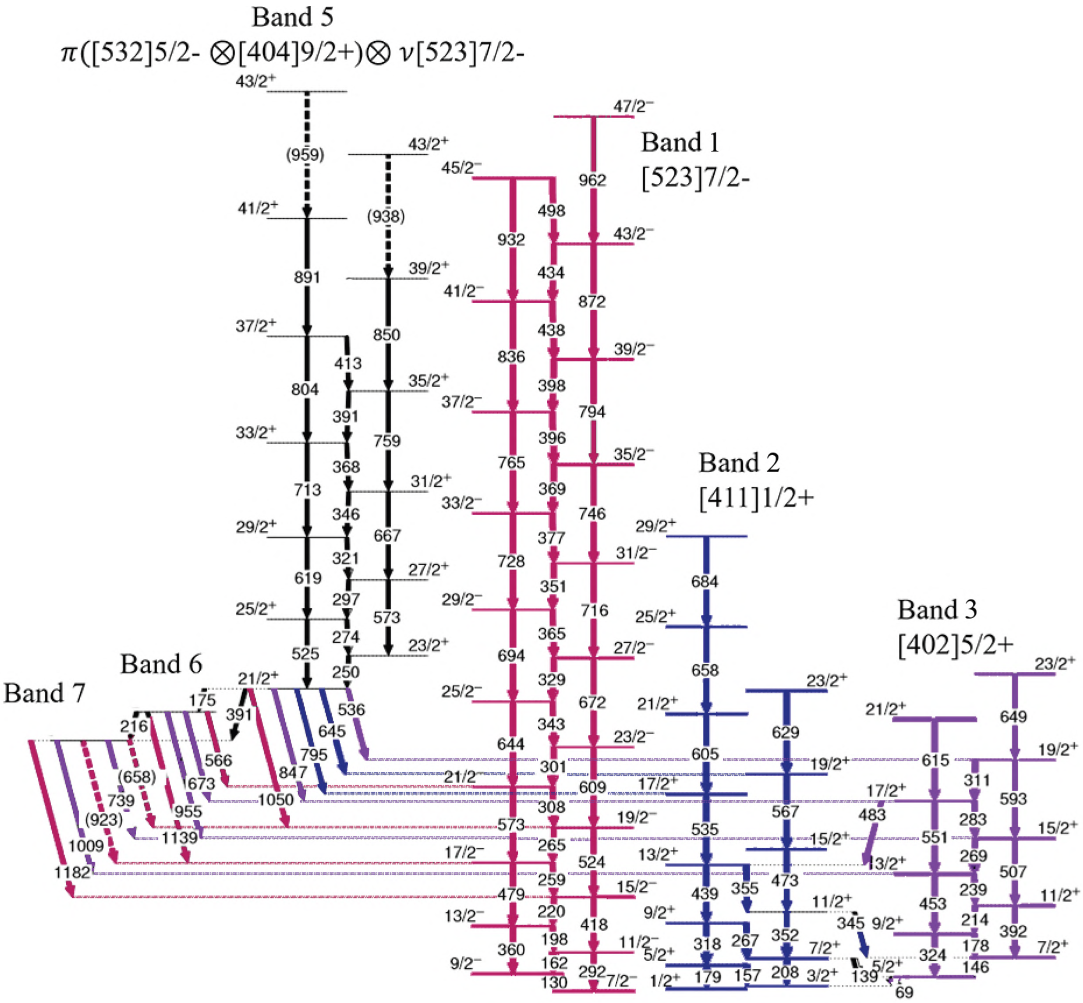
Band 5
π([532]5/2- ⊗[404]9/2+)⊗ ν[523]7/2-
43/2+
(959)
41/2+
891
37/2+
804
33/2+
713
29/2+
619
25/2+
525
21/2+
43/2+
(938)
39/2+
850
413
35/2+
391
759
368
31/2+
346
667
321
27/2+
297
573
274
23/2+
250
Band 6
175
216
391
536
645
795
566
(658)
673
847
739
1050
(923)
955
1139
1009
1182
Band 7
Band 1
[523]7/2-
47/2−
45/2−
962
498
932
43/2−
434
41/2−
872
438
836
39/2−
398
37/2−
794
396
765
35/2−
369
33/2−
746
377
728
31/2−
351
29/2−
716
365
694
27/2−
329
25/2−
672
343
644
23/2−
301
21/2−
609
308
573
19/2−
265
17/2−
524
259
479
15/2−
220
13/2−
418
198
360
11/2−
162
9/2−
292
130
7/2−
Band 2
[411]1/2+
29/2+
684
25/2+
658
21/2+
605
17/2+
535
13/2+
439
355
9/2+
318
267
5/2+
179
157
1/2+
23/2+
629
19/2+
567
15/2+
473
11/2+
352
7/2+
208
3/2+
Band 3
[402]5/2+
21/2+
615
17/2+
483
551
13/2+
453
345
9/2+
324
139
5/2+
69
23/2+
649
19/2+
311
593
283
15/2+
269
507
239
11/2+
214
392
178
7/2+
146

FIGURE 4.10: The final (partial) level scheme for ^{129}Nd. Here, band 5, the bandheads of bands 6 and 7, and all of the γ rays depopulating them are original work. Bands 1, 2 and 3 are constructed using data obtained from the study performed by Zeidan, *et al*. The levels associated with the bandheads of bands 6 and 7 have no definite spin/parity assignments, but their excitation energies are fixed. So too are the excitation energies of all levels presented in this scheme, with the proposed ground state being the $7/2^-$ level of band 1. For easier viewing, the γ rays depopulating band 5 are colour coded to the band that they decay into. The proposed configuration for band 5 is discussed and substantiated in the following section.

4.3.3 Half-life Measurements

Utilising the 847 keV focal-plane γ ray as an event selector, a measurement for the half-life of the isomeric state labelled level A can be made. Here, measurements were made of the timing difference between implantation of a mass-129 recoil into the DSSD and the detection by the focal plane germanium detectors of a γ ray of this energy. Background subtraction was made in the same way as for the γ spectra in Figure 4.2. The results of this measurement are displayed in Figure 4.11. The fit model is $y = Ae^{Bx} + Cx + D$, with $B = -1/t_{1/2}$, where $t_{1/2}$ is the half-life of the state. The measured half-life of the isomer is then $t_{1/2} = (679 \pm 60)$ ns.

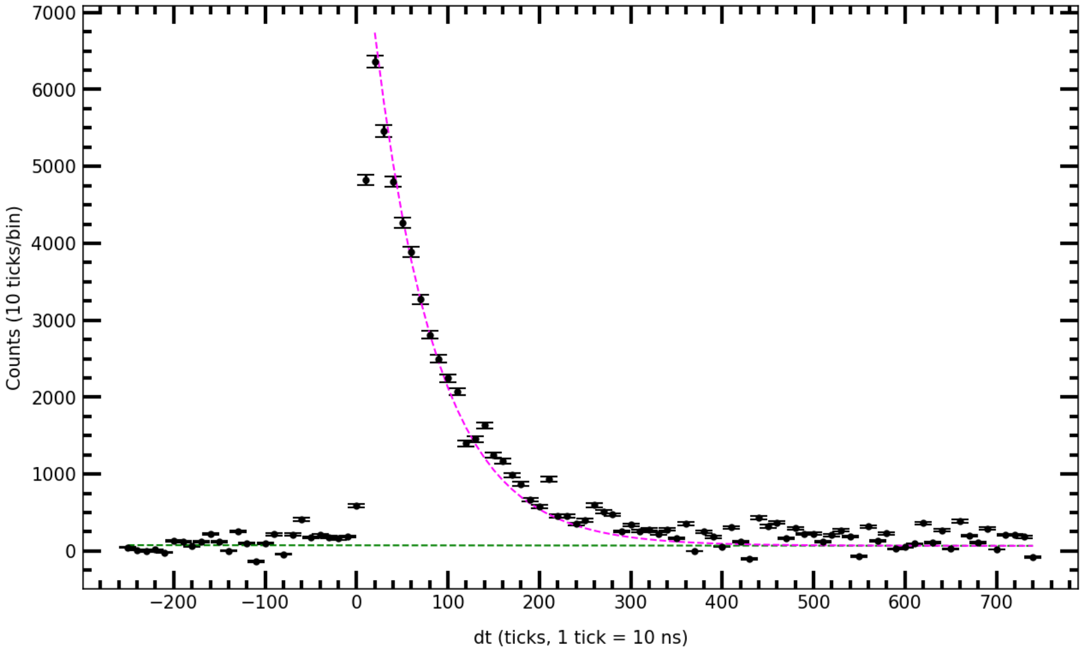

FIGURE 4.11: Time difference between the implantation of a recoil into the DSSD and the detection of an 847 keV γ ray at the focal plane. The fit is a single-term exponential with a single-term polynomial background. Fit parameters $A : 895 \pm 69, B : -0.015 \pm 0.001, C : 0.0009 \pm 0.0030, D : 74 \pm 23$.

Due to the 69 keV γ ray lying among a plethora of contaminant γ rays, it is difficult to measure its half-life using the same method. Instead, the mean lifetime of this transition is measured using the centroid-shift method. An event is selected in sort by gating on a focal-plane γ ray (γ_1). From the remaining unselected γ rays (γ_2) in the event, a matrix is produced with E_{γ_2} on one axis and the measured timing difference between the two γ rays on the other. Selected examples of this analysis is displayed in Figure 4.12. The solid and dotted lines in these figures represent a reflection of the ordering of which energy represents γ_1 and γ_2, respectively. The peak centroid, C, is then yielded from the standard equations [59] of

$$C = \frac{\sum_j n_j t_j}{\sum_j n_j} \text{ and } \Delta C = \sqrt{\frac{\sum_j |n_j|(t_j - C)^2}{(\sum_j n_j)^2}}, \tag{4.1}$$

where n_j is the number of counts in the time bin t_j. The mean lifetime of the state between γ_1 and γ_2 is then equal to half the distance between the two peak centroids

$$\tau = (C_N - C_R)/2. \tag{4.2}$$

Figure 4.12d represents the measured time difference between $\gamma_1 = 551$ keV and $\gamma_2 = 69$ keV. The measured time difference of (36 ± 13) ns can be said to be equal to the mean lifetime of the 69 keV state, if the lifetimes of the intermediary levels are considered negligible. It is known that the lifetime of these levels must be at least faster than 20 ns since they are all observed in the prompt γ^3-coincidence matrix (prompt JUROGAM γ rays only). A more quantitative approach comes from looking at the timing difference (centroid shift) between the 551 keV transition and all the other γ rays below it in the cascade. We expect the shift to be 0 since a picosecond lifetime is ten-thousand times smaller than the 10 MHz precision of the DAQ. This is consistent with what is observed in panels a) through d), supporting the validity of this lifetime measurement method.

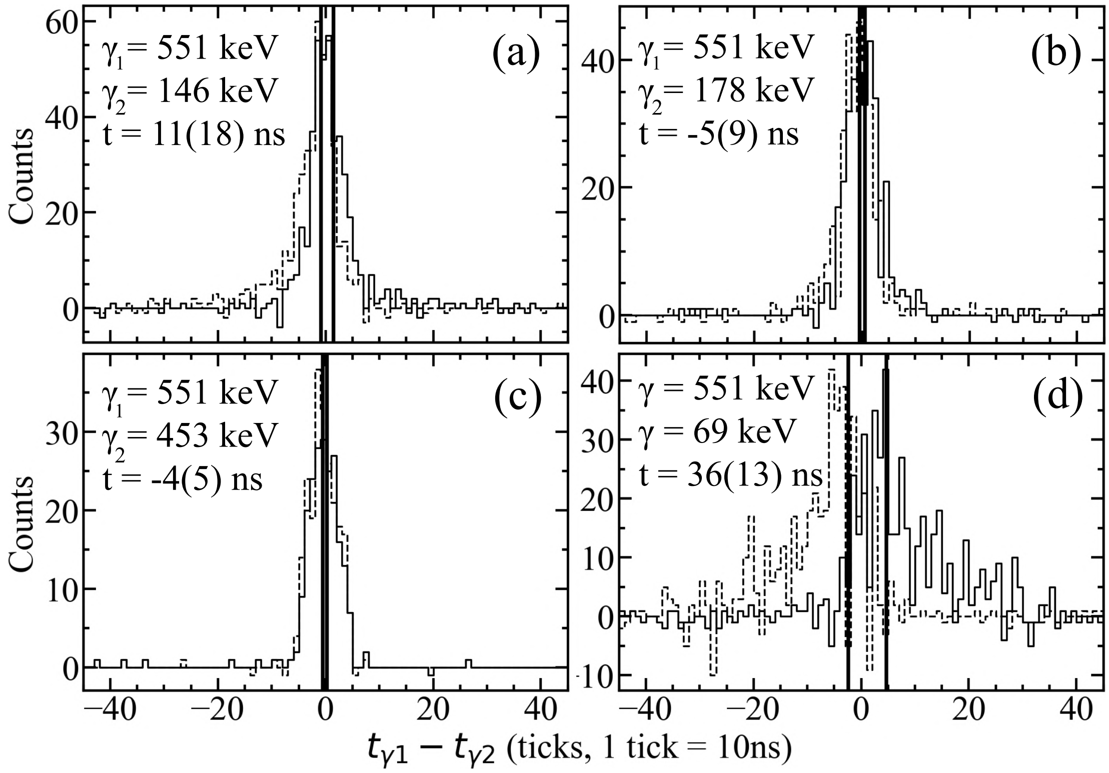

FIGURE 4.12: Measured timing difference between two focal-plane γ-rays. The shift of the peak centroid is representative of the mean lifetime of the level(s) fed and depopulated by the respective transition, as per Equations 4.1 and 4.2.

4.4 Theoretical Comparison and Discussion

The proton Fermi surface for ^{129}Nd lies among low-Ω $h_{11/2}$ states, while the proton region lies among down sloping high-Ω orbitals. That both protons and neutrons lie between closed shells for this nucleus result in it having a large predicted ground-state deformation $\beta_2 = 0.32$ [57]. Inspecting the Nilsson diagram displayed in Figure 4.13, we can see that the closest levels to the proton Fermi surface for $Z = 60$ are the negative parity [550]$1/2^-$, [541]$3/2^-$ and [532]$5/2^-$ orbitals, and the positive parity [411]$3/2^+$, [413]$5/2^+$ and [404]$9/2^+$ orbitals. The neutron levels closest to the $N = 69$ shell gap are the [523]$7/2^-$, [411]$1/2^+$, [541]$1/2^-$, and [402]$5/2^+$; each of these levels were assigned to a band in this nucleus by Zeidan, *et al.*

Bands with so-called "enhanced deformation" have been observed in this mass region [60], built on top of the high-Ω [404]$9/2^+$ intruder orbital. Coupling high-Ω states results in a large K quantum number - the projection of the nuclear spin along the axis of deformation. Changes in this quantum number require a γ-ray having least that many units of spin to be emitted during the decay, or else the transition is hindered - a K isomer. At low spin, excited nuclear states for this nucleus are driven and characterised by the orbital occupied by the single odd neutron. However, as rotational frequency increases, it is possible that a bound proton or neutron pair can break, promoting one of the pair to a previously unoccupied state higher in excitation energy.

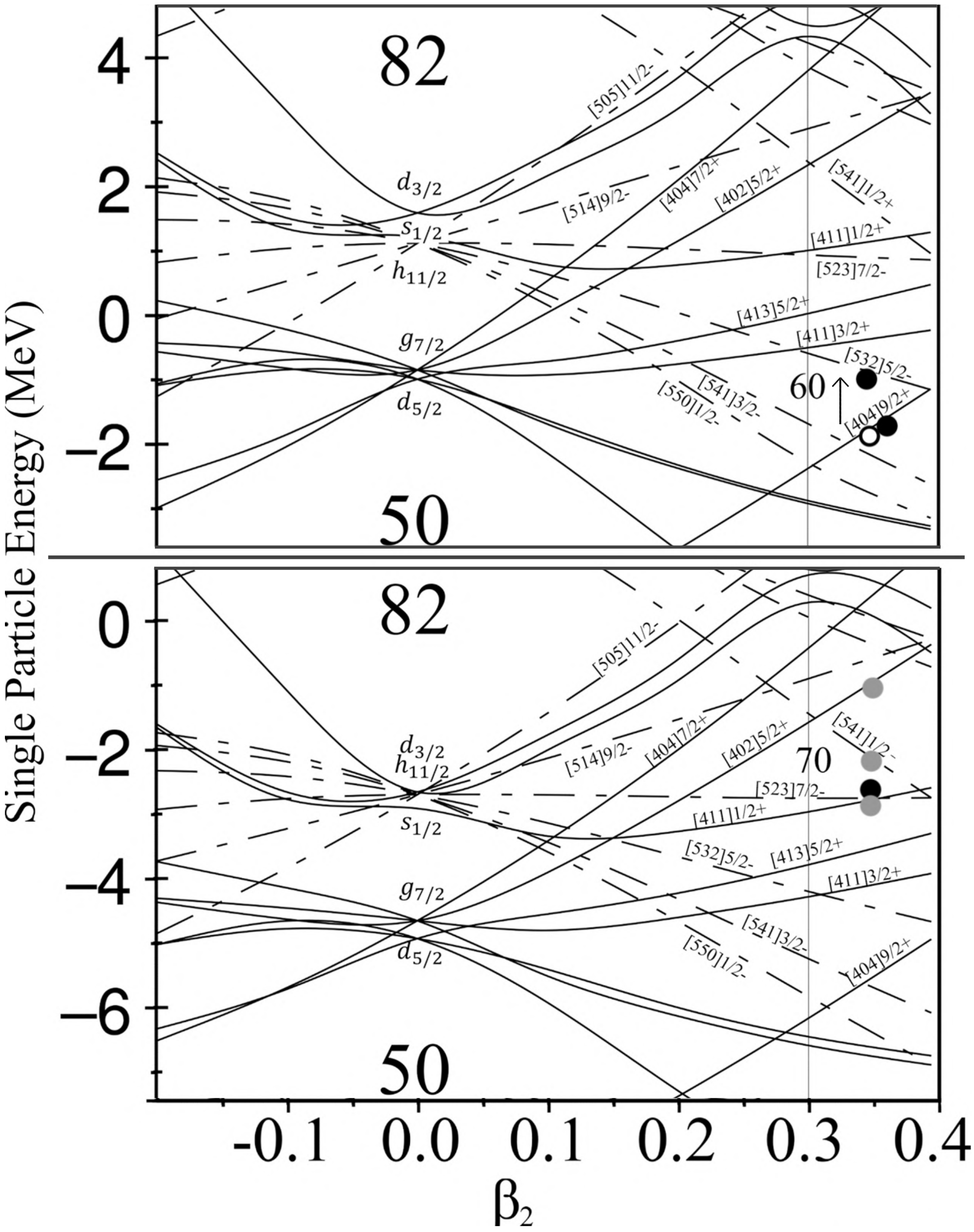

FIGURE 4.13: **Top**: Nilsson diagram for protons centered around the 60 proton shell gap at high deformation. Black circles are proposed configurations for the protons when this nucleus is in the isomeric state at 2283 keV. At the ground-state, both protons are proposed to inhabit the [404]9/2$^+$ state. **Bottom**: Nilsson diagram for neutrons centered around the 70 neutron shell gap at high deformation. The black circle is the proposed level inhabited by the odd neutron when this nucleus is in the isomeric state at 2283 keV. Grey circles represent states with bands known to be built on the odd neutron occupying these states.

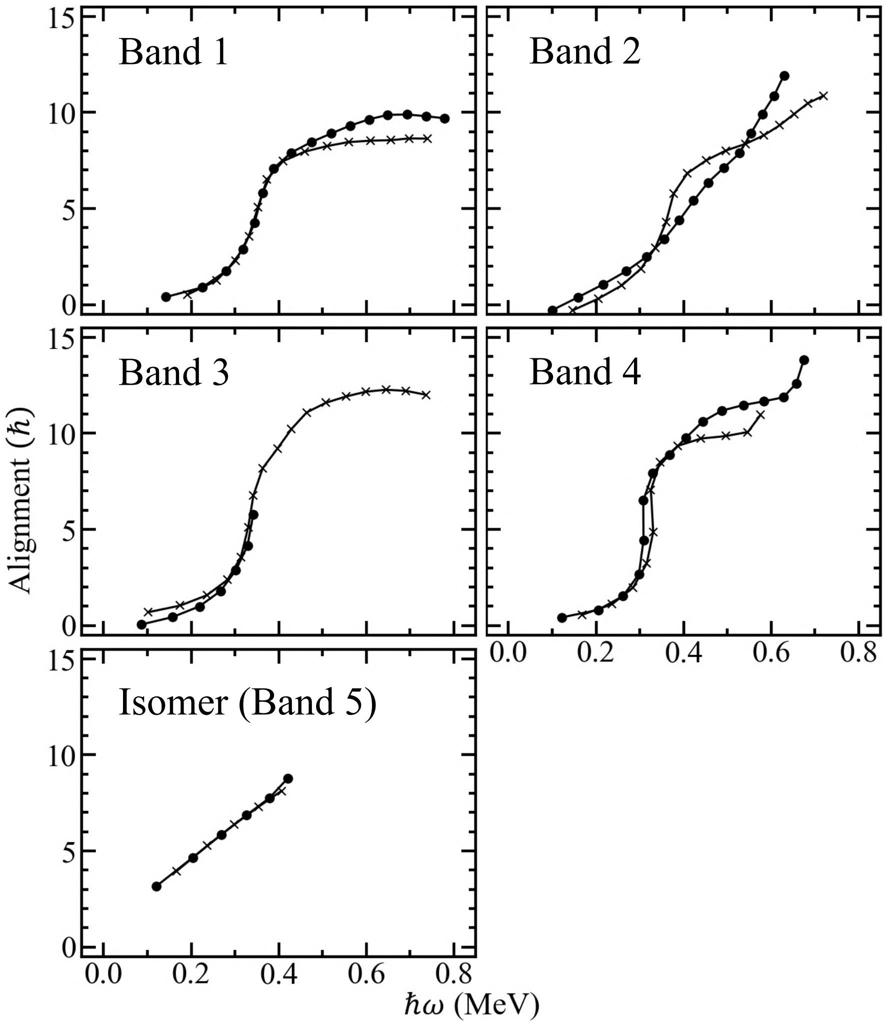

FIGURE 4.14: Experimental single-particle alignment diagrams for the four known bands in ^{129}Nd (data from [58]) and the new $21/2^+$ isomeric band (band 5). Band numbering is the same as in Ref [58] for simple comparison.

Figure 4.14 displays the experimental single-particle alignments for the four one-quasineutron bands identified by Zeidan, *et al*, and the high-spin isomer identified in this work.

Rotation causes Nilsson levels to shift in energy with respect to each other, as well as mixing their respective quantum wavefunctions and lifting the two-fold degeneracy of the level according to its signature quantum numbers. The Cranked Shell Model (CSM) represents a theoretical framework for the rotating nucleus. Figure 4.15 displays the calculated theoretical Routhians (rotating

Hamiltonian) for quasiprotons and quasineutrons for this nucleus. Quasiparticle levels are labelled alphabetically, and the Nilsson orbitals that they are associated with at zero spin are detailed in Table 4.2.

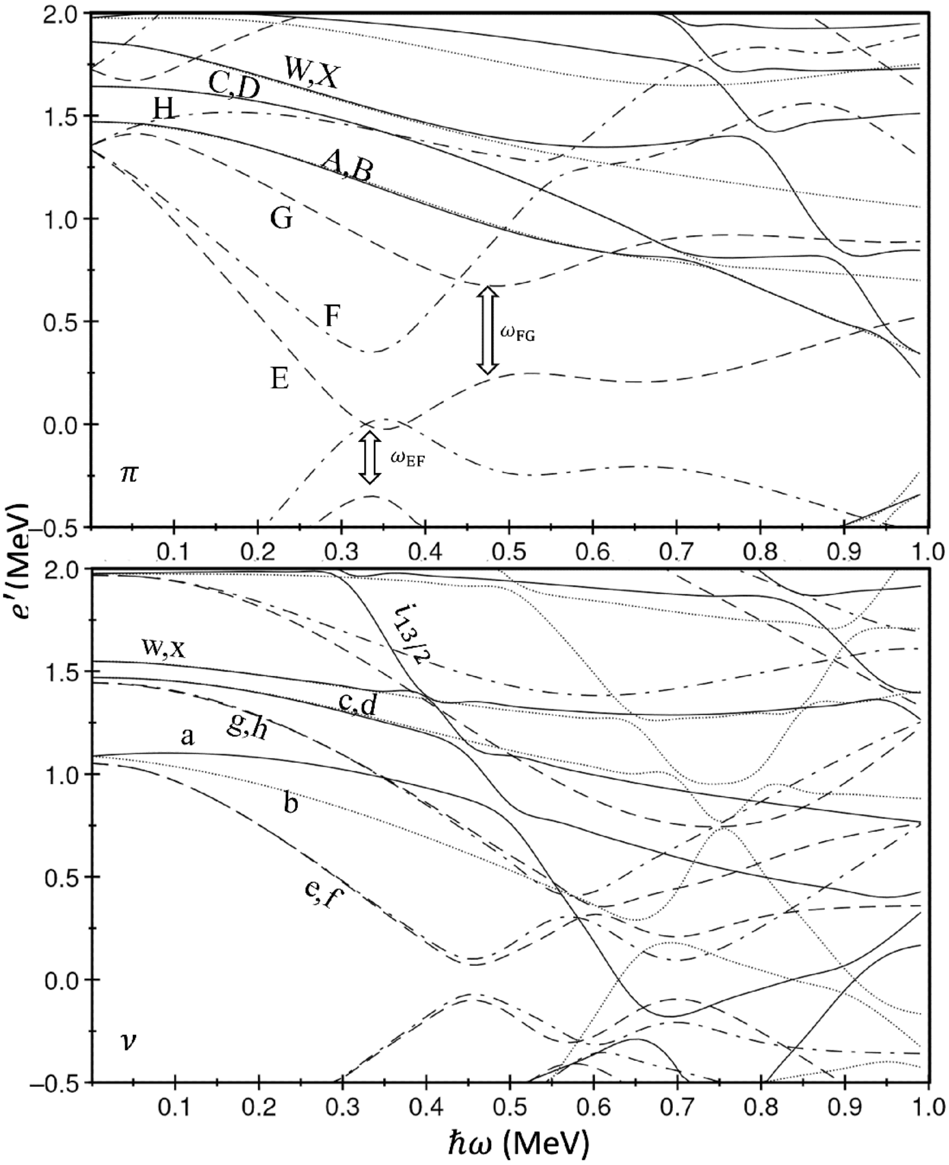

FIGURE 4.15: Cranked Shell Model quasiparticle Routhians (Panel π): protons, (Panel ν): neutrons. Both figures generated using a universal, triaxial Woods-Saxon potential with parameters β_2= 0.305, β_4 = 0.006, γ= -1.9°. Parameters used are the same as in Ref [58] to ensure consistency with their results. Labels referring to Nilsson levels — displayed in Table 4.2 — are only valid at zero spin (i.e $0\hbar\omega$) since rotation causes states to become a mixture of different wavefunctions. (π, α) : solid = (+,+1/2), dotted = (+,–1/2), dot–dash = (–,+1/2), dashed = (–,–1/2).

TABLE 4.2: Quasiparticle labelling scheme for ^{129}Nd along with their assigned Nilsson configuration at zero rotational frequency.

Label	$(\pi,\alpha)_n^a$	Configuration[b]
	Quasiprotons	
A	$(+,-1/2)_1$	$g_{9/2}[404]9/2^+$
B	$(+,+1/2)_1$	$g_{9/2}[404]9/2^+$
C	$(+,-1/2)_2$	$d_{5/2}/g_{7/2}[411]3/2^+$
D	$(+,+1/2)_2$	$d_{5/2}/g_{7/2}[411]3/2^+$
E	$(-,-1/2)_1$	$h_{11/2}[532]5/2^-$
F	$(-,+1/2)_1$	$h_{11/2}[532]5/2^-$
G	$(-,-1/2)_2$	$h_{11/2}[541]3/2^-$
H	$(-,+1/2)_2$	$h_{11/2}[541]3/2^-$
	Quasineutrons	
a	$(+,-1/2)_1$	$s_{1/2}/d_{3/2}[411]1/2^+$
b	$(+,+1/2)_1$	$s_{1/2}/d_{3/2}[411]1/2^+$
c	$(+,+1/2)_2$	$d_{5/2}/g_{7/2}[402]5/2^+$
d	$(+,-1/2)_2$	$d_{5/2}/g_{7/2}[402]5/2^+$
e	$(-,-1/2)_1$	$h_{11/2}[523]7/2^-$
f	$(-,+1/2)_1$	$h_{11/2}[523]7/2^-$
g	$(-,-1/2)_2$	$h_{11/2}[532]5/2^-$
h	$(-,+1/2)_2$	$h_{11/2}[532]5/2^-$

[a] The subscript n numbers the quasiparticle's excitations of a given signature and parity starting with the lowest in energy at $\hbar\omega$ = 0 MeV.
[b] Nilsson configurations only valid at $\hbar\omega$ = 0 MeV.

Though speculation can be made on which quasiparticle orbitals represent a given band based on its intensity compared to which levels are predicted to be yrast at a given spin, less tenuous knowledge can be gained from Pauli blocking arguments. The Pauli exclusion principle forbids two fermions with identical quantum numbers from occupying the same spatial coordinates. Quasiparticle levels with identical (π, α) numbers repel each other. This is analogous to the Nilsson diagram where levels with the same Ω^π quantum numbers repel each other. The sudden increase in alignment at $\hbar\omega = 0.3$ for bands 1 - 4, displayed in Figure 4.14, is associated with the alignment of a pair of $h_{11/2}$ protons, displayed in Figure 4.15. It is immediately obvious that the band built atop the isomeric state does not see this alignment. Following the Pauli blocking argument, this alignment is not seen because a proton must already be occupying the associated $h_{11/2}$ orbital in the configuration for this band. Since neodymium isotopes have an even number of protons $(Z = 60)$, a proton pair must have been broken to achieve this configuration. Including the odd neutron, this would assign band 5's isomeric bandhead a three-quasiparticle configuration. According to the CSM calculations the quasiproton level closest to the Fermi surface — and the one whose first (EF) alignment is blocked — is the $h_{11/2}[532]5/2^-$ orbital, so we assign this as one of the protons. The next closest quasiproton to the Fermi surface is associated with the Nilsson configuration $h_{11/2}[541]3/2^-$. The low-Ω nature of this orbital does not lend itself to the requirement of an overall large K quantum number, required for the state to be a K-isomer. However, the next closest level is the $g_{9/2}[404]9/2^+$ orbital. The large Ω quantum number is conducive to a large overall K. The Nilsson diagram displayed in Figure 4.13 shows how this level is occupied at the $Z = 60$ shell gap. We propose for band 5's isomer configuration that a pair of protons occupying the $[404]9/2^+$ orbital are broken, with one of these protons promoted to the $[532]5/2^-$ state. The quasineutron orbital closest to the Fermi surface is associated with the $h_{11/2}$ $[523]7/2^-$ orbital. From the γ^2 analysis it is known the isomer decays to a band built on this neutron orbital, and its high-Ω number is again convenient for producing a large K value. The proposed configuration $\pi(h_{11/2}[532]5/2^- g_{9/2}[404]9/2^+) \bigotimes \nu h_{11/2}[523]7/2^-$ results in a bandhead $I^\pi = K^\pi = 21/2^+$. With this configuration, it is expected that Pauli blocking would prevent observation of the first (ef) neutron alignment predicted by the CSM calculations at $\hbar\omega = 0.45$ MeV. In addition we would expect that the 2nd proton alignment (FG), predicted at $\hbar\omega = 0.5$ MeV would be observed. Figure 4.14 shows that the start of an alignment between $\hbar\omega = 0.4$-0.45 may be visible for the isomer, but it is not populated to high enough spin to know for sure. Future experiments can differentiate between the proton and neutron alignment predicted at these frequencies by the measured gain in alignment at the upbend; the gradient of the theoretical Routhian yields a predicted gain in alignment associated with that quasiparticle.

A systematic search for similar isomers in this mass region did not yield another isomer with a bandhead spin as high as $21/2^+$, however, a similar structure arises in even-odd neighbour ^{135}Nd [61]. Here, the negative parity ground-state band built atop the $[514]9/2^-$ neutron orbital experiences a band crossing at $I^\pi = 15/2^-$, associated with a broken pair of protons (Figure 4.16). The band above the crossing is assigned the quasiparticle configuration EAe/f, using the same convention as that used in this thesis. The Nilsson orbitals involved are $g_{7/2}$ $[413]5/2^+$, $h_{11/2}$ $[541]3/2^-$ and $h_{11/2}$ $[514]9/2^-$. An interesting feature of this level scheme is the large signature splitting observed at low-spin, uncommonly associated with the high-Ω $[514]9/2^-$ orbital. This can be explained by the nucleus having a large triaxial deformation, with $\gamma = -20^\circ$ as displayed in the bottom-right panel of Figure 4.16. The signature splitting is observed to diminish at high-spin for both the proton breaking observed at spin $17/2^-$ and the proton alignment observed at $23/2^-$. In both cases, the loss of signature splitting is explained as the nucleus shifting towards an axially prolate shape ($\gamma = 0^\circ$) as an aligning pair of quasiprotons come into play. The situation is not identical for ^{129}Nd. A pronounced difference is that the $21/2^+$ isomer (EAe/f) is seen to decay into multiple bands with the odd neutron placed in different Nilsson orbitals. Though the transition into the isomeric state is associated with the loss of signature splitting seen in the low-Ω $[411]1/2^+$ band, there is no irregular signature splitting observed in the high-Ω bands in this nucleus, so - utilising the inverse of the arguments presented for ^{135}Nd - it can not be said that the ground-state of this nucleus is triaxial.

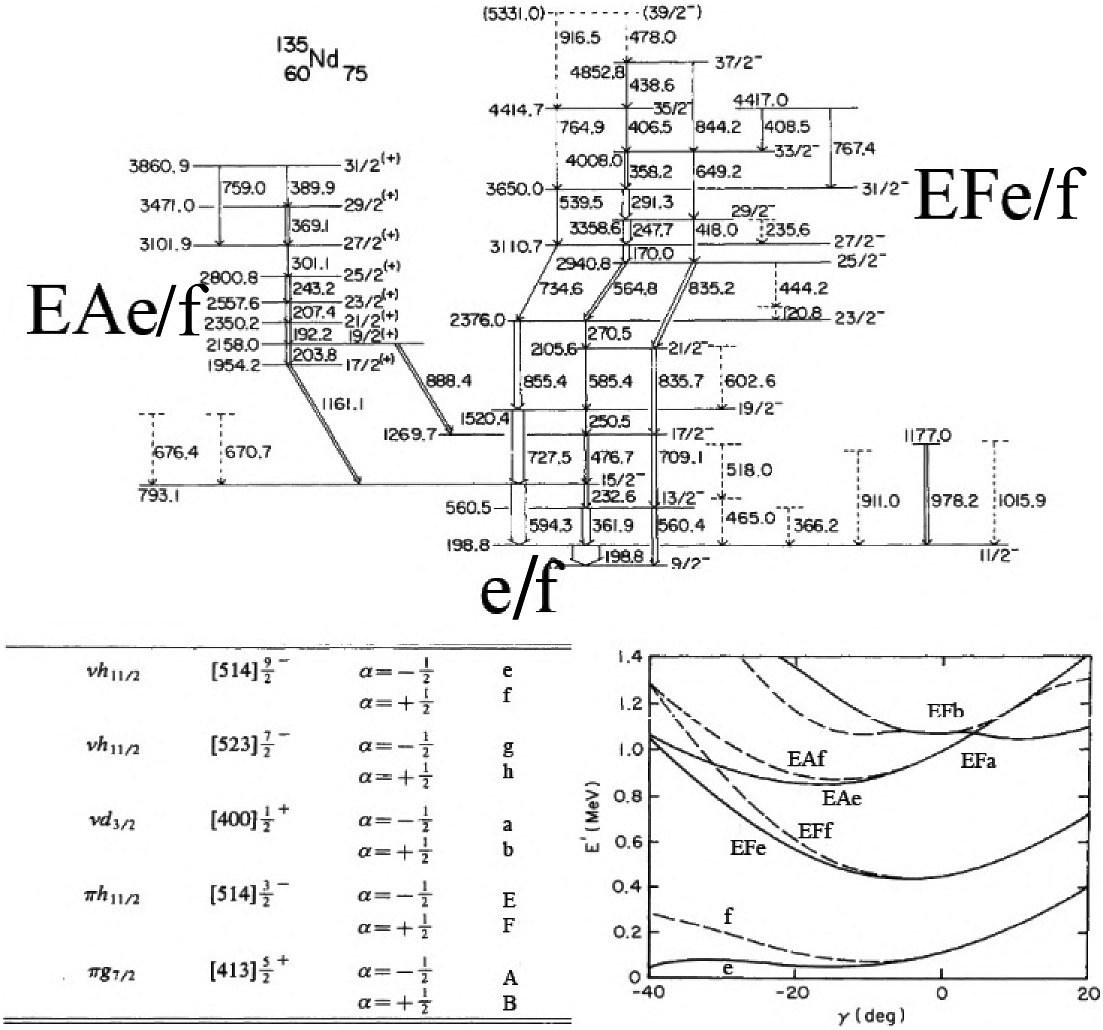

$\nu h_{11/2}$	$[514]\frac{9}{2}^-$	$\alpha=-\frac{1}{2}$	e
		$\alpha=+\frac{1}{2}$	f
$\nu h_{11/2}$	$[523]\frac{7}{2}^-$	$\alpha=-\frac{1}{2}$	g
		$\alpha=+\frac{1}{2}$	h
$\nu d_{3/2}$	$[400]\frac{1}{2}^+$	$\alpha=-\frac{1}{2}$	a
		$\alpha=+\frac{1}{2}$	b
$\pi h_{11/2}$	$[514]\frac{3}{2}^-$	$\alpha=-\frac{1}{2}$	E
		$\alpha=+\frac{1}{2}$	F
$\pi g_{7/2}$	$[413]\frac{5}{2}^+$	$\alpha=-\frac{1}{2}$	A
		$\alpha=+\frac{1}{2}$	B

135 60 Nd 75
EAe/f
EFe/f
e/f
(5331.0)
(39/2⁻)
916.5
478.0
4852.8
37/2⁻
438.6
4414.7
35/2⁻
4417.0
408.5
764.9
406.5
844.2
33/2⁻
767.4
4008.0
358.2
649.2
3860.9
31/2(+)
759.0
389.9
3650.0
31/2⁻
3471.0
29/2(+)
539.5
291.3
29/2⁻
369.1
3358.6
247.7
418.0
235.6
3101.9
27/2(+)
3110.7
170.0
27/2⁻
301.1
2940.8
25/2⁻
2800.8
25/2(+)
243.2
734.6
564.8
835.2
444.2
2557.6
23/2(+)
207.4
2350.2
21/2(+)
120.8
23/2⁻
192.2
19/2(+)
2376.0
270.5
2158.0
2105.6
21/2⁻
1954.2
203.8
17/2(+)
888.4
855.4
585.4
835.7
602.6
1161.1
1520.4
19/2⁻
250.5
1269.7
17/2⁻
1177.0
676.4
670.7
727.5
476.7
709.1
518.0
15/2⁻
793.1
232.6
13/2⁻
911.0
978.2
1015.9
560.5
594.3
361.9
560.4
465.0
366.2
198.8
198.8
9/2⁻
11/2⁻
E′ (MeV)
γ (deg)
1.4
1.2
1.0
0.8
0.6
0.4
0.2
0
-40
-20
0
20
EFb
EAf
EFa
EAe
EFf
EFe
f
e

FIGURE 4.16: Partial level scheme for ^{135}Nd with the bands labelled by their associated quasiparticles. In The Nilsson levels associated with these quasiparticles are detailed in a tabulated format, alongside a plot of total calculated routhian for each quasiparticle configuration as a function of the triaxiality parameter, γ. The labeling convention has been adapted to match that used in this thesis. Reproduced from [61] with permission.

The band associated with a broken pair of protons (EAe/f) is not isomeric in ^{135}Nd. Though ^{129}Nd's quasiparticle configuration is the same, the underlying Nilsson levels associated with these quasiparticles are not. As previously stated, it is the collective of high-Ω, deformation-aligned orbitals coupling together to produce a large *K* value relative to the band that the decay feeds in to that is needed to produce a K-isomer. For ^{135}Nd, the rotationally aligned

[514]3/2^{+} band does not contribute to the overall K-projection. Furthermore, the rotating nucleus mixes states of "good" K, such that the K value associated with this band is not equal to the J value of the bandhead. Comparison between experimental and theoretical B(M1)/B(E2) ratios for this nucleus utilised an "effective" K-value of <K> = 13/2 to achieve the best agreement between experiment and theory. For ^{129}Nd, all three of the quasiparticles comprising the (EAe/f) quasiparticle configuration assigned to the 21/2^{+} isomer are associated with high-Ω, deformation-aligned orbitals. The coupling of the three particles results in a K value of 21/2, relatively high in comparison to the K values of the one-quasineutron bands it decays into and resulting in the isomeric nature of the bandhead.

Levels associated with the alignment or pair breaking of $h_{11/2}$ nucleons are seen across a range of neodymium nuclides in this mass region. A systematic comparison of these states has been compiled and is displayed in Figure 4.17.

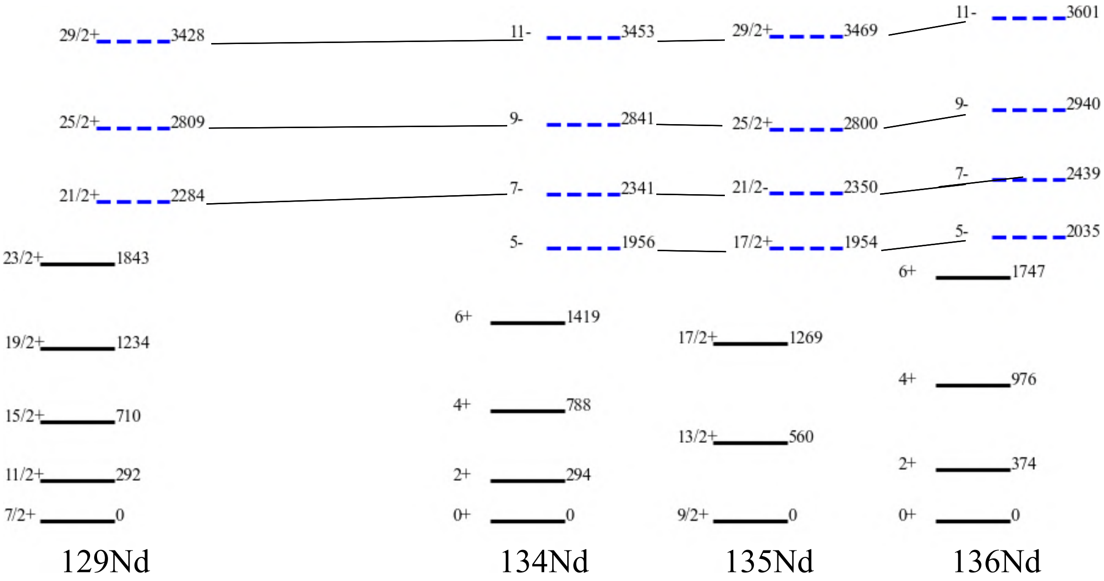
29/2+ 3428
25/2+ 2809
21/2+ 2284
23/2+ 1843
19/2+ 1234
15/2+ 710
11/2+ 292
7/2+ 0
11- 3453
9- 2841
7- 2341
5- 1956
6+ 1419
4+ 788
2+ 294
0+ 0
29/2+ 3469
25/2+ 2800
21/2- 2350
17/2+ 1954
17/2+ 1269
13/2+ 560
9/2+ 0
11- 3601
9- 2940
7- 2439
5- 2035
6+ 1747
4+ 976
2+ 374
0+ 0
129Nd
134Nd
135Nd
136Nd

FIGURE 4.17: Ground-state bands and sidebands associated with the EA (for even-even nuclides) or EAe/f (for odd-even nuclides) quasiparticle configurations for various neodymium isotopes.

For each of the even-even nuclides displayed here, the 5+ states are side-bands associated with the EA configuration. The $17/2^+$ state in ^{135}Nd is then simply the confluence of the EA configuration with the odd quasineutron (EAe/f). The same can be said of the $21/2^+$ (EAe/f) configuration in ^{129}Nd, with the larger Ω values resulting in a higher bandhead spin than its equivalent in ^{135}Nd and the deformation-aligned nature of (EAe/f) orbitals resulting in an isomeric configuration in ^{129}Nd instead of the short-lived states in ^{135}Nd.

4.4.1 Other isomeric states

Assigning any structural configuration to the two levels labelled band 6 and 7 in Figure 4.10 is a difficult task given the lack of experimental information available and any proposed configuration is open to speculation. All of these γ rays are seen in the delayed (1μs) focal-plane γ^2 coincidence matrix. Searches within prompt (JUROGAM) coincidence matrices (γ^2 and γ^3) for the γ-rays depopulating bands 6 and 7 in coincidence with γ-rays within the one-quasineutron bands yielded no significant results that would point to prompt coincidence. Taking into consideration these two facts, it is likely that bands 6 and 7 are isomeric. It was initially considered that the levels were, in fact, part of the same band. However, if the lowest level is isomeric and the level 216 keV above it were part of the same band, we would not expect to see decays out of this higher energy level to the one-quasineutron bands, since such transitions would have to bypass the isomeric bandhead of the lower level. Instead, it is proposed that the levels seen here are two seperate bandheads. Given that they are fed by decays out of band 5's isomeric bandhead, and band 5 is based on a three-quasiparticle structure, it is proposed that bands 6 and 7 are also based on three-quasiparticles. At this point, lack of experimental information about these states opens up the speculative account of the structural configuration of these bandheads. Searches for delayed coincidences between the focal-plane transitions depopulating the bandheads and prompt (JUROGAM) γ rays built on these bandheads yielded no statistically significant results. It is likely that any bands built here are too far away from the yrast line to be significantly populated; the only reason we see the bandheads at all is as a result of their sidefeeding from the decay out of band 5. Focal-plane DCO analysis is not possible since the recoil is no longer moving, preventing definition of a reference axis of direction. Direct half-life measurements of these γ rays was not possible in either the JM06 or M09 data, due to the low number of counts in each photopeak. An upper limit can be placed by the observation that increasing the coincidence window beyond 1 μs for the delayed-coincidence matrix did not result in an increase in statistics for these peaks. Therefore the half-life must be less than 1μs for all transitions involved. The configuration for band 5 was assigned the quasineutron associated with the [523]$7/2^-$ orbital due to this orbital being the closest to the Fermi surface and because of its high-Ω value. Assuming this still holds true, we can simply choose a different shell for the pair broken proton to occupy. With one proton occupying the [404]$9/2^+$ shell, we can place the other proton in one of the [411]$3/2^+$, [413]$5/2^+$, [541]$3/2^-$ or [532]$5/2^-$ shells which, as displayed in Figure 4.15, all remain relatively close together in terms of excitation energy for a broad range of spins. However, there is no reason to suggest that it is not, in fact, the neutron which changes orbital to compose these structures. Indeed, the $21/2^+$ isomer is seen to decay to bands based on three separate neutron orbitals. The next closest neutron orbitals are the [532]$5/2^-$ and [402]$5/2^+$ levels; it is unlikely the [411]$1/2^+$ level is involved since its minimal Ω value would not couple to form a large K value.

To summarise, without experimental information on the multipolarities of the transitions depopulating these states and/or prompt bands built on top of them, it is impossible to make even a tentative proposal for the configuration of these levels. That they depopulate the $21/2^+$ K-isomer and are observed at similar excitation energy hints toward K-isomerism as a likely mechanism for their observed hindrance and, by extension, limits the Nilsson orbitals available for their configuration to mid-Ω levels. However, another isomeric mechanism such as spin-trapping cannot be ruled out.

4.4.2 B(M1)/B(E2) Ratios

Figure 4.18 displays the experimentally determined B(M1)/B(E2) ratios for the rotational band built atop the isomer $21/2^+$ state. It is immediately clear that there is no odd-even staggering (within the bound provided by the error bars), as expected for a non-triaxial axially prolate shape. The weighted average ratio is $(1.8 \pm 0.3)(\mu_N/\mathrm{eb})^2$. An attempt was made to obtain theoretical B(M1)/B(E2) ratios using the semi-classical Donau-Frauendorf geometrical formalism detailed in Chapter 2. The ratios obtained were not found to be consistent with the experimentally measured values. Perpendicular coupling between valence nucleons is appropriate when one particle is rotationally aligned (RAL) and one particle is deformation aligned (DAL). An essential pre-requisite of the formalism is that the J spin vectors of the orbitals comprising a particular band are perpendicular to one another. The proposed configuration for band 5 involves two $h_{11/2}$ orbitals and a $g_{9/2}$ orbital each with mid-to-high Ω values, so do not satisfy the geometrical formalism.

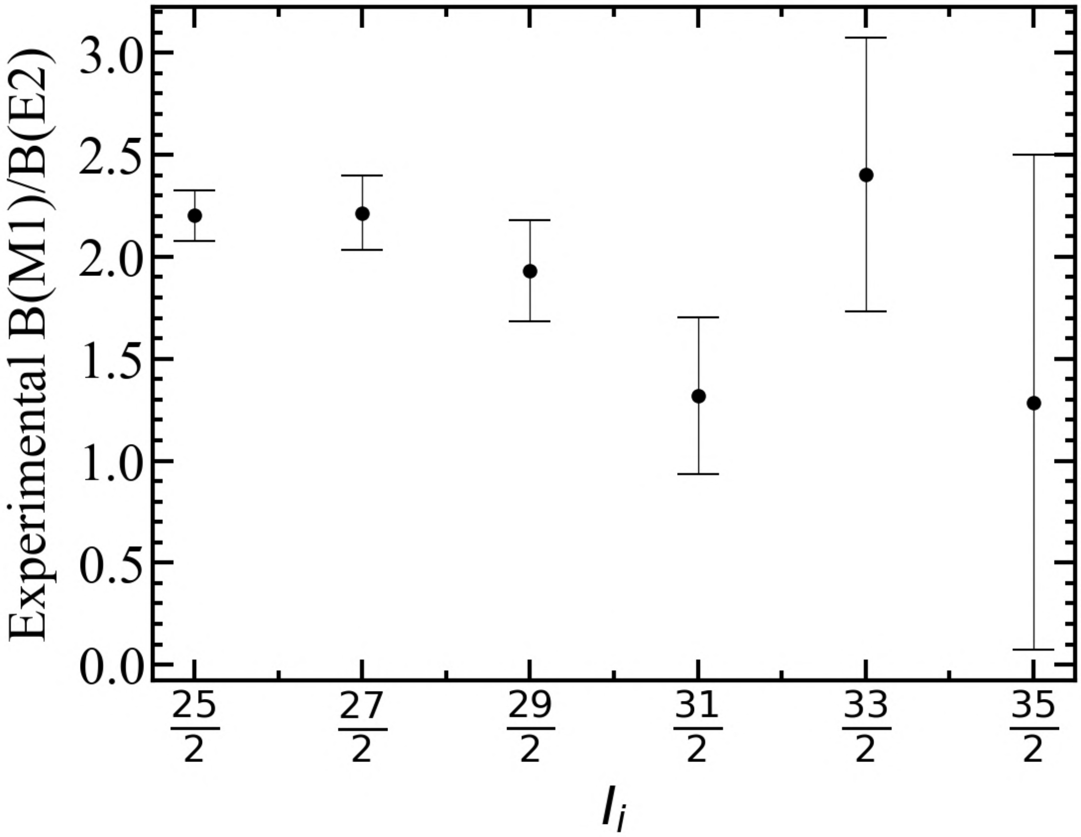

FIGURE 4.18: Experimentally determined B(M1)/B(E2) ratios for the rotational band built atop the isomeric $21/2^+$ state.

Chapter 5

Signature-partner and extensions to the yrast band in $^{131}_{61}$Pm

This chapter presents a study of $^{131}_{61}$Pm, a nucleus that sits in the middle of closed valence shells for both protons and neutrons. Presented here is new work carried out in the study of this nucleus, including band extensions at high and low spin and observation for the first time of the yrast band's signature partner. Reassignment of the yrast structure of this nucleus from [541]$3/2^-$ to [523]$5/2^-$ allows explanation of observed transitions below the previously assigned $11/2^-$ bandhead, in terms of this orbital moving away from the rotationally aligned limit. It is proposed instead that the bandhead has spin/parity $5/2^-$, and the structure of the observed band is investigated within the framework of the Cranked Shell Model. Systematic comparison is made with other odd-Z nuclides in this mass region and predictions are made for various unknown properties in these nuclei. Finally, alternative level schemes are considered assuming that the rotational alignment limit still applies, with the $h_{11/2}$ bandhead retaining its spin/parity assignment of $11/2^-$.

5.1 Previous work

Previously, a single study of the excited states of this nucleus was performed by C.M. Parry, *et al* [62]. Excited states were populated and measured in this nucleus for the first time, with a rotational band — assigned to be built upon Nilsson orbital [541]$3/2^-$ — observed from spin $11/2\hbar$ up to a tentative $47/2\hbar$. Systematic comparisons with other even-N promethium isotopes were made. It was found that the sharpness in single particle alignment smooths out with decreasing neutron number, attributed to the presence of a strong n-p interaction. Experimental data was compared to standard Cranked Shell Model (CSM) calculations and found to be inconsistent with the theoretical predictions. To remedy this, new predictions for proton and neutron alignments, and their respective contributions to the change in dynamic moment of inertia ($\mathcal{J}^{(2)}$), were obtained using extended Total Routhian Surface (TRS) calculations. The theoretical results were in good agreement with experiment, detailing how the alignment gain primarily comes from the alignment of a pair of $h_{11/2}$ neutrons, rather than a pair of protons as previously thought. This extended model was found to be consistent with heavier isotopes, with predicted gains in alignment coming roughly equally from the protons and neutrons. In the present work, comparisons too have been made with various even-N, odd-Z nuclides in the region, with structures attributed to being built upon an odd $h_{11/2}$ proton seen in ^{133}Pm, ^{135}Pm, ^{129}Pr, ^{131}Pr, ^{127}La and ^{129}La, to name but a few. In most of these cases, the $h_{11/2}$ band is seen to decay into a separate positive parity structure built on Nilsson level [411]$3/2^+$ [63, 64, 65].

5.2 Experimental Procedure

The results displayed in this chapter utilise the JM06 dataset. As described in detail throughout chapters 3 and 4, the JM06 experiment benefited from the full JUROGAM array surrounding the target position, but the UoYTube charged-particle detector was not available for event veto. The spectrometer was coupled to the MARA mass spectrometer, focal-plane DSSD and focal-plane HPGe detectors enabling recoil-decay correlation with both particulate and γ radiation. During the JM06 experiment, ^{131}Pm was populated consistently throughout the high and low beam energy portions of the experiment, via the ^{58}Ni(^{78}Kr, αp) reaction, with relative yields in agreement with expectations from the predicted relative yields from the PACE4 calculations displayed in Chapter 1 (Figures 1.1 and 1.2).

5.3 Results

5.3.1 Prompt γ-ray coincidences

In the present study, thirty γ rays belonging to ^{131}Pm were observed, twenty-two for the first time. The level scheme has been extended to a maximum spin $55/2\hbar$ from a minimum spin $5/2\hbar$, with several γ rays observed below the previously assigned $11/2^-$ bandhead. Directional Correlation of Oriented states (DCO) analysis and polarisation measurements were possible for most of these γ rays, allowing quantitative and unambiguous assignment of their multipolarities. These measurements are detailed later in this chapter (Table 5.1) along with the band each γ ray belongs to and their assigned multipolarities. γ-ray linear polarisations were measured utilising the clover detector's sensitivity to Compton scattering as detailed in Chapter 3. Also detailed in Chapter 3, DCO ratios are obtained by measurement of γ-ray intensities at two angular "geometries". γ rays detected in the "central" clover detectors were sorted into a 2D histogram against γ rays detected in the "extreme" angled phase 1 detectors. These matrices are further gated by selection of a single γ ray allowed in any of the detectors. This way, selectivity on a particular transition of interest is greatly improved by reducing background contamination from other decay paths. Furthermore, by allowing the gated γ ray in any detector we effectively "wash out" any subsequent effect on the angular correlations of the other two γ rays, given the isotropic distribution of the JUROGAM spectrometer [66]. For weaker transitions, it proved necessary to dispense with the selective triple-γ method. Instead, γ rays were again sorted into a 2D histogram with clovers against phase 1 detectors. This time, selectivity was improved by making use of MARA's mass resolving power with a matrix being produced for each resolvable mass. γ rays with DCO ratios measured this way are highlighted thusly in the footnote of Table 5.1. It is possible to obtain theoretical DCO ratios obtained for a γ ray of a particular multipolarity when gated on by a γ ray of a particular multipolarity for a particular geometry [47]. Practically, one can obtain reference ratios by gating on γ rays of known multipolarity. Here, we expect values of $\bar{r}_{DCO} = 1.0$ for pure, stretched $(\Delta I = 2)$ quadrupoles and pure, non-stretched $(\Delta I = 0)$ dipoles when gated on by a pure, stretched E2. Similarly, ratios of $\bar{r}_{DCO} = 0.6$ are expected for pure, stretched dipoles when gated by a pure, stretched E2. Ambiguity between the $\bar{r}_{DCO} = 1.0$ γ ray multipolarities can be alleviated when combined with polarisation measurements as detailed in Chapter 3, Figure 3.11.

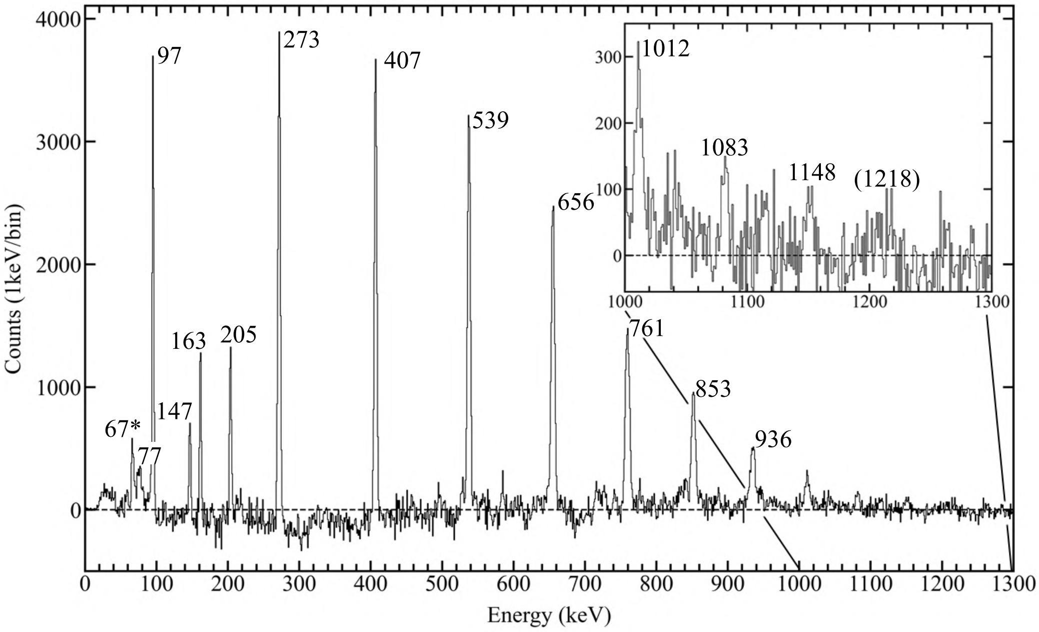

FIGURE 5.1: Sum of doubles gates on triples data using a gate list comprised of the previously known transitions in the yrast band of ^{131}Pm. The yrast rotational cascade is visible, alongside a host of new low-energy transitions. 67 keV is a doublet (66 and 68 keV).

The first γ spectrum for this nucleus is displayed in Figure 5.1. This spectrum consists of a sum of doubles gates on triples data using a gate list the previously known γ rays in this nucleus (all quadrupoles from spin 11/2 to 47/2 in Figure 5.1). This serves two purposes: one, to bring the maximum amount of statistics into each peak for measurement of its centroid (energy) and two, to maximise counting statistics belonging to any peaks at the highest energy range of the spectrum. Indeed, we can see here that several new peaks at the highest energy are observed: 1083 keV (in place of the tentatively assigned 1099 keV γ ray in [62], which is not seen here), 1148 keV and 1218 keV. At the low energy end of the spectrum, several new transitions are brought into stark relief; it is not known if Parry, *et al* [62] observed these since their γ spectrum's axis was truncated below 200 keV. The inconsistent spacing between these γ rays, as well as their varied intensities, provide the first evidence for these transitions not belonging to the yrast $\Delta I = 2$ cascade. This is discussed in greater detail in Section 5.3.2.

The peak at 67 keV is a doublet, and has been assigned as two separate intraband M1 transitions with energies 66 and 68 keV, with the energies of the two bound by the E2 crossovers that flank them. It was not possible to isolate these peaks individually, so direct measurement of their energies was also not possible. Evidence for their placement is displayed in Figure 5.2, where clear evidence of a 67 keV transition is seen in coincidence with the 205 keV intraband M1, and 407 keV. As expected, we don't see 273 keV or 271 keV which cascades in parallel with 205 keV — but we do see γ rays belonging to both bands 1 and 2 higher up the cascade. Band 2's γ rays are present owing to the near identical energy of the 408/406 keV transitions belonging to bands 1/2. An attempt to gate directly on a 67 keV γ ray is also made here; only evidence of the 97 keV and 407 keV transitions are seen due to the low intensity of the 67 keV transition. Indeed, the total internal conversion coefficient for a 67 keV M1 is quite high: 4.91 according to calculations made using BRICC [67].

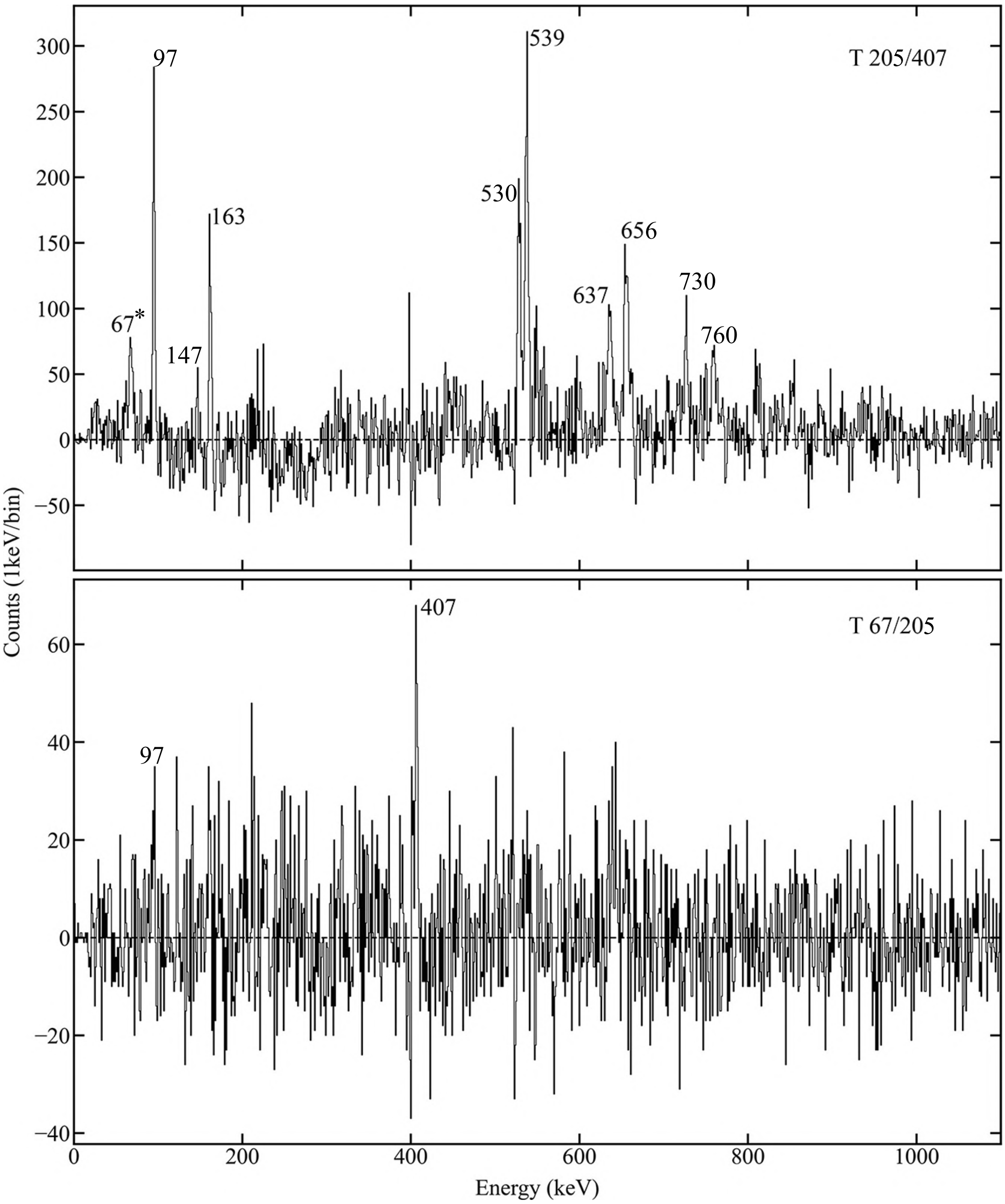

FIGURE 5.2: Top: γ rays observed in coincidence with 205 and 407 keV. Here, the presence of the 67 keV intraband γ ray is clearly displayed along with a myriad of other γ rays belonging to ^{131}Pm. Bottom: An attempt to gate directly on 67 keV only results in evidence of the 97 keV and 407 keV peaks. This is due to the low level of counting statistics associated with the 67 keV γ ray.

Now we turn our attention to the signature partner band. The process detailing the spectroscopy of this band is broadly summarised in Figure 5.4. Gating on the 97 keV and 273 keV transitions (Figure 5.4, first row), hints of the signature partner are immediately obvious - manifesting as a series of less intense photopeaks running alongside those of the yrast band. Here, the 338 keV M1 depopulating the $17/2^-$ state is visible, alongside the 530, 637 and 811 keV E2s that cascade above this state. Gating on members of this band highlighted a problem: both bands seemed to house a "407 keV" transition. By utilising gates that exclusively highlight the γ ray belonging its respective band, it was possible to measure the individual energies of each γ ray. Figure 5.4, row two details this process. The yrast band was gated via 97 keV and 273 keV. This transition pair bypasses the "407 keV" transition in the signature partner, projecting only the "407 keV" transition in the yrast cascade. In a similar vein, the transition in the signature partner band was isolated using a gate on 205 keV and 530 keV. These peaks were fitted with a model composing a single term gaussian superimposed on a linear background. The measured centroid energies are 406.2 keV (signature partner) and 407.7 keV (yrast), yielding an energy difference of approximately 1.5 keV. Ambiguity alleviated, the next step is to measure the intraband M1s depopulating the signature partner band. This was achieved in the first instance by a sum of doubles gates, with list "A" comprising (97, 273, 408, 539 and 656) and list "B" comprising (406, 530, 637, 730 and 811). It is already known from Figure 5.4, first row, that the M1 linking the $17/2^-$ and $15/2^-$ transitions has an energy of 338 keV. "Anchoring" the signature partner band this way allows us to infer the other intraband γ ray energies by measuring the relative difference between $\Delta I = 1$ levels, yielding predicted energies of 205, 460, and 559 keV for the $13/2^- \rightarrow 11/2^-$, $21/2^- \rightarrow 19/2^-$ and $25/2^- \rightarrow 23/2^-$ transitions, respectively. Figure 5.4, row three, shows that transitions of these energies are observed experimentally, highlighted in bold in the figure. Further evidence for these γ rays is detailed in Figure 5.4, row four, where doubles gates on the E2s preceding and proceeding the M1 are displayed. Evidence for 205, 338 and 460 keV is displayed, but the results for 559 keV rendered statistically insignificant counts, so is not displayed here. Finally, a sum of gates across all transitions in the signature partner band is displayed in Figure 5.4, row five. As for the yrast band, this serves to maximise the number of counts observed in each peak for the highest precision centroid measurement and aid with observation of high-energy γ rays.

Evidence of these γ-rays indeed belonging to ^{131}Pm comes from direct measurement of the mass of the recoil associated with these γ rays. Figure 5.3 displays the MWPC-x coordinate of these recoils against the measured γ-ray energy at JUROGAM. Clusters at 97, 273, 408, 539 and 656 keV all line up between MWPC coordinates 1988-2056 and 2460-2524, ranges associated with mass 127/131 recoils for charge states 4+ and 5+, respectively.

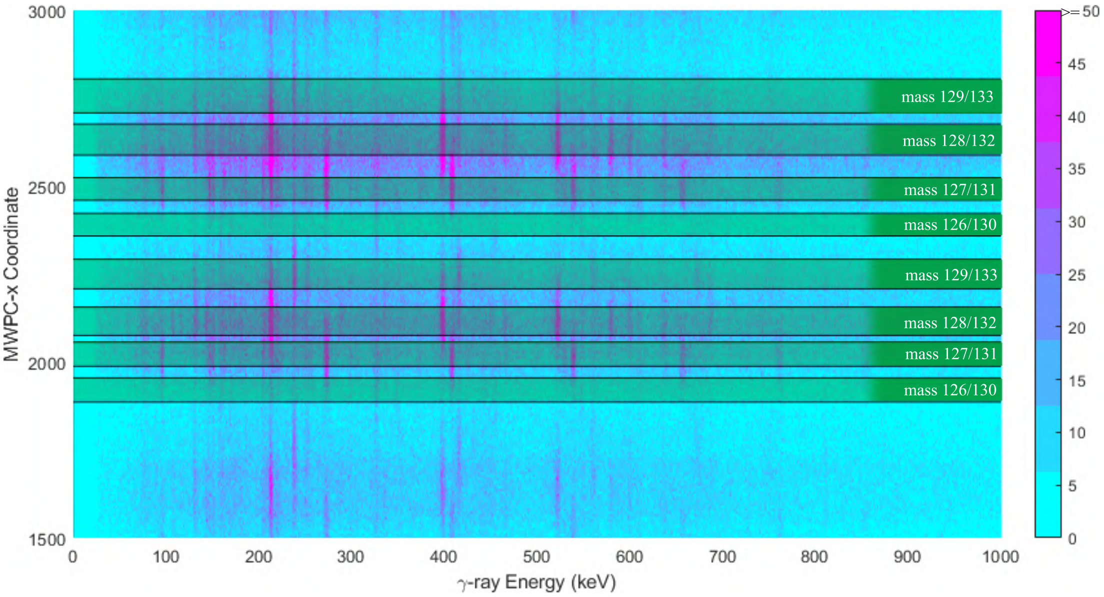

FIGURE 5.3: MWPC-x coordinate against γ-ray energy for all recoils associated with γ rays observed in the decay of ^{131}Pm. MWPC coordinate ranges corresponding to different masses are highlighted.

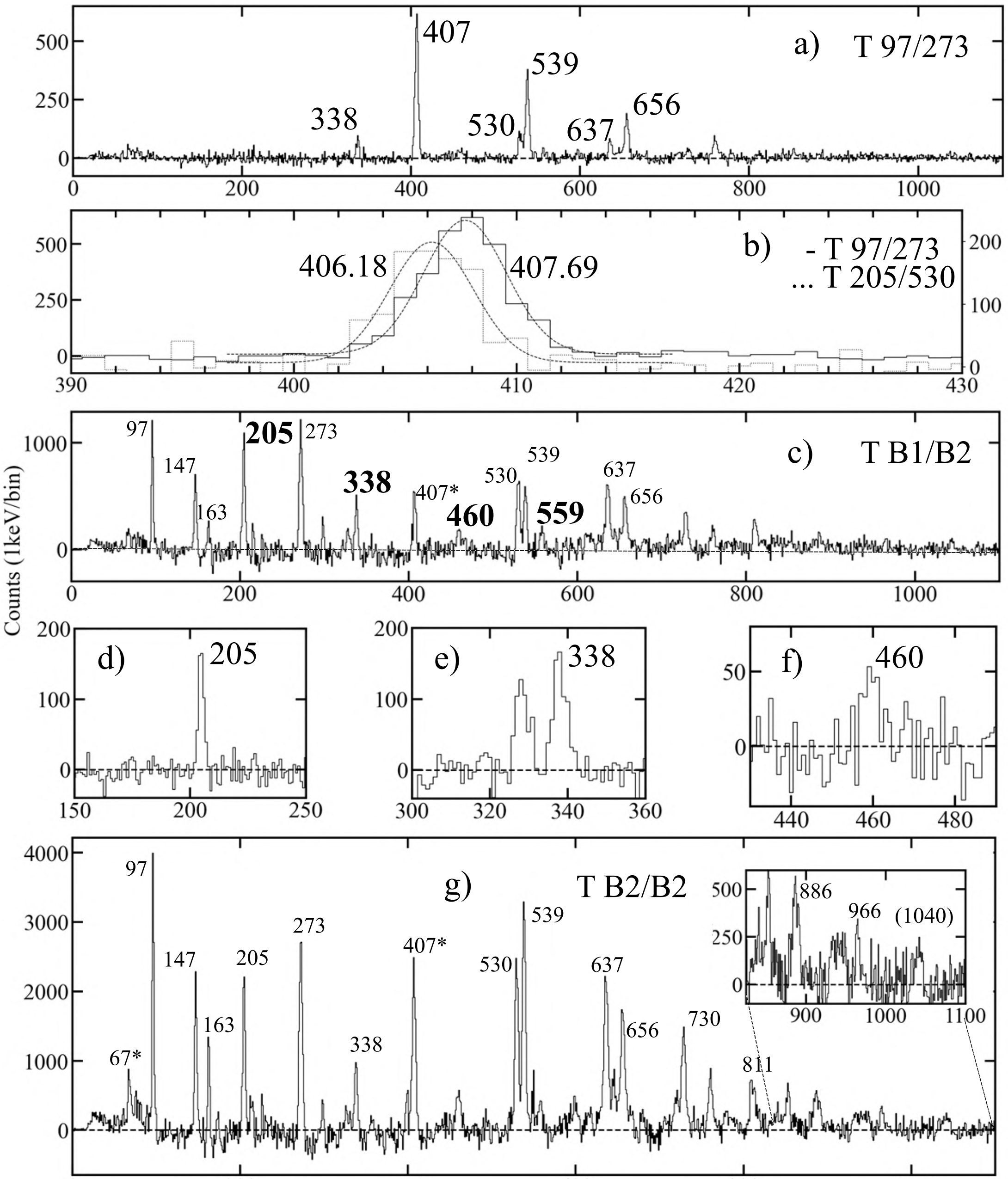

FIGURE 5.4: Panel a): γ rays in coincidence with 97 and 273 keV. Immediately the signature partner can be noticed as a series of peaks running alongside the known yrast peaks. Panel b): measured photopeak centroids for the ≈407 keV peak belonging to each band. The solid line and left-hand y-axis details the peak belonging to the yrast band. The dotted line and right-hand y-axis details the peak belonging to the signature partner. The statistical uncertainty on the yrast/signature partner photopeak centroid is 0.05 and 0.02 keV, respectively. χ^2/NDF for each fit is 8.3 and 2.4. Panel c): sum of doubles gates, with list "A" comprising the lowest five E2 transitions in the yrast band (including 97 keV) and list "B" comprising the lowest five E2 members of the signature partner. Intraband M1s observed here are highlighted in bold text. Panel d): γ rays in coincidence with 97 and 406 keV, highlighting the 205 keV M1 transition between the $13/2^- \rightarrow 11/2^-$ states. Panel e): γ rays in coincidence with 273 and 530 keV, highlighting the 338 keV M1 transition between the $17/2^- \rightarrow 15/2^-$ states. Panel f): γ rays in coincidence with 408 and 637 keV, highlighting the 460 keV M1 transition between the $21/2^- \rightarrow 19/2^-$ states. Panel g): Sum of doubles gates across all transitions in the signature partner band. In panels a), c) and g) 67 keV and 407 keV are doublets as described in the text body.

5.3.2 Extending Below the 11/2$^-$ Level

In the previous study for this nucleus, conducted by C. Parry, *et al* [62], the $11/2^-$ level was assigned as the bandhead — a likely consequence of the non-observation of transitions below 200 keV. Systematic studies of other odd-proton nuclides in the mass region also support this assignment, as detailed in Section 5.4. Parry, *et al*, have the yrast band for this nucleus built on the [541]$3/2^-$ level. The low-Ω value for this orbital justifies the $11/2^-$ spin assignment to the bandhead since the projection of the nuclear-spin along the deformation axis is well within the rotationally aligned limit. However, this work assigns the odd-proton orbital as the mid-Ω [532]$5/2^-$ level. This orbital can no longer be described as rotationally aligned, so the prescription of the bandhead $I^\pi = J^\pi = 11/2^-$ does not apply. The following analysis is presented assuming that the deformation aligned limit applies, prescribing $I^\pi = K^\pi = 5/2^-$ for the bandhead of the observed rotational band. An alternative scenario presuming this assignment is incorrect is detailed in Section 5.6. As displayed in the level scheme for this nucleus (Figure 5.10), the $11/2^-$ level is depopulated by several γ rays which are observed to cascade in parallel to one another (97, 147 and 163 keV), as well as a 66 keV transition which is in coincidence with 97 keV and tentatively in coincidence with 147 keV. The centroid energies of these γ rays were measured using the sum of gates spectrum in Figure 5.1. γ-triples analysis was performed to ascertain the level ordering. 97, 147 and 163 keV in coincidence with 273 keV projects the remaining peaks of the yrast band as detailed in Figure 5.5; all three in coincidence with each other indicates that none of these γ rays "see" each other. Therefore, these γ rays must cascade parallel to one another, and must be below the $11/2^-$ state. Initially, it was proposed that all three γ rays directly depopulate the $11/2^-$ state. However, the observation of coincidence between 66 keV and both 147 and 97 keV (Figures 5.5b, 5.6 and 5.7a) means that 66 keV must feed a level depopulated by both of these other transitions.

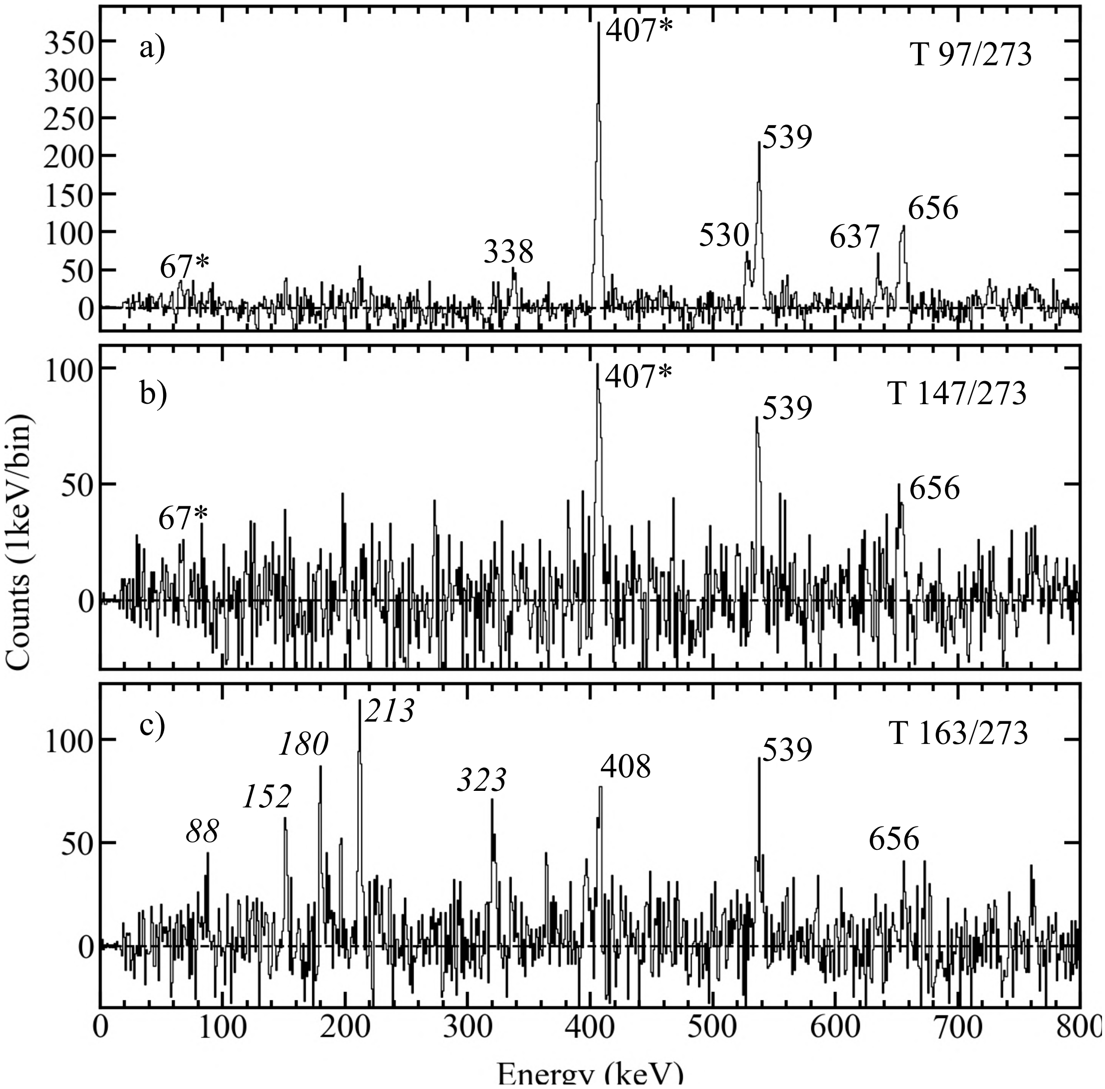

FIGURE 5.5: Panel a): γ rays in coincidence with the 97 keV and 273 keV transitions. Here and in panel b), the 67 keV and 407 keV γ rays are doublets as described in the text. Panel b): γ rays in coincidence with the 147 keV and 273 keV transitions. Panel c): Double-γ gate on triples data on the 163 keV and 273 keV transitions. Contaminant decays not from ^{131}Pm are marked in italic. Here, the 408 keV γ ray is visible without the contamination of the 406 keV γ ray, since the gating transitions of 163 keV and 273 keV cascade in parallel to the 406 keV γ ray.

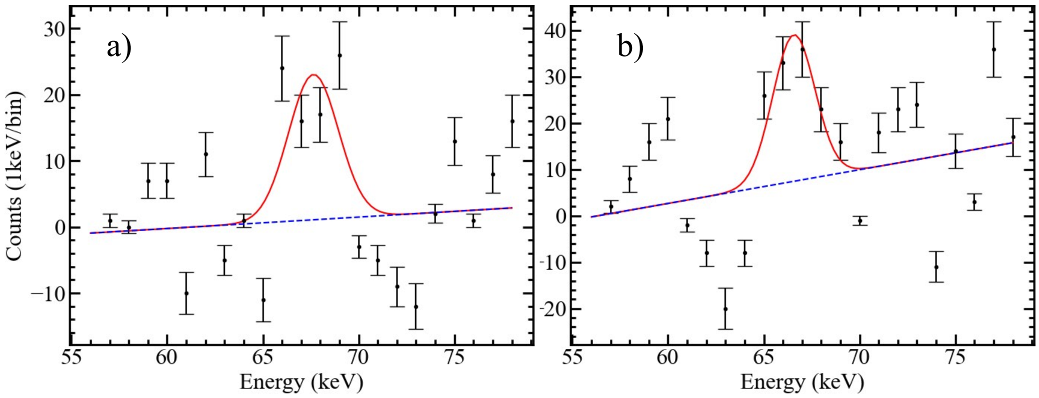

FIGURE 5.6: Panel a): Numerical fit to the 67 keV peak, gated by 147 **and** 273 keV as displayed in Figure 5.5, middle panel. Fit model is a single-term Gaussian overlaid on linear background. Number of counts under the peak is equal to 56 ± 10 after background subtraction. χ^2/NDF = 8.6. Panel b): Numerical fit to the 67 keV peak, gated by 97 **and** 273 keV as displayed in Figure 5.5, top panel. Number of counts under the peak is equal to 110 ± 13 after background subtraction. χ^2/NDF = 10.2.

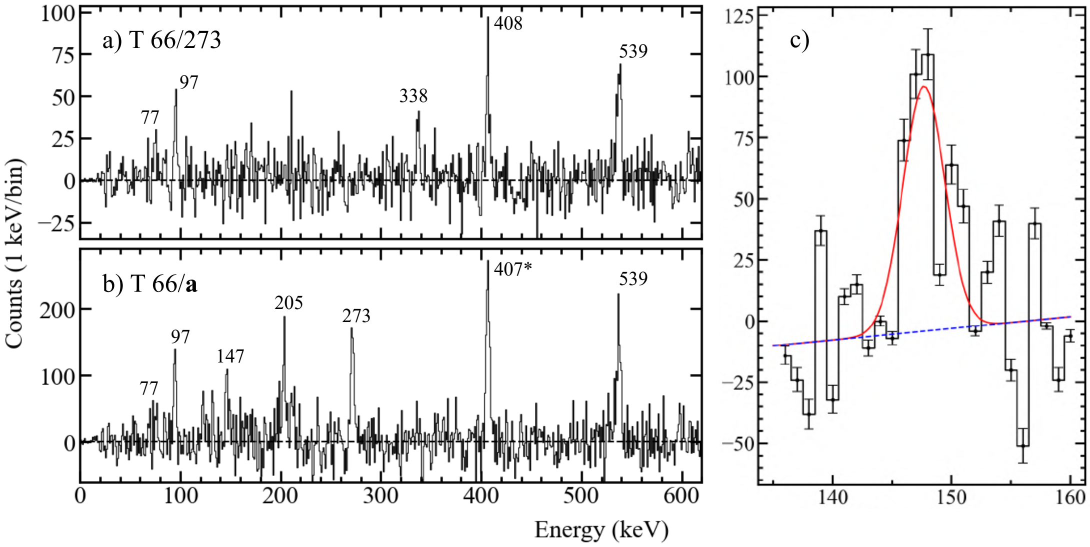

FIGURE 5.7: Panel a): γ rays in coincidence with the 66 keV and 273 keV transitions. Here, the 408 keV γ ray is visible without the contamination of the 406 keV γ ray, since the gating transitions of 66 keV and 273 keV cascade in parallel to the 406 keV γ ray, even considering contamination from 68 and 271 keV. Panel b): Double-γ sum of gates on triples data between 66 keV and a list comprising transitions (205, 273, 408, 539, 650). The purpose for this is to highlight the 147 keV from among background, providing evidence that 66 keV is in coincidence with both 97 and 147 keV. The peak at 407 keV is a doublet, as described in the text. Panel c): Gaussian fit with linear background to the 147 keV peak displayed in panel b). Integrated peak area: 432 ± 238.

A 77 keV transition is observed in coincidence with every other transition, except for 163 keV and 97 keV - which only see γ rays above the $11/2^-$ state. It is not placed in the current level scheme, the reasoning for which is as follows. If a 77 keV transition were in cascade with 66 keV as is necessary to have it coincident with all transitions except 163 keV, this would require a crossover E2 of energy 281 keV between the $13/2^-$ and $9/2^-$ levels, which is not observed experimentally. If it were below 66 keV, the 147 keV transition would be the $11/2^-$ to $7/2^-$ crossover, placing 97 keV either above or below 147 keV, contradictory to the observation that these γ-rays are not coincident. It would also introduce at least one more unit of spin depending on the multipolarity of the 77 keV transition, which would result in the bandhead lying below $5/2^-$, or the other observed transitions would have to be transitions out of the band. This is not a problem in and of itself; the neighbouring odd-Z even-N nucleus, ^{133}Pm, features an experimentally verified $3/2^+$ ground state. Spin/parity assignments are discussed in greater detail in Section 5.5. It could be argued by the same reasoning that 66 keV should be excluded from the level scheme. A 66 keV transition, like the 77 keV transition, is seen in coincidence with every transition except for 163 keV, albeit with greater intensity. The reason 66 keV is included in the level scheme is because its energy matches the difference between 97 and 163 keV, while its placement preserves the mutual exclusivity of 97, 147 and 163 keV. Further experimental evidence for this assignment is provided in Figure 5.8, where coincidence between 97 and 66 keV yields clear evidence of the yrast band, where coincidence between 97 and 77 keV yields no statistically significant photopeaks.

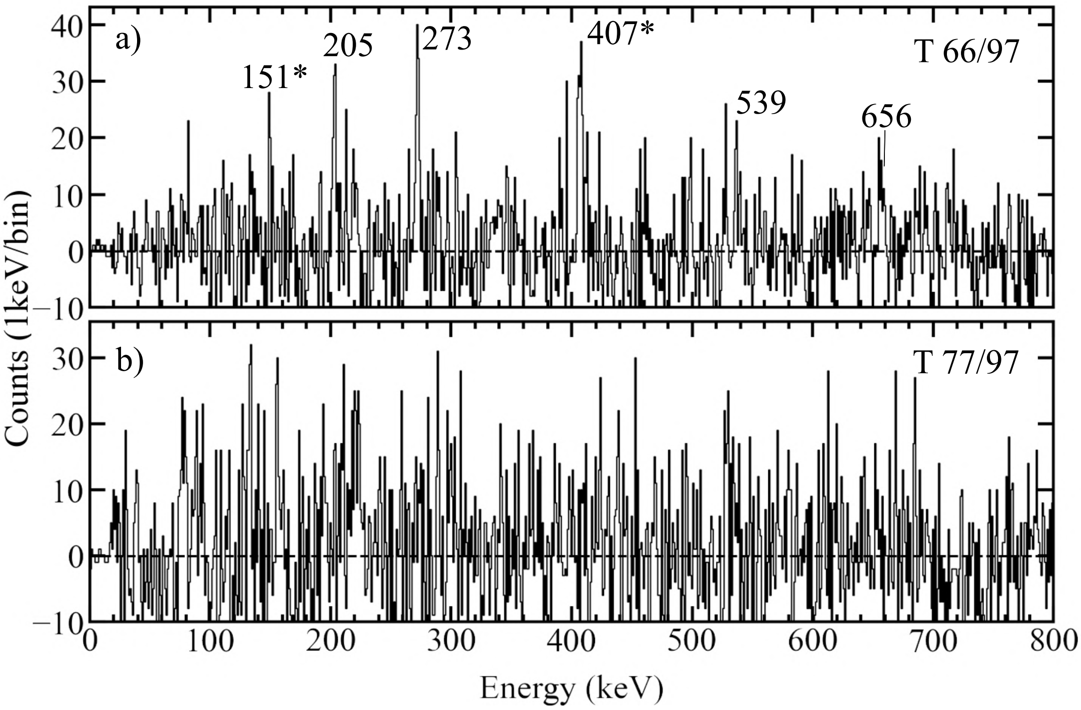

FIGURE 5.8: Panel a): γ rays coincident with 66 keV **and** 97 keV. Evidence for both signatures of the rotational band are observed, providing evidence for the coincidence between 97 keV and 66 keV. Panel b): No γ rays of any statistical significance are observed in coincidence with 77 keV **and** 97 keV. If a transition with energy 77 keV truly belongs to ^{131}Pm, it must be a transition to a level outside of the observed rotational band.

With all of the above reasoning in mind, 147 keV and 163 keV are assigned as crossover E2 transitions between the levels $9/2^-$ and $5/2^-$, and $11/2^-$ and $7/2^-$ respectively. This assignment is consistent with the DCO measurements for these transitions, assigning them quadrupole nature. The 66 keV and 97 keV transitions are then placed as $\Delta I = 1$ transitions cascading in parallel to the 163 keV γ ray. 66 keV has its energy limited by its surrounding transitions to 65.9 keV.

Placement of these transitions implies an E2 crossover transition of energy 271 keV should be present between the $13/2^-$ and $9/2^-$ levels. This assignment is immediately tricky, since the energies of the 271 keV and 406 keV transitions would be very close to the 273 keV and 408 keV γ rays assigned to the yrast band, making difficult the process of uniquely gating on them. Indeed, it has not been discussed in this analysis so far since all of the gated spectra displayed include the influence of the strong 273 keV transition, which would dominate any counts present in coincidence with the 271 keV transition. With that said, evidence can be offered for its existence, as displayed in Figure 5.9. However, before coincidence measurements are analysed, we must first consider background contamination. Though attempts were made to reduce the influence of contaminants by utilising MARA's mass separation capabilities to produce a separate triple-coincidence matrix (cube) for each m/q ratio, it was not possible to eliminate contaminants completely. The biggest contamination comes from ^{131}Nd; since both nuclei are mass 131 we can see that mass gating is no help here. The PACE4 calculations presented in Chapter 1, Figure 1.1, predict ^{131}Nd to be highly populated across both beam energies used in the JM06 experiments. By coincidence, ^{131}Nd shares transitions of near identical energies to ^{131}Pm: 145.9, 405.5, 528.0 and 635.9 keV, making uniquely gating on these energies a challenge.

With these considerations made, we can look at the first doubles gate, set on 147 keV **and** 271 keV. This spectrum, displayed in Figure 5.9, panel a), yields the preferred signature cascade only. However, the transition strength of a 147 keV E2 is low in comparison to that of the 97 keV M1 it would compete with, so this could be attributed to low statistics. The next spectrum gates on 271 keV **and** 406 keV which, as mentioned previously, is tricky because of the close proximity of the gating energies to that of the 273 and 408 keV γ rays. This spectrum yields signs of both the yrast and signature partner bands. Crucially, the signal observed at 530 keV could not be contamination from 273 and 408, since the 406 keV transition cascades in parallel to them both. This is provides strong evidence for a 271 keV transition, distinct from the 273 keV γ ray. The 147 keV E2 is tentatively visible in this spectrum, and a strong 97 keV transition is visible. Again, this is likely a consequence of the transition strength difference. The final spectrum is a double gate on 406 keV

and 530 keV. Here, we see peaks at 97, 147, 205, and 271 keV as expected. The counts at 271 keV are free from contamination from the 273 keV peak, since 406 and 530 keV cascade in parallel to it. However, the intensity of the 147 keV peak is suddenly almost three times that of 97 keV. This can be explained by considering background contamination from ^{131}Nd — 406 keV and 528 keV are strong E2 transitions belonging to the yrast band in this nucleus. 147, 297, and 327 keV are low lying dipoles in ^{131}Nd, causing them to be seen in coincidence with this gate. Since ^{131}Nd and ^{131}Pm have the same mass number, mass gating cannot remove this background.

Finally, the difference between the $7/2^-$ and $5/2^-$ states is assigned a 50 keV M1 transition; a statistically insignificant number of counts are observed at 50 keV in coincidence spectra, so this transition is labelled as tentative. It is hard to observe counts at this low energy due to a combination of factors: x-ray absorbers were installed on JUROGAM resulting in attenuation of low-energy γ rays; the low-energy bound for detector calibration was 81 keV, potentially resulting in mismatched peak centroids for energies below this, and; the internal conversion coefficient for a 50 keV M1 is relatively large at 11.5.

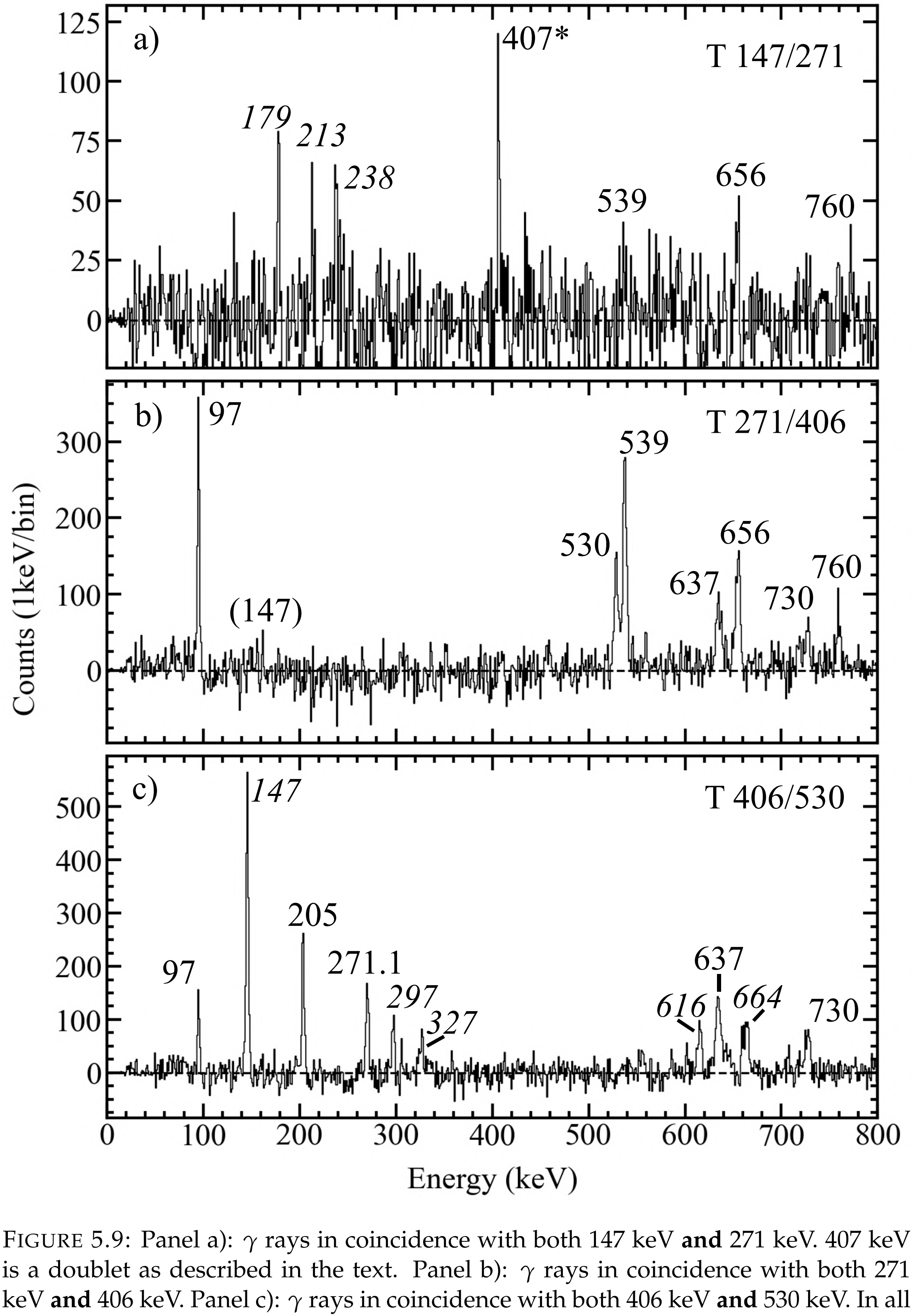

FIGURE 5.9: Panel a): γ rays in coincidence with both 147 keV **and** 271 keV. 407 keV is a doublet as described in the text. Panel b): γ rays in coincidence with both 271 keV **and** 406 keV. Panel c): γ rays in coincidence with both 406 keV **and** 530 keV. In all panels, transitions labelled in italic are contaminants belonging to ^{131}Nd.

TABLE 5.1: List of γ-rays and their measured properties for ^{131}Pm. Quantities in brackets denote uncertainty in the last quoted significant digit. Assigned (λL) values in brackets are tentative.

E_γ, keV [a]	I_γ [b]	$\bar{r}_{DCO}$ [c]	P	(σL)	Band [d]
50(2)[h]	—	—	—	(M1)	1->2
66(2)[h]	—	—	—	(M1)	1->2
68(2)[h]	—	—	—	(M1)	1->2
96.9(1)	—	0.66(5)	—	(M1)	2->1
147.1(1)	—	0.88(6)	—	(E2)	2
162.8(1)	—	1.1(1)	—	(E2)	1
204.7(1)	16	0.63(5)[f]	-1.6(3)	M1	2->1
271.1(1)	10[i]	0.78(4)	—	(E2)	2
272.9(1)	71	0.86(3)	0.2(1)	E2	1
337.8(5)	10	0.6(3)[f]	-1.0(4)	M1	2->1
406.2(6)	100[i]	0.86(5)[f]	0.2(2)	E2	2
407.7(1)	25[i]	0.80(3)	0.2(1)	E2	1
460(1)	—	—	—	(M1)	2->1
529.8(4)	34	0.7(1)	0.4(3)	E2	2
538.6(1)	63	1.0(1)	0.9(3)	E2	1
559(2)	—	—	—	(M1)	2->1
637(1)	8	1.1(1)[f]	0.5(3)	E2	2
656.3(1)	36	1.4(1)	0.05(10)	E2	1
730(1)	15	1.4(2)[f]	1.7(17)[e]	E2	2
760.4(1)	30	1.0(1)	0.6(3)	E2	1
811(1)	—	—	—	(E2)	2
853(1)	14	—	—	(E2)	1
886(1)	—	—	—	(E2)	2
936(1)	9	—	—	(E2)	1
966(1)	—	—	—	(E2)	2
1012(1)	5	—	—	(E2)	1
(1040)(2)	—	—	—	(E2)	2
1083(1)	—	—	—	(E2)	1
1148(1)	—	—	—	(E2)	1
(1218)(2)	—	—	—	(E2)	1

[a] Energy measurement precision quoted representative of the statistical uncertainty in the centroid of a single-term Gaussian fit.
[b] Intensities measured gated by 97 keV and relative to 408 keV. Intensities have not been adjusted for internal conversion.
[c] Apart from where noted, DCOs obtained from a γ-triples matrix of any detector vs clovers vs phase 1s. In all cases the gating γ ray $(E_{\gamma 1})$ was 97 keV except for 147 keV and 97 keV itself, which were both measured using $E_{\gamma 1} = 408$ keV and $E_{\gamma 2/3} = 273$ keV. $E_{\gamma 2/3}$ for all other transitions is then the most intense E2 in that band that isn't the transition itself.
[e] Low statistics cause the uncertainty for this measurement to be large, detailed in Section 5.3.2.
[f] DCO measured using 2D matrix mass gated by mass-131 recoils. Transition of interest gated using 530 keV transition.
[h] Transition's existence implied by the difference between energy levels, but not observed directly due to low statistics at this energy, or ambiguity in gating on this transition.
[i] Counts for this energy include both (271 and 273) / (408 and 406) keV.

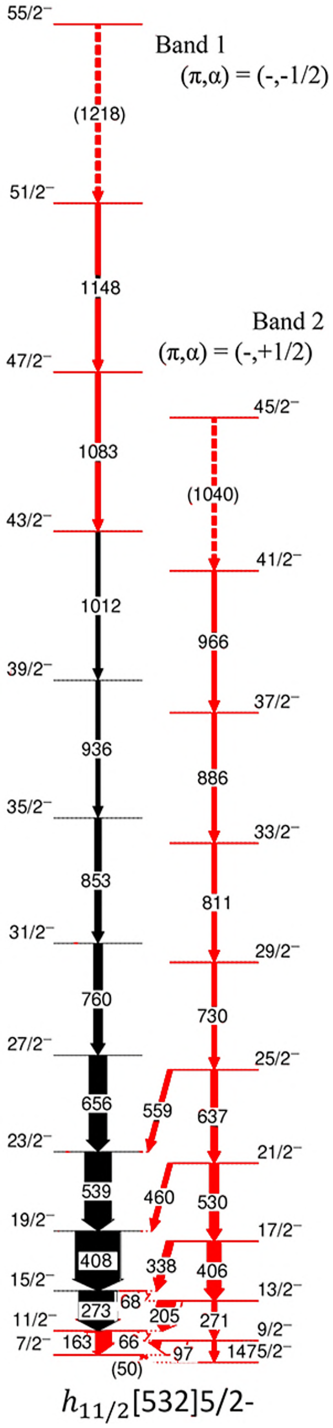
$55/2^-$
Band 1
(π,α) = (-,-1/2)
(1218)
$51/2^-$
1148
Band 2
(π,α) = (-,+1/2)
$47/2^-$
$45/2^-$
1083
(1040)
$43/2^-$
$41/2^-$
1012
966
$39/2^-$
$37/2^-$
936
886
$35/2^-$
$33/2^-$
853
811
$31/2^-$
$29/2^-$
760
730
$27/2^-$
$25/2^-$
656
559
637
$23/2^-$
$21/2^-$
539
460
530
$19/2^-$
$17/2^-$
408
338
406
$15/2^-$
$13/2^-$
68
273
205
271
$11/2^-$
$9/2^-$
$7/2^-$
163
66
97
147
$5/2^-$
(50)
$h_{11/2}[532]5/2$-

FIGURE 5.10: Energy level scheme for ^{131}Pm produced via analysis of double and triple γ ray coincidence matrices. γ rays highlighted in red are new and unobserved before this work. Arrow widths are proportional to the γ ray intensity, with most transitions measured relative to the 97 keV yield. Intensities for transitions not in coincidence with 97 keV have been approximated based on relative peak intensities. Transitions in brackets are tentative and are discussed in more detail in the text body.

5.4 Systematic comparison with other odd-Z even-N Pr, La, Pm and Cs isotopes in the region

TABLE 5.2: Systematic comparison of the relative energy (R.E) level of the $h_{11/2}$ level with respect to the positive parity structure it decays into.

Nucleus	$11/2^-$ R.E (keV)	+parity band-head spin	Isomeric?	γ rays out of the $11/2^-$ level ($\sigma\lambda$)	Notes	Ref
^{123}Cs	151.6	$(1/2^+)$	Yes (1.7s)	61.7 (E3)	-	[68]
^{125}Cs	266.1	$1/2^{(+)}$	Yes (0.9ms)	13 (M2)	-	[69]
^{127}Cs	452.2	$(1/2^+)$	Yes (55μs)	179.3 (M2), 386.3 (E3)	-	[70]
^{129}Cs	575.4	$1/2^+$	Yes (0.72μs)	149(E1), 387(M2), 569(E3)	-	[71]
^{131}Cs	775.28	$5/2^+$	No (10.4ns)	159 (E1), 279 (E1)	-	[71]
^{125}La	8.7	$(3/2^+)$	No decay	N/A	a	[72]
^{127}La	-14.2	$(3/2^+)$	No decay	N/A	a	[72]
^{129}La	172.3	$(3/2^+)$	Yes (0.56 s)	104 (E3)	-	[73]
^{131}La	304.6	$3/2^+$	Yes (170 μS)	109 (M2)	-	[73]
^{133}La	535.6	$5/2^+$	Yes (62 ns)	58 (E1), 405 (M2), 535 (E3)*	-	[73]
^{135}La	785.7	$5/2^+$	No (<20 ns)	202 (E1)	-	[73]
^{129}Pr	382.6	$(3/2^+)$	Yes (unknown)	141 (M2)*, 292 (E3)*	-	[74]
^{131}Pr	152.4	$(3/2^+)$	Yes (5.7 s)	64.8 (E3)	-	[75]
^{133}Pr	192.1	$(3/2^+)$	Yes (1.1 s)	130.4 (E3)	-	[76]
^{135}Pr	358.1	$3/2^+$	Yes (105 μs)	112.6 (M2), 316.6 (E3)	-	[77]
^{137}Pr	561.2	$5/2^+$	Yes (2.7 μs)	331.3 (M2), 563.4 (E3)	-	[78]
^{139}Pr	822	$5/2^+$	Yes (43 ns)	708 (M2), 822 (E3)	-	[79]
^{131}Pm	214^c	-	No (<20 ns)	-	b, c	-
^{133}Pm	129.7	$(3/2^+)$	Yes (8.8 s)	45.2 (E3)*	-	[80]
^{135}Pm	-7	$(5/2^+)$	No decay	N/A	-	[81]
^{137}Pm	-	-	-	-	b	[82]
^{139}Pm	188.7	$(5/2^+)$	Yes (180 ms)	188.7 (E3)	-	[83]

* γ-ray is labelled as tentative.

[a] Energy level of $11/2^-$ state is so low that a γ-decay is either not possible, or not competitive with β-decay.

[b] No positive parity band depopulating the $h_{11/2}$ band has been identified for this nucleus.

[c] The quoted energy is relative to the ground state, which is assumed to be similar to the energy level of the unseen positive parity bandhead.

Most odd-Z even-N nuclides in this mass region have an yrast structure built on an odd $h_{11/2}$ proton, as is the case for ^{131}Pm. It is observed that, in some of these cases, the $11/2^-$ state is isomeric with the nature of isomerism being spin trapping; the $11/2^-$ state is lower in excitation energy than the closest spin state it would otherwise decay into. It is interesting to note that for a few of these nuclides, low and high order multipolarities are competitive with each other. ^{129}Cs is a particularly striking example, with E1, M2 and E3 all depopulating the same state with a half-life of 0.72μs [84]. Here, octopole correlations between the $11/2^-$ and $5/2^+$ states are considered when explaining the enhanced transition strength of the E3. The E1 is hindered by a factor of $\sim 10^7$ compared to the Weisskopf estimate for the transition strength of this multipole. Though some patterns can be picked out from the tabulated form of the data, it is more instructive to look at this data graphically. Figure 5.11 displays the relative energy spacing between the $11/2^-$ bandhead and the positive parity structure it decays in to, for a collective of odd-Z even-N nuclides in the mass-130 region. Relative $11/2^-$ energies for all three of the four nuclei clearly show a parabolic shape. The caesium isotopes show an increase of the spacing with mass number; lack of information for isotopes lighter than mass 123 prevent the extension of this comparison to these nuclides. We would expect the isomeric half-life to increase as relative spacing decreases since this requires γ rays of a higher multipolarity for the decay to occur. As spacing opens up, lower allowed multipolarities allow smaller transition lifetimes. Further insight into factors that might influence or correlate with the half-life of these states is detailed in Figure 5.12.

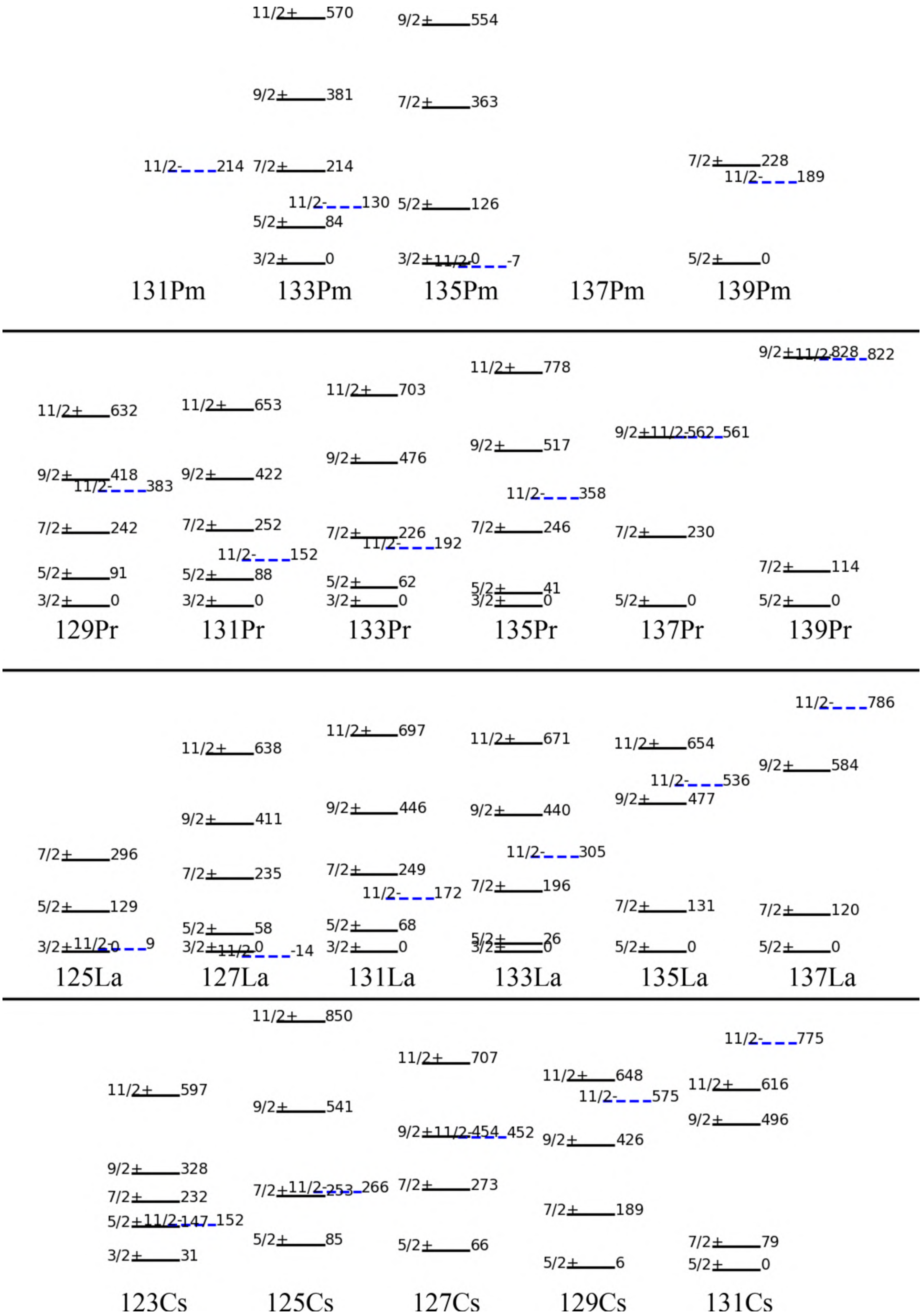
11/2+ 570
9/2+ 554
9/2+ 381
7/2+ 363
11/2- 214
7/2+ 214
7/2+ 228
11/2- 189
11/2- 130
5/2+ 126
5/2+ 84
3/2+ 0
3/2+ 11/2 0 -7
5/2+ 0
131Pm
133Pm
135Pm
137Pm
139Pm
9/2+ 11/2 828 822
11/2+ 778
11/2+ 703
11/2+ 632
11/2+ 653
9/2+ 11/2 562 561
9/2+ 517
9/2+ 476
9/2+ 418
11/2- 383
9/2+ 422
11/2- 358
7/2+ 242
7/2+ 252
7/2+ 226
11/2- 192
7/2+ 246
7/2+ 230
11/2- 152
7/2+ 114
5/2+ 91
5/2+ 88
5/2+ 62
5/2+ 41
3/2+ 0
3/2+ 0
3/2+ 0
3/2+ 0
5/2+ 0
5/2+ 0
129Pr
131Pr
133Pr
135Pr
137Pr
139Pr
11/2- 786
11/2+ 697
11/2+ 671
11/2+ 654
11/2+ 638
9/2+ 584
11/2- 536
9/2+ 477
9/2+ 446
9/2+ 440
9/2+ 411
11/2- 305
7/2+ 296
7/2+ 249
7/2+ 235
11/2- 172
7/2+ 196
5/2+ 129
7/2+ 131
7/2+ 120
5/2+ 58
5/2+ 68
3/2+ 11/2 0 9
3/2+ 11/2 0 -14
3/2+ 0
5/2+ 3/2+ 26 0
5/2+ 0
5/2+ 0
125La
127La
131La
133La
135La
137La
11/2+ 850
11/2- 775
11/2+ 707
11/2+ 648
11/2+ 597
11/2- 575
11/2+ 616
9/2+ 541
9/2+ 496
9/2+ 11/2 454 452
9/2+ 426
9/2+ 328
7/2+ 232
7/2+ 11/2 253 266
7/2+ 273
5/2+ 11/2 147 152
7/2+ 189
5/2+ 85
5/2+ 66
3/2+ 31
7/2+ 79
5/2+ 6
5/2+ 0
123Cs
125Cs
127Cs
129Cs
131Cs

FIGURE 5.11: Systematic comparison of the relative energy spacing between the $h_{11/2}$ level and the positive parity structure it decays into for various odd-Z even-N nuclides in this mass region. ^{131}Pm level assuming ground state is $5/2^-$ level.

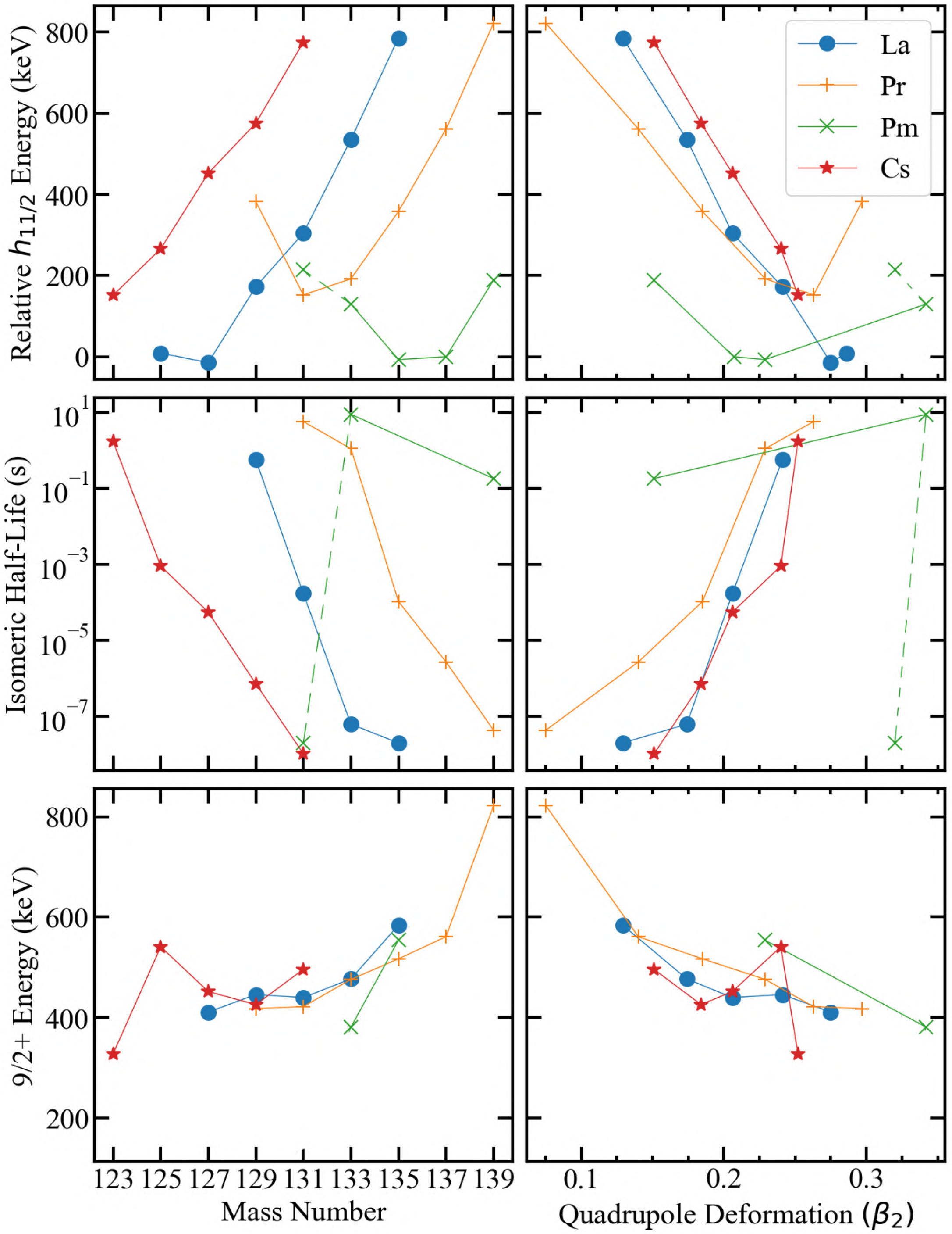

FIGURE 5.12: **Top row**: Relative excitation energy of the $11/2^-$ state for various odd-Z, even-N nuclides plotted as a function of their nuclear mass number, A (left panel), and theoretical ground-state quadrupole deformation, β_2 (right panel). **Middle row**: Isomeric half-life of the $h_{11/2}$ level plotted as a function of mass number, A (left panel), and β_2 (right panel). **Bottom row**: Excitation energy of the $9/2^+$ level for various odd-Z, even-N nuclides plotted as a function of mass number, A (left panel), and β_2 (right panel).

Figure 5.12, top left panel, brings the parabolic pattern of relative $h_{11/2}$ energies into stark relief. The panel underneath this shows the half-life of the isomer as a function of the nuclear mass number, A. The hypothesis that larger relative energy levels lead to shorter half-lives is confirmed here, with the relationship between mass number and the natural logarithm of the half-life being almost linear for caesium, lanthanum and praseodymium. One must not neglect the fact that half-life information is missing for ^{125,127}La, ^{129}Pr and ^{135,137}Pm. If this information were present, we would expect to see the half-life increase again as the relative $h_{11/2}$ energy decreases, reproducing the parabolic shape seen for the $h_{11/2}$ energies. A noteworthy feature of Figure 5.11 is how the lowest positive parity energy levels appear to spread out, increasing in energy with increasing mass. This trend is explored in Figure 5.12, bottom left panel. Here, the energy of the $9/2^+$ level is chosen as representative of this energy spread. The pattern is not as pronounced as the linearity we see for the isomeric half-lives with mass number, but it can be reasonably concluded that the $9/2^+$ energy increases with mass number. It is interesting to note that the parabolic pattern seen for the $11/2^-$ bandheads is not reproduced here. We can also see that the assigned $11/2^-$ bandhead energy of 214keV for ^{131}Pm appears to be in-line with the linear trend for the other promethium isotopes. However, consideration must be made that half-life information is only available for ^{133,139}Pm, and so this linear trend may not be a good indicator of where we expect this bandhead energy to lie.

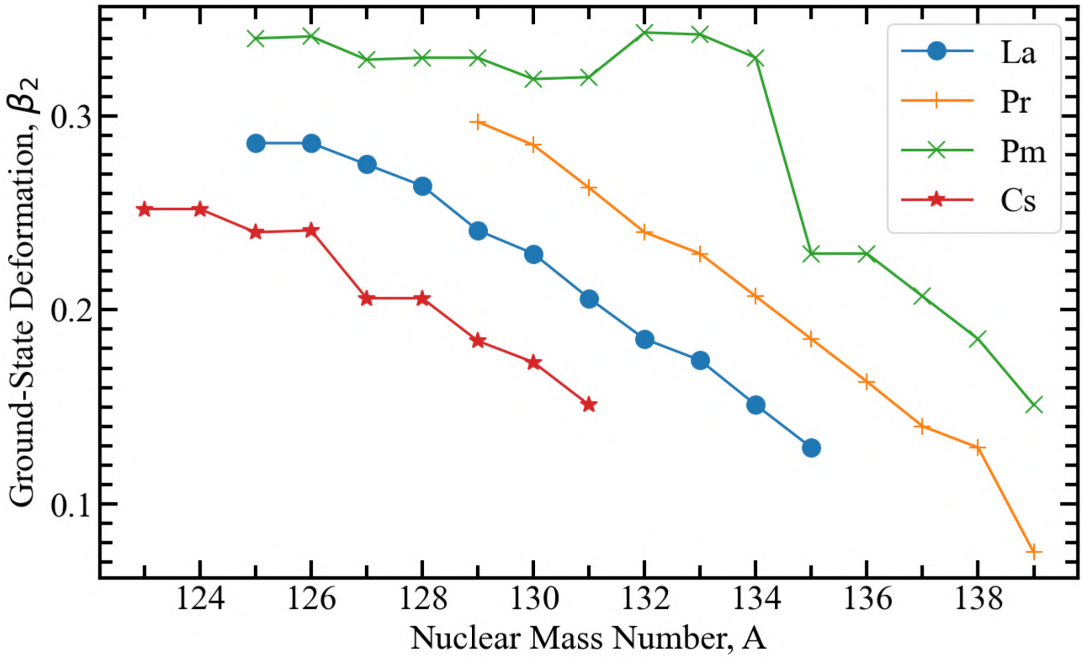

FIGURE 5.13: Theoretical ground-state deformations for various nuclides in the mass-130 region. The ground-state deformations were obtained from Moller, *et al*: Nuclear ground-state masses and deformations [85].

In Figure 5.12, comparisons of the same variables were made against theoretical ground-state deformation, β_2, as well as mass number. The ground-state deformations were obtained from Moller, *et al*: Nuclear ground-state masses and deformations [85]. Here the Strutinsky method is applied, utilising a finite-range droplet model to obtain nuclear bulk properties, with a shell correction obtained from a folded-Yukawa single-particle potential. Overall, for the relative $h_{11/2}$ energies, isomeric half-lives and $9/2^+$ energies, the same patterns are observed as for when they were plotted as a function of nuclear mass. For the $h_{11/2}$ energies (Figure 5.12, top right panel), we obtain a plot that is almost perfectly symmetric with the nuclear masses plot (5.12, top left panel). As neutrons are added, the neutron mass approaches the 82 particle shell gap, and so deformation decreases. An exception appears for our results for ^{131}Pm. Here, the predicted ground state deformation is lower than that for ^{133}Pm, resulting in the parabola turning back on itself like a horseshoe. This observation is contrary to those seen where the variables are plotted as a function of nuclear mass. This can be viewed from several perspectives. The idea that the variables should show the same — albeit symmetrized — pattern when it is plotted as a function of both nuclear mass number and deformation, is predicated on the idea that deformation varies smoothly with mass number. This expectation, however, may be a simplistic one; Moller's predicted ground-state deformations do not vary smoothly with mass for promethium isotopes between A = 120-134 (Figure 5.13). Instead of peaking at a maximum deformation, they oscillate somewhat between β = 0.30-0.34. The masses selected for study for the caesium, praseodymium and lanthanum isotopes are well beyond this oscillatory "maximum", where the deformation once again moves smoothly with mass. Furthermore, to increase the $9/2^{+}$ energy to the approximate 400 keV it would need to be to satisfy these deformation systematics, observation of further transitions summing to $\sim$ 200 keV would be required, and they are not seen in this data. Based on these systematics, loose predictions for the order of magnitude of both the $h_{11/2}$ relative bandhead energy and isomeric half-life are presented in Table 5.3. We can see that the predicted $9/2^{+}$ energy level for ^{131}Pm is similar to the observed 214 keV of the $11/2^{-}$ level for this nucleus. Assuming the positive parity bandhead is $5/2^{+}$, we can see that the energies for the positive and negative parity levels of the same spin will lie at comparable energy. Subsequently, transitions between them will be dramatically hindered by requirement of low transition energy.

TABLE 5.3: Predicted properties for nuclei without experimental measurements for these quantities. Predictions are based on the above systematical comparisons and relationships observed there.

Nucleus	Predicted $h_{11/2}$ relative energy (keV)	Predicted $9/2^+$ energy (keV)	Predicted isomeric half-life (s)
^{131}Pm	-	200	-
^{135}Pm	-	-	No Decay
^{137}Pm	-	700	10^1
^{139}Pm	-	900	-
^{125}Pr	600	400	10^{-6}
^{127}Pr	800	400	10^{-4}
^{129}Pr	-	-	10^0
^{123}La	200	400	10^0
^{125}La	-	400	10^1
^{127}La	-	-	No Decay

5.5 Structure, Alignments and Experimental Routhians

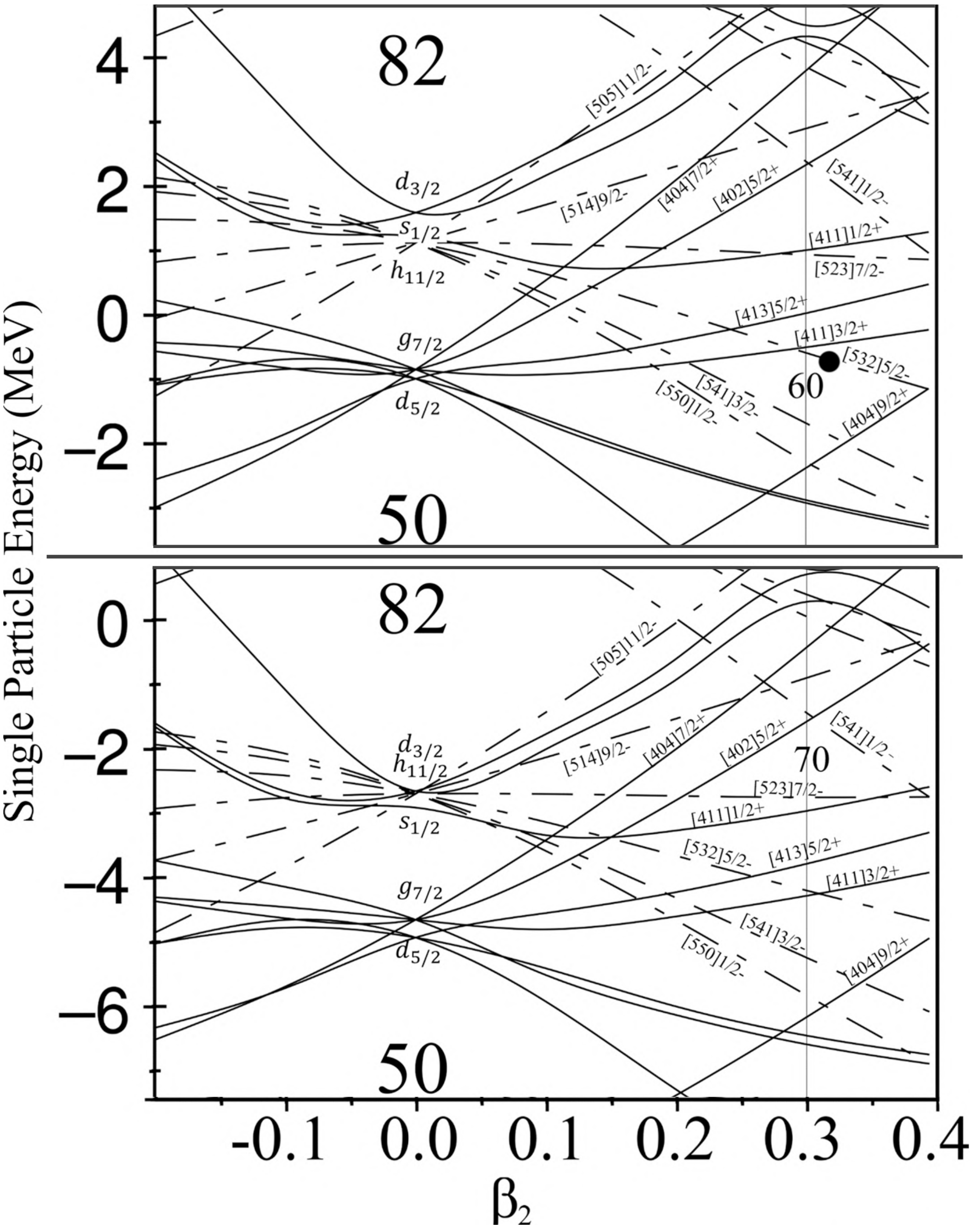

FIGURE 5.14: Nilsson diagram for protons (top) and (neutrons) for prolate deformation only. The deformed shell gap at 60 protons is labelled, along with a vertical line representative of the predicted deformation of ^{131}Pm. The proposed orbital occupied by the odd proton is highlighted with a black dot.

In the study carried out by C. Parry, *et al* [62], the yrast band for ^{131}Pm was assigned to Nilsson level $h_{11/2}[514]3/2^-$. This is contradictory to the level observed in Figure 5.14, where the 61^{st} proton would lie in either the $g_{7/2}[411]3/2^+$ or $h_{11/2}[532]5/2^-$ state. In the present work, a Nilsson diagram generated using a Woods-Saxon potential is used. Older Nilsson diagrams based on a modified harmonic oscillator potential have different relative spacings between shells. The author has been unable to source the diagram used in [62], but speculation can be made. For example, if the relative spacing between the $h_{11/2}$ shell and the $g_{7/2}, s_{1/2}$ shells is increased (which is not unreasonable since they originate from different principal quantum number states 5 and 4, respectively), then it is likely that the $[413]5/2^+$ and/or $[411]3/2^+$ levels would lie below $[514]3/2^-$. This would result in the 61^{st} proton lying in the $[514]3/2^-$ state. Since the Woods-Saxon Nilsson diagram does not rely on empirical κ and μ parameters for each major shell number, it is proposed that the yrast band for this structure is built on the $h_{11/2}[532]5/2^-$ level.

A systematic survey (presented in Section 5.4) of the excited states for odd-even nuclides in this mass region was performed. No nuclides were found to have an $h_{11/2}$ band with its bandhead spin/parity equal to K^π; all bands are assigned a bandhead spin/parity of $11/2^-$. However, all of these nuclides have a smaller predicted deformation than ^{131}Pm, resulting in the $[541]3/2^-$ level lying closer to the Fermi surface. Work performed by S. Xu, *et al*, studying the decay of highly deformed neighbour ^{129}Pm predict a ground-state for this nucleus of $5/2^-$, based on observations of its decay into a 5/2 low-lying state in the daughter nucleus ^{129}Nd via the (EC $+\beta_+$) decay [86]. These experimental findings are compounded by theoretical predictions presented by Moller, *et al*, which have the ground state spin/parity for both ^{129}Pm and ^{131}Pm as $5/2^-$ [87, 88]. Since the predicted [85] ground-state deformations, β_2, are similar for both nuclei (0.30 and 0.29, respectively), it is reasonable to assume that the experimental findings for the ^{129}Pm's ground state apply to ^{131}Pm also.

As described in the introduction to this chapter, it is known that the observed increase in alignment for this nucleus comes primarily from the alignment of a pair of $h_{11/2}$ neutrons - contrary to the predictions of the Cranked Shell Model (CSM). Experimental single particle alignment (i_x), dynamic moment of inertia $\mathcal{J}^{(2)}$ and routhian (e') have been calculated for both bands and are displayed in Figure 5.1. The following discussion will make comparisons between the experimental single-particle alignments and routhians displayed in Figure 5.15, and theoretical CSM routhians displayed in Figure 5.16, calculated using a Woods-Saxon potential [21, 89]. Measured alignment gain is of the order $2\hbar$, in agreement with [62]. Figure 5.1 displays evidence for transitions between the regularly spaced rotational transitions. The extended CSM calculations carried out by Parry, *et al*, predict a large gain in alignment at $\hbar\omega \approx 0.58$ MeV from the alignment of a second pair of $h_{11/2}$ neutrons. It is possible this alignment is being observed here but it can't be said for certain without measurements at high spin.

Success for the Cranked Shell Model is seen when comparing the experimental and theoretical routhians for this nucleus. Experimental signature splitting is minimal at low spin, gradually increasing to a measured signature splitting of 0.22 MeV. The CSM results for protons (Figure 5.16, top panel) reproduce this behaviour almost exactly, with signature splitting gradually increasing to a value of ≈ 0.25 MeV. Comparisons between the theoretical and experimental routhians allow assignment of (π, α) numbers to the bands in Figure 5.10, as well as confirming the assignment of the Nilsson bandhead as $h_{11/2}[532]5/2^-$. The configuration introduces a signature inversion at low spin; the "signature partner" becomes yrast at low spin. This can be seen in the bottom panel of Figure 5.15 as the lines representing the two bands tend toward each other. This is not a problem in and of itself since a small degree of triaxiality would result in such an inversion, and triaxiality is common in this region of γ-soft nuclei [90].

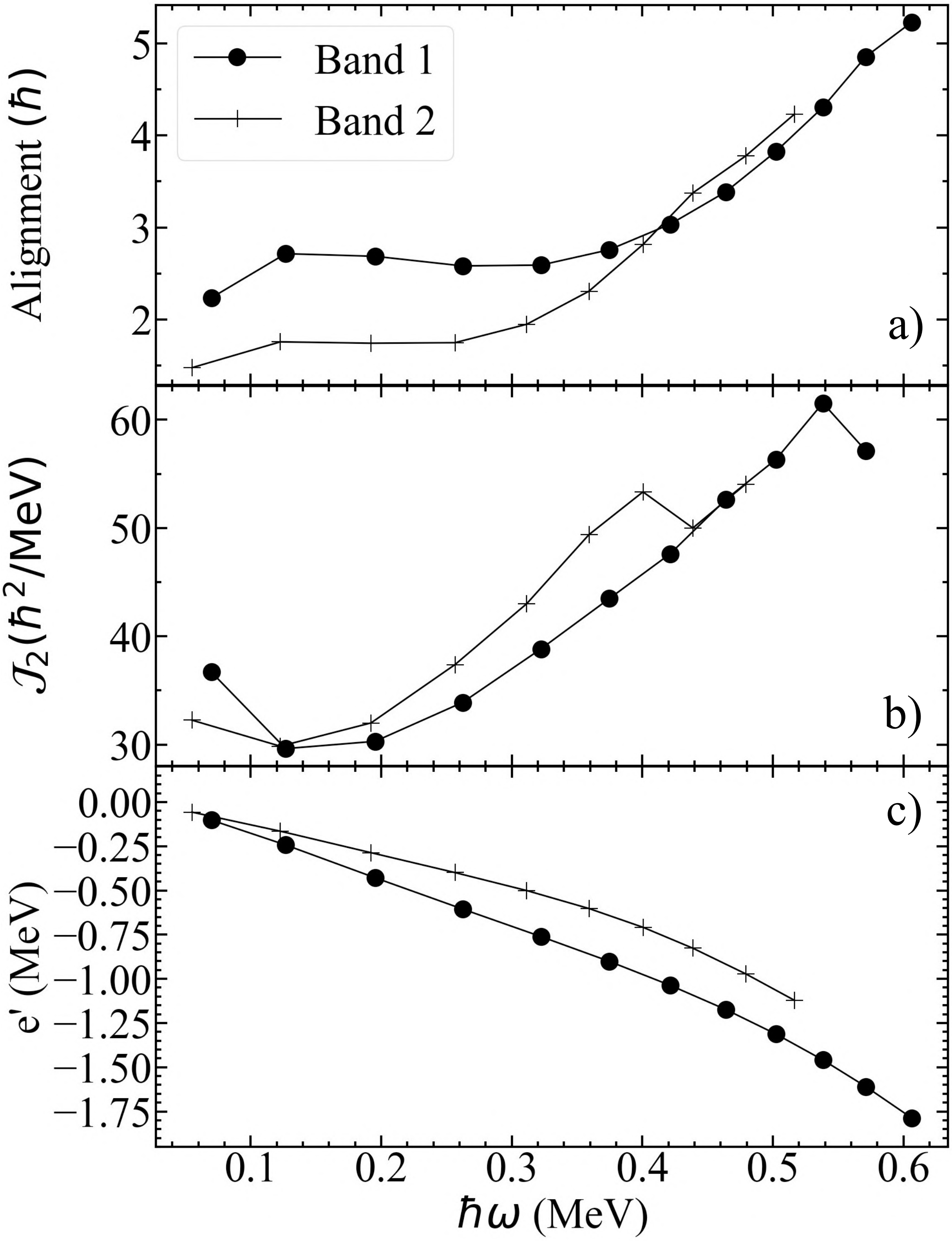

FIGURE 5.15: All figures: solid circles represent the yrast band and crosses represent its signature partner. Harris parameters used in production of this figure, $\mathcal{J}_1 = 29.9\ \hbar^2/\mathrm{MeV}$ and $\mathcal{J}_1 = 15.8\ \hbar^4/\mathrm{MeV}^3$. Panel a): experimental single particle alignment. Panel b): experimental dynamic moment of inertia. Panel c): experimental routhian.

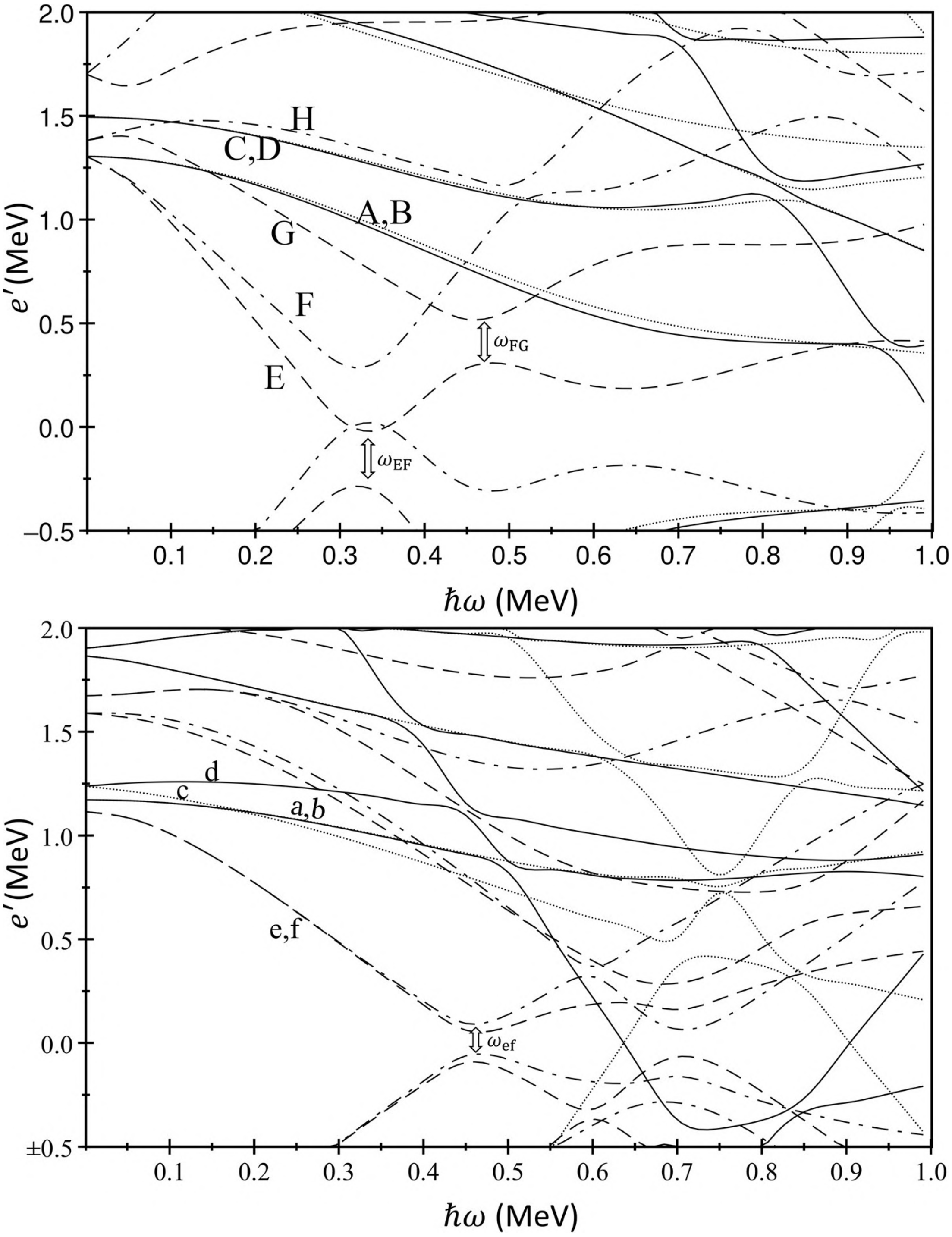

FIGURE 5.16: Cranked Shell Model quasiparticle Routhians (top: protons, bottom: neutrons), generated using a universal, triaxial Woods-Saxon potential. Labels corresponding to Nilsson levels are only valid at zero spin (i.e 0 $\hbar\omega$) since rotation causes states to become a mixture of different wavefunctions. β_2= 0.320, β_4 = 0.0, γ= 0.0°. (π, α) : solid = (+,+1/2), dotted = (+,–1/2), dot–dash = (–,+1/2), dashed = (–,–1/2).

TABLE 5.4: Quasiparticle labelling scheme for ^{131}Pm along with their assigned Nilsson configuration at zero rotational frequency.

Label	$(\pi, \alpha)^a_n$	Configuration^b
	Quasiprotons	
A	$(+, +1/2)_1$	$d_{5/2}[411]3/2^+$
B	$(+, -1/2)_1$	$d_{5/2}[411]3/2^+$
C	$(+, -1/2)_2$	$g_{7/2}[413]5/2^+$
D	$(+, +1/2)_2$	$g_{7/2}[413]5/2^+$
E	$(-, -1/2)_1$	$h_{11/2}[532]5/2^-$
F	$(-, +1/2)_1$	$h_{11/2}[532]5/2^-$
G	$(-, -1/2)_2$	$h_{11/2}[541]3/2^-$
H	$(-, +1/2)_2$	$h_{11/2}[541]3/2^-$
	Quasineutrons	
a	$(+, -1/2)_1$	$g_{7/2}[402]5/2^+$
b	$(+, +1/2)_1$	$g_{7/2}[402]5/2^+$
c	$(+, +1/2)_2$	$s_{1/2}/d_{3/2}[411]1/2^+$
d	$(+, -1/2)_2$	$s_{1/2}/d_{3/2}[411]1/2^+$
e	$(-, -1/2)_1$	$h_{11/2}[523]7/2^-$
f	$(-, +1/2)_1$	$h_{11/2}[523]7/2^-$
g	$(-, -1/2)_2$	$f_{7/2}[541]1/2^-$
h	$(-, +1/2)_2$	$f_{7/2}[541]1/2^-$

[a] The subscript n numbers the quasiparticle's excitations of a given signature and parity starting with the lowest in energy at $\hbar\omega$ = 0 MeV.
[b] Nilsson configurations only valid at $\hbar\omega$ = 0 MeV.

Figure 5.15, top row, indicates that alignment effects start to be observed at $\hbar\omega = 0.45$ MeV. It is predicted here that the proton ω_{FG} and neutron ω_{ef} crossings occur at roughly the same frequency: $\hbar\omega \approx 0.4$ MeV. This is contradictory to the calculations performed by C. Parry, *et al.* However, this does not challenge their main conclusion: that contributions toward the total alignment comes from both protons and neutrons, with the majority coming from the neutrons. Indeed, all that could be concluded from this work alone is that the CSM leaves ambiguity concerning where the gain in alignment comes from, as a result of the lack of a unique crossing frequency.

5.6 Other Considered Level Schemes

Throughout the analysis of the coincidence data, some doubt was cast over the ordering and structural assignments given to the lowest energy transitions belonging to this nucleus. An example is the ordering of the 66 and 147 keV γ rays. In the previous section evidence was presented for a statistically significant level of counts for a 66 keV transition in prompt coincidence with both 97 and 147 keV. Within this section, alternative schemes are proposed assuming this relationship is false, specifically that 66 keV and 147 keV do not decay in cascade. An essential prerequisite to the analysis presented in the previous section is that the projection along the deformation axis of the single-particle angular momentum, Ω, is large (enough) in comparison to the total angular momentum of the state, J, that the rotationally aligned limit no longer applies. The orbital assigned to the odd $h_{11/2}$ proton throughout this analysis has been the [532]$5/2^-$ level. The Ω value for this level places the spin projection somewhere in the middle of two extremes: neither deformation or rotationally aligned. The analysis presented in this chapter assumes that the rotationally aligned regime no longer applies; the bandhead of the yrast cascade is given by $I^\pi = K^\pi = 5/2^-$. This hypothesis is supported by experimental determination of odd-even neighbour ^{129}Pm's ground state as $5/2^-$ [86] and theoretical predictions assigning both ^{129}Pm and ^{131}Pm a ground state of $5/2^-$ [87, 88]. The alternative hypothesis is that the odd proton is still rotationally aligned and that the yrast bandhead is given by $I^\pi = J^\pi = 11/2^-$. This idea is supported by the cranked shell model calculations displayed in Figure 5.16 where the quasiprotons associated with the [413]$5/2^+$ and [532]$5/2^-$ levels become so close they overlap. In addition, the systematical comparison displayed in Table 5.2 found that the spin/parity of the band built on the odd $h_{11/2}$ proton is always given by $I^\pi = J^\pi = 11/2^-$. Extending this comparison to the heavier europium nuclides, we find the lightest (most deformed) odd-even isotope with known excited states is ^{137}Eu, whose yrast cascade looks remarkably similar to ^{131}Pm and whose bandhead is also assigned $11/2^-$ spin/parity. A final consideration to be made is the simple reasoning that 5/2 is closer to 1/2 (rotationally aligned) than 11/2 (deformation aligned).

With all that said, a thorough consideration of alternative schemes has been made - a summary of which is presented in this section. These schemes involve the reordering of the low energy γ rays, limiting the bandhead spin/parity to $11/2^-$ (assuming $I = J$ as per the rotational alignment limit), or both. Figure 5.17 presents all of the alternative schemes that were considered.

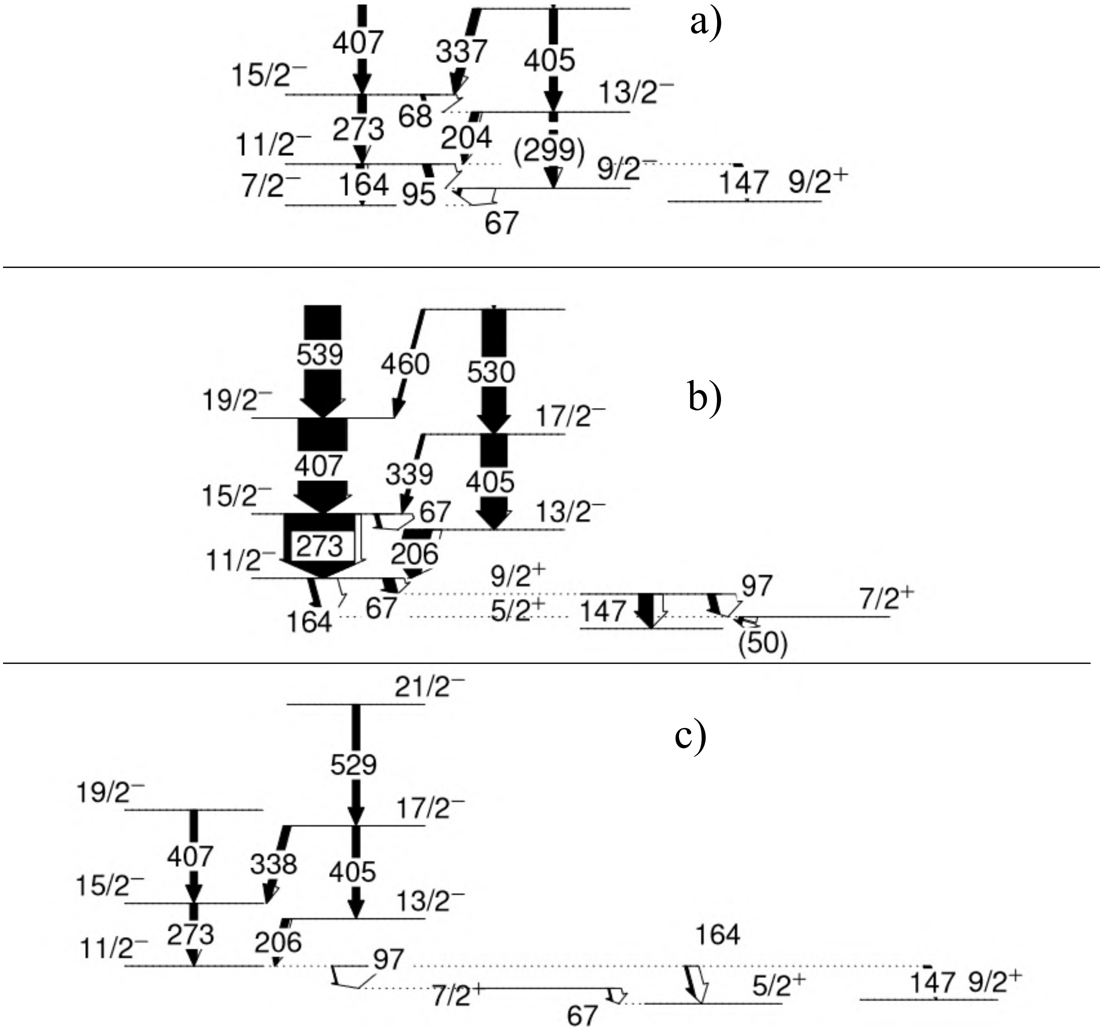
a)
407
337
405
$15/2^-$
$13/2^-$
68
273
204
$11/2^-$
(299)
$9/2^-$
$7/2^-$
164
95
147
$9/2^+$
67
b)
539
460
530
$19/2^-$
$17/2^-$
407
339
405
$15/2^-$
67
$13/2^-$
273
206
$11/2^-$
$9/2^+$
97
$7/2^+$
164
67
$5/2^+$
147
(50)
c)
$21/2^-$
529
$19/2^-$
$17/2^-$
407
338
405
$15/2^-$
$13/2^-$
273
206
$11/2^-$
97
164
$7/2^+$
$5/2^+$
147
$9/2^+$
67

FIGURE 5.17: Three level schemes considered as alternative explanations for the low spin structure of ^{131}Pm.

One immediate consideration is that the coincidence data for this nucleus is subject to considerable background contamination. As mentioned in the previous section, ^{131}Nd shares transitions of near identical energies to ^{131}Pm: 145.9, 405.5, 528.0 and 635.9 keV. Figure 5.17, panel a), details an early idea that the signature partner band extended from spin $13/2^-$ to $9/2^-$ via a 299 keV quadrupole. The coincidence data supported this idea, and 299 keV is equal to the summation of the 204 keV (later remeasured as 205 keV) and 95 keV (later remeasured as 97 keV), both of which would act as the $\Delta I = 1$ transitions. However, 299 keV is an M1 transition belonging to ^{131}Nd. Its presence in this coincidence analysis was as a result of the unfortunate similarity in energies between the 405.5, 528.0 and 635.9 keV γ rays and the 406, 530 and 637 keV γ rays in ^{131}Pm's signature partner. It was proposed for this scheme that 147 keV transitioned directly to a bandhead built atop the [404]$9/2^+$ intruder orbital. However, this configuration can't be true for three reasons. Firstly, the DCO ratio measured for 147 keV was 0.82 ± 0.06, consistent with a quadrupole character and inconsistent with 147 keV spanning a single unit of spin to bridge the $11/2^-$ and $9/2^+$ states. Secondly, 147 keV is seen in coincidence with 299 keV, courtesy of ^{131}Nd, so 147 keV would have to be below 299 keV in this scheme. Finally, bands built on the [404]$9/2^+$ orbital are generally seen to be at much higher excitation energies within this mass region, so this assignment would create an inconsistency. A final problem with this level scheme is the spin/parity of the bandhead. $7/2^-$ is equal to neither J or K. In order to extend the spin down to $5/2^-$, at least two transitions have to be introduced to account for the linking dipole and crossover E2. No further transitions are seen in coincidence with the proposed scheme. This makes sense since 299 keV does not belong to ^{131}Pm in the first place. It was proposed that 147 keV could stand in as the crossover E2 between the $9/2^-$ and $5/2^-$ states, but the ordering of the 97 and 67 keV transitions would have to be reversed, since 97, 147 and 163 keV cascade in parallel (Figure 5.5). This idea is what led to the proposed level scheme for this nucleus presented throughout the bulk of this chapter. One of the biggest problems with this proposal is the systematical inconsistency caused by the assignment of the $h_{11/2}$ bandhead as $I = K = 5/2$. The level scheme presented in panel b) is an attempt to remedy this. This level scheme is almost identical to that presented in Figure 5.10 in terms of the ordering of the transitions. A major change comes from the presumption that rotational alignment still applies here, and the $h_{11/2}$ bandhead is $I = J = 11/2$. Another point worthy of note is that, though the 271 keV transition spanning 13/2 and 9/2 is not presented in this scheme, the energy difference between the two states still allows its assignment, except here its multipolarity would be M2. Questions would then be raised about how an M2 transition is competitive with the 205 keV M1 that depopulates the state. Though this scheme satisfies the systematical observation that the $11/2^-$ state is always seen to decay into a positive parity rotational band, ultimately the deformation aligned scheme presented in Figure 5.10 was preferred as a result of the observed γ ray orderings.

The final scheme presented in panel c) is an attempt to reconcile the observed difference in intensity between the 67 and 97 keV transitions. It is bizarre that the 97 keV transition should be so intense in panel b), given that it is fed only by the weak 67 keV transition. Of course, this paradox is resolved in Figure 5.10 by having the state depopulated by 97 keV and 147 keV fed by both the 67 keV M1 and the 271 keV E2. In the circumstance that we choose to stand by the rotational alignment limit, however, this cannot apply. Instead, we must have 67 keV preceding the 97 keV M1. This then means that 163 keV can decay either to the same level as the one fed by the 67 keV γ ray, or another one of the same energy but different spin/parity. A couple of problems are then raised by this scheme. The first is that the 147 keV transition must be placed such that it transitions directly out of the $11/2^-$ state, since its observed mutual exclusivity to 163 and 97 keV must be preserved. It was proposed 147 keV could decay directly to the lowest level of a band built atop the high-Ω intruder orbital [404]$9/2^{+}$. That 147 keV would then take on an E1 multipolarity is contradictory to both the DCO and linear polarisation measurements made for it. Furthermore, bands built on the [404]$9/2^{+}$ orbital are observed in this mass region to be much higher in excitation energy than the level proposed here. The second problem is that 97 keV and 163 keV would have to take on multipolarities M2 and E3, respectively. Systematic comparisons (Table 5.2) do support the idea that γ rays of these multipolarities can compete, but only one other nucleus sees this happening with a half-life on the order of nanoseconds; ^{133}La has a half-life of 62 ns, but the 535 keV E3 depopulating this state is assigned only tentatively.

To summarise, in the author's opinion the only real choices for this scheme are the one presented Figure 5.10 and the one presented in 5.17b. The observation of the 271 keV transition between the 13/2 and 9/2 states makes the former option a better explanation, since there is no reason here that a 271 keV M2 would be competitive with a 97 keV M1.

Chapter 6

Detailed Gamma-Ray Spectroscopy of ${}^{132}_{61}$Pm

This chapter presents a study of doubly odd nucleus ${}^{132}_{61}$Pm. Doubly odd nuclides can provide a complex collective of nuclear energy levels; the unpaired proton and unpaired neutron couple to each other and a deformed core creating quasiparticle states with the potential for a large K-quantum-number: the projection of the nuclear spin along the axis of deformation. Without the benefit of pairing to increase their binding energy, the odd proton and neutron cause deformation to the core and instability to the nucleus as a whole. Indeed, no doubly odd nucleus beyond ^{14}N is stable. For odd-Z odd-N nuclei in this mass region, it is common that rotational bands well characterised by their quasiparticle nature have been identified. However, their relative excitation energies are often lacking, with the isomeric nature of their bandheads hindering a complete spectroscopy; this is the historical case for ^{132}Pm. Here, we present a more complete spectroscopy of ^{132}Pm including band extensions, connections of two of these bands to the proposed ground state and characterisation of its isomeric states. Bands 1 and 2 of this nucleus are associated with two-quasiparticle structures and are both isomeric, decaying with half-lives of 187 ± 4 ns and 19.9 ± 0.5 μs, respectively. It is proposed that band 2 decays to the ground state of this nucleus by way of a 43 keV M2 transition. This assignment is substantiated by comparison of the measured half-life of the state to the Weisskopf estimate for a transition of this energy and multipolarity, adjusted for its internal conversion. Bands 3 and 4 were not linked to this scheme and remain floating. Band extensions are made at both high and low spin for all four bands and speculation made as to the quasiparticle nature of bands 3 and 4.

6.1 Literature Review

A single study of this nucleus was performed by R. Wadsworth, *et al* [91], using the Daresbury POLYTESSA array. Four floating bands were identified and speculation made about their quasiparticle nature. Since relative excitation energies between the bands were not known and spin/parity information was based on systematic comparison, it was not possible to unambiguously assign a quasiparticle configuration to these bands. Utilising estimated K values of 4, 5, 5 and 5 for bands 1-4, respectively, single-particle alignment and experimental routhian plots were generated. None of the bands were seen to exhibit large signature splitting as is expected for a high-K rotational band, and in agreement with the CSM calculations performed. The alignment plots for both bands 1 and 2 showed no indication of alignment effects at 0.3 $\hbar\omega$, providing evidence for the Pauli blocking of the $h_{11/2}$ proton associated with this crossing. Because of the ambiguity of neither band showing signature splitting, the predicted structure for the bands were $\pi h_{11/2} \otimes \nu h_{11/2}$ and $\pi h_{11/2} \otimes \nu g_{7/2}$ without being able to distinguish which band belongs to which structure. Discussion was made on alignment effects observed for band 4 at $\hbar\omega = 0.3$ MeV. Thus, their favoured candidate for band 4's low spin structure was either $\pi g_{7/2} \otimes \nu g_{7/2}$ or $\pi g_{7/2} \otimes \nu h_{11/2}$. Band 3's configuration was deemed to be unclear.

In order to get a clear idea of what other studies have identified in terms of band structure, a systematic survey of other odd-odd nuclei in this mass region was performed, looking for similar bands. The results are detailed in Table 6.1. The contradictory nature of bandhead spin/parity assignments for doubly odd nuclei is obvious from a glance at Table 6.1. Most bands are floating, and those that are not usually decay into an isomeric state which itself is floating. Not one band from any of these nuclei has an experimentally verified excitation energy relative to its ground state. Furthermore, inconsistency can be seen in spin/parity assignments for bands who share the same proton and neutron configuration. For example, bands assigned as being based on the $\pi\ h_{11/2}[541]3/2^{-} \otimes \nu\ h_{11/2}[523]7/2^{-}$ configuration are found in ^{134}Pm and ^{128,130,132}Pr nuclei. However, in all four cases the bandhead J^{π} and K^{π} are inconsistent. In the cases where bands are not isomeric, the bandhead J^{π} does not have to correspond with the K^{π} of its constituent proton and neutron. For nuclear shapes that are both static and symmetric, K is a good quantum number. However, triaxial deformation and rotation can mix states of good K, producing an effective $<K>$ value. Inconsistency between the K values is usually a result of fixing the K input parameter to Donau-Frauendorf theoretical B(M1)/B(E2) calculations as $<K>$, where $<K>$ is whatever value gives the best fit to the experimentally determined ratios. Inconsistency between coupling modes are also seen for identical configurations. Perpendicular coupling is appropriate when high and low-Ω orbitals are coupled. Parallel coupling, also known as the Gallagher-Moskowski rule [92], is appropriate in case of J spin vectors that are approximately parallel to one another.

TABLE 6.1: Compilation of the band configurations, bandhead excitation energies (where known), proton-neutron coupling mode, isomerism and other notes for various odd-odd nuclides in this mass region. Where multiple spins have been listed for K, this has resulted from coupling the spins parallel or antiparallel, with each possibility allowed in the context of the level scheme and selection rules.

Nucleus	J^π	K^π	Band Configuration	E (keV)	Coupling Mode	Isomeric?	Ref	Notes
134Pm	(8+)	8+	$\pi h_{11/2}[541]3/2^-$ $\nu h_{11/2}[523]7/2^-$	(7- band-head)+272	Perpendicular	No (272 keV, E1)	[93]	a
	(7-)	7-	$\pi g_{7/2}[413]5/2^+$ $\nu h_{11/2}[523]7/2^-$	Floating	Perpendicular	Yes	[93]	-
136Pm	(8+)	8+	$\pi h_{11/2}[541]3/2^-$ $\nu h_{11/2}[514]9/2^-$	Floating	Perpendicular	Yes (43 keV E1, 1.5μs)	[94]	-
	(5-)	?	$\pi g_{7/2}[413]5/2^+$ $\nu h_{11/2}[514]9/2^-$	Floating	Unknown	Yes (β_+, 107s)	[94]	-
138Pm	(8+)	8+	$\pi h_{11/2}[541]3/2^-$ $\nu h_{11/2}[514]9/2^-$	(5- band-head)+594	Perpendicular	Yes (174 keV E1, 21ns)	[95]	-
126Pr	(5+)	1+ 2+	$\pi h_{11/2}[541]3/2^-$ $\nu h_{9/2}/f_{7/2}[541]1/2^-$	(6+ band-head)+106	Parallel	No (106 keV Dipole)	[96, 97]	b
	(7+) (8+)	5+	$\pi h_{11/2}[541]3/2^-$ $\nu h_{11/2}[523]7/2^-$	(6+ band-head)+68	Parallel	Unknown	[96, 97]	b
128Pr	(6+)	5+	$\pi h_{11/2}[541]3/2^-$ $\nu h_{11/2}[523]7/2^-$	Floating	Parallel	Unknown	[96, 97]	a
	(7+)	1+ 2+	$\pi h_{11/2}[541]3/2^-$ $\nu h_{9/2}/f_{7/2}[541]1/2^-$	(6+ band-head)+530	Parallel	No	[96, 97]	-
	(4-)	1- 2-	$\pi h_{11/2}[541]3/2^-$ $\nu d_{3/2}/s_{1/2}[411]1/2^+$	Floating	Parallel	Unknown	[96, 97]	-
	(8-)	4-	$\pi h_{11/2}[541]3/2^-$ $\nu d_{5/2}[402]5/2^+$	(4- band-head)+365	Parallel	No	[96, 97]	-
	(8-)	8-	$\pi g_{9/2}[404]9/2^+$ $\nu h_{11/2}[523]7/2^-$	Floating	Parallel	Yes (>80ns)	[96, 97]	-
130Pr	(6+)	5+	$\pi h_{11/2}[541]3/2^-$ $\nu h_{11/2}[523]7/2^-$	(5+ band-head)+62	Parallel	No	[98]	-
	(6-)	4-	$\pi h_{11/2}[541]3/2^-$ $\nu g_{7/2}[402]5/2^+$	(5+ band-head)+58	Parallel	No	[98]	-
132Pr	(8+)	5+	$\pi h_{11/2}[541]3/2^-$ $\nu h_{11/2}[523]7/2^-$	(5+ band-head)+98	Parallel	No	[98]	-
	(6-)	4-	$\pi h_{11/2}[541]3/2^-$ $\nu g_{7/2}[402]5/2^+$	(5+ band-head)+381	Parallel	No	[98]	-

[a] Preferred odd-spins expected for this band, as per Equation 6.1.

[b] Authors of references, Hartley and Petrache, disagree over bandhead spin/parity assignments.

6.2 γ-ray spectroscopy

^{132}Pm was populated via the $^{58}Ni +^{78} Kr \longrightarrow^{132}$ Pm $+ \, n3p$ reaction. The following analysis is from the low-energy portion of the JM06 data, where ^{132}Pm was populated with a greater cross section. The following results utilise this part of the data only, since inclusion of the high beam energy data introduces a large background signal.

6.2.1 Prompt γ-ray coincidences

Band 1

The first spectra displayed are those detailing prompt γ rays measured using JUROGAM, associated with band 1. Figure 6.1 shows spectra comprising sums of doubles gates on triples data, where the transitions inside each gate list are the stretched E2 cascades for even (Figure 6.1a) and odd (Figure 6.1b) spin $\Delta I = 2$ cascades. Except where noted, for this band and all bands in this chapter ordering of transitions in the cascade have been confirmed using doubles gates on triples data, where statistics allow such a measurement. Ordering of γ rays can also be substantiated by "intensity arguments"; the low-spin states have a larger intensity owing to side-band feeding. The state at the base of this band is isomeric, and is discussed in more detail in Section 6.2.2.

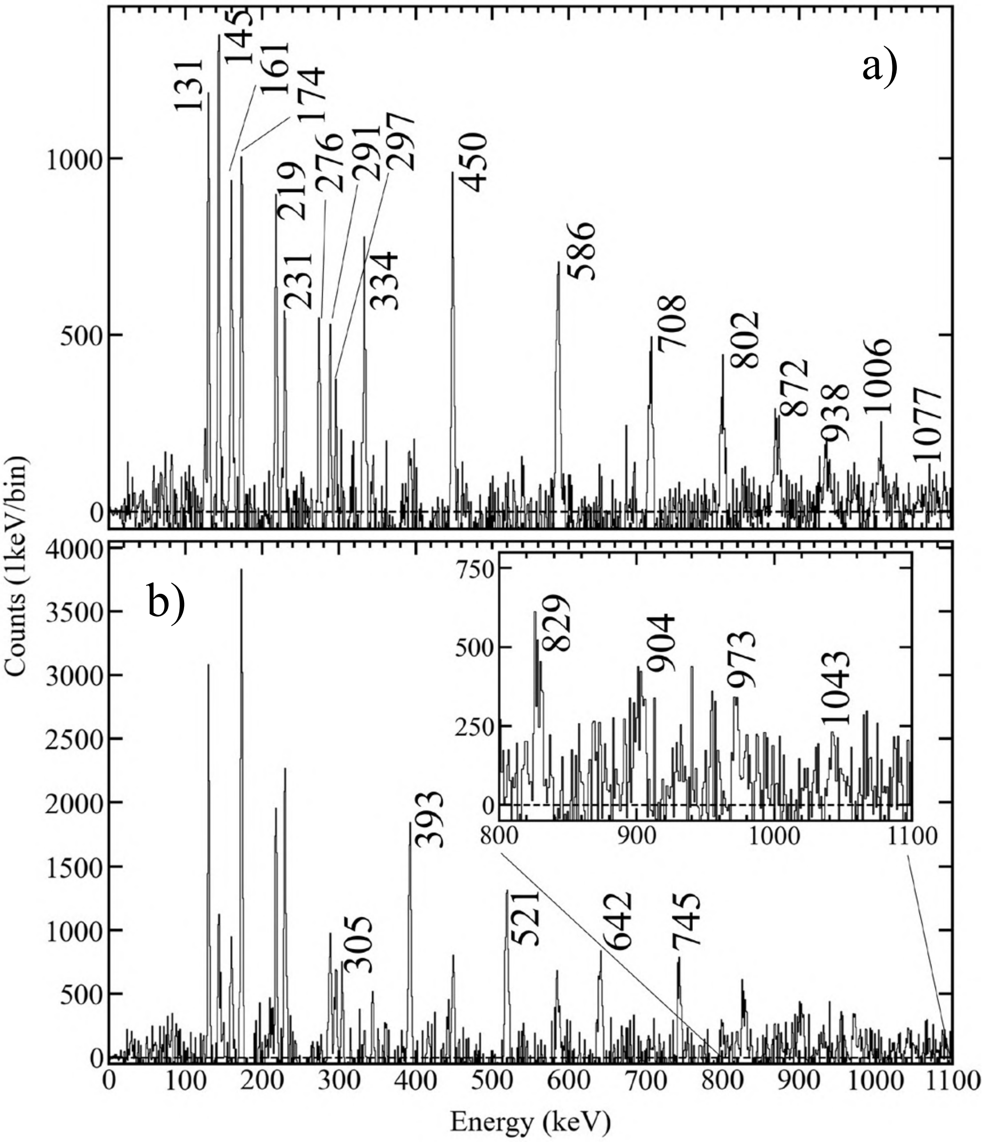

FIGURE 6.1: ^{132}Pm Band 1. Panel a): sum of doubles gates on triples data using a gate list comprised of all E2 transitions between even-spin levels in band 1. Panel b): sum of doubles gates on all E2 transitions between odd-spin levels in band 1.

Band 2

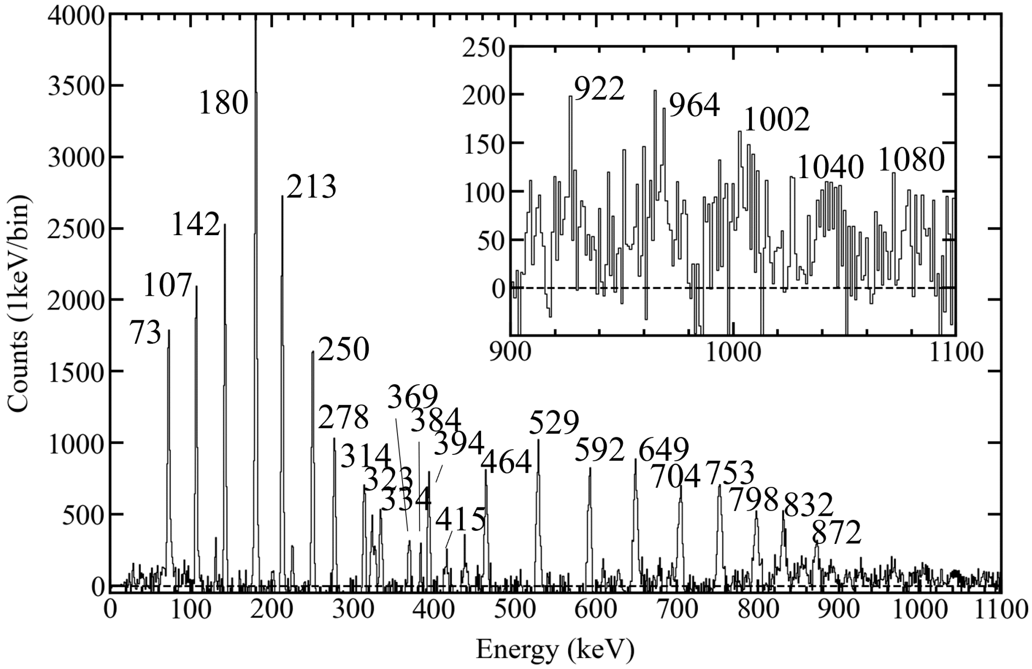

FIGURE 6.2: ^{132}Pm Band 2. Sum of doubles gates on all γ rays assigned as belonging to band 2 and above $I^{\pi} = 5^{-}$, as displayed in Figure 6.15.

Figure 6.2 displays a sum of doubles gates across all transitions in band 2. The ordering of five transitions at the highest energy range of the spectrum have been made considering the approximately consistent spacing between levels in a rotational cascade, coupled with intensity arguments. As well as extensions at the top of the band, extensions have been made to the low-spin section of the band. Figure 6.2 displays a 73 keV transition which is shown to be in coincidence with the other members of this band. A detailed coincidence analysis is detailed in Figure 6.3. The top panel of this Figure shows the projection of γ rays in coincidence with 73 keV **and** 73 keV. The figure displays evidence for the lowest M1 members of band 2. Further evidence is detailed in the bottom panel of this figure, where the projection of γ rays in coincidence with 73 keV **and** 107 keV are displayed. Despite 73 keV being one of the gating γ rays, a small peak is visible at 73 keV in this spectrum. From this we must conclude that the low end of band 2 is extended by two individual γ rays each with energy 73 keV. Since these transitions are in cascade, it is not possible to distinguish between their individual energies within the precision of the JUROGAM spectrometer.

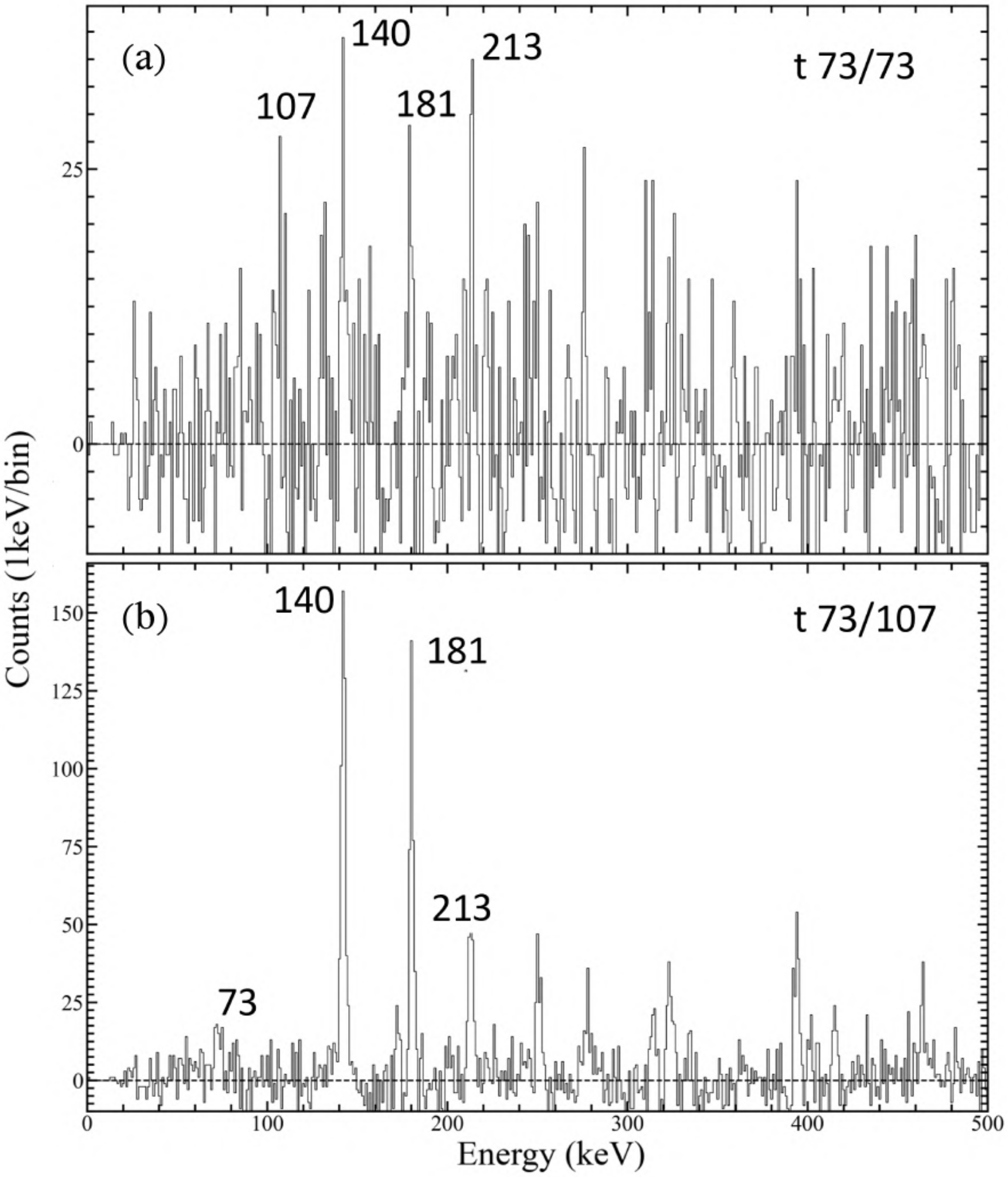

FIGURE 6.3: Panel a): γ rays in coincidence with 73 keV **and** 73 keV. The lowest four M1 transitions of band 2 are visible, providing evidence for the existence of two 73 keV transitions at the base of band 2. Panel b): γ rays in coincidence with 73 keV **and** 107 keV. A peak at 73 keV is visible along with various known members of band 2.

By consideration of the Weisskopf estimates at this low energy, one can initially presume the multipolarity of these 73 keV γ rays to be $\Delta I = 1$ transitions. With these transitions placed as "linking" transitions, it is possible to infer the existence of a pair of "crossover" E2 transitions, with energy equal to the sum of the linking transitions that lie parallel to them. In this case we look for crossover transitions of energy 180 keV (73+107) and 146 keV (73+73).

Figure 6.4 displays the projection of γ rays in coincidence with 180 keV **and** 142 keV. Similarly to the previous case with the 73 keV doublet, despite 180 keV being one of the gating transitions, a small peak is visible at 180 keV. The inset of this figure details a simple numerical fit to this data of a gaussian curve superimposed on a linear background. The background subtracted number of counts under the curve is 305 ± 34. Unlike the previous case with the 73 keV doublet, it is possible to uniquely gate on the two 180 keV transitions to measure their individual energies. The M1 can be distinguished by gating on 107 keV **and** 142 keV. Since the 107 keV transition runs parallel to the 180 keV E2, no trace of this E2 should be seen in the spectrum. The E2 can be distinguished by gating on 323 keV **and** 464 keV. The 323 keV transition runs in parallel to the 180 keV M1 preventing traces of this γ ray within the spectrum. The individual energies are displayed in Table 6.3.

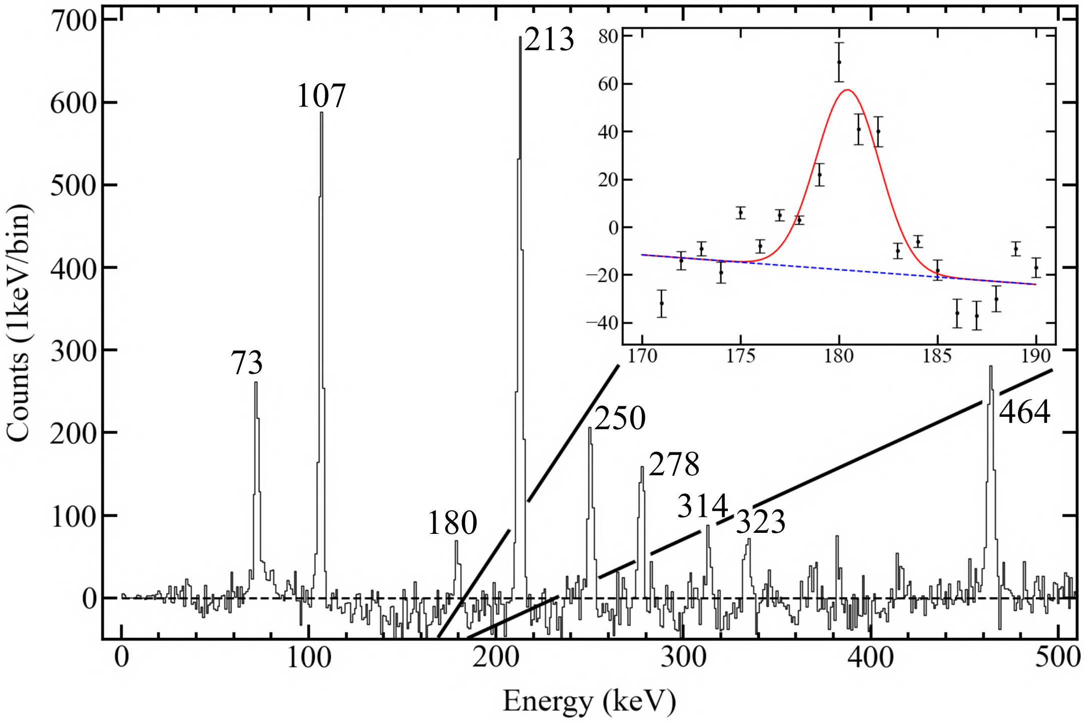

FIGURE 6.4: γ rays observed at JUROGAM in coincidence with both 142 keV **and** 180 keV. A small peak at 180 keV is visible, along with various other members of band 2. **Inset:** numerical fit to the 180 keV peak of a single term Gaussian superimposed on a linear background. The background subtracted number of counts under the curve is 305 ± 34. χ^2/NDF: 8.4.

A crossover E2 transition with energy 146 keV was not observed in this data set. Considering the Weisskopf estimates for transitions of energies 146 and 180 keV (Table 6.2) we can see that the relative transition rate for a 146 keV γ ray is almost three times slower than the 180 keV E2.

TABLE 6.2: Weisskopf single-particle estimates of transition rate for 146 and 180 keV γ rays.

Energy (keV)	M1 (s)	E2 (s)
146	7.08×10^{-12}	8.57×10^{-9}
180	3.78×10^{-12}	3.01×10^{-9}

Coupled with the small number of counts observed for the 180 keV transition, it is clear to see that one would need a greater amount of counting statistics to hope to observe this 146 keV transition. An alternative idea is that the multipolarity of the final 73 keV transition is in fact of electric dipole (E1) character, and this transition depopulates the band instead of acting as a linking transition. Unfortunately, the same ambiguity that prevents unique gating on the individual energies also prevents us from performing a DCO analysis on these transitions. Reasoning for both of these transitions having M1 character is made in Section 6.4.

Bands 3 and 4

Figure 6.5 details the observed prompt γ rays for band 3. It was not possible through analysis of both prompt and delayed coincidence matrices to link this band to bands 1 and 2. Furthermore, ambiguity surrounding its experimental single-particle alignment and signature splitting prevent definite assignment of its Nilsson bandhead; this is discussed in detail in Section 6.4. The bottom panel of this Figure features some interesting peaks at energies 854, 966 and 1091 keV. Low statistics prevent a thorough analysis of the ordering of these peaks by way of doubles gating; it is unknown at this time whether they belong to band 3 and, if they do, what their ordering is. Despite this, extensions over previous work have been made by consideration of energy spacing and intensities, as was done for bands 1 and 2. For the preferred-spin (lower energy) cascade, transitions 774, 886, 951 and 1028 keV are new. For the non-preferred side, transition 1025 keV is new.

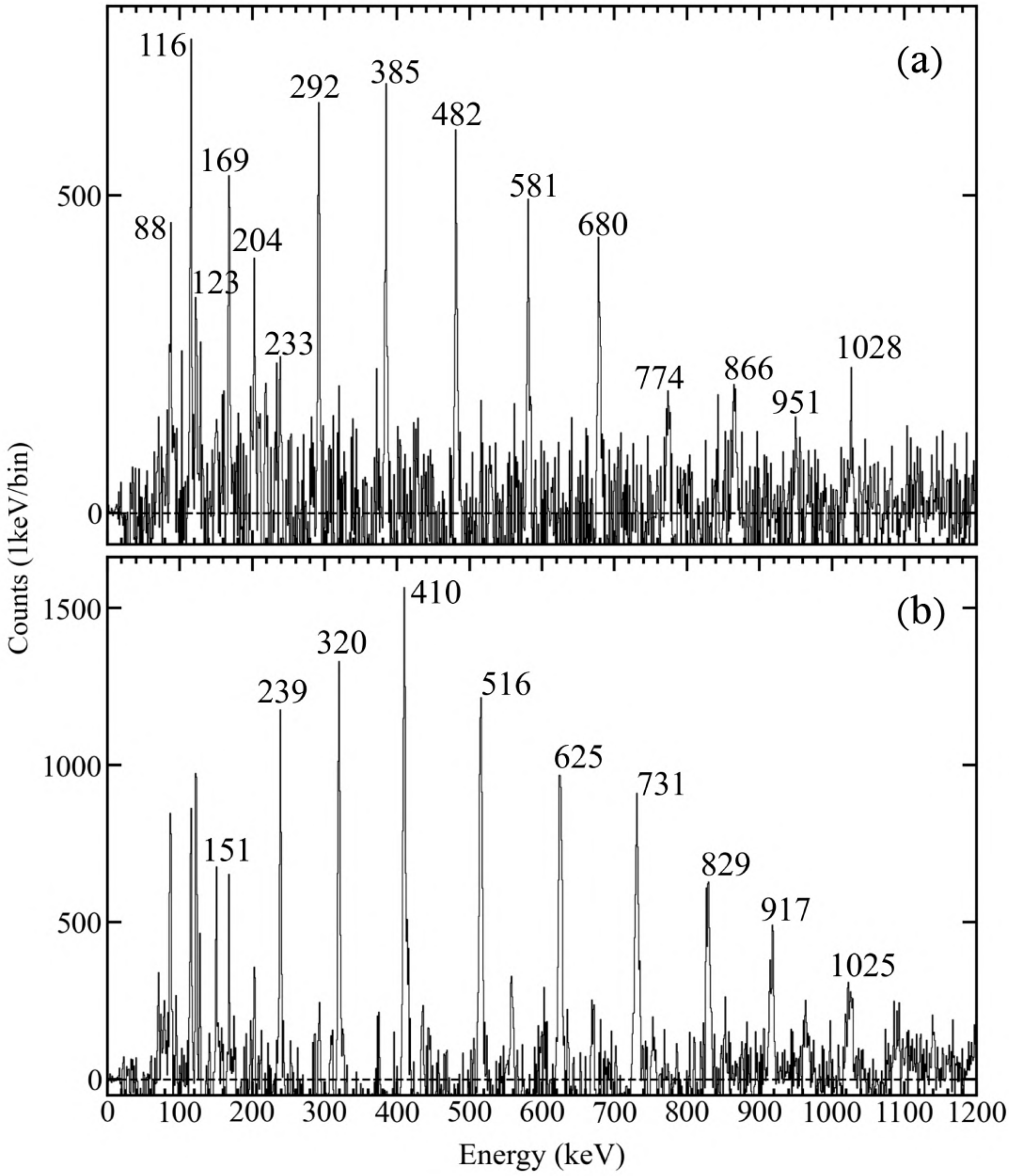

FIGURE 6.5: ^{132}Pm Band 3. Panel a): sum of doubles gates on all γ rays in the preferred signature (lowest energy) cascade (204, 292, 385, 482, 581, 680, 774, 866, 951, 1028 keV). Panel b): sum of doubles gates on all γ rays in the non-preferred signature (higher energy) cascade (239, 320, 410, 516, 625, 731, 829, 917, 1025 keV).

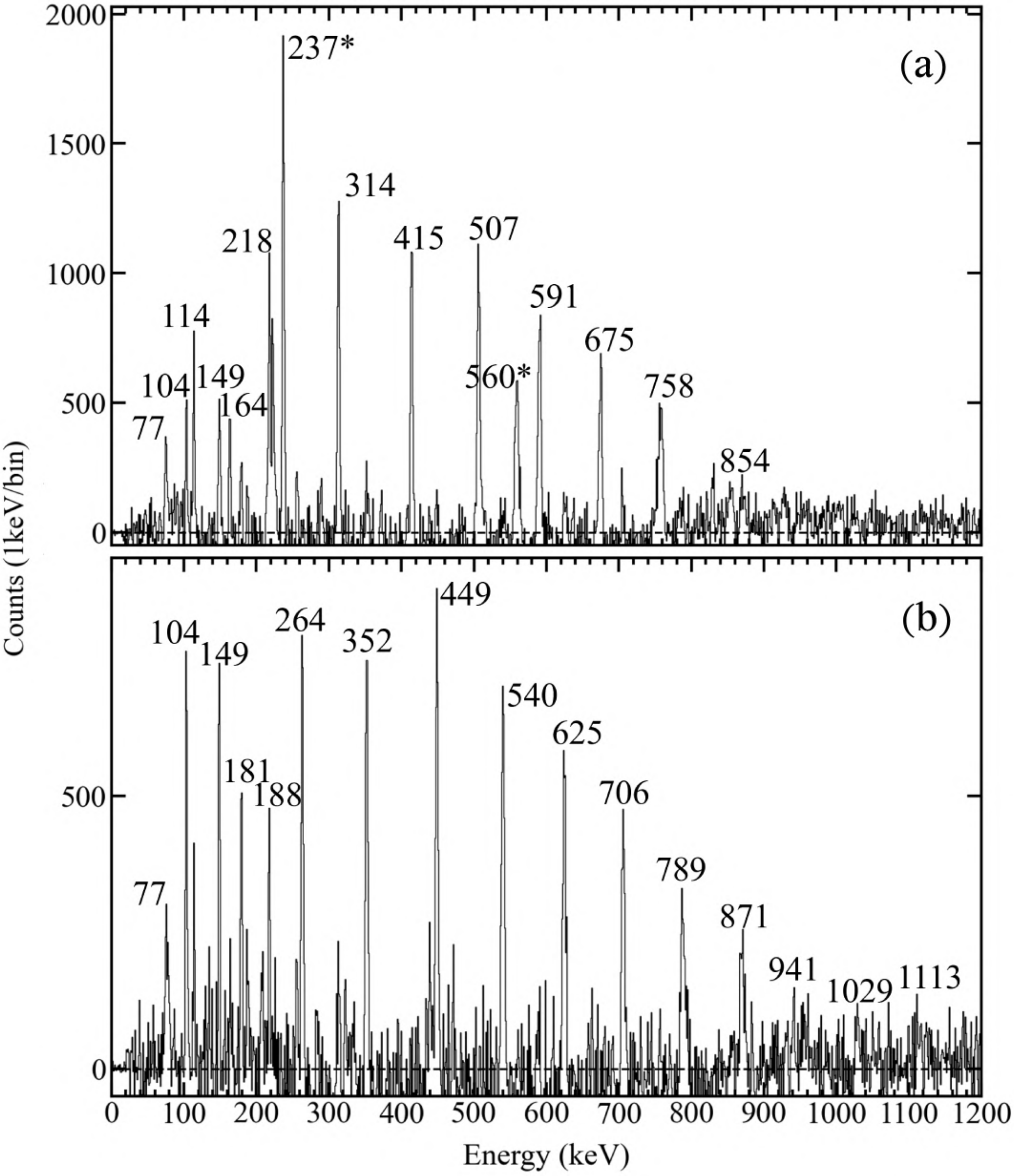

FIGURE 6.6: ^{132}Pm Band 4. Panel a): sum of doubles gates on all γ rays in the preferred signature (lowest energy) cascade (181, 264, 352, 449, 540, 625, 706, 789, 870, 941, 1029, 1113 keV). Panel b): sum of doubles gates on all γ rays in the non-preferred signature (higher energy) cascade (218, 314, 414, 507, 590 674, 758, 854, 928 keV). Transitions marked with a * are contaminants from a nucleus other than ^{131}Pm.

Like band 3, it was not possible to link band 4 to the other observed bands. Also like band 3, it was not possible to assign band 4 a unique Nilsson configuration. Figure 6.6 details the γ rays observed for this band. Extensions over previous works have been made at the top and bottom end of the band, with transitions 77, 181, 870, 928, 941, 1029 and 1113 keV newly observed.

Evidence of these γ-rays belonging to ^{132}Pm comes from direct measurement of the mass of the recoil associated with these γ rays. Low counting statistics for bands 3 and 4 prevent production of a plot of MWPC-x against γ-ray energy as was done for ^{131}Pm (Figure 5.3). Figure 6.7 displays the MWPC-x coordinate of recoils associated with γ rays from all four bands. That the curves line up with each other, and are all within coordinate ranges associated with mass 128/132 recoils provides evidence for these γ rays belonging to ^{132}Pm.

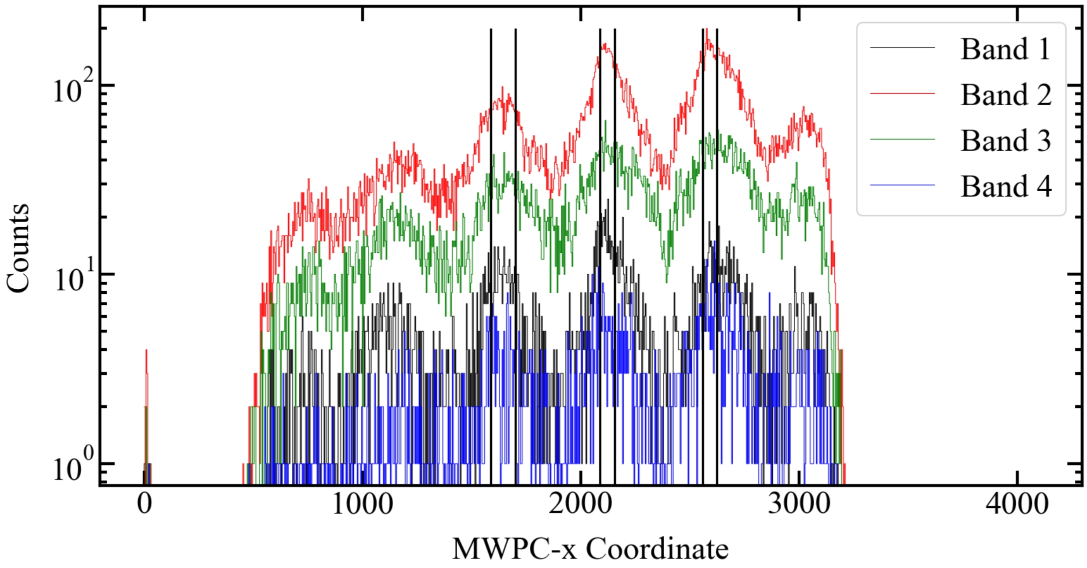

FIGURE 6.7: MWPC-x coordinates associated with recoils selected by correlation with prompt γ rays observed in each band of ^{132}Pm. Black vertical lines indicate MWPC-x coordinate ranges associated with mass 128/132 recoils.

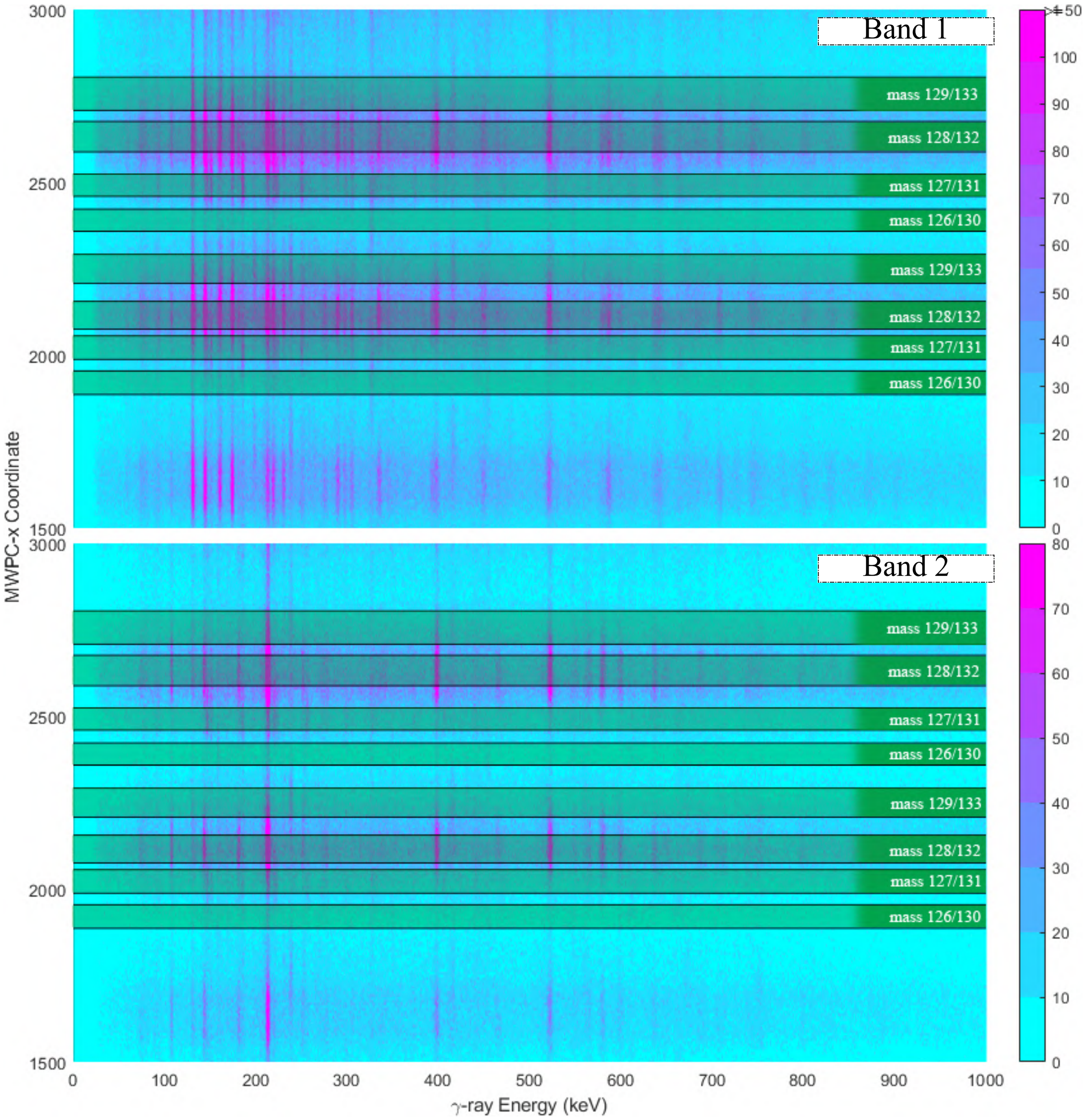

FIGURE 6.8: MWPC-x coordinate against γ-ray energy for all recoils associated with γ rays observed in the decay of bands 1 and 2 in ^{132}Pm. MWPC coordinate ranges corresponding to different masses are highlighted.

Counting statistics for bands 1 and 2 are plentiful and facilitate a plot of MWPC-x coordinate against γ-ray energy for both bands, displayed in Figure 6.8. γ rays associated with both bands cluster unambiguously in rows along MWPC-x coordinates associated with mass 128/132 recoils.

6.2.2 Delayed γ rays

This section details the spectroscopy of delayed γ rays emitted by ^{132}Pm as it decays out of isomeric states. As detailed in Chapter 3, the flight time of a recoil traversing the recoil separator is around 450 ns. This makes the experimental setup sensitive to isomeric decays with half-lives anywhere from around 50 ns to 200 μs. The upper limit is mediated by the implantation rate into the DSSD and is discussed in more detail in Chapter 7. ^{132}Pm was first identified in this dataset by observation of a strong 73 keV delayed γ ray. This γ ray was later found to be associated strongly with band 1. Rather than systematically test every delayed γ ray, it is instead useful to select events using the prompt γ rays observed at JUROGAM. Great care is required when selecting events utilising γ rays at the target position: there are vastly more of them compared to those observed at the focal plane, owing to the variety of decay energies observed from a high-spin cascade. This can introduce some ambiguity in any given selected event, since a γ ray of a particular energy may belong to multiple bands or nuclides. To mitigate this, a selected event must fulfil the criteria of having two coincident γ rays from a predefined list (an **and** gate), instead of just one. This is similar to the triples coincidence analysis made possible by the RADWARE cube. It is less likely, though not impossible, that two particular energies will belong to multiple bands. Event selectivity can be further improved through the use of time gates and mass selection. In the former case, a sort is first performed where a matrix is produced tabulating focal-plane γ energy against the time difference between recoil implantation and the subsequent γ decay. This is visualised in Figure 6.9.

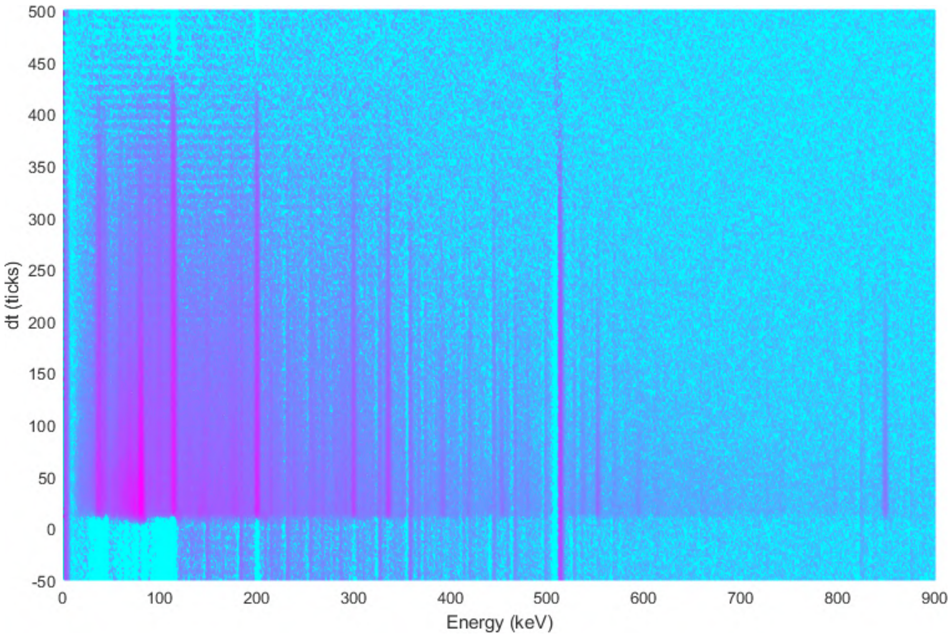

FIGURE 6.9: 2-dimensional histogram of focal-plane γ-ray energy against the time difference between recoil implantation and the subsequent γ decay.

Here, several strong lines indicate the energy γ rays associated with isomeric states and decrease in intensity along the y-axis according to the lifetime of these states. By limiting the prompt-γ event selection to events where the focal-plane γ rays are emitted within a few half-lives of the decay we are searching for, we can dramatically limit the amount of background contamination seen. Mass gating is rather more simple. As detailed in Chapter 3, MARA separates out recoils according to their m/q ratio. Here, only events satisfying a gate allowing mass-128 and mass-132 recoils are selected. Gate lists are composed for each of the bands, comprising transitions which are members of that band. The results of this search are detailed in Figure 6.10.

An immediate reaction is that all four bands seem to show association with the same transitions. To verify these coincidences, a new sort is performed where events are selected using the focal-plane transitions observed in Figure 6.10. From these events, prompt γ matrices are plotted and checked for γ rays associated with bands 1 - 4. For band 1, strong (delayed) coincidence was observed between the 43, 63 and 73 keV focal-plane γ rays and its prompt transitions. For band 2, coincidence was observed between its prompt γ rays and the 43 keV delayed transition. Of important note is that the K_α and K_β internal conversion x-ray energies for promethium are 38 and 43 keV, respectively. It is expected that the intensity of the K_β peak be around one-fifth that of the K_α peak [99]. Bands 1 and 2 clearly do not obey this proportionality, with the K_β peak at least twice as intense as the K_α in both cases. This information, coupled with the observed coincidence between 43 keV and the prompt radiation associated with bands 1 and 2, leads us to assign 43 keV as a true γ ray. 112 keV was not found to be in coincidence with any of the four bands. This transition is overwhelmingly associated with ^{131}Nd. Its presence in this spectrum is the result of the lack of selectivity offered by gating using prompt γ rays, combined with the fact that the mass gate will sometimes allow through events from neighbouring masses whose events have particularly high m/q ratios for that mass and charge state. Similarly 79 keV was not found to be in coincidence with band 3. This transition is instead associated with ^{130}Pr. This elimination process leaves us with three candidate γ rays: 43 and 73 keV, and tentatively 63 keV. In an attempt to whittle down the list, another sort was performed requiring *three* coincident prompt γ rays to be observed from each gate list. The results of this search are displayed in Figure 6.11. The higher selectivity comes at the expense of statistics; it can be observed that bands 3 and 4 do not display any major photopeaks. This can be explained by considering that either bands 3 and 4 have isomeric half-lives longer than the experimental boundary, or they both decay to the ground state, or they are not sufficiently populated to yield statistically significant levels of counts with this high-fold selectivity. Band 2 registers a peak at 43 keV, while band 1 shows peaks at 38, 43, 63 and 73 keV.

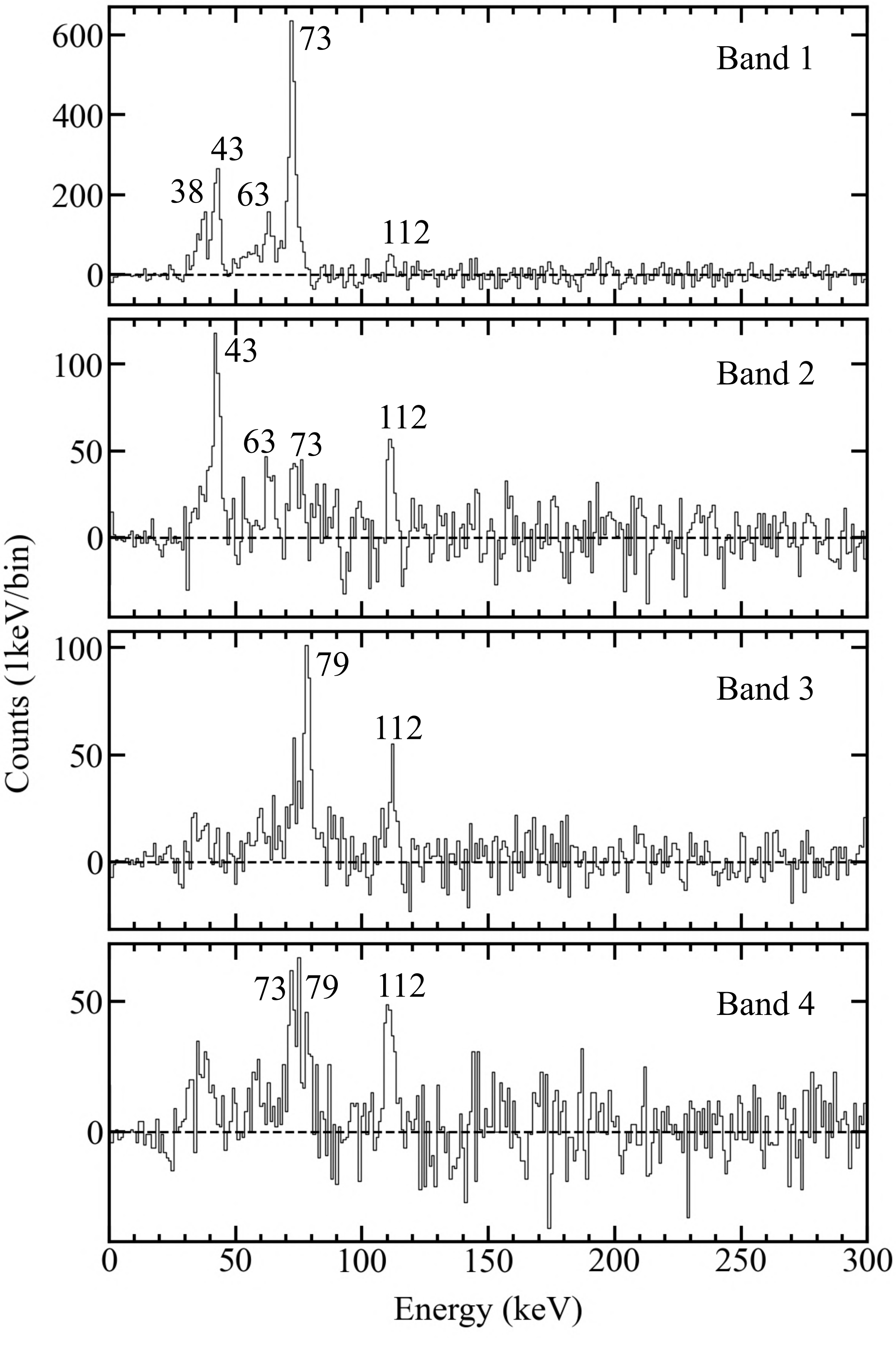

FIGURE 6.10: Focal-plane γ singles observed by tagging on a combination of any two coincident prompt γ rays observed by JUROGAM, from a gate list composed of γ rays belonging to the band labelled on the figure panel.

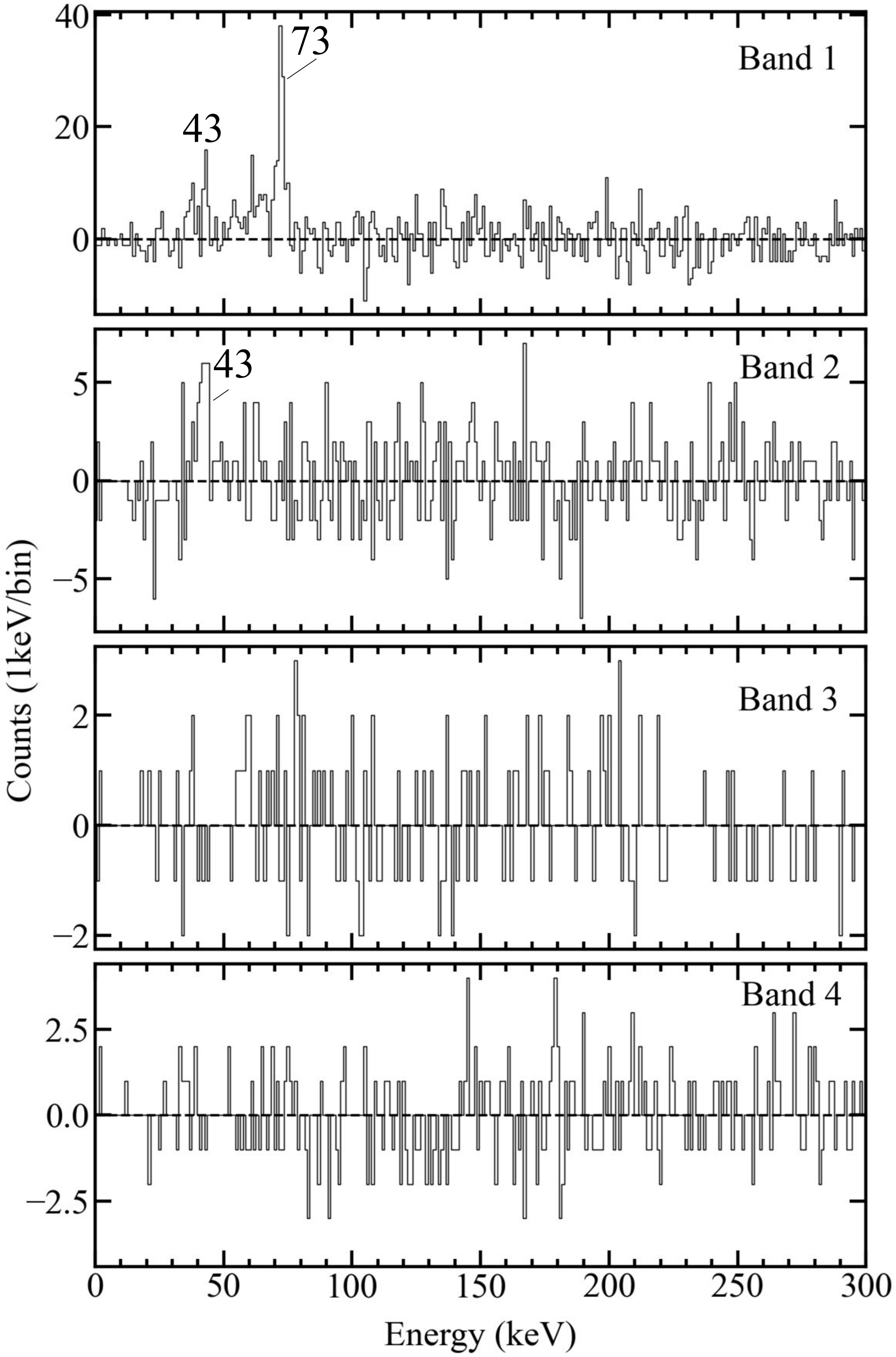

FIGURE 6.11: Focal-plane γ singles observed by tagging on a combination of any three coincident prompt γ rays observed by JUROGAM, from a gate list composed of γ rays belonging to the band labelled on the figure panel.

To facilitate the focal-plane $\gamma\gamma$ coincidence analysis, a mass-gated $\gamma\gamma$ matrix was produced tabulating all focal-plane γ rays following implantation of a mass 132 (or mass 128) recoil. In order to be incremented into the matrix, the γ rays must be detected within a $\pm$20 ns time window of each other. Figure 6.12 shows the γ rays in fast coincidence with 73 keV at the focal plane. A background gate is set at 63 keV. It can be seen that 73 keV is in coincidence with another transition of energy 73 keV. Recalling the prompt γ^3 triples analysis, we already know that band 2 has two 73 keV transitions at low spin. At least one of the 73 keV γ rays seen at the focal plane must not belong to band 2, since it is depopulating band 1. This presents us with two possible explanations: either there are three 73 keV γ rays in cascade (one out of band 1 directly followed by the two M1s in band 2), or the 73 keV out of band 1 only sees the second of the two M1 γ rays in band 2. To test the former option, events were selected within a sort by gating on a 73 keV transition at the focal plane. From these events, the remaining focal-plane γ rays were sorted into a $\gamma\gamma$ matrix. Within this matrix, a gate is placed for 73 keV. The projection is displayed in Figure 6.13. A small number of counts can be seen around 73 keV. The small count may be due to the small number of focal plane germanium detectors utilised but it is more likely that the counts seen here are false correlations between the intense 73 keV peak and the Compton background at the focal plane. It is therefore proposed that the 73 keV transition out of band 1 sees only the second of the two γ rays in band 2.

63 keV was shown to be weakly coincident with 73 keV, but could not be placed within the level scheme with any certainty. This transition is not observed in coincidence with band 2 or the 43 keV γ ray depopulating it, which suggests that it cascades in parallel to the 73 keV γ ray depopulating band 1. Coincidence between 63 keV and 73 keV could then be explained by a linking transition of 9 keV, which is not observed here. Without larger γ^3 counting statistics, it cannot be ruled out that coincidence between 73 keV and 63 keV

is just due to contamination from the shoulder of the intense 73 keV peak. it Finally, 43 keV is not seen to be in fast coincidence with any of these γ rays. We know from the delayed coincidence analysis that 43 keV is seen by both bands 1 and 2; that it is not seen in coincidence with 73 keV here is because the 43 keV transition has a longer half-life than the 20 ns time gate placed on this coincidence matrix. This idea is substantiated by evidence of delayed coincidence between 43 keV and 73 keV in a delayed (1μs coincidence window) focal-plane $\gamma\gamma$ matrix as displayed in Figure 6.14.

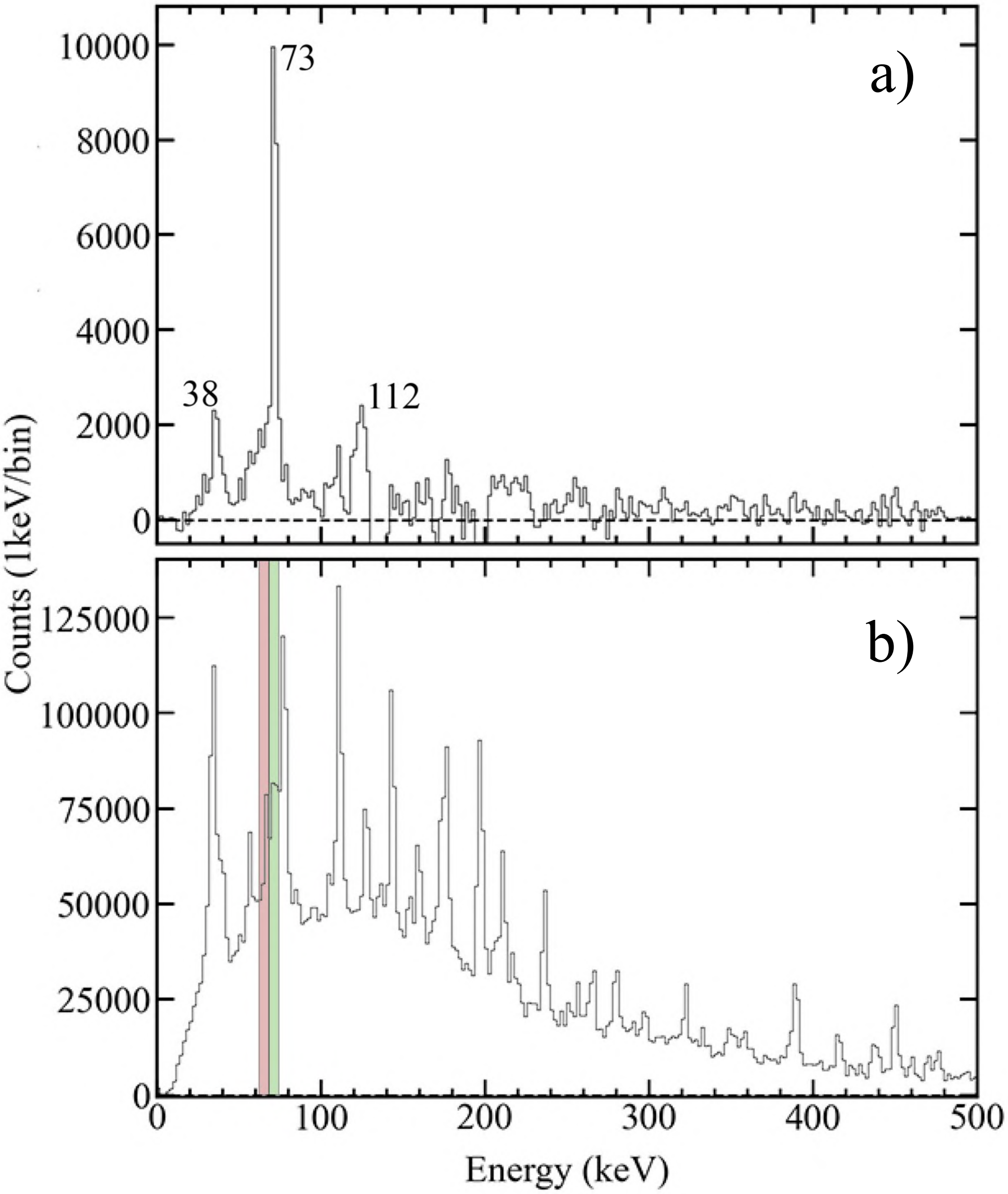

FIGURE 6.12: Panel b): Projection of the focal plane $\gamma\gamma$-coincidence matrix. γ rays incremented into this matrix are measured in correlation with any recoil implantation into the DSSD. The γ rays themselves must be measured within a coincidence window of 100 ns of each other. The green and red bars represent a gate and background gate on 73 keV and 63 keV, respectively. Panel a): Results of the gating procedure displayed in the bottom panel. Here a striking peak at 73 keV is visible, offering evidence of two 73 keV γ rays seen in cascade at the focal plane.

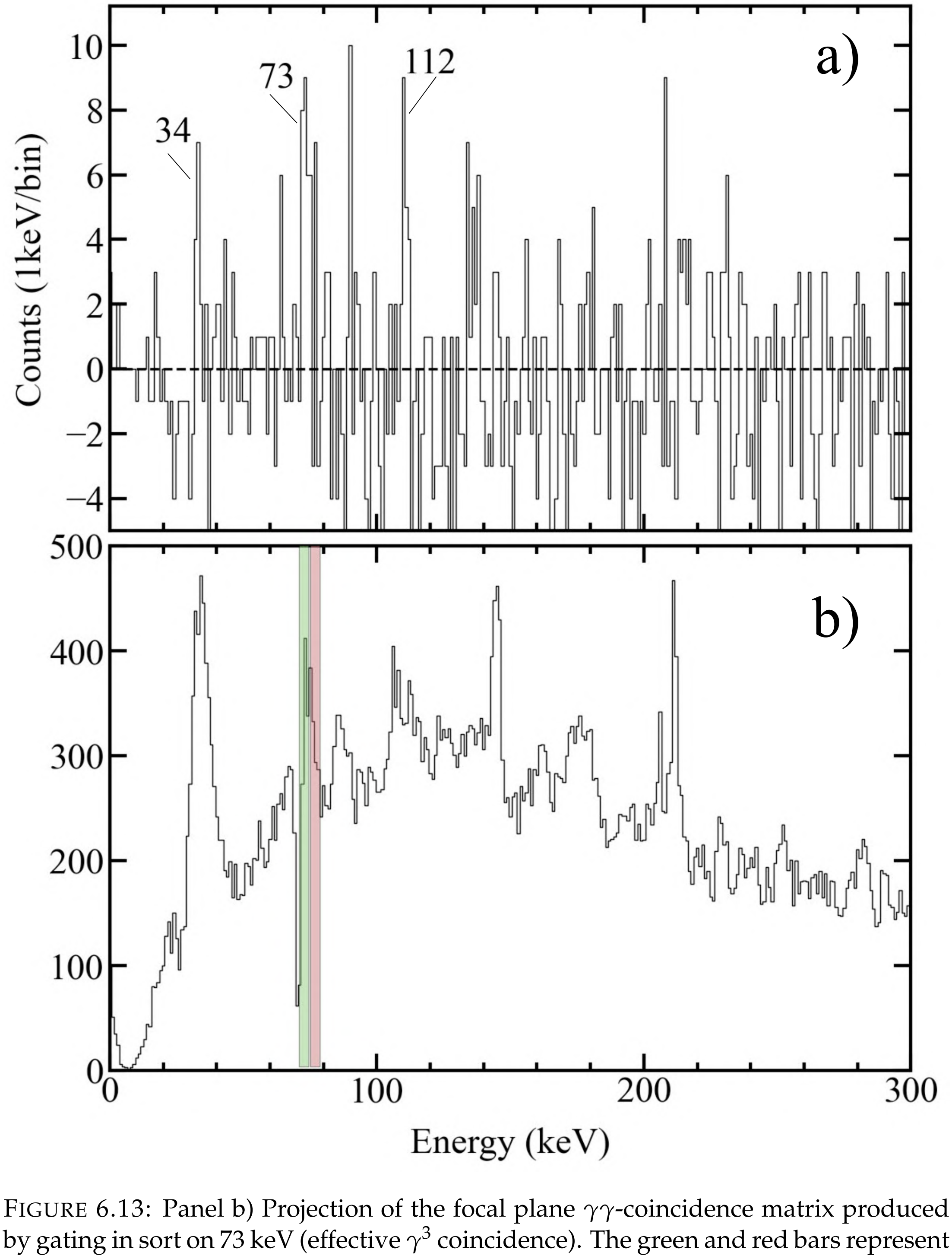

FIGURE 6.13: Panel b) Projection of the focal plane $\gamma\gamma$-coincidence matrix produced by gating in sort on 73 keV (effective γ^3 coincidence). The green and red bars represent a gate and background gate on 73 keV and 78 keV, respectively. Panel a) Results of the gating procedure displayed in the bottom panel. Some counts are visible at 73 keV, but are not statistically significant.

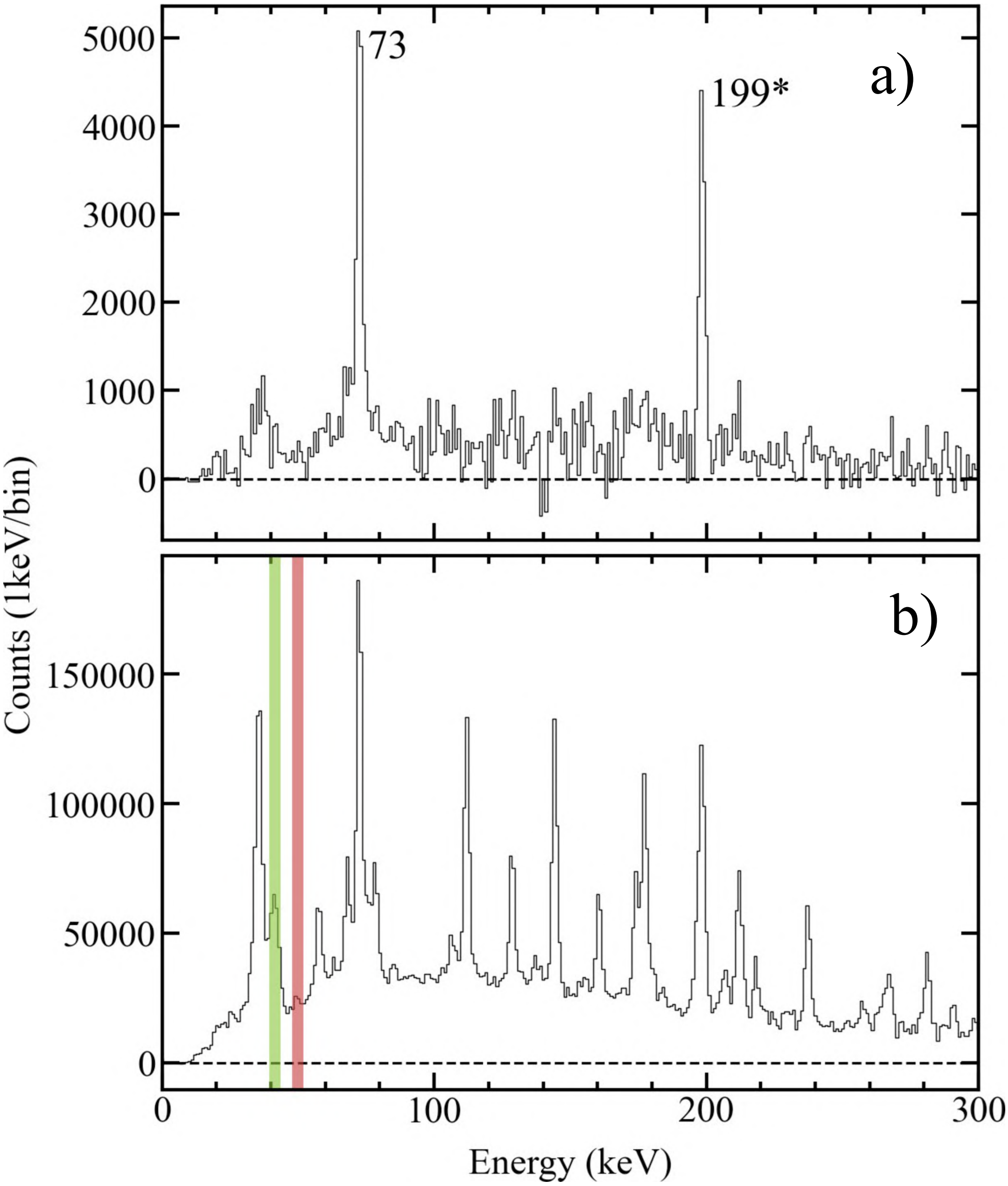

FIGURE 6.14: Delayed coincidence between 43 keV and 73 keV in a (1μs coincidence window) focal-plane $\gamma\gamma$ matrix. The 199 keV transition seen in this coincidence matrix is associated with the (8+) isomeric state in ^{128}Pr.

Table 6.3 and Figure 6.15 catalogue every γ ray observed in the decay of ^{132}Pm. In total, 121 γ rays were observed, 32 of which have been observed for the first time. The level scheme displayed in Figure 6.15 has been constructed following γ doubles/triples analysis from both prompt and delayed coincidence matrices. Spin/parity assignments are tentative and discussed in greater detail in Section 6.4. DCO (Directional Correlation of Oriented States) analysis and measurement of γ-ray linear polarisations have been made following the same methodology as in the previous two chapters. For all four bands, DCO ratios have been measured from γ spectra gated by a stretched E2. Owing to the lower population of bands 3 and 4, DCO ratios were measured from a mass-gated $\gamma\gamma$ matrix, dispensing with the more selective "triple"-γ selection method. The measured ratios for the low-energy transitions in bands 3 and 4 are higher than that which is expected for γ rays of dipole character ($R_{DCO} \approx 0.6$ in this work). These high ratios can come as a result of high M1/E2 mixing.

The isomeric nature of the four rotational bands precludes relative intensity measurements between the bands. Instead, relative intensities presented are between transitions belonging only to that band, with a 100% intense transition picked for each band. Intensity measurements are measured with an accuracy of ±5% for energies between 100-500 keV, and ±10% for energies outside this range. Transitions that don't have a quoted intensity can be assumed to have less than 5% of the maximum intensity. Transitions out of an isomeric state don't have measured intensities owing to being measured with the focal-plane spectrometer and not JUROGAM. For the intensity measurements, γ rays in band 1 were selected using the 73 keV delayed transition, γ rays in band 2 were selected using the 43 keV delayed transition, γ rays in band 3 were selected using the 88 keV prompt transition and γ rays in band 4 were selected using the 104 keV prompt transition.

TABLE 6.3: List of γ rays and their measured properties for ^{132}Pm. Quantities in brackets denote uncertainty in the last quoted significant digit. Assigned (λL) values in brackets are tentative.

E_γ, keV	I_γ^c	DCO	Linear Polarisation	Measured (λ L)	Assigned (λ L)	Band
43.1(5)	*d*	—	—	—	(M2)	2→ 5
73.0(2)	*d*	—	—	—	(E1)	1→ 2
131.18(8)	100	0.57(5)	—	Dipole	(M1)	1
144.60(9)	78	0.48(3)	-1.9(5)	M1 (ΔI=1)	M1	1
160.7(1)	58	0.39(3)	-0.5(2)	M1 (ΔI=1)	M1	1
174.27(8)	60	0.52(4)	-0.8(2)	M1 (ΔI=1)	M1	1
219.1(2)	53	0.32(6)	—	Dipole	(M1)	1
230.6(2)	29	0.76(8)	-1.0(2)	M1 (ΔI=1)/E1(ΔI=0)	M1 [a]	1
275.7(1)	45	1.2(2)	0.5(1)	E2 (ΔI=2)	E2	1
290.9(2)	30	0.6(1)	—	Dipole	(M1)	1
297.0(3)	20	0.4(2)	—	Dipole	(M1)	1
305.1(1)	59	0.8(1)	0.5(1)	E2 (ΔI=2)	E2	1
334.9(1)	55	0.8(1)	0.8(2)	E2 (ΔI=2)	E2	1
346(1)	8	—	—	—	(M1)	1
362(2)	4	—	—	—	(M1)	1
383(2)	4	—	—	—	(M1)	1
393.4(5)	41	0.8(1)	—	Quadrupole	(E2)	1
449.5(1)	54	1.1(1)	0.7(2)	E2 (ΔI=2)	E2	1
521.3(1)	63	0.8(1)	0.7(2)	E2 (ΔI=2)	E2	1
586.4(3)	66	0.8(2)	—	Quadrupole	(E2)	1
642.4(8)	42	0.9(3)	—	Quadrupole	(E2)	1
708.2(4)	27	—	—	—	(E2)	1
744.5(3)	37	—	—	—	(E2)	1
802.0(6)	34	—	—	—	(E2)	1
829.6(8)	20	—	—	—	(E2)	1
872.4(8)	8	—	—	—	(E2)	1
903.5(9)	8	—	—	—	(E2)	1
938(1)	—	—	—	—	(E2)	1
974(1)	—	—	—	—	(E2)	1
1007(2)	—	—	—	—	(E2)	1
1043(2)	—	—	—	—	(E2)	1
1077(2)	—	—	—	—	(E2)	1
72.7(1)[b]	*b*	—	—	—	(M1)	2
72.7(1)[b]	*b*	—	—	—	(M1)	2
106.74(6)	66	0.5(1)	—	Dipole	(M1)	2
142.31(8)	72	0.62(5)	0.02(25)	M1 (ΔI=1)	M1	2
179.7(3)	—	—	—	—	(E2)	2
180.20(3)	80	0.44(5)	-0.1(2)	M1 (ΔI=1)	M1	2
212.8(1)	71	0.6(1)	-0.2(1)	M1 (ΔI=1)	M1	2
250.4(5)	—	1.7(5)	—	Quadrupole	(E2)	2
250.0(1)	—	0.5(1)	—	Dipole	(M1)	2
277.5(1)	13	0.8(1)	-0.8(2)	M1 (ΔI=1)	M1	2
314.1(2)	24	—	—	—	(M1)	2

E_γ, keV	I^c_γ	DCO	Linear Polarisation	Measured (λ L)	Assigned (λ L)	Band
323.3(5)	23	0.8(1)	0.6(2)	E2 (ΔI=2)	E2	2
334.4(3)	18	—	—	—	(M1)	2
369.4(3)	10	—	—	—	(M1)	2
383.5(3)	3	—	—	—	(M1)	2
393.9(2)	100	1.2(2)	0.3(2)	E2 (ΔI=2)	E2	2
415.0(9)	27	—	—	—	(M1)	2
464.4(2)	40	1.9(2)	0.5(1)	E2 (ΔI=2)	E2	2
528.6(1)	42	1.0(1)	0.5(1)	E2 (ΔI=2)	E2	2
591.9(2)	41	2.9(1)	1.2(2)	E2 (ΔI=2)	E2	2
648.9(2)	43	0.8(1)	1.1(2)	E2 (ΔI=2)	E2	2
703.8(2)	28	1.8(2)	0.7(2)	E2 (ΔI=2)	E2	2
752.8(2)	27	1.3(2)	1.1(2)	E2 (ΔI=2)	E2	2
798.1(3)	22	2.5(3)	2.2(3)	E2 (ΔI=2)	E2	2
831.7(3)	22	—	—	—	(E2)	2
872.3(5)	17	—	—	—	(E2)	2
922(1)	—	—	—	—	(E2)	2
964(1)	—	—	—	—	(E2)	2
1002(1)	—	—	—	—	(E2)	2
1040(2)	—	—	—	—	(E2)	2
1080(2)	—	—	—	—	(E2)	2
87.5(2)	*e*	0.56(3)	—	Dipole	(M1)	3
115.6(1)	*f*	0.87(2)	—	Quadrupole	(M1)	3
122.9(1)	72	0.88(3)	—	Quadrupole	(M1)	3
150.6(3)	59	0.82(5)	—	Quadrupole	(M1)	3
168.6(2)	16	1.04(2)	—	Quadrupole	(M1)	3
204(1)	*g*	1.01(3)	—	Quadrupole	(E2)	3
233.2(6)	—	—	—	—	(M1)	3
238.9(6)	61	1.01(3)	—	Quadrupole	(E2)	3
292.2(3)	43	1.11(2)	0.4(2)	E2 (ΔI=2)	E2	3
320.1(3)	65	0.92(2)	0.7(2)	E2 (ΔI=2)	E2	3
384.8(5)	40	0.96(6)	2.1(3)	E2 (ΔI=2)	E2	3
409.6(3)	51	0.94(2)	0.6(2)	E2 (ΔI=2)	E2	3
481.7(4)	26	0.87(4)	1.8(4)	E2 (ΔI=2)	E2	3
515.9(3)	78	1.03(2)	0.3(3)	E2 (ΔI=2)	E2	3
581.2(4)	100	0.83(6)	—	Quadrupole	(E2)	3
625.3(4)	66	1.08(3)	0.2(2)	E2 (ΔI=2)	E2	3
679.5(8)	57	1.4(1)	—	Quadrupole	(E2)	3
730.6(4)	30	1.0(1)	—	Quadrupole	(E2)	3
774.3(5)	15	1.2(1)	—	Quadrupole	(E2)	3
829.4(3)	38	0.96(5)	—	Quadrupole	(E2)	3
865.8(4)	8	0.9(2)	—	Quadrupole	(E2)	3
916.8(5)	—	—	—	—	(E2)	3
951.0(4)	—	—	—	—	(E2)	3
1025(2)	—	—	—	—	(E2)	3
1028(2)	—	—	—	—	(E2)	3
77.2(5)	*f*	0.62(3)	—	Dipole	(M1)	4
103.6(2)	*e*	0.87(2)	—	Quadrupole	(M1)	4
113.9(1)	*f*	0.82(2)	—	Quadrupole	(M1)	4
149.2(9)	39	0.89(1)	—	Quadrupole	(M1)	4

E_γ, keV	I^c_γ	DCO	Linear Polarisation	Measured (λ L)	Assigned (λ L)	Band
164(1)	23	0.91(2)	—	Quadrupole	(M1)	4
181(1)	[g]	0.94(3)	—	Quadrupole	(E2)	4
187.9(8)	18	—	—	—	(M1)	4
217.8(2)	[g]	0.91(1)	0.1(2)	E2 (ΔI=2)	E2	4
223(1)	—		—	—	(M1)	4
227(1)	—		—	—	(M1)	4
263.5(2)	85	1.12(2)	0.5(2)	E2 (ΔI=2)	E2	4
284.1(5)	—	—	—	—	(M1)	4
313.5(2)	70	1.22(1)	0.1(2)	E2 (ΔI=2)	E2	4
352.1(2)	73	0.91(1)	1.3(2)	E2 (ΔI=2)	E2	4
414.5(2)	91	0.99(1)	0.5(2)	E2 (ΔI=2)	E2	4
449.1(2)	63	1.02(3)	0.8(2)	E2 (ΔI=2)	E2	4
506.6(8)	68	0.97(2)	—	Quadrupole	(E2)	4
540.2(4)	44	1.09(3)	—	Quadrupole	(E2)	4
590.5(1)	100	1.09(5)	0.9(2)	E2 (ΔI=2)	E2	4
624.7(2)	100	1.04(5)	—	Quadrupole	(E2)	4
674.5(4)	91	1.04(5)	—	Quadrupole	(E2)	4
706.1(2)	84	1.0(1)	—	Quadrupole	(E2)	4
757.6(2)	52	1.2(1)	—	Quadrupole	(E2)	4
788.8(3)	36	1.0(1)	—	Quadrupole	(E2)	4
854.0(5)	27	0.8(2)	—	Quadrupole	(E2)	4
870.5(7)	—	—	—	—	(E2)	4
928(1)	—	—	—	—	(E2)	4
941(2)	—	—	—	—	(E2)	4
1029(2)	—	—	—	—	(E2)	4
1113(2)	—	—	—	—	(E2)	4

[a] Expected $\Delta I = 1$ character.

[b] Inability to uniquely gate on these transitions precludes unique measurement of their individual energies and intensities.

[c] Intensities presented are relative to the strongest γ ray in each band. The quoted figures are not comparable between bands. The counts have been efficiency corrected but not corrected for internal conversion.

[d] Transition is out of an isomeric state and does not have a measured intensity.

[e] γ ray used (gated) to select this band so doesn't have a measured intensity.

[f] γ ray energy outside the range of efficiency calibration 121.8 — 1408.0 keV, so accurate efficiency correction was not possible.

[g] γ ray energy cascades in parallel to the gating γ ray, so does not appear in spectrum used to measure intensities.

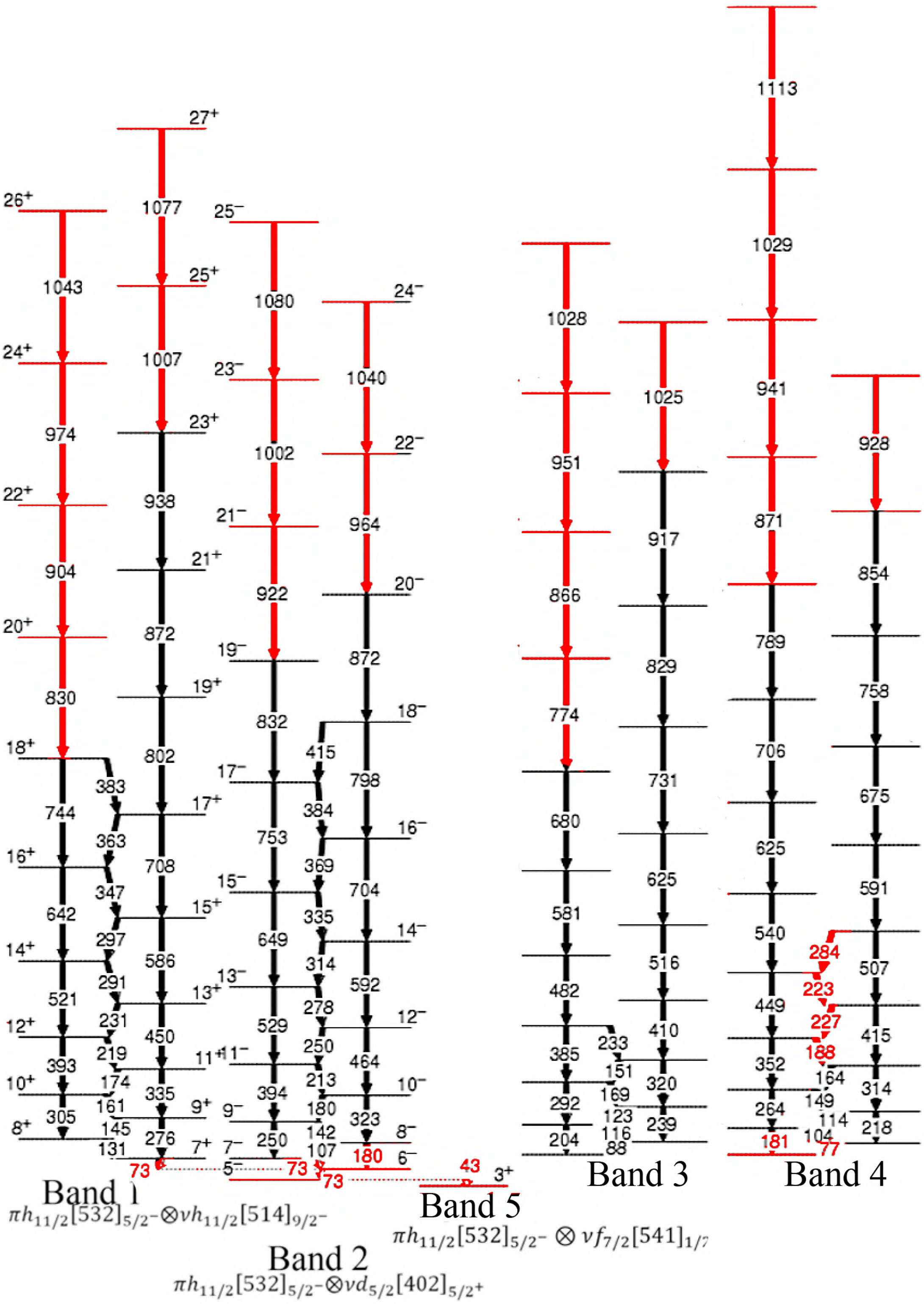
26+
1043
24+
974
22+
904
20+
830
18+
744
16+
642
14+
521
12+
393
10+
305
8+
383
363
347
297
291
231
219
174
161
145
131
73
27+
1077
25+
1007
23+
938
21+
872
19+
802
17+
708
15+
586
13+
450
11+
335
9+
276
7+
Band 1
πh11/2[532]5/2−⊗νh11/2[514]9/2−
25−
1080
23−
1002
21−
922
19−
832
17−
753
15−
649
13−
529
11−
394
9−
250
7−
5−
73
415
384
369
335
314
278
250
213
180
142
107
73
24−
1040
22−
964
20−
872
18−
798
16−
704
14−
592
12−
464
10−
323
8−
180
6−
Band 2
πh11/2[532]5/2−⊗νd5/2[402]5/2+
43
3+
Band 5
πh11/2[532]5/2− ⊗ νf7/2[541]1/7
1028
951
866
774
680
581
482
385
292
204
233
151
169
123
116
88
1025
917
829
731
625
516
410
320
239
Band 3
1113
1029
941
871
789
706
625
540
449
352
264
181
284
223
227
188
164
149
114
104
77
928
854
758
675
591
507
415
314
218
Band 4

FIGURE 6.15: ^{132}Pm energy level scheme. Ordering of γ rays has been determined using double and triple γ coincidence analysis as detailed in the text. Structural configuration assignments are discussed in Section 6.4. Levels and γ rays highlighted in red are new to this work.

6.3 Half-life measurements

With all of the prompt and focal-plane transitions identified, isomeric half-lives can be measured. Measurement of the half-life for the 7^+ state of band 1, depopulated by a 73 keV γ ray, is displayed in Figure 6.16. In a recoil-tagged focal-plane γ spectrum, the 73 keV peak suffers major contamination from a strong 79 keV peak, associated with ^{130}Pr. Further event selectivity is enabled by requiring observation by JUROGAM of any two of the prompt γ rays belonging to band 1 of this nucleus. The resultant focal-plane γ spectrum is then free of contamination from the strong 79 keV peak. The half-life measurement then comes from the time difference between recoil implantation and subsequent 73 keV γ decay. Though gating on 73 keV should technically introduce two components to the lifetime plot, this is not a hindrance here since the half-life of the second (M1) 73 keV γ ray must be much smaller than that of the delayed transition because it is seen within the 20 ns prompt coincidence window at the target position. The model for the numerical fit is $y = Ae^{Bx} + Cx + D$, with $B = -1/t_{1/2}$, where $t_{1/2}$ is the half-life of the state. The measured half-life of the isomer is then $t_{1/2} = (187 \pm 4)$ ns.

Measurement of the half-life of the isomeric state at $E = 43$ keV is tricky owing to the 43 keV γ ray lying among the broad region of internal-conversion x-rays. Gating on this energy in a matrix of energy against recoil-γ time difference — as was performed in Figure 6.16 — yields a multitude of half-life components associated with the plethora of x-rays. To circumvent this issue, the photopeak area for the 43 keV transition was measured in increasing intervals of 400 ticks (4 μs) after implantation. Assuming that the intensity of the x-ray background is constant, the exponential decrease in intensity is then representative of the extended lifetime of this isomeric state. The result of these measurements is displayed in Figure 6.17. Figure 6.17, panel (a), is illustrative of the loss of transition intensity after representative periods of time have elapsed. The stark contrast between the half-lives of the isomers associated with the 43 and 73 keV transitions is visible here; even after 40 μs have elapsed, there is still a statistically significant level of counts at 43 keV and the counts at 73 keV have faded to background. Figure 6.17, panel (b), displays the natural logarithm of the peak area as a function of the time following recoil implantation. From the straight-line fit, we obtain a half-life of $t_{1/2} = (19.9 \pm 0.5)\ \mu$s.

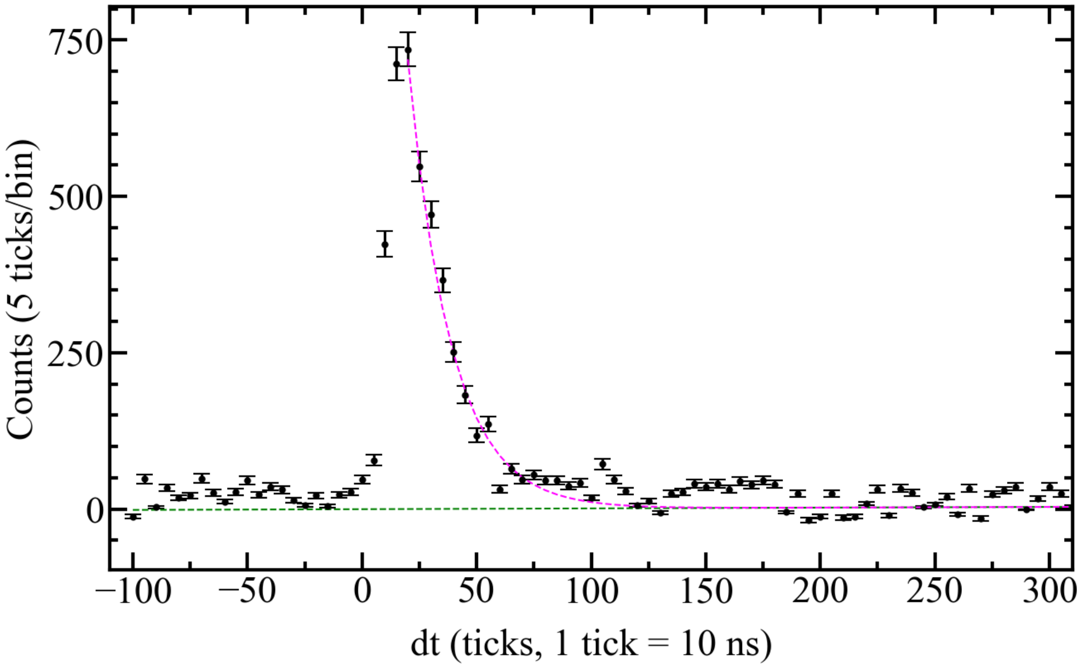

FIGURE 6.16: Timing difference between the implantation of a mass-132 recoil into the DSSD and a subsequent 73 keV γ-decay out of the isomeric state at the base of band 1. The fit is a single-term exponential, with a straight-line background. $A : 209 \pm 92, B : -0.053 \pm 0.001, C : 0.012 \pm 0.003, D : -0.1 \pm 1.7$

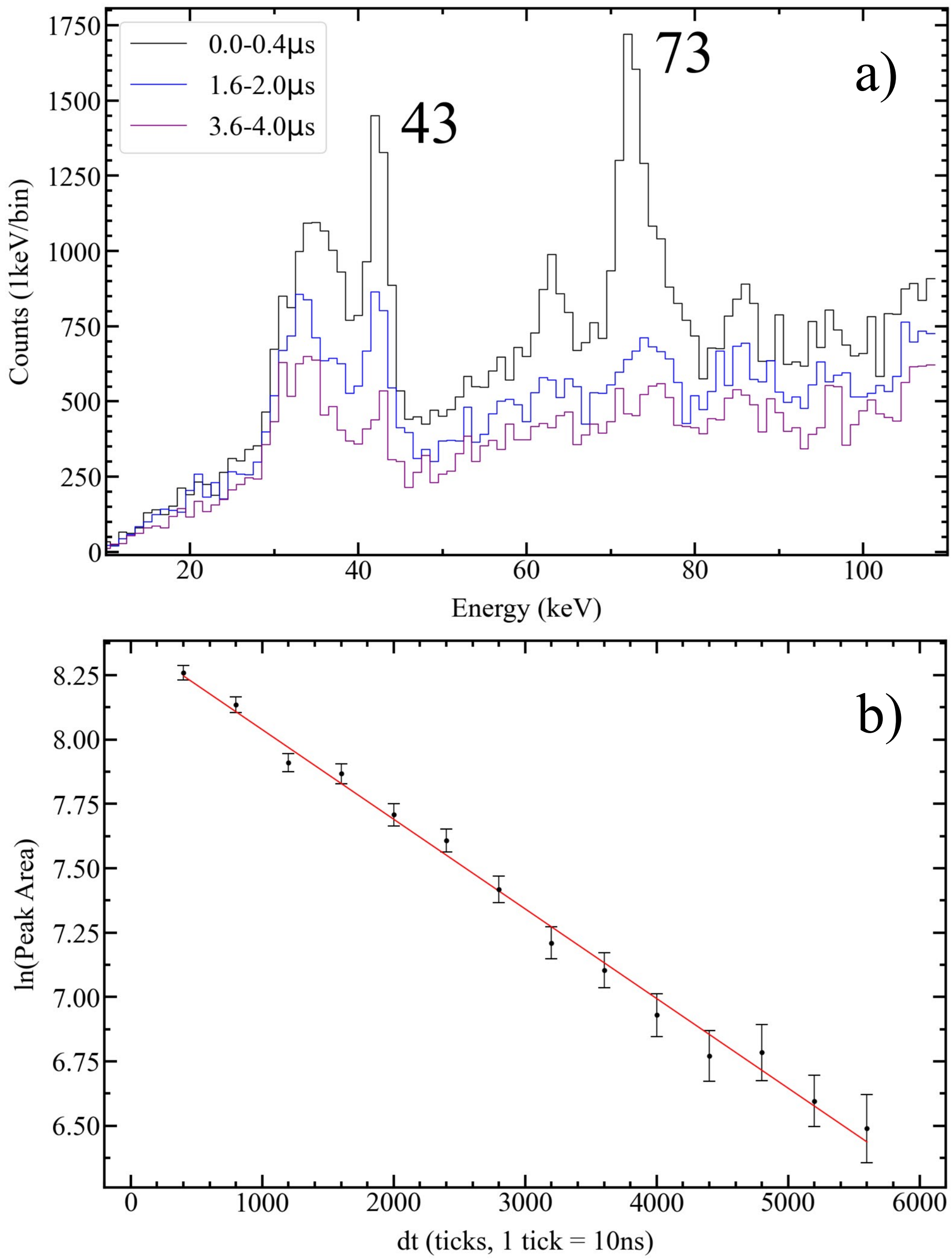

FIGURE 6.17: Panel a): 43 and 73 keV transitions associated with two isomeric states in ^{132}Pm measured for three 400 tick wide intervals after recoil implantation. Panel b): Photopeak area for the 43 keV transition as a function of time following recoil implantation. Numerical fit is modelled by a straight line, fit parameters: $m : -(3.48 \pm 0.09) \times 10^{-4}, c : 8.34 \pm 0.03, \chi^2/NDF : 0.78$

6.4 Discussion

Given the broad inconsistencies found throughout the systematic survey (Table 6.1), the following analysis shies away from relying too heavily on systematic comparison for assignment of band configurations. Starting from the beginning, we summarise what we know so far. In the present study, observation of delayed γ rays following the isomeric decay of bands 1 and 2 allowed fixture of their relative excitation energies, with band 1 seen to be higher in excitation energy than band 2. Furthermore, the isomeric nature of band 1 and 2 allow fixation of their bandhead spin/parity values as $I = K = \Sigma\Omega$. Sharing the same number of protons as its neighbour, ^{131}Pm, and a similar deformation, we expect to see some structures built on the same $h_{11/2}$ proton. The isomeric nature of bands 1 and 2 point to K-hindrances for the decays out of these bands. The relatively short half-lives of these bands (146 ns and 2.8 μs) indicate that the change in K is likely not very large. The spin/parity for the ground state of this nucleus has been previously assigned as 3^+, from consideration of angular momentum and energy conservation from the β_+ decay into the neodymium daughter [100]. The ground state deformation of this nucleus is predicted by P. Moller, *et al* [57], to be $\beta_2 = 0.34$ with negligible β_3 and β_4 components. With this in mind, we consult the Nilsson diagrams for protons and neutrons as displayed in Figure 6.18.

The Fermi surface for protons lies among the bottom end of the $h_{11/2}$ shell, with low to mid-Ω orbitals available for occupation. The neutron Fermi surface lies in the middle of $h_{11/2}$ shell with mid to high-Ω orbitals available for occupation. At this deformation, there are also substantial intrusions from low-Ω $f_{7/2}$ and extrusions from high-Ω $g_{7/2}$ and $d_{5/2}$ orbitals.

Experimental single-particle alignments, routhians and dynamic moments of inertia for bands 1 - 4 are displayed in Figures 6.19 and 6.20. The bandhead spin used in the production of these plots, I, for bands 1 and 2 is assigned as

7^+ and 5^-, respectively. Their assignment comes from comparison with the theoretical routhian curves displayed in Figure 6.21 and is discussed below. The bandhead spin for bands 3 and 4 was assigned as $I = 5$ for both bands. This value is not from any theoretical comparison or experimental observation and was picked purely so alignment and routhian curves could be plotted.

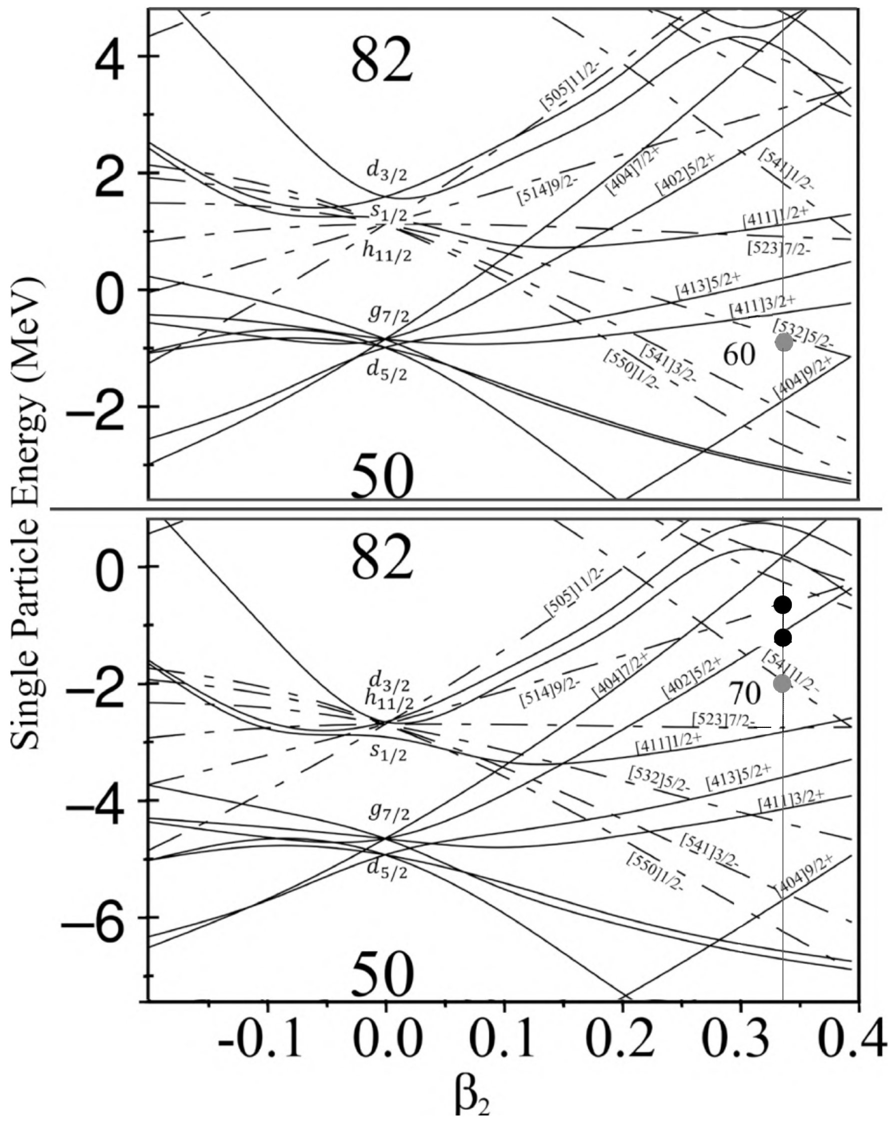

FIGURE 6.18: Nilsson diagram calculated using a Woods-Saxon potential for protons (**top**) and neutrons (**bottom**) focused on Z = 60 and N = 70, respectively. A vertical line is rendered at $\beta_2 = 0.34$, representative of the predicted deformation of this nucleus. Grey dots represent the proposed orbitals occupied by the nucleons in the ground state. Black dots represent the proposed orbitals occupied in isomeric states.

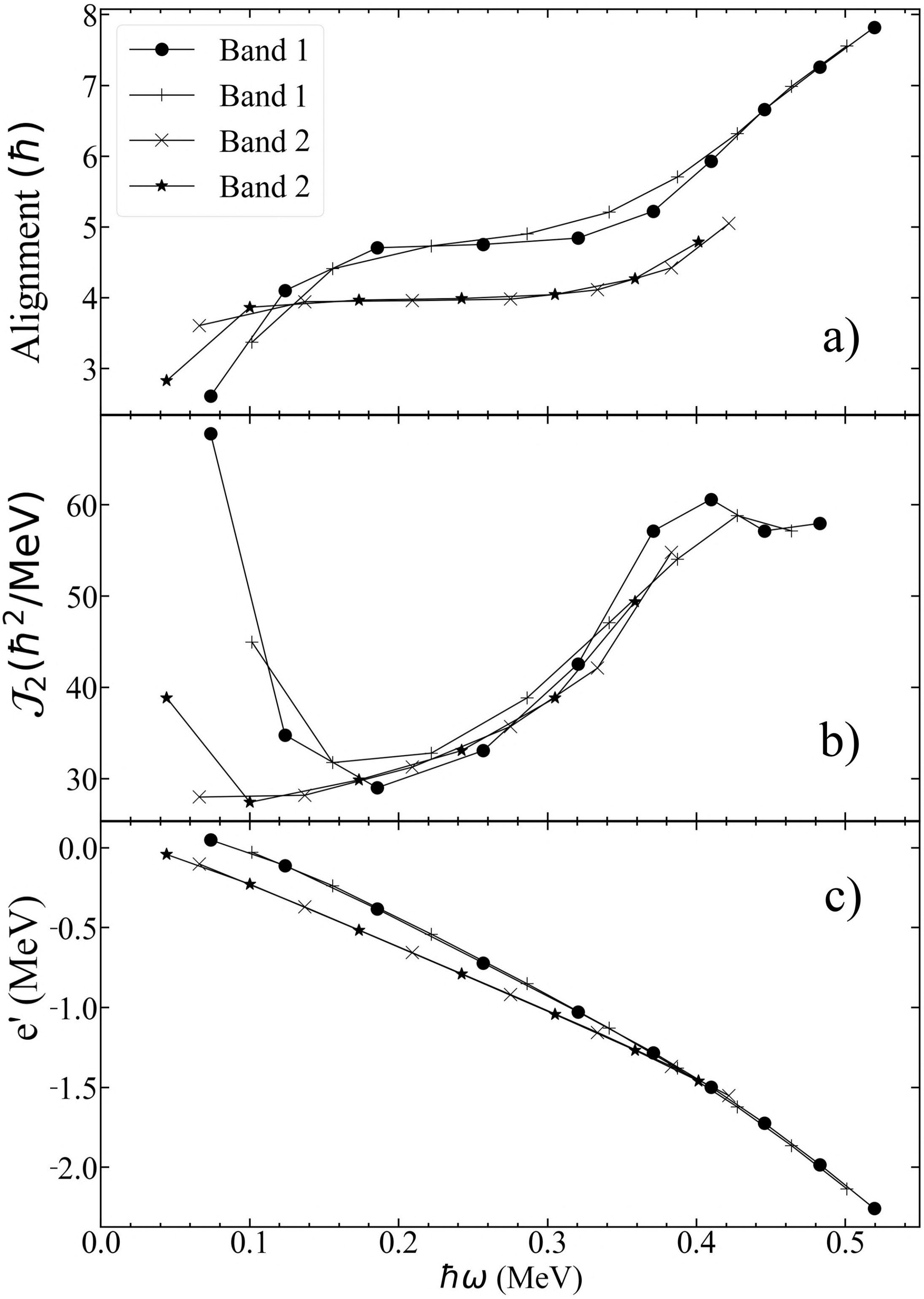

FIGURE 6.19: Experimental single-particle alignment, dynamic moment of inertia and experimental routhian for bands 1 and 2 in ^{132}Pm. Harris parameters used in production of this figure: $\mathcal{J}_0 = 29.9\,\hbar^2/\mathrm{MeV}$ and $\mathcal{J}_1 = 15.8\,\hbar^4/\mathrm{MeV}^3$.

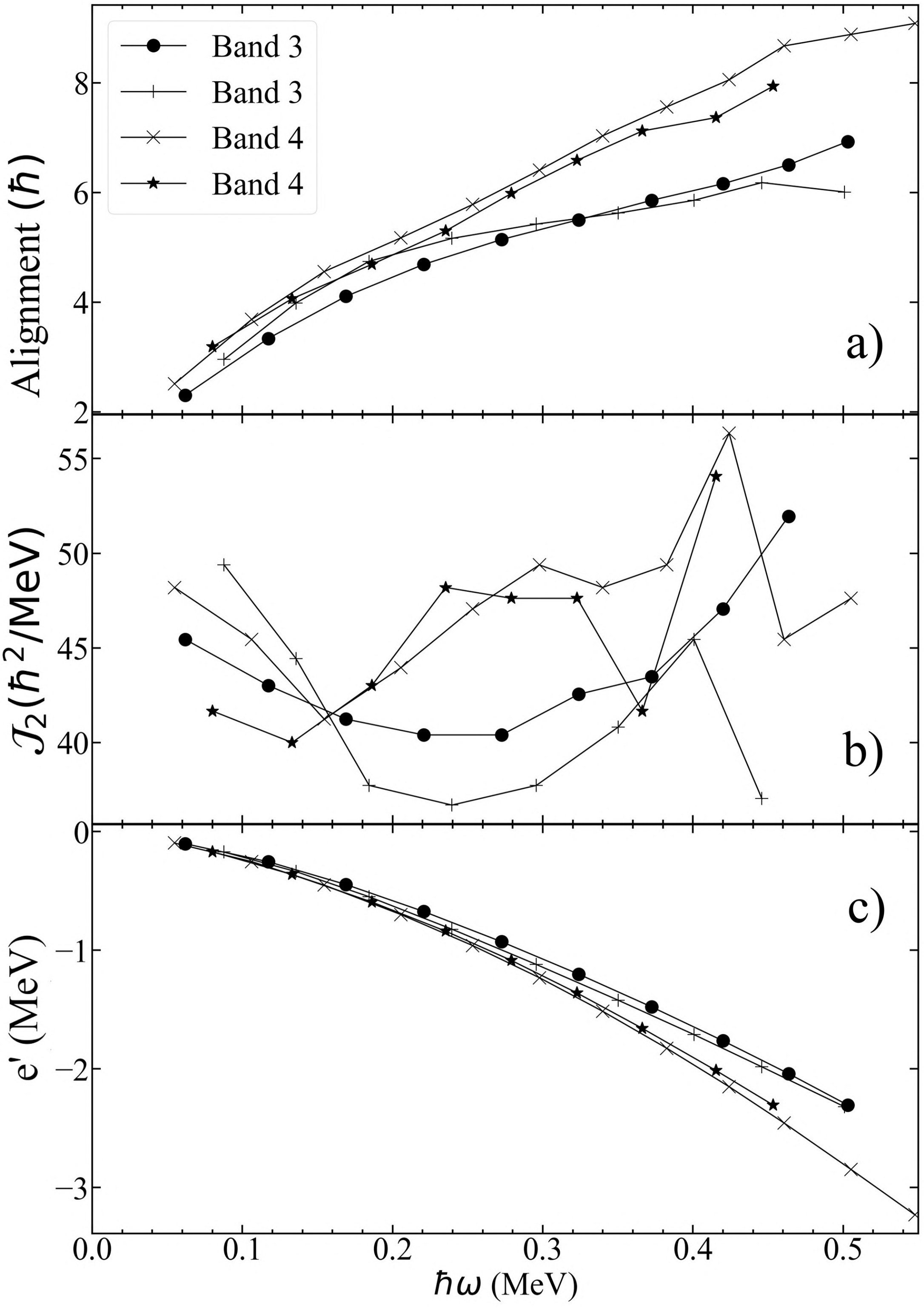

FIGURE 6.20: Experimental single-particle alignment, dynamic moment of inertia and experimental routhian for bands 3 and 4 in ^{132}Pm. Harris parameters used in production of this figure: $\mathcal{J}_0 = 29.9\,\hbar^2/\mathrm{MeV}$ and $\mathcal{J}_1 = 15.8\,\hbar^4/\mathrm{MeV}^3$

Figure 6.21 displays corresponding cranked shell model quasiparticle routhians for both protons and neutrons. The states seen here are labelled according to the standard alphabetical labelling scheme, which is summarised in Table 6.4. The Nilsson levels associated with these quasiparticles at zero rotational frequency are listed here too.

TABLE 6.4: Quasiparticle labelling scheme for ^{132}Pm along with their assigned Nilsson configuration at zero rotational frequency.

Label	$(\pi,\alpha)_n^a$	Configuration^b
	Quasiprotons	
A	$(+,+1/2)_1$	$d_{5/2}[411]3/2^+$
B	$(+,-1/2)_1$	$d_{5/2}[411]3/2^+$
C	$(+,-1/2)_2$	$g_{7/2}[413]5/2^+$
D	$(+,+1/2)_2$	$g_{7/2}[413]5/2^+$
E	$(-,-1/2)_1$	$h_{11/2}[532]5/2^-$
F	$(-,+1/2)_1$	$h_{11/2}[532]5/2^-$
G	$(-,-1/2)_2$	$h_{11/2}[541]3/2^-$
H	$(-,+1/2)_2$	$h_{11/2}[541]3/2^-$
	Quasineutrons	
a	$(+,-1/2)_1$	$g_{7/2}[402]5/2^+$
b	$(+,+1/2)_1$	$g_{7/2}[402]5/2^+$
c	$(+,+1/2)_2$	$s_{1/2}/d_{3/2}[411]1/2^+$
d	$(+,-1/2)_2$	$s_{1/2}/d_{3/2}[411]1/2^+$
e	$(-,-1/2)_1$	$h_{11/2}[514]9/2^-$
f	$(-,+1/2)_1$	$h_{11/2}[514]9/2^-$
g	$(-,-1/2)_2$	$f_{7/2}[541]1/2^-$
h	$(-,+1/2)_2$	$f_{7/2}[541]1/2^-$

[a] The subscript n numbers the quasiparticle's excitations of a given signature and parity starting with the lowest in energy at $\hbar\omega$ = 0 MeV.

[b] Nilsson configurations only valid at $\hbar\omega$ = 0 MeV.

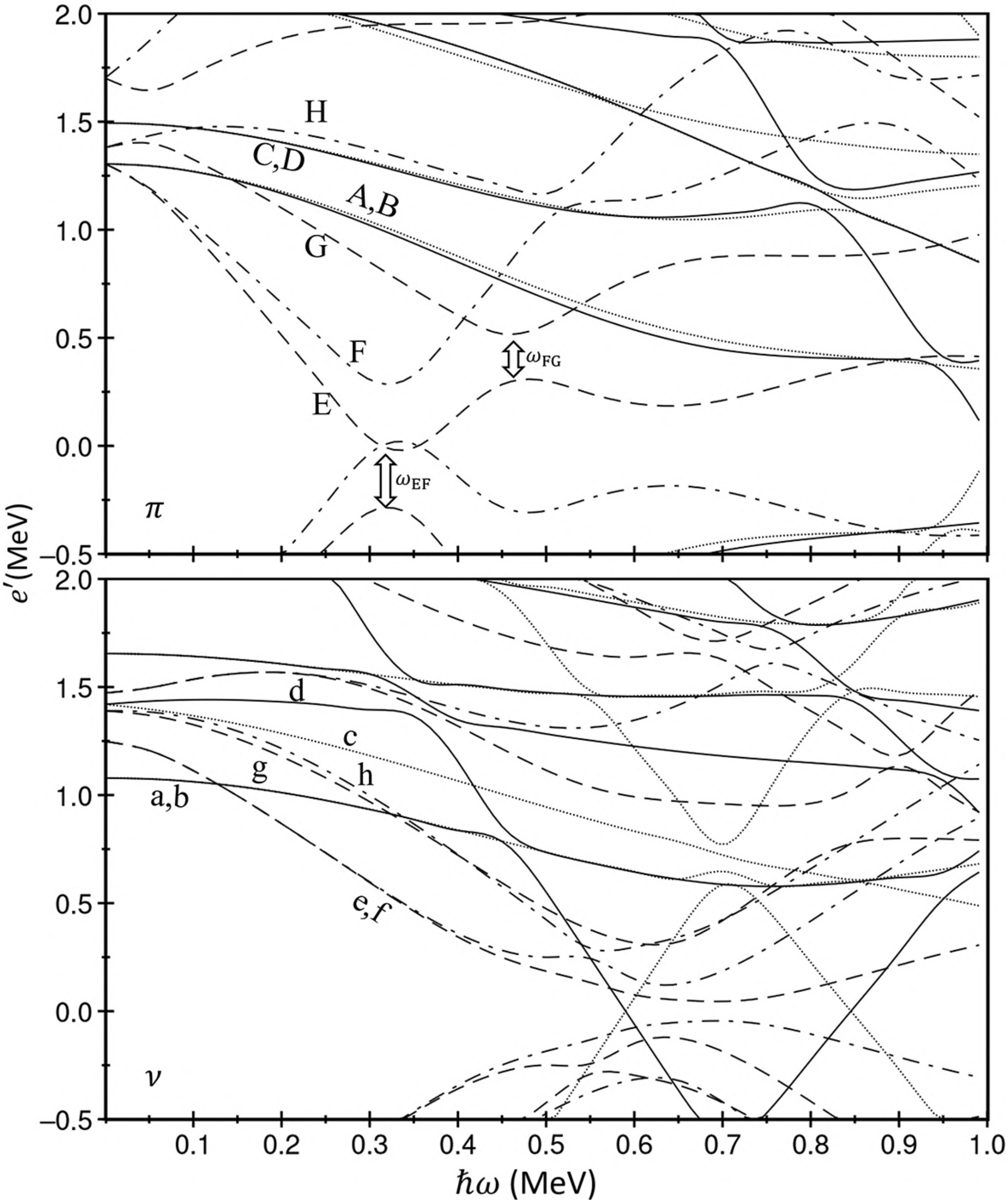

FIGURE 6.21: Cranked Shell Model quasiparticle Routhians (Panel π: protons, Panel ν: neutrons), generated using a universal, triaxial Woods-Saxon potential. Labels corresponding to Nilsson levels are only valid at zero spin (i.e $0\hbar\omega$) since rotation causes states to become a mixture of different wavefunctions. β_2= 0.340, β_4 = 0.0, γ = 0.0°. (π, α) : solid = (+,+1/2), dotted = (+,–1/2), dot–dash = (–,+1/2), dashed = (–,–1/2)

We can see from the alignment plots that bands 1 and 2 see a gentle alignment gain beyond $\hbar\omega = 0.35$ MeV and bands 3 and 4 do not see any alignment effects; the $h_{11/2}$ proton alignment expected at $\hbar\omega = 0.35$ MeV is notably absent for all four bands, so we must conclude that a proton is occupying this orbital for each band and is causing the Pauli blocking of the low-spin crossing. Evidence for this interpretation can be obtained from doubly odd neighbour, ^{134}Pm. This nucleus exhibits a striking $h_{11/2}$ proton alignment at precisely $\hbar\omega = 0.3$ MeV. The alignment for the other band is notably less intense, sloping gently upward beyond $\hbar\omega = 0.35$ MeV in a similar manner to all four bands observed in the present work. The latter band was designated as being built upon an $h_{11/2}$ proton, and so is the case in this work with all bands being assigned as being based on at least one quasiproton with Nilsson configuration $\pi h_{11/2}[532]5/2^-$.

The alignment seen by bands 1 and 2 at $\hbar\omega = 0.4$ MeV is likely the second (FG) proton crossing, predicted by the CSM calculations to occur at $\hbar\omega \approx 0.45$ MeV. Extending these bands to higher spin, we would also expect to see the EH proton crossing at $\hbar\omega = 0.6$ MeV. Turning our attention to the neutrons, we see that the levels closest to the Fermi surface are $[514]9/2^-$, $[402]5/2^+$, $[411]1/2^+$ and $[541]1/2^-$. We know from the γ-coincidence analysis that band 1 lies higher in excitation energy than band 2. It is therefore appropriate that band 1 has a higher spin than band 2. The isomeric nature of both bands also points to these bands having a high-K configuration. Thankfully, the available states make these assignments simple, with only two of the four closest to the Fermi surface offering a high-Ω value. Considering all of the above, we assign the neutron $[514]9/2^-$ configuration to band 1 and the $[402]5/2^+$ configuration to band 2. The two-quasiparticle configuration for both bands is then, band 1: $\pi[532]5/2^- \otimes \nu[514]9/2^-$ and, following the Gallagher-Moszkowski coupling rules, we obtain a bandhead $I^\pi = K^\pi = 7^+$, and band 2: $\pi[532]5/2^-$

$\otimes\nu[402]5/2^+$ resulting in bandhead $I^\pi = K^\pi = 5^-$. This requires the multipolarity of the 73 keV transition depopulating band 1 to be E1. It also indicates that both 73 keV transitions in band 2 should have an M1 multipolarity, or else the rest of the band will have the wrong parity for this configuration. Systematic comparison shows that the band built on the $\pi h_{11/2} \otimes \nu h_{11/2}$ configuration is commonly assigned as being depopulated by a single E1 transition; Wadsworth, *et al*, measured an angular correlation ratio of 0.82 for this transition in ^{134}Pm, consistent with dipole nature [93]. The proposed configuration for bands 1 and 2 also results in their 7+ and 7- states having the same excitation energy within the precision of the γ spectrometer and the systematic error bounds brought on by gain matching. For a doubly odd nucleus, the expected preferred (energetically favoured) signature of a configuration is defined by

$$\begin{aligned} \alpha_f &= j \bmod 2, \\ &= j_p \bmod 2 + j_n \bmod 2, \end{aligned} \tag{6.1}$$

where j_p and j_n are the total angular momenta of the shells associated with the unpaired valence proton and neutron, respectively. For the $\pi h_{11/2} \otimes \nu h_{11/2}$ and $\pi h_{11/2} \otimes \nu d_{5/2}$ configurations proposed for bands 1 and 2, the preferred signature is $\alpha = 1$ (odd spins), which is in agreement with the assigned spin/parities for these bands. Similar $\pi h_{11/2} \otimes \nu h_{11/2}$ configurations are observed in odd-odd neighbours ^{132}Pr and ^{134}Pm, where the proposed bandhead spin/parity is even. Following the arguments proposed in this chapter, it is reasonable to conclude that the $\pi h_{11/2} \otimes \nu h_{11/2}$ bands in each of these nuclei should have their bandhead spin/parities lowered by $1\hbar$ such that the predicted preferred signature is energetically preferred and these levels are in agreement with those in this chapter.

Band 2 is seen to decay into the proposed ground state by a delayed (19.9

μs) 43 keV transition. The ground state for this nucleus has previously been assigned as 3^+ based on consideration of preferred ground states given observed β_+ decay feeding into the 2^+ and 4^+ states of the neodymium daughter [100]. In order for a single γ ray to make the transition from the 5^- bandhead of band 2 to the 3^+ ground state, it must have an M2 multipolarity.

TABLE 6.5: Weisskopf single-particle estimates of transition rate for 43 and 73 keV. Owing to the low energy of these transitions, the estimates have been adjusted to account for their internal conversion coefficients which can be significant within this energy regime.

Energy (keV)	E1 (s)	M1 (s)	E2 (s)	M2 (s)
43	7.31×10^{-12}	1.01×10^{-10}	6.67×10^{-8}	2.48×10^{-6}
73	1.07×10^{-12}	1.48×10^{-11}	3.79×10^{-8}	4.60×10^{-7}

Table 6.5 displays the Weisskopf estimates for 43 and 73 keV γ rays of various multipolarities. Since the internal conversion coefficients can be significant for transitions of this energy (43 keV M2 has an internal conversion coefficient of 132 according to BrIcc [67]) the Weisskopf estimates have been adjusted to account for this. It can be seen that the predicted transition rate for a 43 keV M2 is 2.48×10^{-6} s, which is consistent with the order of magnitude of the half-life measured for this transition. Table 6.5 also highlights the significant K-hindrance seen by the 73 keV E1 depopulating band 1. With a measured half-life of 194 ns and a ΔK value of 2 between the bandheads of bands 1 and 2, this transition occurs 1.4×10^5 times slower than the Weisskopf estimate for a 73 keV E1. The ground-state configuration is proposed to be $\pi[532]5/2^- \otimes \nu[541]1/2^-$. Given the single 43 keV transition out of band 2, it makes sense for a single particle to change configuration. This idea is further substantiated by the Weisskopf estimate for this transition having a similar predicted transition rate to the observed half-life. This configuration also results in a bandhead which matches the pre-existing proposal for the ground-state spin/parity of this nucleus, 3^+. Nothing definitive can be said about

the neutron configuration for bands 3 and 4. By process of elimination from the closest states available to the Fermi surface, the remaining candidates are the low-Ω [541]1/2$^-$ and [411]1/2$^+$ orbitals. Also close to the Fermi surface at low-spin is the [523]7/2$^-$ orbital. Because of the predicted close proximity of the two negative parity orbitals, the predicted signature splitting for the quasineutrons based on [541]1/2$^-$ is very low, contrary to what is usually expected for a low-Ω orbital. Here, the two $(\pi, \alpha) = (-, +1/2)$ levels repel each other at low spin. The small but consistent signature splitting is consistent with that seen for band 3. Similarly the quasineutron orbitals i and j — associated with the [523]7/2$^-$ orbital — have zero signature splitting at low spin, but increases to large signature splitting as rotational frequency increases. This could be consistent with band 4's experimental routhian, but the band is not observed to high enough frequency to reproduce the theoretically predicted splitting. It is possible that these bands are based on more than two quasiparticles, their high spin and probable high K values dramatically hindering their decay time.

6.4.1 B(M1)/B(E2) Ratios

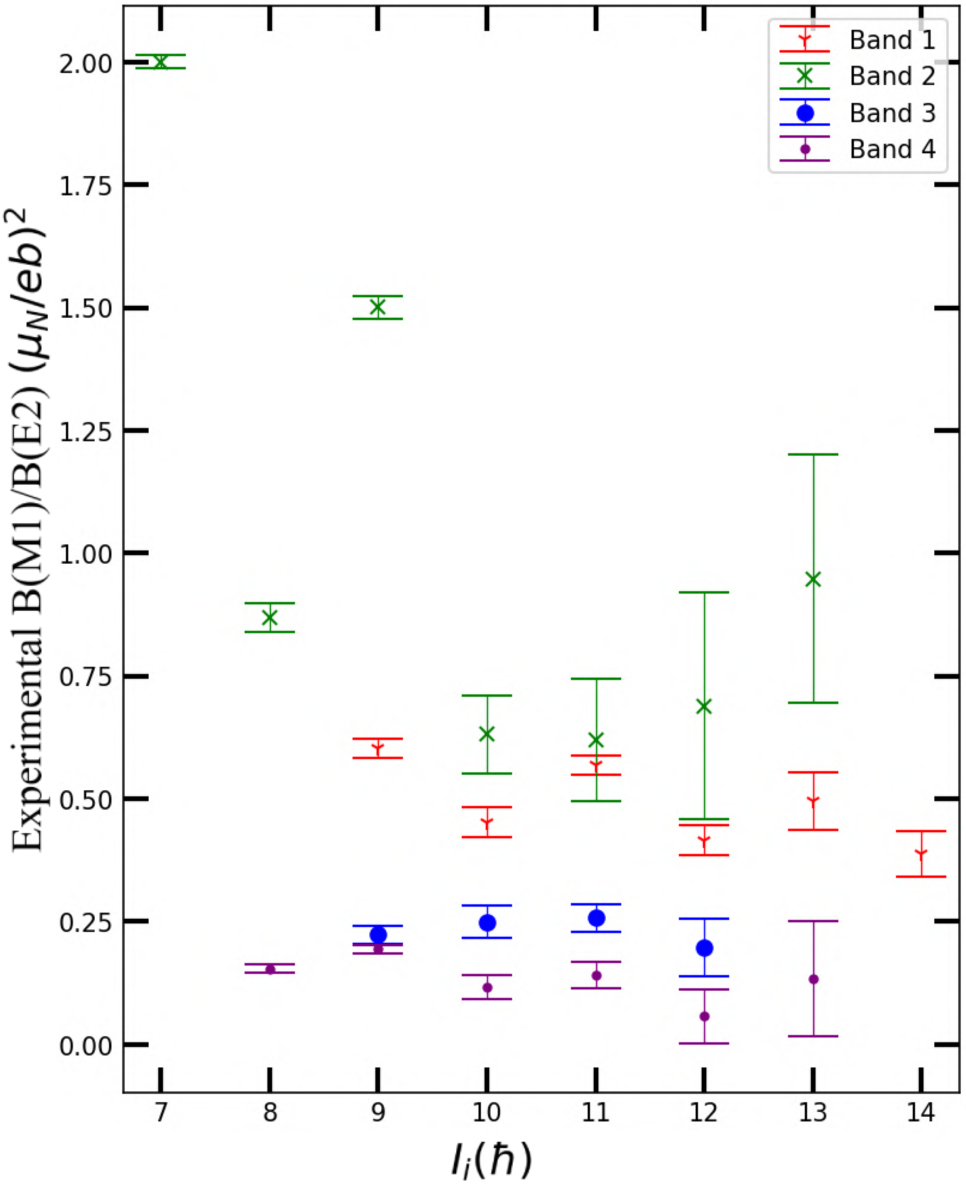

FIGURE 6.22: Experimental B(M1)/B(E2) ratios determined for each of the four rotational bands in ^{132}Pm.

The average ratios for the four bands are, respectively, 0.49 ± 0.08, 1.04 ± 0.48, 0.23 ± 0.02 and 0.13 ± 0.04 $(\mu_N/eb)^2$. As was the case with ^{129}Nd, an attempt was made to obtain theoretical B(M1)/B(E2) ratios using the Donau-Fraeundorf geometrical formalism detailed in Chapter 3. The ratios obtained were not found to be consistent with the experimentally measured values. An essential pre-requisite of the formalism is that the J spin vectors of the orbitals comprising a particular band are perpendicular to one another. The proposed configuration for bands 1 and 2 involves three $h_{11/2}$ orbitals and a $d_{5/2}$ orbital each with mid-to-high Ω values, so do not satisfy the geometrical formalism.

Chapter 7

Conclusion

Though the experimental setup at JYFL-ACCLAB was able to provide for a rich and complete spectroscopy for the three nuclides discussed in this thesis, this was not without shortfall. In addition, other limitations were encountered resulting from the initial experimental parameters which ultimately prevented study of additional nuclei. Contained within this chapter are discussions concerning these limitations, proposed future improvements, as well as a summary on the work performed.

7.1 ^{129}Nd

Utilising the technique of recoil-isomer tagging, three new isomeric states in ^{129}Nd were observed at excitation energies of 1893, 2109 and 2284 keV, respectively. The isomer at 2284 keV decays with a measured half-life of 679 ± 60 ns. Excited rotational states built on this bandhead were observed using the JUROGAM spectrometer. By interpretation of experimental alignments and Pauli blocking arguments, it was possible to characterise this band as involving at least one $h_{11/2}$ proton meaning that a proton pair must be broken. The other proton is likely occupying the intruder $[404]9/2^+$ orbital, assigned through consideration of the high quadrupole deformation of this nucleus ($\beta_2 = 0.32$) and the observation of rotational bands built on this orbital for many nuclei in this mass region. The other two isomeric states are not populated strongly, and were only identified by the observed side feeding of their bandheads from the decay of the yrast isomer. Lack of counting statistics prevented a reliable measurement of the half-life of these states. Lack of Pauli blocking arguments prevented definite assignment of bandhead spin/parities and speculation was made as to the potential three-quasiparticle nature of these states. In addition, the relative excitation energies of three of the four previously known one-quasineutron bands have been fixed, with the $7/2^-$ state of the $[523]7/2^-$ band assigned as the ground state. Future experiments studying this nucleus and utilising a spectrometer sensitive to the highest spin states could identify single particle alignments at high rotational frequency, definitively assigning the yrast isomer's configuration. Improvements too could be made to the number of counting statistics at the focal plane, allowing measurement of a half-life for the non-yrast isomeric states.

7.2 ^{131}Pm

The sole previous study of excited states in this nucleus [62] identified a cascade of stretched E2 transitions, assigned to the rotationally aligned $[541]3/2^-$ orbital. This study preceded theoretical works by Xu, *et al* [101], and Moller, *et al* [87], which both suggest the spin/parity of the ground state for this nucleus is $5/2^-$. Indeed, the experimental results of the γ-ray spectroscopy performed in the present study are consistent with a ground-state $5/2^-$, with the rotational signature partner and extensions down to the $5/2^-$ state observed for the first time. A systematic comparison was made with other odd-Z even-N nuclides in the mass region, with the observed excitation energies and level lifetimes fitting systematic trends against mass-number, but not predicted deformation. The lack of consistency with deformation was discussed in the context of the light promethium isotopes having an irregular relationship between mass number and deformation, as well as incomplete information for the lightest (most deformed) praseodymium, lanthanum and caesium isotopes precluding the completion of systematic trend lines for these elements. Experimental limitations were largely due to the poor performance of the JUROGAM spectrometer at low transition energies leading to low statistics for the 67 keV peak. The assignment of 67 keV as an M1 results in an expected internal conversion coefficient of 4.9, but the low statistics meant that DCO and linear polarisation measurements were not possible and its coincidence with 147 keV could not be verified with absolute certainty. Subsequently, alternative level schemes assuming different multipolarities and ordering for these γ rays were considered, with reasoning made that these level schemes are not preferred. A final issue was that contaminant transitions from ^{131}Nd of a similar energy to those seen in this nucleus could not be filtered out using mass selection techniques. Installation of the UoYTube charged particle detector could have helped here by vetoing events coincident with a higher amount of evaporated protons, though the usefulness of this method will likely be limited owing to promethium and neodymium being separated by one proton.

7.3 ^{132}Pm

The sole previous study of this nucleus identified four rotational bands. However, ambiguity between their experimental single particle alignments left the bands without a definite quasiparticle configuration. As is common for doubly-odd nuclei in this mass region, the known bands are left "floating", with their excitation energies relative to the ground state unknown. The work presented in this thesis identified new prompt and delayed transitions, allowing fixation of the excitation energy of bands 1 and 2 relative to each other, and potentially to the ground state. The low frequency alignment associated with an $h_{11/2}$ proton was not observed in any of the four bands, indicating that this proton is involved in each band's configuration. Band 1 was observed to lie higher in excitation energy than band 2 and decays into band 2 via a 73 keV transition with a half-life of 187 ± 4 ns. These bands are assigned the two quasiparticle configurations $\pi[532]5/2^- \otimes \nu[514]9/2^-$ and $\pi[532]5/2^- \otimes \nu[402]5/2^+$. The implied multipolarity of the 73 keV transition out of Band 1 being an E1 is consistent with systematic comparisons of other doubly-odd nuclei in the region. Band 2 is observed to decay out of its isomeric bandhead by a 43 keV transition with a half-life of 19.9 ± 0.5 μs. Though direct measurement of the multipolarity of this transition was not possible, comparisons between theoretical single-particle transition rates (Weisskopf estimates) and the required spin/parity difference between the 5^- bandhead and the 3^+ ground state imply an M2 multipolarity for this transition. Beyond band extensions at both high and low energy, no further information was obtained for bands 3 and 4 meaning that they remain floating and without spin/parity assignments. Lack of observed focal plane transitions in coincidence with these bands imply that they either decay directly to the ground state, or their isomeric half-life is so long lived that the JUROGAM-MARA experimental setup is not sensitive to their decay.

7.4 Limitations of the JM06 Experiment and Future Improvements

Experimental limitations specific to the nuclei studied in this thesis have been discussed in the previous sections. This was more for completeness and it should not be thought that the data analysis was hindered by these limitations. However, certain experimental conditions and missing detector equipment resulted in significant hindrances for potential analysis of other nuclei. A major loss for the experimental setup was the UoYTube charged particle detector, used to veto events associated with a number of evaporated protons immediately following the formation of the recoil. It was decided the detector should not be included since its significant outgassing lead to an increase in vacuum pressure resulting in sparking at the electrostatic deflector. Without UoYTube, it was not possible to assign new bands observed at JUROGAM to a definite proton number.

Another problem with the experimental setup was the higher than optimal beam rate, picked to minimise sparking in the electrostatic deflector. The high beam rate resulted in a high recoil implantation rate. As discussed above, this was problematic when correlating γ rays seen at the focal plane with prompt transitions, and vice versa. Unfortunately, this high implantation rate also prevented the unambiguous identification of potential excited states in the beta-delayed proton emitting nucleus, ^{131}Sm. Figure 7.1, top panel displays focal plane γ rays associated with beta-delayed protons with an energy range of 1.5 - 7.0 MeV. Highlighted are the two lowest E2 transitions in the ^{130}Nd grand-daughter nucleus, a clear signature of the beta-delayed proton decay of ^{131}Sm. Figure 7.1, bottom panel displays the prompt radiation seen in delayed correlation with the 159 and 324 keV focal-plane γ rays. The spectrum is littered with contaminants, with a large unsubstracted Compton continuum contaminating the weakest transitions in this nucleus. Despite this, some strong peaks were still visible amongst the background. The low level of counting statistics meant that a $\gamma\gamma$-coincidence analysis was impossible. ^{131}Sm has an odd-neutron, and by comparison with its isotone neighbours ^{129}Nd and ^{127}Ce we can expect any of three bands to manifest at low spin: bands with moderate signature splitting built on the [523]$7/2^-$ or [402]$5/2^+$ orbitals, or a band built on [411]$1/2^+$ with large signature splitting.

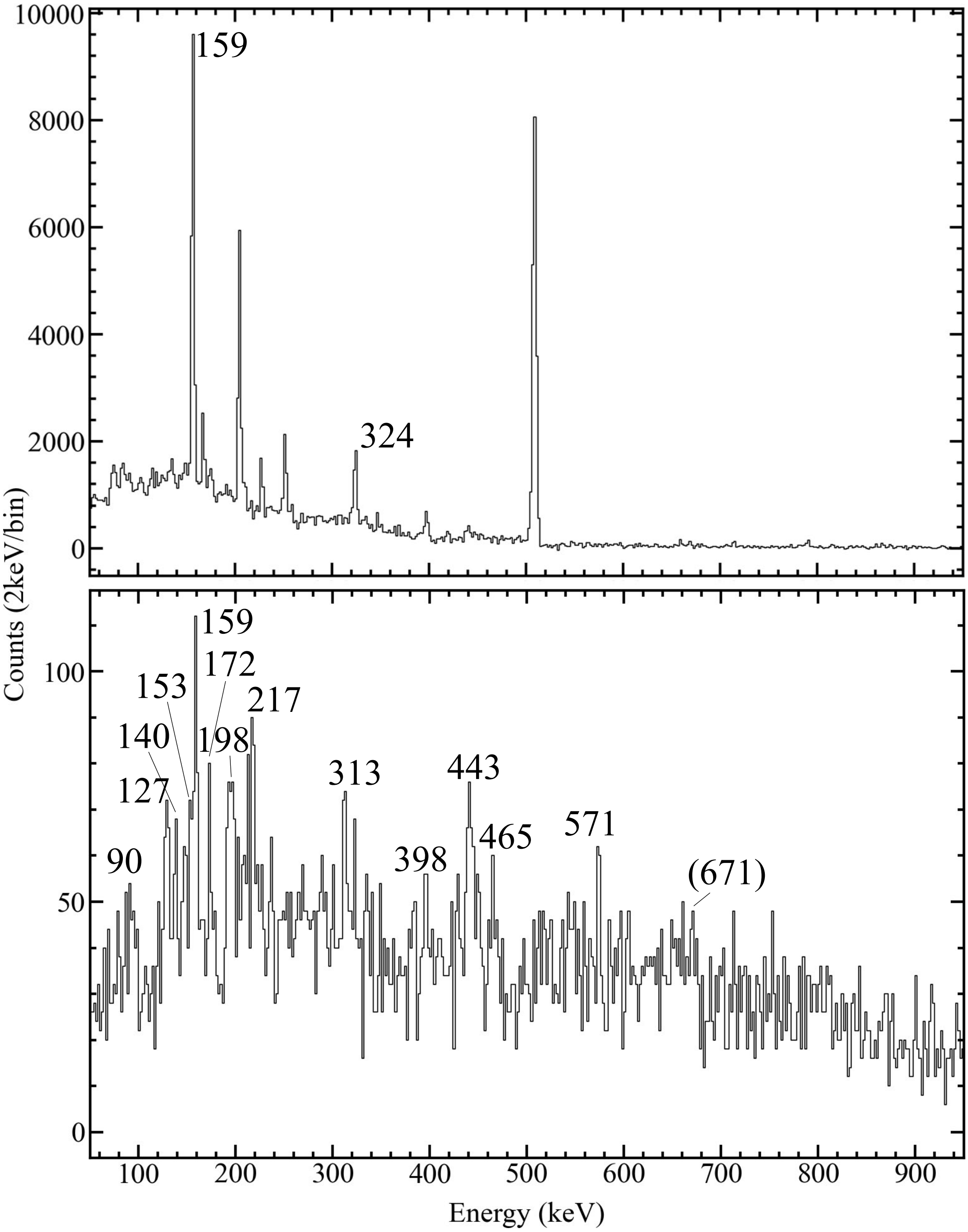

FIGURE 7.1: Top panel: focal-plane γ rays associated with beta-delayed protons with an energy range of 1.5 - 7.0 MeV. Bottom panel: prompt radiation seen in delayed correlation with the 159 and 324 keV focal-plane γ rays.

Because of their regular spacing, we can assume 313, 443 and 571 keV are crossover transitions in cascade. The irregular spacing and intensity patterns of the low energy transitions suggests that the large signature splitting option is likely. A proposed partial level scheme assembled largely by comparison with the ^{129}Nd [411]1/2$^+$ band is displayed in Figure 7.2. It can be seen that the proposed E2 transitions result in excitation energies consistent with those seen in the [411]1/2$^+$ band in ^{129}Nd. The lowest level transition is labelled "x" and left as ambiguous. Future experiments should run with a lower beam rate such that the recoil-decay correlations are consistent with ^{131}Sm recoils only.

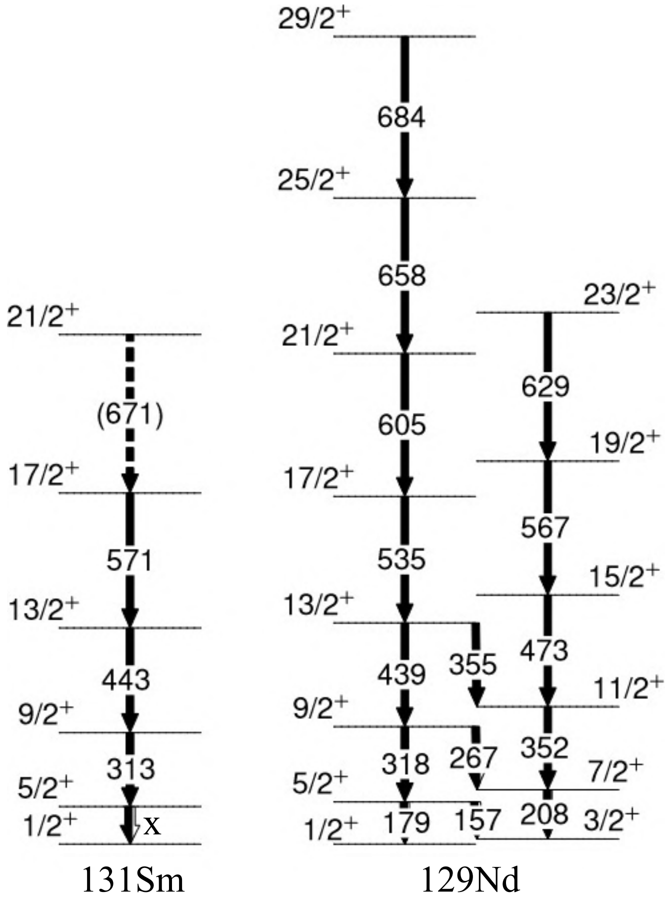
29/2+
684
25/2+
658
23/2+
21/2+
21/2+
629
(671)
605
19/2+
17/2+
17/2+
567
571
535
15/2+
13/2+
13/2+
443
439
355
473
11/2+
9/2+
9/2+
313
318
267
352
7/2+
5/2+
5/2+
1/2+
x
1/2+
179
157
208
3/2+
131Sm
129Nd

FIGURE 7.2: Proposed partial level scheme for transitions obtained via recoil-decay correlation with the beta-delayed proton decay of ^{131}Sm. The observed transitions are proposed to be part of a very signature split band based on the [411]1/2$^+$ orbital; comparison is made with the band built on this orbital in isotone neighbour ^{129}Nd.

Appendix A

Relativistic Doppler Correction

The kinetic energy of a relativistic moving particle is given by

$$E_k = m_0c^2 \left(\frac{1}{\sqrt{1-\beta^2}} - 1 \right), \beta = \frac{v}{c} \tag{A.1}$$

where m_0 is the rest mass of the particle, c is the speed of light and v is the velocity of the particle. For the JM06 run, the beam energy was 390 MeV while optimised for production of ^{131}Eu and 364 MeV while optimised for ^{129}Nd. Because of inelastic interactions in the target, the energy of the recoil entering MARA is somewhat less. According to calculations from the software SRIM the average kinetic energy of a recoil entering MARA is $E_k = 186$ MeV. Rearranging Equation A.1 for β, we obtain

$$\beta = \sqrt{1 - \left(\frac{1}{\frac{E_k}{m_0c^2} + 1} \right)}. \tag{A.2}$$

Inserting $E_k = 186$ MeV and, assuming a recoil mass of $m_0 = 131u = 122026.5$ MeV/c^2, we obtain a value for β equal to 0.0551, which is consistent with the experimentally determined Doppler shift measured in Chapter 3.

Appendix B

Phase 1 Gain Matching

The phase 1 detectors used in the JUROGAM array throughout the JM06 run showed significant deviations from the known "true" energy of photopeaks when using the "online" gain coefficients. The detectors were recalibrated by measurement of new gain matching coefficients using the calibration data taken at the start and end of the experimental run. The germanium detector calibration was performed using a combined ^{152}Eu^{133}Ba source. For each detector and each peak, the channel peak was fitted using a simple single-term gaussian imposed on a linear background. The fitting process was performed using a custom python script and checked by hand for accuracy. The measured centroid of each peak is then plotted against the known "true" energy for that peak as detailed in Figure B.1. This plot is then fitted according to Equation 3.26 and the coefficients A, B, C are extracted. The final gain matching coefficients are detailed in Table B.1 for completeness.

TABLE B.1: Phase 1 gain-matching coefficients used in the JM06 run. Parameter D is reserved for a cubic polynomial but this is not used here as a quadratic polynomial was deemed sufficient. The detector number corresponds phase 1 detector numbers as they are used in the tdrnames.txt configuration file.

Det Num	A	B	C	D
800	-1.8079709092E-01	2.0653145379E-01	-4.9425923056E-08	0
801	-2.2042566154E-01	3.0648954952E-01	1.4610233515E-08	0
802	6.0084477294E-01	2.8538811779E-01	1.5920867243E-07	0
803	-2.2226451408E-01	1.6078190743E-01	-2.2060105568E-08	0
804	-2.0291318167E-01	1.6149621927E-01	-2.7451806955E-08	0
805	5.0737694237E-01	2.0465262560E-01	2.9331182182E-08	0
806	-1.2166394488E+00	2.9409499009E-01	-2.1744366432E-07	0
807	-1.3321832323E+00	2.1872776118E-01	-1.1747120598E-07	0
832	-1.2234256180E-02	1.8440809762E-01	2.4448554331E-08	0
833	-1.2739091969E-01	3.0957576793E-01	-2.0885386133E-09	0
847	3.2415079400E-01	9.6276930703E-01	-3.7614661282E-07	0
835	-1.3958467341E+00	2.0732954417E-01	-1.0080756796E-07	0
836	-2.6414811085E+01	3.5998125996E-01	-3.3051593526E-06	0
837	-1.3591139286E+00	2.2979938176E-01	-1.1782483065E-07	0
838	-2.6020898432E+01	3.0488951751E-01	-2.3355107132E-06	0

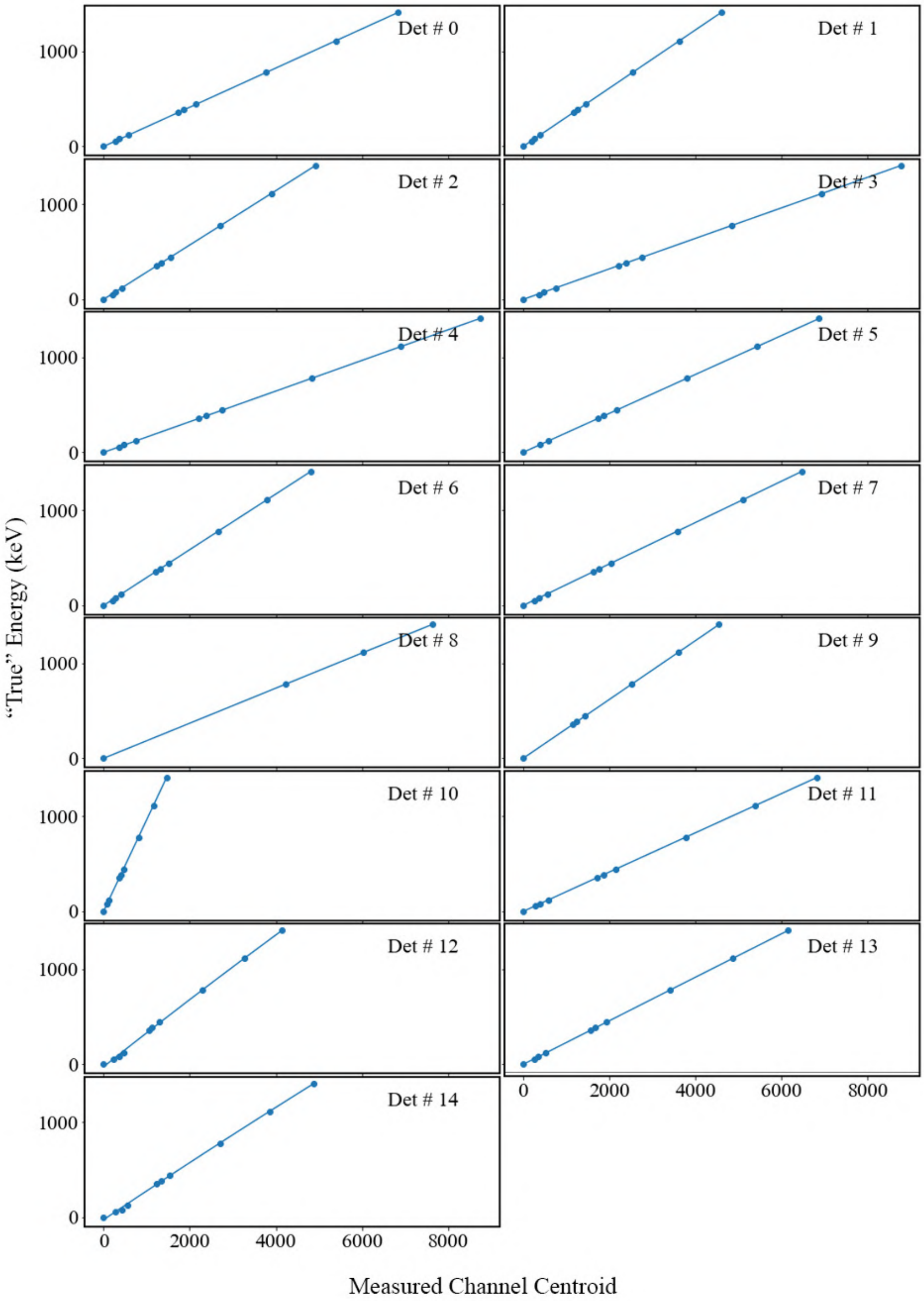

FIGURE B.1: Measured channel centroid for each phase 1 detector, for each of major the peaks in the ^{152}Eu^{133}Ba spectrum, against the "true" energy of each of these peaks. Coefficients obtained from the second-order polynomial fitting were used for gain matching of these detectors throughout the analysis of this data.

Bibliography

[1] J. S. Lilley, *Nuclear Physics - Principles and Applications.*, ch. Occurrence and stability of nuclei, p. 1.4.3. Manchester physics series, Wiley, 2013.

[2] K. S. Krane, *Introductory Nuclear Physics*, pp. 284–285. New York, US: John Wiley Sons, 3 ed., 1988.

[3] A. A. Harms, D. R. Kingdon, K. F. Schoepf, and G. H. Miley, *Principles of Fusion Energy*, ch. Fusion Fuels, pp. 8–10. WORLD SCIENTIFIC, 2000.

[4] J. Beringer *et al. Phys. Rev. D*, vol. 86, p. 010001, 2012.

[5] J. S. Lilley, *Nuclear Physics - Principles and Applications.*, ch. Semi-empirical mass formula, p. 2.2.2. Manchester physics series, Wiley, 2013.

[6] A. J. Sarty, K. G. R. Doss, G. Feldman, E. L. Hallin, R. E. Pywell, G. A. Retzlaff, D. M. Skopik, H. R. Weller, W. R. Dodge, J. W. Lightbody, J. S. O'Connell, and C. C. Chang, "Measurement of the reaction ^{3}He(γ,pp)n and its relation to three-body forces," *Phys. Rev. C*, vol. 47, pp. 459–467, Feb 1993.

[7] P. Mermod, J. Blomgren, B. Bergenwall, A. Hildebrand, C. Johansson, J. Klug, L. Nilsson, N. Olsson, M. Österlund, S. Pomp, U. Tippawan, O. Jonsson, A. Prokofiev, P.-U. Renberg, P. Nadel-Turonski, Y. Maeda, H. Sakai, and A. Tamii, "Search for three-body force effects in neutron–deuteron scattering at 95 MeV," *Physics Letters B*, vol. 597, no. 3, pp. 243–248, 2004.

[8] H.-W. Hammer, A. Nogga, and A. Schwenk, "Three-body forces: From cold atoms to nuclei," *Reviews of Modern Physics*, vol. 85, pp. 197–217, jan 2013.

[9] I. Tanihata, H. Hamagaki, O. Hashimoto, Y. Shida, N. Yoshikawa, K. Sugimoto, O. Yamakawa, T. Kobayashi, and N. Takahashi, "Measurements of interaction cross sections and nuclear radii in the light p-shell region," *Phys. Rev. Lett.*, vol. 55, pp. 2676–2679, Dec 1985.

[10] B. P. Abbott, R. Abbott, and T. D. Abbott, "Gravitational waves and gamma-rays from a binary neutron star merger: GW170817 and GRB 170817a," *The Astrophysical Journal*, vol. 848, p. L13, oct 2017.

[11] O. Tarasov and D. Bazin, "Lise++: Radioactive beam production with in-flight separators," *Nuclear Instruments and Methods in Physics Research Section B: Beam Interactions with Materials and Atoms*, vol. 266, no. 19, pp. 4657–4664, 2008. Proceedings of the XVth International Conference on Electromagnetic Isotope Separators and Techniques Related to their Applications.

[12] J. H. Hubbell, W. J. Veigele, E. A. Briggs, R. T. Brown, D. T. Cromer, and R. J. Howerton, "Atomic form factors, incoherent scattering functions, and photon scattering cross sections," *Journal of Physical and Chemical Reference Data*, vol. 4, no. 3, pp. 471–538, 1975.

[13] G. Gamow and E. Rutherford, "Mass defect curve and nuclear constitution," *Proceedings of the Royal Society of London. Series A, Containing Papers of a Mathematical and Physical Character*, vol. 126, no. 803, pp. 632–644, 1930.

[14] C. F. v. Weizsäcker, "Zur theorie der kernmassen," *Zeitschrift für Physik*, vol. 96, pp. 431–458, Jul 1935.

[15] C. H. Townes, H. M. Foley, and W. Low, “Nuclear quadrupole moments and nuclear shell structure,” *Phys. Rev.*, vol. 76, pp. 1415–1416, Nov 1949.

[16] E. Anders and N. Grevesse, “Abundances of the elements: Meteoritic and solar,” , vol. 53, pp. 197–214, Jan. 1989.

[17] O. Haxel, J. H. D. Jensen, and H. E. Suess, “On the "magic numbers" in nuclear structure,” *Phys. Rev.*, vol. 75, pp. 1766–1766, Jun 1949.

[18] R. D. Woods and D. S. Saxon, “Diffuse surface optical model for nucleon-nuclei scattering,” *Phys. Rev.*, vol. 95, pp. 577–578, Jul 1954.

[19] E. S. Paul, “Nuclear Models - Lecture 10,” November 2018.

[20] J. Wood, K. Heyde, W. Nazarewicz, M. Huyse, and P. van Duppen, “Coexistence in even-mass nuclei,” *Physics Reports*, vol. 215, no. 3, pp. 101–201, 1992.

[21] S. Cwiok, J. Dudek, W. Nazarewicz, J. Skalski, and T. Werner, “Single-particle energies, wave functions, quadrupole moments and g-factors in an axially deformed woods-saxon potential with applications to the two-centre-type nuclear problems,” *Computer Physics Communications*, vol. 46, no. 3, pp. 379–399, 1987.

[22] C. R. Bingham, L. L. Riedinger, L. H. Courtney, Z. M. Liu, A. J. Larabee, M. Craycraft, D. J. G. Love, P. J. Nolan, A. Kirwan, D. Thornley, P. Bishop, A. H. Nelson, M. A. Riley, and J. C. Waddington, “Three band cross-ings in the yrast structure of 162Hf,” *Journal of Physics G: Nuclear Physics*, vol. 14, pp. L77–L84, may 1988.

[23] I. Ragnarsson, T. Bengtsson, W. Nazarewicz, J. Dudek, and G. A. Leander, “Band termination at very high spin in ^{158}Yb,” *Phys. Rev. Lett.*, vol. 54, pp. 982–985, Mar 1985.

[24] S. G. Frauendorf, R. Bengtsson, and S. Frauendorf, "Quasiparticle spectra near the yrast line," *Nuclear Physics*, vol. 327, pp. 139–171, 1979.

[25] G. D. Dracoulis, "Isomers, nuclear structure and spectroscopy," *Physica Scripta*, vol. T152, p. 014015, jan 2013.

[26] R. Helmer and C. Reich, "Decay of an isomeric state in 178Hf with K$\geq$16," *Nuclear Physics A*, vol. 114, no. 3, pp. 649–662, 1968.

[27] S. G. Frauendorf, R. Bengtsson, S. Frauendorf, and F.-R. May, "Quasiparticle levels in rotating rare earth nuclei: A cranked shell-model dictionary," vol. 35, 1986.

[28] F. Donau and S. Frauendorf, *Proc. Conf. on High Angular Momentum Properties of Nuclei*, vol. 4, p. 143. Harwood, 1982.

[29] K. S. Krane, *Introductory Nuclear Physics*, ch. Gamma Decay, p. 327. New York, US: John Wiley Sons, 3 ed., 1988.

[30] K. S. Krane, *Introductory Nuclear Physics*, ch. Gamma Decay, pp. 327–328. New York, US: John Wiley Sons, 3 ed., 1988.

[31] K. S. Krane, *Introductory Nuclear Physics*, ch. Gamma Decay, pp. 327–335. New York, US: John Wiley Sons, 3 ed., 1988.

[32] J. S. Lilley, *Nuclear Physics - Principles and Applications.*, ch. Gamma Emission, pp. 3.2 – 3.2.2. Manchester physics series, Wiley, 2013.

[33] J. M. Blatt and V. F. Weisskopf, *Theoretical Nuclear Physics*, pp. 623–627. Springer, New York, NY, 1952.

[34] R. Bass, "Fusion of heavy nuclei in a classical model," *Nuclear Physics A*, vol. 231, no. 1, pp. 45–63, 1974.

[35] J. Newton, F. Stephens, R. Diamond, W. Kelly, and D. Ward, “Gamma-ray de-excitation of compound-nucleus-reaction products,” *Nuclear Physics A*, vol. 141, no. 3, pp. 631–640, 1970.

[36] P. J. Twin, *Superdeformation in 152Dy*, pp. 59–68. Boston, MA: Springer US, 1988.

[37] J. Simpson, “The Euroball Spectrometer,” *Zeitschrift für Physik A Hadrons and Nuclei*, vol. 358, pp. 139–143, Feb 1997.

[38] W. Korten and S. Lunardi, “Achievements with the euroball spectrometer,” tech. rep., EUROBALL Coordination Committee, 2003.

[39] B. Haas, “Identical superdeformed bands,” *Progress in Particle and Nuclear Physics*, vol. 38, pp. 1–14, 1997.

[40] M. A. Riley, J. Simpson, and E. S. Paul, “High resolution gamma-ray spectroscopy and the fascinating angular momentum realm of the atomic nucleus,” *Physica Scripta*, vol. 91, p. 123002, nov 2016.

[41] P. Rahkila, “Grain—a java data analysis system for total data readout,” *Nuclear Instruments and Methods in Physics Research Section A: Accelerators, Spectrometers, Detectors and Associated Equipment*, vol. 595, p. 637–642, Oct 2008.

[42] D. Radford, “Radware.” https://radware.phy.ornl.gov/.

[43] J. Mayer, “HDTV: A Nuclear Spectrum Analysis Tool.”

[44] E. Liukkonen, “The Jyväskylä K130 Cyclotron Project,” tech. rep., Department of Physics, University of Jyväskylä, May 1989.

[45] J. Pakarinen, J. Ojala, P. Ruotsalainen, H. Tann, H. Badran, T. Calverley, J. Hilton, T. Grahn, P. Greenlees, M. Hytönen, A. Illana Sison, A. Kauppinen, M. Luoma, P. Papadakis, J. Partanen, K. Porras, M. Puskala,

P. Rahkila, K. Ranttila, and G. Zimba, “The Jurogam 3 Spectrometer,” *The European Physical Journal A*, vol. 56, 05 2020.

[46] I. A. Alnour, H. Wagiran, N. Ibrahim, S. Hamzah, W. B. Siong, and M. S. Elias, “New approach for calibration the efficiency of HpGe detectors,” *AIP Conference Proceedings*, vol. 1584, p. 30005, 2014.

[47] K. Krane, R. Steffen, and R. Wheeler, “Directional correlations of gamma radiations emitted from nuclear states oriented by nuclear reactions or cryogenic methods,” *Atomic Data and Nuclear Data Tables*, vol. 11, no. 5, pp. 351–406, 1973.

[48] P. Jones, L. Wei, F. Beck, P. Butler, T. Byrski, G. Duchêne, G. de France, F. Hannachi, G. Jones, and B. Kharraja, “Calibration of the new composite “clover” detector as a Compton polarimeter for the EUROGAM array,” *Nuclear Instruments and Methods in Physics Research Section A: Accelerators, Spectrometers, Detectors and Associated Equipment*, vol. 362, no. 2, pp. 556–560, 1995.

[49] E. S. Paul, D. B. Fossan, K. Hauschild, I. M. Hibbert, P. J. Nolan, H. Schnare, J. M. Sears, I. Thorslund, R. Wadsworth, A. N. Wilson, J. N. Wilson, and I. Ragnarsson, “High-fold γ-ray spectroscopy of ^{117}I: Coexistence of collective and noncollective structures,” *Phys. Rev. C*, vol. 59, pp. 1984–1998, Apr 1999.

[50] P. Ruotsalainen, *Gamma-ray spectroscopy employing JUROGAM 3 and MARA – in-beam studies of N $\approx$ Z nuclei at JYFL, NuSpin 2019*.

[51] J. Sarén, *The ion-optical design of the MARA recoil separator and absolute transmission measurements of the RITU gas-filled recoil separator*. PhD thesis, University of Jyväskylä, 2011.

[52] F. Asaro, F. L. Reynolds, and I. Perlman, "The Complex Alpha-Spectra of Am^{241} and Cm^{242}," *Phys. Rev.*, vol. 87, pp. 277–285, Jul 1952.

[53] F. Asaro, S. G. Thompson, and I. Perlman, "The Alpha Spectra of Cm^{242}, Cm^{243}, and Cm^{244}," *Phys. Rev.*, vol. 92, pp. 694–702, Nov 1953.

[54] F. Asaro and I. Perlman, "The Alpha-Spectra of Pu^{239} and Pu^{240}," *Phys. Rev.*, vol. 88, pp. 828–831, Nov 1952.

[55] S. Antman, D. Landis, and R. Pehl, "Measurements of the fano factor and the energy per hole-electron pair in germanium," *Nuclear Instruments and Methods*, vol. 40, no. 2, pp. 272–276, 1966.

[56] C. Beausang, D. Prevost, M. Bergstrom, G. deFrance, B. Haas, J. Lisle, C. Theisen, J. Timár, P. Twin, and J. Wilson, "Using high-fold data from the new generation of -ray detector arrays," *Nuclear Instruments and Methods in Physics Research Section A: Accelerators, Spectrometers, Detectors and Associated Equipment*, vol. 364, no. 3, pp. 560–566, 1995.

[57] P. Möller, A. Sierk, T. Ichikawa, and H. Sagawa, "Nuclear ground-state masses and deformations: FRDM(2012)," *Atomic Data and Nuclear Data Tables*, vol. 109-110, pp. 1–204, may 2016.

[58] O. Zeidan, D. J. Hartley, L. L. Riedinger, M. Danchev, W. Reviol, W. D. Weintraub, J.-y. Zhang, A. Galindo-Uribarri, C. J. Gross, S. D. Paul, C. Baktash, M. Lipoglavsek, D. C. Radford, C. H. Yu, D. G. Sarantites, M. Devlin, M. P. Carpenter, R. V. F. Janssens, D. Seweryniak, and E. Padilla, "Rotational structures in ^{129}Nd and signature splitting systematics of the $\nu h_{11/2}$ bands in $a \sim 130$ nuclei," *Phys. Rev. C*, vol. 65, p. 024303, Jan 2002.

[59] H. Mach, R. Gill, and M. Moszyński, “A method for picosecond lifetime measurements for neutron-rich nuclei: (1) outline of the method,” *Nuclear Instruments and Methods in Physics Research Section A: Accelerators, Spectrometers, Detectors and Associated Equipment*, vol. 280, no. 1, pp. 49–72, 1989.

[60] B. Smith, L. Riedinger, H. Jin, W. Reviol, W. Satuła, A. Galindo-Uribarri, D. Sarantites, J. Wilson, D. LaFosse, and S. Mullins, “Enhanced deformation in light Pr nuclei,” *Physics Letters B*, vol. 443, no. 1, pp. 89–96, 1998.

[61] W. F. Piel, C. W. Beausang, D. B. Fossan, L. Hildingsson, and E. S. Paul, “Collective band structures in the γ-soft nucleus ^{135}Nd,” *Phys. Rev. C*, vol. 35, pp. 959–967, Mar 1987.

[62] C. M. Parry, A. J. Boston, C. Chandler, A. Galindo-Uribarri, I. M. Hibbert, V. P. Janzen, D. T. Joss, S. M. Mullins, P. J. Nolan, E. S. Paul, P. H. Regan, S. M. Vincent, R. Wadsworth, D. Ward, and R. Wyss, “Yrast structures in the neutron-deficient $^{127}_{59}$Pr$_{68}$ and $^{131}_{61}$Pm$_{70}$ nuclei,” *Phys. Rev. C*, vol. 57, pp. 2215–2221, May 1998.

[63] D. C. B. Watson, P. J. Bishop, M. J. Godfrey, A. N. James, I. Jenkins, T. P. Morrison, P. J. Nolan, M. A. Skelton, K. L. Ying, K. A. Connell, and J. Simpson, “Investigation of triaxiality in the a = 129 region,” Tech. Rep. Daresbury 1986-1987 Annual, 1987.

[64] Y. He, M. J. Godfrey, J. Jenkins, A. J. Kirwan, S. M. Mullins, P. J. Nolan, E. S. Paul, and R. Wadsworth, “Rotational band structures in ^{129}La,” *Journal of Physics G: Nuclear and Particle Physics*, vol. 18, pp. 99–119, jan 1992.

[65] N. Ganbaatar, Y. Kormitski, K. A. Mezilev, Y. N. Novikov, A. M. Nurmukhamedov, A. Potempa, E. Senyavski, and F. Tarkani, “New Isomer States of the Nuclei ^{131}Pr, ^{138}Pm, ^{146}Tb,” in *Program and Theses*, 1983.

[66] E. Paul, A. Boston, D. Joss, P. Nolan, J. Sampson, A. Semple, F. Farget, A. Gizon, D. Santos, B. Nyakó, N. O'Brien, C. Parry, and R. Wadsworth, "Detailed spectroscopy of the normally deformed states in 132Ce," *Nuclear Physics A*, vol. 619, no. 1, pp. 177–201, 1997.

[67] T. Kibédi, T.W. Burrows, M.B. Trzhaskovskaya, P.M. Davidson, C.W. Nestor, Jr., "Evaluation of theoretical conversion coefficients using BrIcc," *Nucl. Instr. and Meth. A*, vol. 589, pp. 202–229, 2008.

[68] G. Marguier, A. Charvet, J. Genevey, C. Richard-Serre, A. Knipper, and G. Walter, "The decay of 1.7 s ^{123m}Cs and 5.9 min ^{123}Cs," *Journal of Physics G: Nuclear Physics*, vol. 7, pp. 101–113, jan 1981.

[69] J. R. Hughes, D. B. Fossan, D. R. LaFosse, Y. Liang, P. Vaska, and M. P. Waring, "Alignment effects in odd-mass Cs isotopes: Spectroscopy of ^{125}Cs," *Phys. Rev. C*, vol. 44, pp. 2390–2399, Dec 1991.

[70] C. Droste, D. Chlebowska, J. Dobaczewski, F. Dönau, A. Kerek, G. Leander, J. Srebrny, and W. Waluś, "Collective quadrupole dynamics and the band structure of the nucleus ^{127}Cs," *Nuclear Physics A*, vol. 341, no. 1, pp. 98–124, 1980.

[71] U. Garg, T. P. Sjoreen, and D. B. Fossan, "Collective properties of the odd-mass Cs nuclei. I. ^{127,129,131,133}Cs," *Phys. Rev. C*, vol. 19, pp. 207–216, Jan 1979.

[72] K. Starosta, C. Droste, T. Morek, J. Srebrny, D. B. Fossan, D. R. LaFosse, H. Schnare, I. Thorslund, P. Vaska, M. P. Waring, W. Satuła, S. G. Rohoziński, R. Wyss, I. M. Hibbert, R. Wadsworth, K. Hauschild, C. W. Beausang, S. A. Forbes, P. J. Nolan, and E. S. Paul, "Band structure of the odd-even ^{125}La, ^{127}La nuclei," *Phys. Rev. C*, vol. 53, pp. 137–150, Jan 1996.

[73] J. Leigh, K. Nakai, K. Maier, F. Pühlhofer, F. Stephens, and R. Diamond, "Energy-level systematics of odd-mass lanthanum isotopes; a new coupling scheme," *Nuclear Physics A*, vol. 213, no. 1, pp. 1–21, 1973.

[74] A. Gizon, J. Genevey, G. Cata-Danil, D. Barnéoud, R. Béraud, A. Emsallem, C. Foin, J. Gizon, C. F. Liang, P. Paris, I. Penev, A. Plochoki, and B. Weiss, "Decay of 129Nd to low-lying states in 129Pr," *Zeitschrift für Physik A Hadrons and Nuclei*, vol. 358, pp. 369–371, Dec 1997.

[75] J. Genevey, A. Gizon, C. Foin, D. Bucurescu, G. Căta-Danil, B. Weiss, D. Barnéoud, T. von Egidy, J. Gizon, C. Liang, and P. Paris, "Non-yrast level structures in the isotopes 131Pr and 131La," *Nuclear Physics A*, vol. 611, no. 2, pp. 247–269, 1996.

[76] S.-W. Xu, Y.-X. Xie, X.-D. Wang, Z.-K. Li, B. Guo, C.-G. Leng, C.-F. Wang, and Y. Yu, "(EC + β+) decay of 133Sm and 1.1 s isomer of 133Pr," *The European Physical Journal A - Hadrons and Nuclei*, vol. 11, pp. 277–278, Jul 2001.

[77] T. Conlon, "New M2 isomers in neutron deficient I, La and Pr associated with a deformed nuclear shape," *Nuclear Physics A*, vol. 213, no. 3, pp. 445–460, 1973.

[78] N. Xu, C. W. Beausang, R. Ma, E. S. Paul, W. F. Piel, D. B. Fossan, and L. Hildingsson, "High spin states in ^{137}Pr," *Phys. Rev. C*, vol. 39, pp. 1799–1808, May 1989.

[79] S. Muralithar, K. Rani, R. P. Singh, R. Kumar, J. J. Das, J. Gehlot, K. S. Golda, A. Jhingan, N. Madhavan, S. Nath, P. Sugathan, T. Varughese, M. Archunan, P. Barua, A. Gupta, M. Jain, A. Kothari, B. P. A. Kumar, A. J. Malyadri, U. G. Naik, R. Kumar, R. Kumar, J. Zacharias, S. Rao, S. K. Saini, S. K. Suman, M. Kumar, E. T. Subramaniam, S. Venkataramanan, A. Dhal, G. Jnaneswari, D. Negi, M. K. Raju, T. Trivedi, and R. K. B. and,

"Indian national gamma array at IUAC," *Journal of Physics: Conference Series*, vol. 312, p. 052015, sep 2011.

[80] P. Regan, R. Wadsworth, J. Hughes, G. Gyapong, W. Gelletly, M. Godfrey, I. Jenkins, Y.-J. He, S. Mullins, P. Nolan, J. Simpson, B. Varley, and D. Watson, "Spectroscopy of the light rare-Earth nuclei 133Pm and 133Sm: Configuration-dependent pairing and evidence for strong residual proton-neutron interactions in neighbouring odd-N and odd-Z nuclei," *Nuclear Physics A*, vol. 533, no. 3, pp. 476–504, 1991.

[81] M. A. Riley and E.S. Paul. private communication.

[82] G. Nowicki, J. Buschmann, A. Hanser, H. Rebel, H. Faust, D. Habs, H. Klewe-Nebenius, and K. Wisshak, "The level scheme of 137Nd from (, n) reactions and from -decay of the 11/2 isomer of 137Pm," *Nuclear Physics A*, vol. 249, no. 1, pp. 76–92, 1975.

[83] N. Xu, C. W. Beausang, E. S. Paul, W. F. Piel, P. K. Weng, D. B. Fossan, E. Gülmez, and J. A. Cizewski, "Observation of both $h_{\frac{11}{2}}$ proton and neutron alignments in ^{139}Pm," *Phys. Rev. C*, vol. 36, pp. 1649–1652, Oct 1987.

[84] J. Chiba, R. S. Hayano, M. Sekimoto, H. Nakayama, and K. Nakai, "Band Structures of the ^{135}La, ^{133}La and ^{129}Cs Nuclei," *J.Phys.Soc.Jap.*, vol. 43, p. 1109, 1977.

[85] P. Möller, A. Sierk, T. Ichikawa, and H. Sagawa, "Nuclear ground-state masses and deformations: Frdm(2012)," *Atomic Data and Nuclear Data Tables*, vol. 109-110, pp. 1–204, 2016.

[86] Xu, S.-W., Xie, Y.-X., Xu, F.-R., Li, Z.-K., and Wang, X.-D., "First decay study of the new isotope 129Pm near the proton drip line," *Eur. Phys. J. A*, vol. 21, no. 1, pp. 75–77, 2004.

[87] P. MÖLLER, J. NIX, and K.-L. KRATZ, "Nuclear properties for astrophysical and radioactive-ion-beam applications," *Atomic Data and Nuclear Data Tables*, vol. 66, no. 2, pp. 131–343, 1997.

[88] P. Möller, M. Mumpower, T. Kawano, and W. Myers, "Nuclear properties for astrophysical and radioactive-ion-beam applications (ii)," *Atomic Data and Nuclear Data Tables*, vol. 125, pp. 1–192, 2019.

[89] W. Nazarewicz, J. Dudek, R. Bengtsson, T. Bengtsson, and I. Ragnarsson, "Microscopic study of the high-spin behaviour in selected A $\approx$ 80 nuclei," *Nuclear Physics A*, vol. 435, no. 2, pp. 397–447, 1985.

[90] P. Von Brentano, O. Vogel, I. Wiedenhoever, R. Kuehn, and A. Gelberg, *Triaxiality in odd and even nuclei of the A=130 mass region*. Romania: World Scientific, 1996.

[91] R. Wadsworth, G. J. Gyapong, J. R. Hughes, P. H. Regan, D. L. Watson, E. Dragulescu, P. J. Nolan, M. J. Godfrey, I. Jenkins, Y. J. He, B. J. Varley, W. Gelletly, and J. Simpson, "Rotational Structures in ^{132}Pm," Tech. Rep. Daresbury 1990-1991 Annual, 1991.

[92] C. J. Gallagher and S. A. Moszkowski, "Coupling of angular momenta in odd-odd nuclei," *Phys. Rev.*, vol. 111, pp. 1282–1290, Sep 1958.

[93] R. Wadsworth, S. Mullins, P. Bishop, A. Kirwan, M. Godfrey, P. Nolan, and P. Regan, "Rotational bands in the doubly odd N = 73 nucleus 134Pm," *Nuclear Physics A*, vol. 526, no. 1, pp. 188–204, 1991.

[94] C. W. Beausang, L. Hildingsson, E. S. Paul, W. F. Piel, N. Xu, and D. B. Fossan, "Similar rotational band structures in doubly-odd ^{136}Pm and ^{134}Pr," *Phys. Rev. C*, vol. 36, pp. 1810–1819, Nov 1987.

[95] C. W. Beausang, P. K. Weng, R. Ma, E. S. Paul, W. F. Piel, N. Xu, and D. B. Fossan, "Rotational band structures in doubly odd ^{138}Pm," *Phys. Rev. C*, vol. 42, pp. 541–549, Aug 1990.

[96] C. M. Petrache, M. Nespolo, S. Brant, G. Lo Bianco, D. Bazzacco, S. Lunardi, P. Spolaore, M. Axiotis, N. Blasi, G. de Angelis, T. Kröll, N. Marginean, T. Martinez, R. Menegazzo, D. R. Napoli, B. Quintana, A. Saltarelli, A. Ventura, and D. Vretenar, "Spectroscopy near the proton drip line in the deformed $a = 130$ mass region: The ^{126}Pr nucleus," *Phys. Rev. C*, vol. 64, p. 044303, Sep 2001.

[97] D. J. Hartley, L. L. Riedinger, M. Danchev, W. Reviol, O. Zeidan, J.-y. Zhang, A. Galindo-Uribarri, C. J. Gross, C. Baktash, M. Lipoglavsek, S. D. Paul, D. C. Radford, C.-H. Yu, D. G. Sarantites, M. Devlin, M. P. Carpenter, R. V. F. Janssens, D. Seweryniak, and E. Padilla, "Toward complete spectroscopy of ^{128}Pr and rotational structures in ^{126}Pr," *Phys. Rev. C*, vol. 65, p. 044329, Apr 2002.

[98] C. Petrache, S. Brant, D. Bazzacco, G. Falconi, E. Farnea, S. Lunardi, V. Paar, Z. Podolyák, R. Venturelli, and D. Vretenar, "Detailed spectroscopy and IBFFM interpretation of the odd-odd nuclei 132Pr and 130Pr," *Nuclear Physics A*, vol. 635, no. 3, pp. 361–383, 1998.

[99] B. Cullity, S. Stock, and S. Stock, *Elements of X-ray Diffraction*. Addison-Wesley series in metallurgy and materials, Prentice Hall, 2001.

[100] M. O. Kortelahti, B. D. Kern, R. A. Braga, R. W. Fink, I. C. Girit, and R. L. Mlekodaj, "Transitional nuclei in the rare-earth region: Energy levels and structure of ^{130,132}Ce, ^{132,134}Nd, and ^{134}Pm, via β decay of ^{130,132}Pr, ^{132,134}Pm, and ^{134}Sm," *Phys. Rev. C*, vol. 42, pp. 1267–1278, Oct 1990.

[101] G. Canchel, R. Béraud, E. Chabanat, A. Emsallem, N. Redon, P. Dendooven, J. Huikari, A. Jokinen, V. Kolhinen, G. Lhersonneau, M.

Oinonen, A. Nieminen, H. Penttilä, K. Peräjärvi, J.C. Wang, and J. Äystö, "A new isomer in ^{125}La," *Eur. Phys. J. A*, vol. 5, no. 1, pp. 1–2, 1999.